

Kati Tschöpe

# Degradation of Cathode Lining in Hall-Héroult Cells

Autopsies and FEM Simulations

Thesis for the degree of Philosophiae Doctor

Trondheim, November 2010

Norwegian University of Science and Technology  
Faculty of Natural Sciences and Technology  
Department of Materials Science and Engineering



**NTNU – Trondheim**  
Norwegian University of  
Science and Technology

**NTNU**

Norwegian University of Science and Technology

Thesis for the degree of Philosophiae Doctor

Faculty of Natural Sciences and Technology  
Department of Materials Science and Engineering

© Kati Tschöpe

ISBN 978-82-471-2475-8 (printed ver.)  
ISBN 978-82-471-2476-5 (electronic ver.)  
ISSN 1503-8181

Doctoral theses at NTNU, 2010:241

IMT-Report 2010:131

Printed by NTNU-trykk

---

This thesis has been submitted to

Department of Materials Science and Engineering  
Norwegian University of Science and Technology

in partial fulfilment of the requirements for  
the academic degree

**Philosophiae Doctor**

September 2010

## Preface

The present dissertation is based on work carried out at Inorganic Materials and Ceramics Research Group, the Department of Materials Science and Engineering (DMSE), the Norwegian University of Science and Technology, NTNU, under the supervision of Prof. Tor Grande. The work was done during the period August 6<sup>th</sup> 2007 to September 2010.

All sample preparations and experiments have been conducted by the author, except the following characterization work: Electron probe microanalysis (EPMA) was done by Morten Peder Raanes at DMSE, NTNU. X-ray diffraction analysis and subsequent evaluation with UniQuant was performed by Lorentz Petter Lossius from Hydro Aluminium-Primary Metal Technology in Årdal. The thermal conductivity samples 3ACarbonSlice1/6, 3ALensSlice2/3/4 were measured with the LaserFlash LFA457 by Anne Støre from SINTEF.

Part of this dissertation have been published in the following papers:

- ◆ Kati Tschöpe, Christian Schøning and Tor Grande, "Autopsies of Spent Pot Lining - A Revised View", *Light Metals (TMS)*, 2009, pp. 1085-1090.
- ◆ Kati Tschöpe, Jørn Rutlin and Tor Grande, "Chemical Degradation Map for Sodium Attack in Refractory Linings", *Light Metals (TMS)*, 2010, pp. 871-876.
- ◆ Kati Tschöpe and Tor Grande, "Degradation of Cathode Linings in Hall-Héroult Cells - An Autopsy Study of Three Shut Down Cells", 2010, to be submitted.

## Acknowledgements

The pursuit of a Ph.D. project is comparable to climbing one of Norway's high peaks. It is both a painful and enjoyable experience. The way up is lined with bitterness, hardships and frustration. Going ahead, step by step is only possible through a strong will, encouragement, trust and with the kind help of others. Finally standing on top and enjoying the great scenery, combines not only what has been created and what lies behind, it also holds the future. Taking all this in mind, I realized that, in fact only teamwork brought me to where I am now. Thus though it will not be enough to express my gratitude in words to all those people who helped me, but I would still like to give many thanks to all these people.

First of all, I give my sincere thanks to my supervisor Professor Tor Grande, who accepted me as his Ph.D. student without any hesitation after he accompanied my diploma thesis. During all this time he offered me so much advice, through his impressive broad knowledge of material science, enthusiasm and perpetually positive attitude. He always managed to supervise me patiently and guided me into the right direction. I learned a lot from him. His confidence in me and my work was invaluable for me. It helped me to recharge my batteries every day, to have the power and to motivate myself to finish my dissertation successfully. I would also like to thank him for guiding me through the time of writing this dissertation. I appreciate the critical reading and quick response to my drafts even if when his schedule called for 48 working hours per day.

Special thanks are also given to my college, office neighbor, friend and "refractory twin" Zhaohui Wang. Her insights and complementary perspectives have led to fruitful discussions regarding this project. Her help, experience, friendship and lively character was and still is very important to me.

I am indebted to the technical staff supporting the "Ceramic Group" for always being helpful. Especially chief engineer Morten Peder Raanes, senior engineer Yingda Yu, engineer Elin Nilsen and Dr. Julian Tolchard did a very good job to assist me with the electron microscopes. In general, I would like to express my appreciation to all persons in our institute who have offered me their time and support, when I needed it.

I would like to thank senior advisor Christian Schøning, research manager Egil Skybakmoen and chief scientist Asbjørn Solheim from SINTEF Materials and Chemistry for their friendly nature, the good collaboration, including scientific and non-scientific discussions, help with performing autopsies in Sunndalsøra and Årdal and the impressive trips to San Francisco and Seattle. Furthermore I got very kind assistance by the technical staff from SINTEF, namely engineer Ove Darell, Dr. Ove Paulsen and research engineer Anne Støre. They helped me with sample preparations, provided equipments and knowledge not only for thermal conductivity measurements.

I also want to acknowledge Hydro Aluminium AS for allowing the publication of the

---

present work. During the last three years regular meetings between Hydro-SINTEF-NTNU were held in order to collect new results and discuss it directly with the industry. This experience and their response was really important for me and I like to thank all members of the entire BIP-group for this unforgettable time. In this context I like to thank Dr. Nancy Jorunn Holt for all the organizational aspects and here friendly nature. I wish to thank Dr. Jørn Rutlin, who was the responsible person at Hydro (particularly for this project) for his kind support and response to my papers and manuscript. I am grateful to Dr. Lorentz Petter Lossius from Hydro Aluminium-Primary Metal Technology in Årdal, who performed the XRF measurements and subsequent evaluation with UNIQuant. Financial support from Hydro Aluminium AS and the Research Council of Norway through the project "Project Innovations for High Current Density (PIHDC); Sub-project 5-Development of tools for simulations of degradation of cathode linings" is gratefully acknowledged.

During this work Professor Zhiliang Zhang from the department of structural engineering at NTNU introduced me to the complex world of the finite element method. I am very thankful to him, especially that he never lost his patience with me. Great support with the simulation software was given through Dr. Bertil Nistad, who is an application engineer at COMSOL and their support desk. Thanks for the help to solve the problems and to approve my solutions.

Special thanks go to Professor Lars Arnberg, whom I met in 2006 at the Technical University Bergakademie Freiberg. He provided me the first contact to the NTNU and taught me the pronunciation of my first and favorite norwegian word "jordbærsyltetøy". He is a reliable, caring and important person not only for me.

I have spent some wonderful years in Trondheim and I owe that to a big extent to some wonderful and exotic friendships, thanks to all of you!

Last, but not least, I like to thank my family. They never lost their faith and trust in me! I received their support whenever I needed it. I am specially very grateful to my mother Thurit Tschöpe. Her understanding and her love encouraged me to work hard and to continue my education to reach the point where I am now. Her firm, but at the same time relaxed and kind-hearted personality has affected me to be steadfast and never bend due to difficulties. She always lets me know that she is proud of me and that she loves me, which motivates me to work hard and to do my best.

Finally I like to dedicate this work to my deep love Thomas Ludwig. We went through everything together, since we were 15 years old. I cannot express in words what I feel for you and how I appreciate your support especially during the last three years. You gave me the courage to continue and you found your own unconventional way to stop me, when I doubted myself. I thank you for all and I hope that our dream never ends...

## Summary

The aluminium industry is continually facing the problem to lower the energy consumption and to increase the productivity by improving the current high amperage cell technology. Another challenge is to eliminate cell failures, which cause disturbances or premature cell shutdowns. The degradation of the cathode lining and cathode heave are two of the key factors which influence the performance and lifetime of the cathode, and the present study has focused on these two phenomena.

Autopsies of cathodes after pot failures or shutdowns of cells have frequently been used to identify the cause of pot failures and the degradation of the cathode lining. The sequence of materials observed from the carbon cathode to the non-reacted refractory lining has been considered to reflect the situation in the lining before the pot was taken out of service. In this work it was demonstrated that this is not necessarily the case based on annealing experiments of spent pot lining (SPL) samples and X-ray diffraction analysis and electron microscopy of the corresponding specimens. The annealing experiments demonstrated that the thermal gradient in the lining is reversed during cooling and that the physical appearance of the lining reflects a combination of the cooling and operation of the cell. A revised view of the analysis of SPL is presented taking into consideration the presence of a molten phase below the carbon cathode. This molten phase consists mainly of bath components and is therefore non-viscous in nature. Solid particles originating from the pristine material or precipitated reaction products are also possibly present. Since the cell is well insulated in the bottom the cathode lining is cooled from the top to the bottom when the cell is shut down. Thus the molten phase solidifies from top to the bottom in the lining, which was supported by the experimental findings.

Sodium was identified to govern the degradation of the refractory lining based on electron microprobe analysis of the reaction front in the SPL. Since only sodium was found in the first few millimeters of the reaction front, this region was termed the "first reaction front". Furthermore, fluorides originating from the penetrating bath were detected in a certain distance and this was denoted the "second reaction front". The strong reductive nature of sodium was demonstrated by Si(s) droplets found in the SPL down to the first reaction front. The presence of Si also permitted a possible explanation for the nature of the transport of sodium from the carbon cathode to the reaction front. Inside and below the carbon cathode Na(g) is dissolved and transported through the bath. Below the build-up layer oxidation of Na(g) to Na<sup>+</sup> takes place accompanied by the reduction of SiO<sub>2</sub> to Si(s). Reported data on the mobility of the different ions in relevant viscous melts revealed that in contrast to diffusion of sodium, the mobility of oxygen is strongly dependent on the viscosity of the molten phase formed at the reaction front. Furthermore it was proposed that the degradation reaction with sodium is faster than the diffusion. Thus the rate limiting step for the degradation of refractory linings is the mobility of O<sup>2-</sup> ions. The viscous barrier was therefore

---

proposed as a barrier for the diffusion of  $O^{2-}$  and  $F^{-}$  and not  $Na^{+}$  ions as previously proposed.

The chemical reactions caused by sodium infiltration were qualitatively explained by the construction of a chemical degradation map. The degradation map corresponds to a predominance phase diagram showing the stable phases present as a function of  $SiO_2/Al_2O_3$  ratio in the refractory lining and the amount of sodium infiltrated in the lining. Through experimental observations it was demonstrated that the degradation map is a useful tool for the evaluation of autopsies of SPL and the prediction of the mineralogical composition of SPL.

The thermal conductivity of SPL samples was determined by the Laser Flash method. The results demonstrated that the thermal conductivity decreases with increasing temperature. Compared to the pristine materials the SPL exhibited an increase in thermal conductivity, which depends on the respective density and chemical composition. It was possible to distinguish between crystalline and amorphous materials. This was also reflected by the measurements of the top and bottom part of the lens build up. Simulations of the heat transfer in cathode bottom linings were performed to study the consequences of the increase in thermal conductivity due the chemical degradation. The simulations showed that an overall increase in heat loss occurred, but was damped by the decrease of cathode block thickness and the growth of the build-up layer. Moreover, the importance of an the insulation layer with respect to a stable thermal balance was addressed.

It has been shown in this study that a significant amount of liquid phase is present below the carbon block during operation. The buoyancy force in the liquid phase has previously been suggested to contribute to the cathode heave. Estimation of the forces demonstrated that the buoyancy force alone is not enough to lift a cathode block and cause the observed cathode heave. Computer simulations in 2D using finite element method were performed to identify the stress level acting on the collector bar and to identify possible forces leading to the cathode heave phenomenon. The influence of sodium expansion was also taken into consideration. The simulation demonstrated that the forces acting upwards are indeed caused by thermal expansion and by the sodium infiltration of the carbon block. The thermal expansion of the materials was proposed to be the main reason for the cathode heave and that the chemical expansion due to sodium infiltration gives an additional contribution to the stress build up. The "weak part" of the cell lining was identified, which corresponds to the region in the lining with the strongest temperature gradient. The deformations obtained by the simulations were qualitatively consistent with typical observation of cathode heave.



# Contents

<b>Preface</b>	<b>v</b>
<b>Acknowledgement</b>	<b>vii</b>
<b>Summary</b>	<b>ix</b>
<b>1 Introduction</b>	<b>1</b>
1.1 Aluminium Electrolysis And Cell Design . . . . .	1
1.2 The Cathode Lining . . . . .	4
1.3 Aim Of The Work . . . . .	6
<b>2 Cathode Lining Materials</b>	<b>7</b>
2.1 Carbon Lining Materials . . . . .	7
2.2 Refractory Lining Materials . . . . .	11
2.3 Amorphous Oxides . . . . .	15
<b>3 Review of Previous Investigations on Degradation of Cathode Linings</b>	<b>17</b>
3.1 Autopsies . . . . .	17
3.2 Laboratory Investigations . . . . .	18
3.3 Chemical Degradation of Carbon Blocks . . . . .	19
3.3.1 Sodium Generation . . . . .	19
3.3.2 Carbon Intercalation Compounds . . . . .	21
3.3.3 Sodium Penetration in the Carbon Lining . . . . .	21
3.4 Chemical Degradation of Refractory Materials . . . . .	24
3.4.1 Visual Appearance of Spent Pot Lining . . . . .	24
3.4.2 Main Secondary Phases Formed During Degradation . . . . .	25
3.4.3 Phase Relations During Sodium Fluoride Attack . . . . .	26
3.4.4 The Role of Sodium . . . . .	32
3.4.5 Diffusion Barrier . . . . .	33
3.4.6 Sodium Diffusivity in the Refractory Lining . . . . .	35
3.5 Cathode heave . . . . .	39
3.6 Chemical Degradation of Sidewall Blocks . . . . .	42
<b>I Investigation of Spent Pot Lining (SPL)</b>	<b>45</b>
<b>4 Experimental</b>	<b>46</b>
4.1 Spent Cathode Lining Autopsies . . . . .	46
4.2 Sampling . . . . .	47
4.3 Characterization Methods . . . . .	49

<b>5</b>	<b>Results</b>	<b>55</b>
5.1	Visual Observations . . . . .	55
5.2	Mineralogical and Chemical Analysis . . . . .	56
5.2.1	Spent Carbon Cathode Block . . . . .	56
5.2.2	Lens Build-Up and Reaction Front . . . . .	59
5.3	Annealing Test . . . . .	65
5.4	Density and Thermal Expansion . . . . .	67
5.4.1	Spent Carbon Cathode Block . . . . .	67
5.4.2	Lens Build-Up and Reaction Front . . . . .	68
5.5	Thermal Conductivity . . . . .	69
5.5.1	Spent Carbon Cathode Block . . . . .	69
5.5.2	Lens Build-Up and Reaction Front . . . . .	72
<b>6</b>	<b>Discussion</b>	<b>74</b>
6.1	Two Reaction Fronts in the Refractory Lining . . . . .	74
6.1.1	Diffusion Mechanism of Attacking Agent at Reaction Front . . . . .	74
6.1.2	The Importance of the Thermal History of SPL . . . . .	77
6.2	Carbon Cathode . . . . .	79
6.3	Thermal Conductivity . . . . .	80
<b>7</b>	<b>Degradation Map for the Sodium Attack</b>	<b>85</b>
7.1	Introduction . . . . .	85
7.2	Thermodynamic Calculations . . . . .	85
7.3	Boundaries of Stability Fields . . . . .	88
7.4	Degradation Map . . . . .	89
7.5	Application of the Degradation Map . . . . .	91
7.5.1	Analyses of SPL . . . . .	91
7.5.2	Reaction Path in the $\text{Na}_2\text{O}-\text{Al}_2\text{O}_3-\text{SiO}_2$ Phase Diagram . . . . .	92
<b>8</b>	<b>Cathode Heave Phenomena</b>	<b>94</b>
8.1	Consideration of Buoyancy Force . . . . .	94
8.2	The Buoyancy Force Acting on the Cathode Block . . . . .	95
<b>9</b>	<b>Conclusion Part I</b>	<b>98</b>
<b>II</b>	<b>Thermo-Mechanical Model of the Cathode Lining</b>	<b>101</b>
<b>10</b>	<b>The Finite Element Methods</b>	<b>102</b>
10.1	Introduction . . . . .	102
10.2	COMSOL - A Software Based on FEM . . . . .	104
10.3	Calculation of the Thermal Field . . . . .	105
10.3.1	Governing Equation . . . . .	105
10.3.2	Subdomain Settings . . . . .	106
10.3.3	Boundary Conditions . . . . .	106

---

10.4 Calculation of the Thermal-Stress Field . . . . .	107
10.4.1 Governing Equation . . . . .	107
10.4.2 Subdomain Settings . . . . .	111
10.4.3 Boundary Conditions . . . . .	111
10.5 Implementation of Chemical Expansion . . . . .	111
<b>11 FEM Simulation of Cathode Lining</b>	<b>113</b>
11.1 The Cell Model . . . . .	113
11.2 Material Properties . . . . .	114
11.3 Constraints and Simplifications . . . . .	115
11.4 Results . . . . .	118
11.4.1 The Thermal Gradient in the Cathode . . . . .	118
11.4.2 Thermal Stress Model . . . . .	121
11.4.3 Influence of Sodium Expansion . . . . .	126
11.5 Discussion . . . . .	130
<b>12 Conclusion Part II</b>	<b>132</b>
<b>13 Outlook</b>	<b>133</b>
<b>Bibliography</b>	<b>135</b>
<b>Appendix</b>	<b>146</b>
A Part I . . . . .	146
B Part II . . . . .	163
B.1 Thermal Model . . . . .	163
B.2 Thermal-Mechanical Model . . . . .	170
B.3 Chemical Expansion . . . . .	173



# 1 Introduction

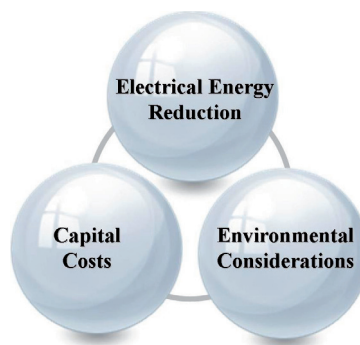
## 1.1 Aluminium Electrolysis And Cell Design

Primary aluminium is industrially produced by an energy intensive, two-step process. The main target is the conversion of the ore (bauxite) into pure metal according to the overall electrochemical reaction 1.1



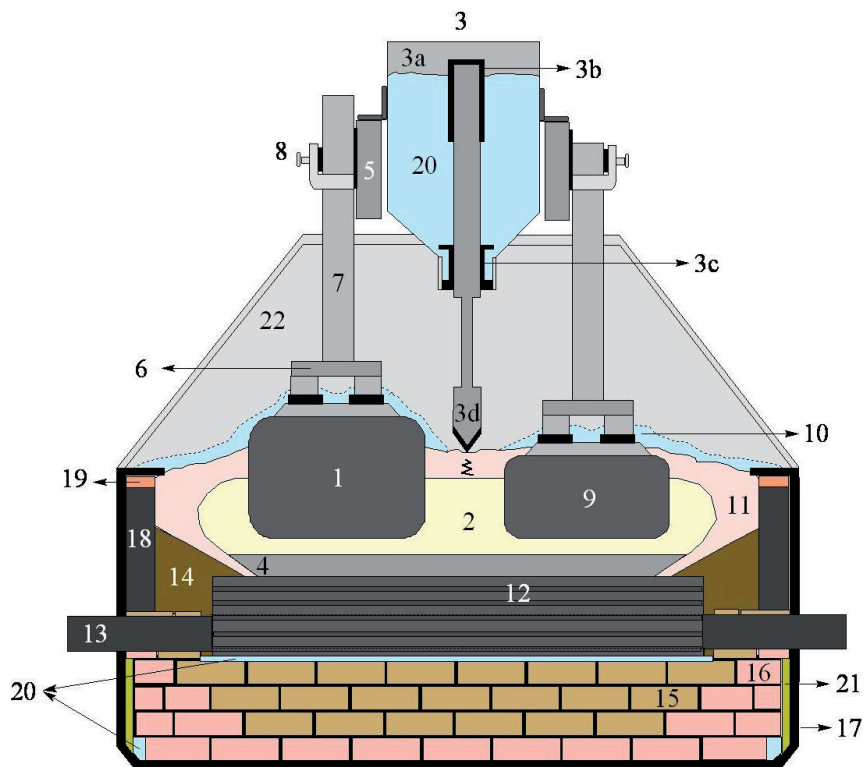
Technically, the two process steps are independent of each other. The first process step involves the refining of the raw material bauxite (ore), which contains 30-60 % alumina  $\text{Al}_2\text{O}_3$  [1] to pure alumina  $\text{Al}_2\text{O}_3$ . This is known as the Bayer process (1887), developed by the Austrian chemist Karl Joseph Bayer (1847-1904). The second step is an electrochemical reduction, where a chemical compound, in this case alumina, is decomposed into its elements, influenced by an applied electrical current.

The first attempts to create an electrolysis process were taken by the chemists Charles Martin Hall (1863-1914) and Paul Louis Toussaint Héroult (1863-1914). Independent of each other they conceived and patented their idea to produce aluminium with fused-salt electrolysis in 1886. The method was named after both inventors, and has since become known as the "Hall-Héroult process". The basic principles have remained unchanged for more than 100 years now, but the efficiency of the process has increased continuously through scientific and technological progress. The driving force for new developments revolve around the three major cost factors [2] as shown in Fig 1.1. The key factors are reduced energy consumption, improved productivity, longer cell service lifetime, and reduced environmental impact by reducing harmful emissions. Today aluminium electrolysis is a highly advanced technology.



**Figure 1.1:** The three major cost factors in primary aluminium production.

In principle, it is difficult to electrolyse pure alumina, because of its high melting point of 2045 °C. Hall and Héroult discovered that it is possible to dissolve 2-8 % alumina in the rather exotic salt cryolite ( $\text{Na}_3\text{AlF}_6$ ), and to decompose this mixture by means of electrolysis [3]. Cryolite is an uncommon mineral that was only found at the west coast of Greenland. Due to the lack of natural cryolite sources, it is nowadays replaced by the synthetic version. The Hall-Héroult process takes place in an electrolytic "cell" or so-called "pot". The single pots are usually arranged in long rows, the so called "potlines". The pots can be aligned side-by-side or end-by-end. The fundamentals of aluminium electrolysis are well described by several authors [1, 3–5]. An illustration of a modern cell is shown in Fig. 1.2.



**Figure 1.2:** Schematic drawing of the main features of an Hall-Héroult aluminium reduction cell: (1) anode (prebaked); (2) electrolyte (bath); (3) Alumina point feeder, (3a) alumina hopper (3b) air cylinder, (3c) metering chamber, (3d) crust breaker; (4) aluminium pad; (5) anode beam (current supply); (6) anode yoke and stubs (iron); (7) anode rod (aluminium); (8) anode clamp; (9) spent anode (butt); (10) alumina crust/ cover; (11) crust (sideedge); (12) cathode carbon block; (13) current collector bar (steel); (14) ramming paste; (15) refractory; (16) insulation; (17) steel shell; (18) sidewall block; (19) castable; (20) alumina; (21) rockwool and (22) gas collection hood (removable). The details in the lining may vary.

The cell consists of an anode and a cathode. In between the electrodes is the molten cryolite based electrolyte (bath) with dissolved alumina. Besides cryolite and 2-5 wt%

alumina from the Bayer-Process, the bath contains typically 10-12 wt% aluminium fluoride ( $\text{AlF}_3$ ) and about 5 wt% calcium fluoride ( $\text{CaF}_2$ ). Some plants also add lithium fluoride ( $\text{LiF}$ ) and/or magnesium fluoride ( $\text{MgF}_2$ ) to the bath [5]. The liquidus temperature of the bath is commonly about 950 °C, and its composition is a compromise between e.g. electrical conductivity, current efficiency, alumina and metal solubility, density and vapor pressure [5]. This molten mixture is named "bath" or "electrolyte" and it works mainly as a solvent for alumina and enables its electrolytic decomposition to form pure aluminium at the cathode and carbon dioxide gas at the anode.  $\text{Al}_2\text{O}_3$  is fed to the bath through holes punched in the crust. This is done by point feeders in 1 to 2 kg doses every 1 to 2 minutes [3]. Careful control of the alumina concentration is of essential importance. Too high feeding may lead to "sludge" or "muck" formation of undissolved bath/alumina [6, 7]. The mixture of bath and undissolved alumina will sink down, because of higher density and is then difficult to remove. Too low alumina content, on the other hand, may lead to the so-called anode effect, which interrupts the normal anode process by an abrupt increase in cell voltage and a rapid increase in bath temperature [8]. During an anode effect perfluorocarbon gases are generated, which are harmful greenhouse gases [5].

The bath height is quite stable, commonly around 20 cm and the temperature during cell operation is typically between 950°C and 965°C [1]. The anodes, made of carbon, are immersed into the bath from the top. Oxygen from the alumina reacts at the anode and forms  $\text{CO}_2$ . The anode is consumed and the carbon dioxide exits through holes in the crust and is collected below the hood.

Aluminium oxide is an ionic compound. In the molten or dissolved state the ions are free to move [5]. Pure aluminium is formed at the bath/metal interface. It slides under the bath, because of the higher density and deposits at the cathode surface, where it is protected against oxidation. In this way the molten aluminum metal accumulates. It forms a "pad" or pool between the cathode surface and below the bath, which acts as the "real" cathode. The thickness of the molten metal layer is around 20 cm [9]. The aluminium is tapped from this layer on a daily basis into vacuum crucibles, ready to be transported into the cast house. However, the surface of the aluminium pad is not stable during operation, caused by motions and waves due to the magnetic field and convection in the electrolyte. A certain space between anode and cathode, or so called interpolar distance (4-5 cm) is necessary to prevent short-circuits [3, 9].

There are two main kinds of anode designs used in modern aluminium cells: The prebaked and the continuous self baking Søderberg anode [5]. Søderberg is the old technology and will be phased out and replaced successively by the former one. This is due to lower energy consumption and lower emissions. Thus in this thesis it is focused on the prebaked technology, which uses multiple anodes in each cell. These anodes are made of petroleum coke and coal tar pitch, moulded into blocks, baked in separate furnaces and then placed in the cell [3]. Anodes are working as current suppliers. Thus they need to be connected to the bus bar system. In each case, an iron stub and an aluminium rod is casted or rammed into the top of the anode block. A typical feature of the Hall-Héroult process is that the anodes are consumed. The height needs

to be adjusted regularly while the anode is consumed to ensure a constant interpolar distance [3]. Therefore the rod ends are flexible fixed to the bus bar system by clamps. Anode removal and replacement by overhead crane needs to be done, when one third to one fourth of the original anode size is left (called "spent anode" or "butt"). The anode change induces disturbances in the temperature and current distribution. When the anodes get in contact with air, they immediately burn away. For protection a "layer of alumina" covers the anode surface on top of the "crust". In operation, the bath freezes on top and at the sidewalls of the cell, forming a "sideledge" which protects this part from severe attack by the molten aluminum and the molten electrolyte [3].

Although the molten metal is the actual acting cathode, the name "cathode" is usually used for the entire lower cell construction or so called "lining". This includes the bath/electrolyte, the molten aluminium pad, the carbon blocks including the collector bars, the baked ramming paste, the refractories and insulations, surrounded and supported by an outer steel shell. Collector bars are embedded steel rails into the bases of the carbon block, sealed with cast iron and run horizontally through the entire bottom lining. They serve as electrical current collectors and both ends stick out of openings in the steel shell. Those parts are connected with the electrical bus to interlink the single cells [3, 5].

The lining can be further classified into "bottom and side lining" as well as into "carbon and non-carbon lining". The non-carbon group contains dense refractories (such as high alumina and chamotte) and thermal insulation bricks (such as diatomaceous, vermiculite, calcium silica or others). They are placed between the steel shell and the carbon blocks to form the foundation of the cell superstructure. The carbon part of the lining consists mainly of silicon carbide sidewall blocks and prebaked carbon bottom blocks. They are jointed together by using a ramming paste or carbonaceous "seam mix" [3].

## 1.2 The Cathode Lining

The cathode lining, is one of the most important parts in Hall-Héroult cells, to ensure an appropriate service life time. The industry has been able to prolong the average lifetime of the cell lining from 1000 days in 1948 to an average of 2500 days today, mainly due to the improvements in materials quality and operational procedures, innovations in cell design as well as process automations [3]. During the last decades, the substitution of anthracite with graphitized carbon materials has been a significant achievement due to the reduction of the electrical resistivity and a lower total expansion [8]. At the same time the thermal conductivity of the cathode has increased, shifting the isotherms downwards in the lining. Refractory layers are installed below the carbon blocks to maintain the desired heat balance and to protect the insulation bricks underneath against higher temperatures and chemical attack [3]. They have not been improved to the same extent as the carbon materials. The most common refractory materials are found in the  $\text{Al}_2\text{O}_3\text{-SiO}_2$  system. These materials are called aluminosilicates



and are distinguished by their alumina content [10]. Alumino-silicates have been and still are the preferred refractory materials due to good performance, light weight, availability and moderate costs [1,3,5]. Despite these properties the refractory material cannot completely withstand the permanent chemical attack caused by the uptake of sodium and electrolyte/ bath components. During operation sodium followed by bath components will percolate downward through the carbon cathode block, which causes swelling, heaving [3] and cracking. Cracks are in general one of the main reasons for early cathode failures [3, 8].

Underneath the carbon block sodium and bath components start to deteriorate the refractory lining [10–23]. This leads to significant mineralogical transformations in the material. Hence the material performance changes over time, resulting in increased heat loss through the cathode lining, a rise in mechanical stresses (due to swelling) and in the worst case it causes a complete pot failure [3, 24]. An increase in the energy consumption due to thermal instabilities and a shorter lifetime of the cell results in earlier needs for delining and relining are among others unwanted consequences. Since these material and operating expenses have a significant effect on the production costs, the aluminium producers are aiming to decrease the number of unscheduled shut downs and increase the average service life span to about 3000-4000 days [25, 26].

To date, a significant body of research has been conducted in order to gain a qualitative understanding of the degradation of the cathode bottom lining materials by means of autopsies of shut down cells and/or laboratory investigations [3, 8]. It was found that sodium plays an important role not only in the carbon cathode, but also in the side lining and in contact with alumino-silicate materials. Despite the intensive efforts and due to the complex interaction of bottom lining materials during degradation, some phenomena are still not well understood. This concerns the interpretation of autopsy of spent pot lining (SPL), the initiation of the degradation at the reaction front in the refractory lining and the cathode heave phenomenon. So far there are no conclusive answers to this issues.

### 1.3 Aim Of The Work

The present work has been one of five sub-projects (SP5) in the project "Innovations for High Current Density" (PI-HCD). This research program is financed by the Research Council of Norway and Hydro Aluminium. It is undertaken at NTNU in cooperation with the research institute SINTEF. The main goal of SP5 is to gain better understanding of the deterioration of cathode lining materials in aluminium electrolysis cells and to quantify the phenomena through the use of computational tools. The project is devoted to develop models based on the Finite Element Method (FEM) and to describe the rate of aging and/or degradation based on a qualitative understanding of the aging phenomena.

The aim of the first part of the work was to confirm previous qualitative understanding of the degradation mechanism of the cathode lining, and to possibly develop a quantitative model to describe the degradation and to investigate the changes in the thermal conductivity of lining materials. An associated PhD study [27–30] has focused on side lining materials, while in this work the refractory lining has been in focus.

Several autopsies of spent pot lining were conducted. During the analysis of the data from the autopsies, it was discovered that the reversed thermal gradient in the lining during cooling has previously been ignored. A revised view of the analysis of SPL was therefore presented. Moreover, chemical and mineralogical characterization of the SPL was performed to investigate the reaction front, which previously has not been studied in detail. Here, the importance of sodium as a degradation agent was confirmed, and a degradation map of sodium attack was constructed. Based on the experimental observations, the deterioration mechanism at the reaction front was proposed. Finally, SPL samples were used to measure the change in thermal conductivity of the materials to investigate the effect of aging of the lining on the thermal insulation of the cathode lining.

The second part was devoted to the cathode heave phenomenon. Computer simulations using FEM were performed in order to study the influence of the thermal history and the chemical diffusion of sodium on the materials behaviour. The simulations were correlated to industrial findings. The task described here was complex in nature and is cross-disciplinary. This involves knowledge in chemistry/materials science, solid state mechanics and FEM modelling. The main goal of the computations was to identify the driving force for the observed cathode heave in aluminium electrolysis cells.

## 2 Cathode Lining Materials

### 2.1 Carbon Lining Materials

The materials used for cathode lining constructions, see Fig. 1.2 are located in the overall group of refractory materials and can be subdivided into carbon and non-carbon materials. The non-carbon materials in the following are denoted as refractory lining materials.

The carbon lining has basically two main functions. It contains the molten constituents (aluminium metal and electrolyte) and conducts electricity. Monolithic, prebaked and glued semi-monolithic carbon cathodes are common types of industrial cathodes. The monolithic lining design was developed by the Hall-Héroult process inventors and in 1920 the first cells with prebaked cathodes appeared [3].

#### Cathode Blocks

Currently the most frequent industrial design of cathodes are prebaked carbon blocks [3]. The carbon block is a composite material with a heterogeneous and porous structure. It is made of carbon aggregates with a wide particle size variation between producers bound by a pitch-based binder phase. The joints and seams are rammed with paste. Carbon cathode blocks are available in a variety of qualities and shapes, due to the raw material availability at relatively low costs. The property and design demands can vary between potlines. Important criteria are cell sizes, current density, electromagnetic and thermal load characteristics [5] as well as available handling equipment for relining operations.

In brief, the need for better material in terms of chemical resistance and electrical conductivity has led the carbon producers to improvements of their products during the last decades [3]. The cathode quality can be influenced by the filler material, binder properties, baking temperature, bulk and real densities, total porosity, electrical resistivity, ash content and sodium expansion. According to Sørli and Øye [3] four different types of blocks can be classified into the following materials:

1. Amorphous (anthracitic) blocks:
  - ◆ No long-range ordered crystalline material
  - ◆ Made of anthracite aggregate and pitch-based binder
  - ◆ None or only the filler material is graphitized
  - ◆ Baked/fired at 1200 °C

- ◆ Subclassified into gas or kiln calcined anthracite without graphitization, (GCA), electrically calcined (ECA) and semi-graphitic blocks (partly graphitic carbon)

2. Graphitic blocks:

- ◆ All carbon varieties in the form of graphite polymorphs are included (means 100 % graphite), irrespective of structural defects
- ◆ Baked/fired only at 1200 °C
- ◆ The binder is not graphitized

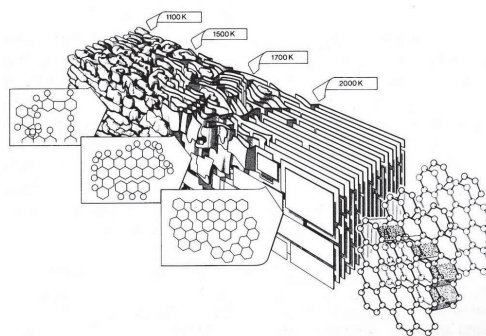
3. Semi-graphitized blocks:

- ◆ Made of coke aggregates and coal tar pitch, complete block consists of graphitizable materials (filler and binder)
- ◆ Baked/fired between 2000-2300 °C
- ◆ The content of graphite is not 100 %

4. Graphitized blocks:

- ◆ Made of coke aggregates and coal tar pitch, complete block consists of graphitizable materials (aggregate and binder)
- ◆ Baked/fired between 2500-3000 °C
- ◆ 100 % graphitic material

The carbon cathode blocks are produced by extruding or vibrating the raw materials (coke and pitch binder) into rectangular shapes, which are heat treated to temperatures between 1000 and 3000 °C [3]. As the temperature of the material increases the structure approaches a more graphitic structure, shown in Fig. 2.1 [31].



**Figure 2.1:** The carbon structure at various heat treatment temperatures [31].

During forming, the particles tend to orient parallel or perpendicular to the extrusion and vibration direction, respectively. Thus the materials properties are dependent on the measurement direction. Today, it is common to use more graphitized carbon blocks instead of amorphous carbon to reduce the electrical resistivity, and to increase the thermal stability during the heat up of the cell [3]. The choice to use fully graphitized blocks is desirable for the operation, but is accompanied with higher cost. The focus in this work lies on graphitized carbon cathodes. A flow sheet of the production of graphitized blocks is shown in Fig. 2.2. The dry aggregate is calcined petroleum coke. After shaping, these blocks are pre-baked at about 900 °C. In addition, they may be impregnated with pitch and re-baked, to reduce the open porosity, before they are graphitized [3].

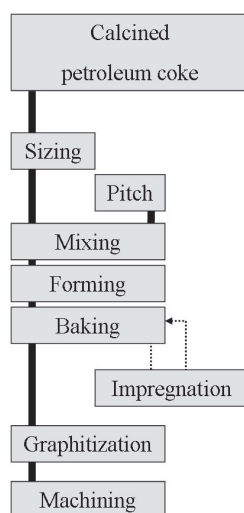


Figure 2.2: Flow sheet for production of graphitized carbon blocks (redrawn from [3]).

## Graphite

In graphite, all carbon atoms are  $sp^2$  hybridized. Three out of four valence electrons of each atom are covalently bond with three other neighbors from the same plane [32]. The bond angle is  $120^\circ$ , with a C-C bond of  $1.418 \text{ \AA}$  and a high strength. They form two dimensional, six-membered rings that link up to form flat layers. These layers are arranged in parallel, stack on top of each other, with a fixed distance of  $3.35 \text{ \AA}$  and kept together by weak van der Waals forces. Thus they are able to slide over one another. The fourth valence electron forms delocalized  $\pi$  bonds, which spread uniformly over all carbon atoms [31, 33]. These electrons are free to move within the layer. Due to this graphite conducts electricity along but not perpendicular to the planes of carbon atoms. The structural development of the final graphitized state is shown in Fig. 2.1.

## Binder

Coal tar pitch is the most important binder for prebaked carbon blocks and is commonly the main component in the cold ramming pastes [3]. The pitch is a residue produced by distillation or heat treatment of coal tar. Coal tar is the by-product when coal is carbonized in the coke oven process for the production of metallurgical coke [32]. Binder pitches are solid at room temperature and consist of complex mixtures of numerous polyaromatic hydrocarbons (PAH) and other organic compounds. It exhibits a broad softening range instead of a defined melting temperature.

## Ramming Paste

Gaps between the prebaked carbon blocks and the lining materials are filled and sealed with ramming paste [3]. The main purpose is to protect the inner parts of the cathode against bath and metal penetration. Furthermore, it keeps the lining dimensional stable, by absorbing the thermal expansion during preheating of the cell to some extent. A proper installation of the ramming paste is important, since it is the weakest part in the cathode lining in terms of where severe pot failures may be initiated. The potlife might be influenced by the performance and the quality of the ramming paste. Properties like temperature window, compactability, shrinkage upon baking and quality of carbon filler and binder [3] are of consideration.

Ramming pastes consist of a filler component (anthracite with or without graphite additions) and a binder. The binder is based on coal tar and/or coal tar pitch and softener additions. This depends on the application temperature. The industry separates between hot (up to 170 °C), cold (at room temperature) and tepid pastes (up to 50 °C) [34]. The latter two mentioned pastes are nowadays the dominating ramming materials used with prebaked cathode blocks because of better handling conditions and lower polyaromatic hydrocarbons (PAH) emissions.

## Sidewall Material

The sidewalls of the cathode lining can be made from prebaked carbon blocks, ramming paste or a combination of both and alternatively from silicon carbide and/or from materials containing silicon carbide. During the last decades  $\text{Si}_3\text{N}_4$  bonded SiC materials have become state-of-the-art sideling materials in aluminium electrolysis cells [35, 36]. They possess excellent oxidation resistance, poor electrical conductivity and high thermal conductivity [3, 36, 37] compared to traditional carbon linings.  $\text{Si}_3\text{N}_4$ -SiC materials are produced from SiC-particles (from the Acheson process), fine grained silicon powder and a binder.

The blocks are heat treated in a nitrogen atmosphere at temperatures of about 1400 °C. The Si reacts with nitrogen and a microporous  $\text{Si}_3\text{N}_4$  binder phase is formed between the large SiC grains. The typical content of SiC and  $\text{Si}_3\text{N}_4$  varies between

72-80 wt% and 20-28 wt% respectively [36]. The silicon nitride phase has two crystal modifications ( $\alpha$  and  $\beta$ - $\text{Si}_3\text{N}_4$ ). Thus the  $\alpha/\beta$ - $\text{Si}_3\text{N}_4$  ratio can vary within one block due to temperature gradients and presence of oxygen during the nitration process. The main advantage of  $\text{Si}_3\text{N}_4$  bonded SiC blocks is that the total thickness of the sidewall material and sideledge can be reduced. In modern aluminium smelters block thicknesses of 5-10 cm are used [29]. This is advantageous for high amperage cells since a reduction of the sideling blocks allows the use of larger anodes [36–39]. The main disadvantage is the price, which is twice as much compared to other sidewall materials [3, 8]. This can be compensated by reduction of the sideling thickness.

Recently the sidewall block producers have made a step forward by developing self-bonded sideling blocks with 95 wt% SiC (Sicatec 95) and no  $\text{Si}_3\text{N}_4$  phase. This material provides a high thermal conductivity and perfect cryolite resistance capability [40]. The Sicatec 95 is believed to substitute the  $\text{Si}_3\text{N}_4$  bonded SiC materials in the near future, to keep pace with the technical trend of increasing cell amperage in the aluminium reduction cells. The suitability of Sicatec 95 as a replacement for common sideling material is under evaluation by the aluminium industry.

## 2.2 Refractory Lining Materials

The refractories ability to withstand high temperatures is compared to other properties of minor importance, since the operation temperature in the aluminium production process is not particularly high compared to other metallurgical processes. General requirements for a refractory material in aluminium reduction cells are as follows [3]:

- ◆ Ability to withstand high temperatures and sudden temperature changes
- ◆ Resistance to chemical attack, no contamination of other materials in contact
- ◆ Resistance to load and abrasive forces
- ◆ Low coefficient of thermal expansion
- ◆ Should easily be installed, low in costs
- ◆ Protect the steel shell against metal, electrolyte (penetration barrier) and high temperatures
- ◆ Save thermal energy (reduced heat loss to the surroundings)
- ◆ Maintain the designed heat balance throughout the service life of the cell (to get sufficient ledge control)
- ◆ Increase pot life-time

It is important to distinguish between refractory and insulation materials. They are similar in composition (inorganic oxides), but the main difference is the density. The former have lower insulation properties due to lower porosity. Insulation materials exhibit a significantly higher porosity (minimum 45 %, usually 60-90 % and in extreme

cases up to 99 % [41]) and a high thermal insulation, but a decrease in chemical and physical resistivity. Unfortunately, no single material combines all requirements mentioned above. Consequently, cathode linings are multi-layer constructions using mainly dense and insulating refractories in combination. Whereby the former protects the latter. The variation range of refractory linings in different smelters are narrow within each plant. Thus three main types of materials can be classified according to their function and position in the cathode lining [3]: bedding materials, dense refractory materials and insulation materials.

### **Bedding Materials**

During installation of the bottom lining the surface of the refractory layer towards the cathode block is usually not completely even [3, 5]. For this purpose a powdered layer acting as level support is poured on top of the underlying lining. It usually consists of alumina, but crushed fireclay or ramming paste are also used as well. The disadvantage of these materials is that they are not able to stop or slow down the penetration of molten materials and gases, but they are available and inexpensive [3, 17].

### **Dense Refractory Materials**

Underneath the carbon block a layer of dense refractory material is installed. They protect the insulation material below against high temperatures and chemical attack, and they act as solid support for the cathode blocks. The most common dense materials used in the industry are alumino-silicate based materials and olivine (silica and magnesia) bricks. Fireclay bricks (chamotte) with relatively high silica content [10] have long been the first choice based on their good performance, abundant supply of the raw materials and moderate costs. The present work is limited to refractory materials based on alumino-silicates. They are located in the  $\text{SiO}_2\text{-Al}_2\text{O}_3$  system (see Fig. 2.3), where the two end members  $\text{SiO}_2$  and  $\text{Al}_2\text{O}_3$  form the basis of silica and high alumina bricks respectively.

Chamotte ( $\leq 45\% \text{ Al}_2\text{O}_3$ ) and high-alumina ( $> 45\% \text{ Al}_2\text{O}_3$ ) constitute the major groups of alumino-silicates [10]. The former involves clay, kaolin and their calcined products (chamotte). The latter is fabricated from alumina rich alumino-silicates, like andalusite ( $\text{Al}_2\text{SiO}_5$ ), sillimanite (polymorph of andalusite), and mullite ( $3 \text{ Al}_2\text{O}_3 \cdot 2 \text{ SiO}_2$ ), as well as sintered bauxite and corundum. The refractoriness of the chamotte materials increases with increasing alumina content. The  $\text{SiO}_2$  content varies between 50-80 % [3].

Chamotte bricks are made from a mixture of clay binder, water and already calcined clay (or raw chamotte), to control shrinkage during drying and firing in tunnel furnaces (special geometries are fired in single furnaces). Calcined clay is produced at 1250-1400 °C in shaft- or rotary kilns [41]. One important property of clays is that they become plastic and deformable in contact with water. During heating the kaolin



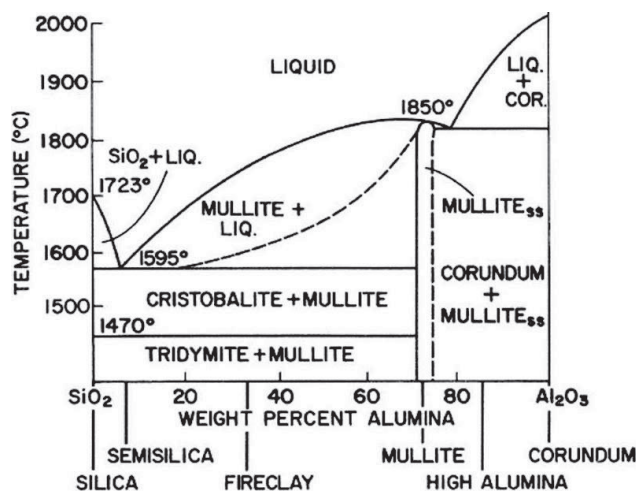


Figure 2.3: The phase diagram for  $\text{Al}_2\text{O}_3$ - $\text{SiO}_2$  showing common refractory compositions [42].

minerals lose their crystal water and metakaolin with low crystal order appears. At approximately 925 °C the lattice network of kaolin breaks down and at 950 °C the reaction between  $\text{Al}_2\text{O}_3$  and  $\text{SiO}_2$  to mullite takes place. Above 1100 °C only mullite ( $3 \text{ Al}_2\text{O}_3 \cdot 2 \text{ SiO}_2$ ), cristobalite (high temperature polymorph of  $\text{SiO}_2$ ), and an amorphous phase (silica rich glass, sometimes higher than 50 %) exists. After firing and cooling the mineral composition is not in equilibrium (depends on the flux) [41]. The dominating phases in chamotte bricks are mullite (25-50 %),  $\alpha$ -cristobalite respectively  $\alpha$ -quartz (up to 30 %), and an amorphous phase (silica rich glass 25-50 %) [3]. The chemical composition and bulk density of dense refractory materials in aluminium electrolysis cells are given in Table 2.1.

Table 2.1: Chemical composition and bulk density of the most common refractory materials [10].

Material	Chemical Composition [wt%]						Bulk Density [g/cm <sup>3</sup> ]
	$\text{Al}_2\text{O}_3$	$\text{SiO}_2$	MgO	CaO	$\text{Fe}_2\text{O}_3$	$\text{Na}_2\text{O}$	
Alumina (powder)	≈ 100						1.0
<b>Alumino-silicates</b>							
High-alumina bricks	46-90	10-49					2.3-3.3
Firebricks	18-45	50-75	<0.5	<0.5	1-2	1-3	2.0-2.2
<b>Anorthite</b>							
Chemobar (powder)	3	48		15	1	3	2.1
<b>Olivine</b>							
Forsterite bricks		41	51		7		2.7
Drycast (powder)	12	44	37		5		2.3
Olibar 1901 (powder)	4	44	42		7		2.3

### Insulation Materials

Commonly used insulation bricks are made of one of the following raw materials:

- ◆ Diatomite (mainly  $\text{SiO}_2$ )
- ◆ Perlite (mainly  $\text{SiO}_2$  and  $\text{Al}_2\text{O}_3$ )
- ◆ Vermiculite (contains mainly  $\text{SiO}_2$ ,  $\text{Al}_2\text{O}_3$  and  $\text{MgO}$ )
- ◆ Calcium silicate (nearly 50:50  $\text{SiO}_2$  and  $\text{CaO}$ )

They belong to the group of inorganic and mineralogical insulation materials. Insulation bricks with low thermal conductivity have the ability to maintain the heat balance during operation, which decreases the energy consumption. Further demands on these materials are resistivity to molten metal and electrolyte components, as well as mechanical/chemical stability [17,43]. These bricks should have porosity as high as possible, but the drawback is that the dimensional stability decreases. For this reason they are only used in the bottom part of the lining and are protected by several layers of dense refractory materials.

Moler bricks are commonly used as insulation material in cathode linings [3]. They are made of diatomaceous earth (silica 72-77 %) and clay. The bricks are fired and designed for a maximum service temperature of 900-1000 °C. The dominating mineral phases in this material are quartz and mullite. Moler bricks are characterized by their insulating properties, low bulk density (550 - 950  $\text{kg/m}^3$ ), high porosity (60-80 %), low thermal conductivity, high mechanical strength (good thermal shock resistance), low weight, non-wetting behaviour to molten aluminium and increasing strength at rising temperatures. With reference to [44] various grades of Moler insulating bricks are available and divided into two main groups:

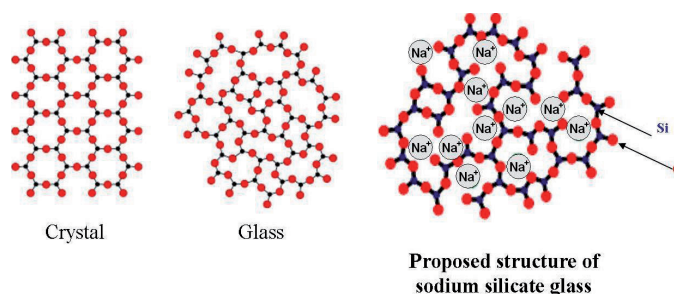
- ◆ Porous grades (HIPOR, HIPOROS, POROS) suitable up to 950 °C,
- ◆ Solid grades (SUPRA, M-EXTRA) suitable up to 1000 °C.

The Moler bricks HIPOR and SUPRA are typical materials used. Moler materials exhibit reasonable resistance to attacking slags or melts, because of their high content of amorphous silica. This ability increases by using the more dense qualities. Since the refractory properties are not satisfactory enough, these bricks are used as back-up insulation, behind the refractory lining (bottom part of the cathode lining).

## 2.3 Amorphous Oxides

The following section is dedicated to alkali ions and their presence in amorphous oxides. Amorphous oxides are present in the virgin refractory bricks. As shown later amorphous oxides are also formed during chemical attack on refractory materials.

The first researchers, who described the structure differences between glass and crystal were V.M. Goldschmidt and Zachariasen (1932) [45]. They found that glasses and crystals of the same composition have the same states of bonding or units of structure, because of the very small energy differences between them. Silicates are used as an example, where the  $[\text{SiO}_4]$ -tetrahedrons are arranged regularly in crystals, but in glass they form a random network as shown in Fig. 2.4.

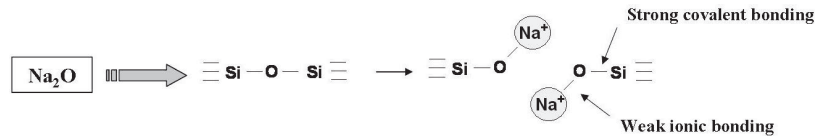


**Figure 2.4:** Two-dimensional diagram of an ordered  $\text{SiO}_2$  network in crystalline and random (glassy) form [46], proposed structure of sodium silicate glass [45].

Zachariasen [47] formulated four main conditions under which an oxide glass will form. The involved cations can be classified into network/glass formers (incl. Si, Ge, B, As and P), modifiers (incl. alkalis and alkaline earth) and intermediates [45,48,49]. This enabled Warren (1937) [50] to interpret X-ray diffraction patterns of glasses. Since alkali ions are held much more loosely in the silicate structure than other constituents, their diffusion is generally much more rapid [48].

In a  $\text{Na}_2\text{O}-\text{Al}_2\text{O}_3-\text{SiO}_2$  glasses,  $\text{SiO}_2$  is the network former,  $\text{Na}_2\text{O}$  the network modifier and  $\text{Al}_2\text{O}_3$  is acting as an intermediate or conditional glass former [45]. If modifying alkali ions are added, they will cause significant changes in the oxide glass structure. In pure  $\text{SiO}_2$  glass (fused silica/quartz glass), two  $\text{Si}^{4+}$  ions are irregularly bound via bridges, made of oxygen ( $\text{O}^{2-}$ ) ions to build a three-dimensional network. Every  $\text{O}^{2-}$  links the glass forming tetrahedra through so called bridging oxygens to the neighboring cations, if only glass forming oxides are involved. If  $\text{Na}_2\text{O}$  is added as a network modifier, the bridges are bursting and neighboring  $\text{Si}^{4+}$  are formed as shown in Fig. 2.5. They in turn connect to single bond  $\text{O}^{2-}$  or so called non-bridging oxygens. Therefore, no direct bonding among another occurs anymore. Each of the negatively charged, single coordinated and non-bridging oxygens can bind loosely to the positive charged  $\text{Na}^+$  ion. The overall structure will then be a mixture of covalent and ionic bonds [51]. This weakens the overall glass structure and effects the physical properties. Since every  $\text{Na}^+$  ion will produce non-bridging oxygens, the amount of

added modifying alkali ions will influence the appearance of the network according to Greaves [51].



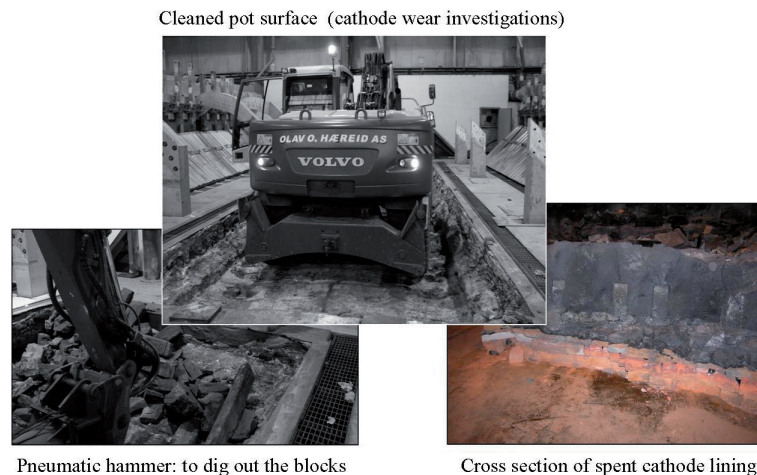
**Figure 2.5:** Sketch of the influence of an alkali oxide to the glass system.

In crystalline silicates,  $\text{Al}^{3+}$  is found in 4 as well as in 6-coordinated sites. Like mentioned before, the addition of modifying ions will break up the silica structure and will convert bridging oxygens into non-bridging ones. The continuous addition of  $\text{Al}_2\text{O}_3$  to a sodium silicate glass structure up to a ratio of  $\frac{\text{Al}}{\text{Na}} = 1$ , can be divided into three steps. First, each 4-coordinated  $\text{Al}^{3+}$  will substitute a  $\text{Si}^{4+}$  ion in the tetrahedral structure, since both are close enough in size ( $\text{Al}^{3+}$  4-coord. =  $0.39 \text{ \AA}$ ;  $\text{Si}^{4+}$  4-coord. =  $0.26 \text{ \AA}$ ) [45]. This will return non-bridging oxygens into bridging oxygens, because each  $\text{Al}^{3+}$  connects to  $\frac{3}{2} \text{O}^{2-}$  and thus half non-bridging oxygen supplied by a  $\text{Na}^+$  ion is consumed. Consequently, the  $\text{Na}^+$  ions are decreasing their preference to specific positions and thus increasing their mobility. In brief, conditional oxides are not able to form a glass alone, unless they are brought together with other network forming oxides.

## 3 Review of Previous Investigations on Degradation of Cathode Linings

### 3.1 Autopsies

The term autopsy is commonly known as a procedure that consists of a thorough examination of a human body to determine the cause and manner of death and to evaluate any disease or injury that may be present. This description can be transferred to other fields of application where the principle procedure is similar. Cathode autopsies in the aluminium industry are performed after failures or normal cell shut-downs to investigate the status of the cathode lining and possible reasons for unscheduled breakdowns. The diagnostic inspection can vary between a full examination to a very limited sampling [3]. The major steps are shown in Fig. 3.1.



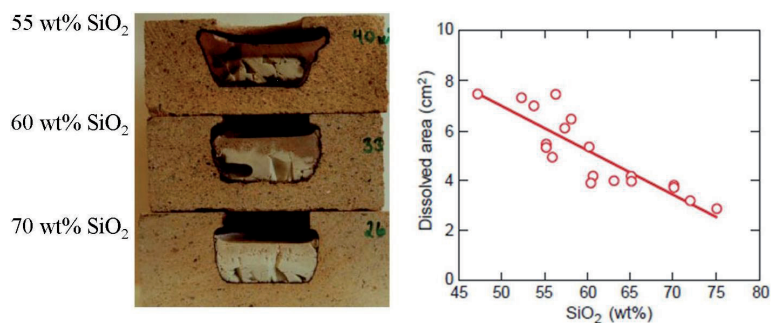
**Figure 3.1:** Pictures illustrating the main steps in autopsy of a shut down cell.

An autopsy with a full examination is performed after cooling the cell down (around 4 days) without external support like watering and removing the remaining bath and metal. To obtain a complete picture or finding the reason for failure a data collection, which contains different steps, is essential. First, prerecorded relevant cell data are collected, e.g. cell design, cell age, material data, start-up and operational history as well as special events. Afterwards the exposed cathode surface and pot dimensions are measured accurately to detect possible heaving effects, cracks, expansions and displacements spots. Surface data is of special interest for cathode wear investigations [3, 52–54]. Before starting to dig out blocks, points of interest or failure need to be identified. If considering a failure, the blocks around this area need to be removed

without destroying the spot of interest. If only a repair is necessary the digging is restricted to only the region where the failure has occurred. The digging step is performed with a pneumatic hammer and the leavings are vacuumed or scooped out until a full cross-section can be inspected. The third step contains systematic photographic documentation, surveying and sampling. The final step is to investigate the samples with respect to chemical and mineralogical analysis and microscopy. The reactions confirmed by analyses of SPL are reviewed in Chapter 3.4.

### 3.2 Laboratory Investigations

The physical properties of refractory materials are given by the suppliers and are measured by means of international standards. Despite that no international agreement on a method for testing the cryolite [10] or sodium resistance are available. The most important method to evaluate the cryolite resistance of cathode and refractory materials is the crucible- or cup-test method [10, 21, 55]. The test method has been proposed as an ISO-standard. The cup is prepared by drilling a cylindrical core in the material to be tested. The cup is filled with eutectic mixture of cryolite and sodium fluoride, heated for 24 hours at 950 °C in air. Afterwards, the brick is cut diagonally through the middle of the core as shown in Fig. 3.2.



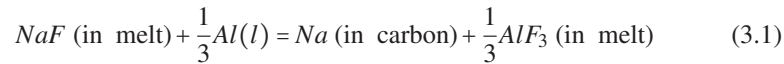
**Figure 3.2:** Firebricks with various silica content after the cryolite resistant tests (left). Relation between silica-content and cryolite resistance (right) [11].

The cross section is examined to measure the reacted volume of the brick. The photographs in Fig. 3.2 (left) illustrates the cup-test with different silica content in the fireclay bricks [11]. Due to the separation of a highly reactive fluoride melt on top and a relatively non-reacting and viscous silica-rich melt on the bottom, the deterioration zone reduces as the silica content of the alumino-silicate refractory material increases. The graph in Fig. 3.2 (right) shows that the cryolite resistance increases with the silica content of the virgin firebrick material. Further test methods which have been developed are the finger-test [10] and polarised-test [56]. The so called Sodium vapor-test is used to investigate the sodium resistance of cathode [57] as well as refractory materials. The samples are subjected to gaseous sodium at a known partial pressure of Na.

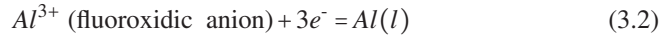
### 3.3 Chemical Degradation of Carbon Blocks

#### 3.3.1 Sodium Generation

Sodium is formed at the interface between the molten electrolyte and the aluminium metal ("real" cathode) by reduction of  $\text{Na}^+$ , which is the main "free" cation present in the cryolite-alumina mixture, according to the chemical reaction (3.1) [58]



Sodium is also produced due to direct reduction at the cathode surface (3.3) [57]. The primary deposition of aluminium is



While the direct electrochemical deposition is

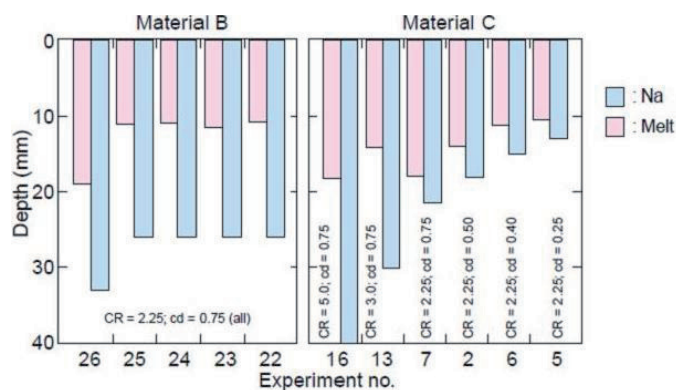


Pure sodium has a higher deposition potential of 1.44 V than aluminium which is deposited at 1.20 V (3.2) [3]. Thus, there should be only a minor driving force for sodium to deposit at the cathode during the operation of an aluminium electrolysis cell. Unless the activity of sodium ( $a_{\text{Na}}$ ) decreases, the deposition potential will also decrease [57]. During the initial period of cell start-up, Eq. (3.3) is the main reaction for producing Na. It allows the concentration of sodium to build up at the cathode surface and penetrate into the material.

Later, when the "soaking-time" is over and Al metal is poured into the cell, the activity and thus the deposition potential of sodium in liquid aluminium increases, until it is overcoming the value of aluminium. In turn, Eq. (3.1) becomes the source for elemental sodium [3]. Reaction (3.1) produces a greater amount of sodium (is shifted towards the right hand side), the more basic the bath is (higher cryolite ratio) [59, 60]. Even though it has a slightly positive  $\Delta G_K^\circ_{1233\text{K}}$  value of 68 [kJ/mol], coming from the fact that the sodium activity is not unity during cell operation, sodium gets stabilized by the bonding to carbon. This might be due to adsorption or formation of intercalation compounds [26, 58]. This scenario proceeds until the carbon cathode is saturated with Na.

With the presence of an electric field in the cell  $\text{Na}^+$  ions are able to travel towards the cathode surface. The NaF content at the cathode/electrolyte interface is therefore higher than for the bulk composition [26]. Hence, the sodium amount generated cannot be calculated directly in the bulk composition of the bath [58]. The activity of sodium in the aluminium layer at the cathode will be higher than expected from the electrolyte composition [1]. Sodium may appear as dissolved species in the electrolyte, in the molten aluminium and in the carbon lining [3].

The carbon cathode is one of the most important parts of the aluminium electrolysis cell, and it undergoes changes during the start-up phase and routine operation. In principle, carbon is not wetted by liquid aluminium and poorly wetted by the bath components (fluoride melt). Thus it is expected that the carbon material is impervious to penetration [3]. However, it is well known that after a certain period of time, the carbon blocks will be fully penetrated by bath components (mainly NaF and cryolite). It has been found that sodium, produced at the interface between the molten electrolyte and aluminium metal, inevitably infiltrates the cathode carbon during cell operation. The liquid aluminium does not enter the carbon pores (10-26 vol% apparent porosity). The sodium-uptake in the carbon block explains the cathode swelling [3]. Moreover, it has been shown that it changes the wetting properties with respect to the liquid bath. Sodium "opens" the path or makes it more likely that bath components penetrate the carbon through pores and cracks of the cathode. In brief, both (Na and bath components) are penetrating the cathode material in a defined sequence. From Brilliot et al. [61] it is known that the electrolyte-front follows in a certain distance and does not overcome the sodium-front (Fig. 3.3).



**Figure 3.3:** Melt and sodium front measurements (optical microscopy and phenolphthalein test).  $N_2$  atmosphere. Electrolysis time 1h 30 min, except for exp. 26 it was 3 hours, CD in  $A/cm^2$ . B: Electrocalcined atracite,  $\approx 20\%$  graphite added, baked to  $\approx 1200^\circ C$ . C: Graphitic 100% graphite, baked to  $\approx 1200^\circ C$  [60].

A general method to detect the penetration depth of sodium is the phenolphthalein paper test [3]. Studies by P. Brilliot et al. [61] and L.P. Lossius et al. [62] using samples, either from industrial cells and/or from experiments in laboratory scales, were dedicated to identify the penetration and chemical reactions occurring in carbon cathode materials during aluminium electrolysis. They investigated the dependence on initial bath chemistry, current density, polarization, pressure and atmosphere in carbon cathodes. An overview is given by Sørli and Øye [3].

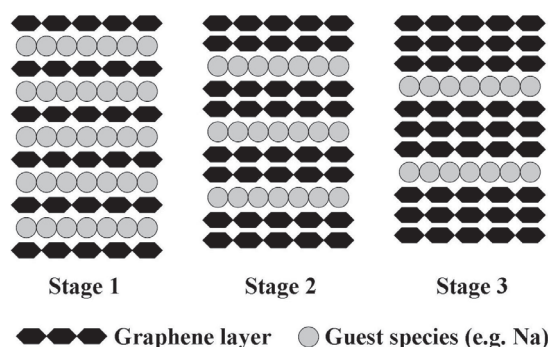
From numerous autopsy studies of SPL the presence of sodium metal and components, like sodium fluoride (NaF), cryolite ( $Na_3AlF_6$ ), chiolite ( $Na_5Al_3F_{14}$ ),  $\beta$ -alumina ( $Na_2O \cdot 11Al_2O_3$ ), sodium carbonate ( $Na_2CO_3$ ), sodium cyanate (NaCN), aluminium nitrite (AlN) and aluminium carbide ( $Al_4C_3$ ) have been identified. The latter is also



the phase of interest in cathode wear investigations [54]. The direct relationship between cathode expansion and sodium penetration during electrolysis was first proven by Rapoport and Samoilenko in 1957 [63]. Their apparatus (with some minor modification) is still in use and enables the direct measurement of dilatation undergone by the carbon material during electrolysis. The exact mechanism of sodium penetration into carbon and its expansion is yet not well understood [26, 58].

### 3.3.2 Carbon Intercalation Compounds

Most studies propose that sodium forms intercalation compounds with graphite (carbon cathode) [3, 58]. Carbon intercalation compounds (GIC's) are formed by the insertion of foreign atoms between the graphene layers, which cause the cathode to expand. Here first-, second- and third stage intercalation are distinguished, shown in Fig. 3.4. A summary of binary and ternary sodium carbon intercalation compounds is given in a recent review paper by P.Y. Brisson et al. [58].



**Figure 3.4:** Separation of graphene layers through first-, second- and third stage intercalation compounds. The principle is redrawn from [64].

The sodium uptake in less ordered forms of carbon (amorphous carbon) is higher than in graphite. Furthermore, the absorption decreases with increasing graphitization grade and temperature, but is favored by small amounts of impurities. In brief, well-graphitized carbon is always more resistant to sodium attack than any other form of carbon used. The different sodium saturation concentrations for common cathode materials are summarized in Table 3.1.

### 3.3.3 Sodium Penetration in the Carbon Lining

The properties and behaviour of carbon materials in terms of sodium handling are complex and highly dependent on the micro- and crystallographic, or mesoscopic structure, described in Section 2.1. The sodium penetration through the carbon is not definitely clear, but the transport has been related to two main mechanisms. Dell [65] proposed the vapor transport in the gas phase through pore network, because the

**Table 3.1:** Virgin density, approximated apparent porosity and sodium saturation amount in common used cathode materials for aluminium electrolysis [62]; (a) gas or kiln anthracite + 30 wt% graphite filler blocks, baked to 1200 °C, (b) electrocalcined anthracite, partly graphitized + 30 wt% graphite filler, blocks baked to 1200 °C, (c) semigraphitic, all aggregate graphitized, baked to 1200 °C and (d) semigraphitized, graphitizable filler, whole blocks calcined above 2300 °C.

Material	Density [kg/m <sup>3</sup> ]	Porosity [vol %]	Na Saturation	
			[wt %]	[kg/m <sup>3</sup> ]
(a) GCA	1530 to 1550	16 to 19	4	60 to 70
(b) ECA	1540 to 1550	16 to 20	4	60 to 70
(c) SG	1590 to 1650	19 to 23	2	30 to 35
(d) SGZ	1620 to 1650	23 to 26	1	15 to 20

sodium is above its boiling point of 883 °C [26] at the cathode surface. From [3, 4] it is known that sodium vapor can completely degrade carbon materials in just a few hours. At some point, capillary condensation takes place, which is the multilayer adsorption of sodium atoms at the pore surface [66]. The pore space becomes filled with condensed liquid from the vapor phase up to saturation.

Another diffusion mechanism was proposed by Dewing [67]. He found that the rate of penetration of the reaction front inside the carbon follows the square route of time. This led to the assumption that the sodium penetrates by solid diffusion through the carbon lattice and along grain boundaries. Since then the solid diffusion process has been mostly considered to be dominating [58]. Vapor diffusion might take place as well, since the carbon cathode is not homogeneous and has considerable porosity.

Sodium has been found to migrate relatively quickly through the carbon structure. Diffusion coefficients for various carbon qualities has been reported [4, 59, 67, 69] with rather large values for lattice diffusion. Some data for different carbon cathode qualities are summarized in Table 3.2. The diffusion coefficients are hard to compare from literature since many factors may influence the measurement like:

- ◆ Current density (CD)
- ◆ Temperature
- ◆ Cryolite ratio (CR)
- ◆ Cathode quality

The sodium diffusion coefficient increases with current density (CD) and temperature (T) [59, 60, 69–71] and has recently been shown that if CD, T and CR are kept constant, the diffusivity is scaled by the graphitization grade [57, 69]. It increases according to the following sequence:

graphitized > graphitic > semigraphitized > semigraphitic > amorpheus.

**Table 3.2:** Sodium diffusion coefficients in various carbon cathode qualities at different temperatures  $T$  [°C], current densities  $i_c$  [A/cm<sup>2</sup>] and cryolite ratios (CR) [57, 68, 69].

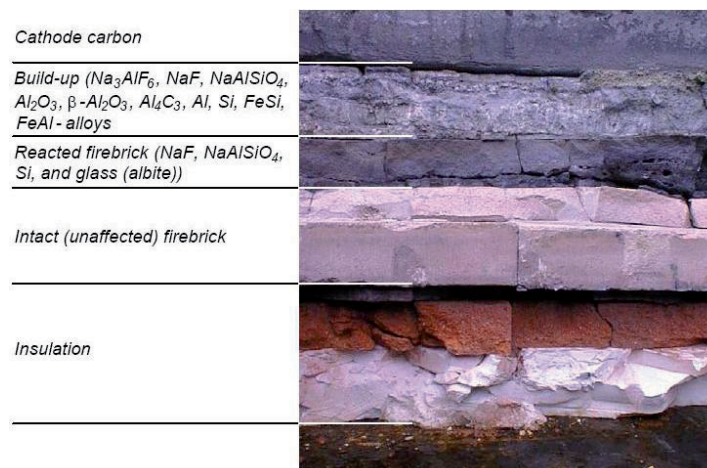
<b>T</b>	<b><math>i_c</math></b>	<b>CR</b>	<b>Amorphous</b>	<b>Semi-Graphitic</b>	<b>Semi-Graphitized</b>	<b>Graphitic</b>	<b>Graphitized</b>	<b>Graphite</b>
920	0.7	2.2			0.4-0.8·10 <sup>-5</sup>			
950			8.4·10 <sup>-5</sup>					
970	0.7	2.2	4.3·10 <sup>-5</sup> 1.4·10 <sup>-5</sup>		0.5-1.2·10 <sup>-5</sup>			
	0.98		4.0·10 <sup>-5</sup>					
	0.06			1.21·10 <sup>-4</sup>		5.0·10 <sup>-4</sup>		3.2·10 <sup>-4</sup>
	0.2			1.86·10 <sup>-4</sup>		2.0·10 <sup>-5</sup>		8.0·10 <sup>-4</sup>
	0.2						2.1·10 <sup>-4</sup>	9.0·10 <sup>-4</sup>
	0.2						2.6·10 <sup>-4</sup>	2.4·10 <sup>-3</sup>
980	0.7	4	2.4·10 <sup>-4</sup>	3.99·10 <sup>-4</sup>	8.0·10 <sup>-5</sup>		4.6·10 <sup>-4</sup>	2.4·10 <sup>-3</sup>
	0.7		3.5·10 <sup>-4</sup>				5.3·10 <sup>-4</sup>	4.7·10 <sup>-3</sup>
	0.7		2.1·10 <sup>-4</sup>				8.4·10 <sup>-4</sup>	1.6·10 <sup>-3</sup>
	1		4.2·10 <sup>-4</sup>				5.7·10 <sup>-4</sup>	1.2·10 <sup>-3</sup>
	1		4.6·10 <sup>-4</sup>				5.5·10 <sup>-4</sup>	5.0·10 <sup>-3</sup>

### 3.4 Chemical Degradation of Refractory Materials

#### 3.4.1 Visual Appearance of Spent Pot Lining

The refractory layers are installed to protect the insulation material below, but they cannot withstand chemical attack completely [3, 8]. Sodium is known to be the first penetration component downwards through the cathode block, as discussed in Section 3.3, followed by the fluoride containing melt [61]. During degradation significant mineralogical transformations in the refractory lining have been shown to occur [3, 8, 11].

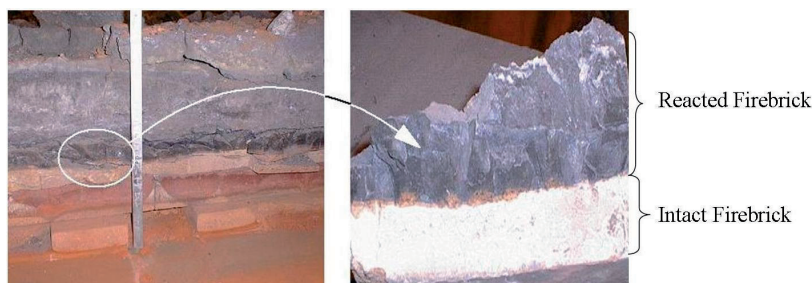
The visual appearance and extension of the reaction zone in SPL can be different from cell to cell, depending on cell age and operational conditions. However, the secondary phases appear to be the same, even though the amount varies quite substantially. Typically, the SPL consists of intact, but sometimes compressed insulation bricks underneath reacted refractories. In shutdown cells two layers in the spent refractory lining are visually distinguishable, as shown in Fig. 3.5.



**Figure 3.5:** Different layers in a cathode bottom lining after 1500 days in operation [72].

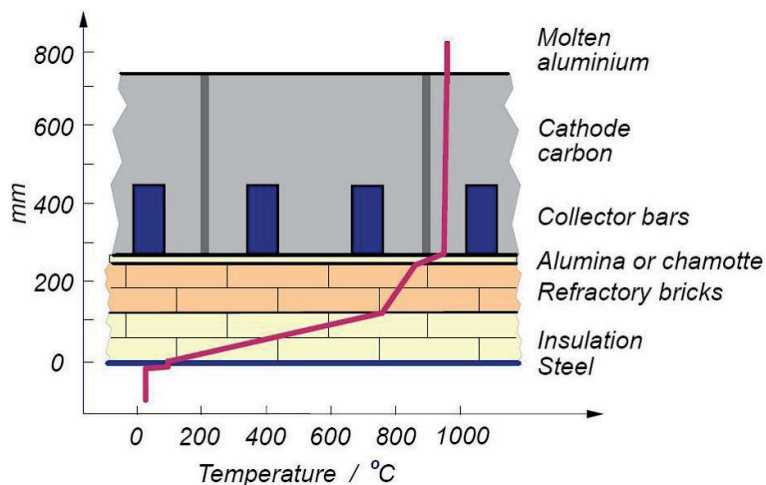
The upper part (towards the carbon block) is inhomogeneous, white greyish in colour and named "build-up". Besides minor amounts of phases like aluminium (Al),  $\text{Al}_4\text{C}_3$ , FeSi, and Fe-Al alloys it has been shown that mainly NaF,  $\text{Na}_3\text{AlF}_6$  and  $\beta\text{-Al}_2\text{O}_3$  are present. The crystalline like structure of this layer is littered with voids and gaps. The appearance of the subsequent part is opposed to this uniform, black and dense and named "reacted part". In this area, large amounts of nepheline ( $\text{NaAlSiO}_4$ ) and glassy phase have been found. The glass is assumed to be close to albite ( $\text{NaAlSi}_3\text{O}_8$ ) [3, 8]. The intersection between the reacted part and intact firebrick is a sharp interface, named "reaction front", as shown in Fig. 3.6 [72]. Here, the sequence and diffusion mechanism of attacking agents at the reacting front is not known. In the literature, the

"build-up" and reacted firebrick are commonly termed "lens build-up" material [3].



**Figure 3.6:** The sharp boundary between glassy reacted layer and intact firebrick of 1800 days old cell [72].

The estimation of temperatures in the lining during operation are based on calculations using the properties of virgin materials, as shown in Fig. 3.7. Thermodynamic calculations of reactions between refractories and attacking agents are summarized in Sections 3.4.3 and 7.2 as well as in the literature [3]. They show good agreements with autopsy or laboratory findings.



**Figure 3.7:** Schematic cross-section through a common bottom lining. The figure also shows the temperature gradient in the lining, calculated with data and dimensions as for new material [21].

### 3.4.2 Main Secondary Phases Formed During Degradation

Intensive efforts have been done to investigate the secondary phases formed during degradation [3, 13–16, 19]. For this purpose thermodynamic calculations, laboratory experiments and autopsy findings were accomplished and compared. In this context,

the attack by bath components was for a long time considered to be more relevant for the degradation of the refractory lining than attack by sodium [10, 11, 17, 18, 73, 74]. The importance of sodium attack has been stressed in a recent paper by Schøning and Grande [12] and was further pursued by Solheim et al. [20]. A combination of bath and sodium has also been discussed by Solheim et al. [21], Siljan et al. [22] and Pelletier et al. [23].

The main phases formed in the reaction between refractory lining and NaF/Na are nepheline ( $\text{NaAlSiO}_4$ ), cryolite ( $\text{Na}_3\text{AlF}_6$ ) and Si metal [11–13]. Dependent on the refractory composition,  $\beta$ - $\text{Al}_2\text{O}_3$  and albite ( $\text{NaAlSi}_3\text{O}_8$ ) preferably as a glass are also possible products. The detailed formation of these phases, based on thermodynamic calculations, will be discussed in the following section 3.4.3 and later in section 7.2.

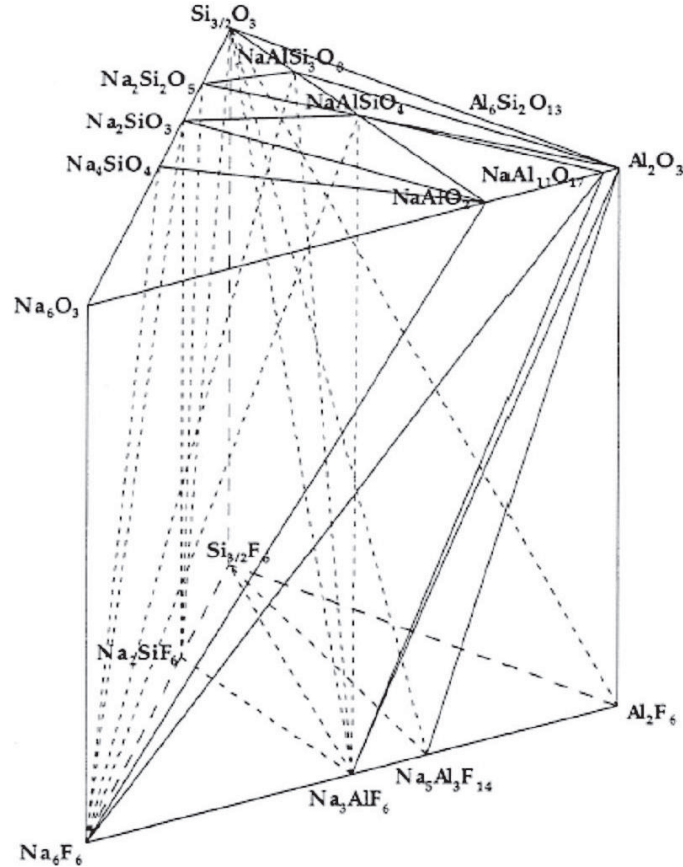
### 3.4.3 Phase Relations During Sodium Fluoride Attack

The degradation of refractory linings can be separated into pure NaF or Na attack. The stable compounds formed during degradation of alumino-silicate refractories have been summarized in particular phase diagrams or so called "degradation maps" [22,23].

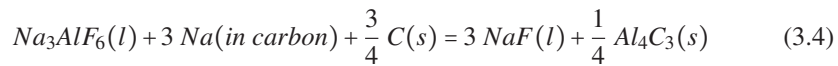
The mineralogical changes of the lining materials due to the reaction with molten fluorides are thoroughly investigated (Section 3.4). Rutlin and Grande [74] studied the quaternary reciprocal system  $\text{Na}_2\text{O-SiO}_2\text{-Al}_2\text{O}_3\text{-NaF-SiF}_4\text{-AlF}_3$  and their coexisting lines and phases during deterioration of alumino-silicate refractories. They reported a phase diagram, see Fig. 3.8 where the refractories are located on the  $\text{Si}_{3/2}\text{O}_3\text{-Al}_2\text{O}_3$  edge. The composition of the refractory material corresponds to a point on this silica-alumina line. During the degradation process, the position of this initial point shifts as more fluoride bath is added. The end point is the composition of the attacking bath. For pure NaF attack, this is the  $\text{Na}_6\text{F}_6$  point in Fig. 3.8. The connection of these two points describes the degradation path. The path and stability fields varies depending on the  $\text{SiO}_2/\text{Al}_2\text{O}_3$  ratio of the initial refractory material and the amount of attacking agent. Each crossed domain shows the coexisting phases as a function of the overall composition.

Schøning et al. [10] have published a degradation map of a fluoride attack, shown in Fig. 3.9. It is defined by six different stability regions, which correspond to six quaternary phase diagrams. Fig. 3.9 demonstrates that if fireclay materials are exposed to penetrating fluoride melts, nepheline and albite (preferably as glass) are the secondary silicate phases, besides minerals like  $\alpha/\beta$ -alumina. The construction of the map, based on the main possible thermodynamic reactions, is summarized below.

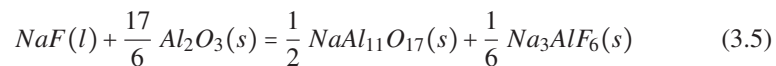
In the cathode carbon block the chemical composition of the fluoride melt, which is mainly a mixture of cryolite ( $\text{Na}_3\text{AlF}_6$ ) and sodium fluoride (NaF), becomes enriched in NaF and thus changes into a basic electrolyte, with a cryolite ratio (CR)>3 according to Eqs. (3.1) and (3.4) [3, 17]

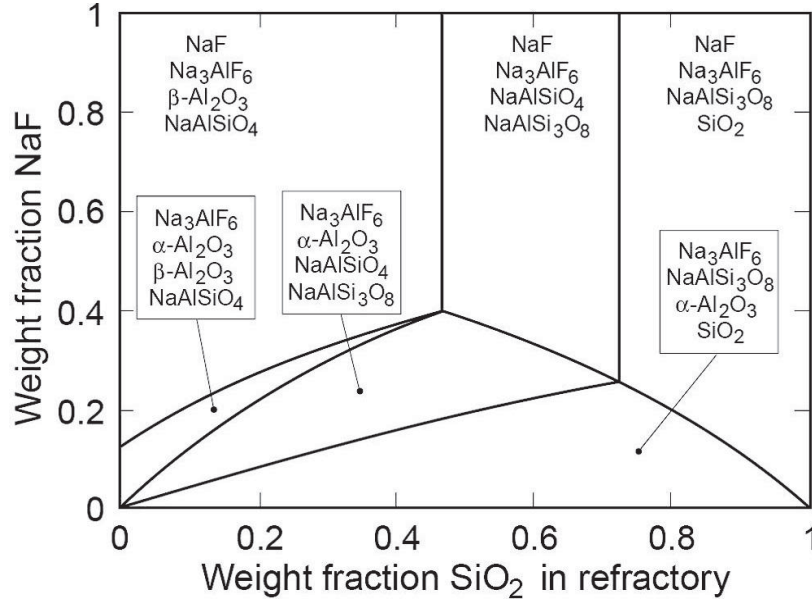


**Figure 3.8:** Coexistence lines in the quaternary reciprocal  $\text{Na}_2\text{O}-\text{SiO}_2-\text{Al}_2\text{O}_3-\text{NaF}-\text{SiF}_4-\text{AlF}_3$  at sub-solidus temperature [74].



Thus the percolating bath (mainly a mixture of cryolite and NaF), which attacks the refractory material is represented by pure NaF in the thermodynamic calculations. In contact with the refractory layer, the resulting mineral phases are dependent on the  $\text{SiO}_2/\text{Al}_2\text{O}_3$  ratio of the initial lining material. First, the focus is on the chemical reactions between pure alumina and cryolite melts (represented by NaF). Besides the dissolution of alumina in the fluoride melt, the only chemical reaction to be considered is the formation of a less dense  $\beta$ -alumina ( $\text{Na}_2\text{O} \cdot 11\text{Al}_2\text{O}_3$ ) phase, according to Eq. (3.5)





**Figure 3.9:** Phase compositions due to chemical reaction between aluminosilicate materials and sodium fluoride. The phase composition is given as a function of the silica content in the refractory material and the weight fraction of NaF relative to the amount of aluminosilicate material [10].

The solidus temperature  $T_s$  is 888 °C at excess NaF, shown in Table 3.3. It corresponds to the ternary eutectic, where  $\beta$ -alumina coexists with NaF(s) and  $\text{Na}_3\text{AlF}_6$ (s) [10]. The solubility of alumina decreases with increasing NaF-content. An increasing amount of cryolite turns the melt more acidic, which enhances the deterioration of high alumina linings [10]. At  $\text{CR} < 3$ ,  $T_s$  drops by more than 200 °C [75].

Next, high alumina and chamotte refractory linings are considered. Here, mullite [ $3\text{Al}_2\text{O}_3 \cdot 2\text{SiO}_2$ ] was chosen as a reference compound for sodium fluoride and cryolite attack. As seen from the stoichiometry, mullite has a surplus of alumina compared to chamotte materials. Due to the presence of silica Eq. (3.6) bricks with high alumina content convert to  $\beta$ -alumina and nepheline ( $\text{NaAlSiO}_4$ ) as given by Eq. (3.5)



In case the penetrating melt is in surplus compared to the lining material (mullite), the lining components will be completely consumed and converted during the reaction with the bath as shown by Eq. (3.7)

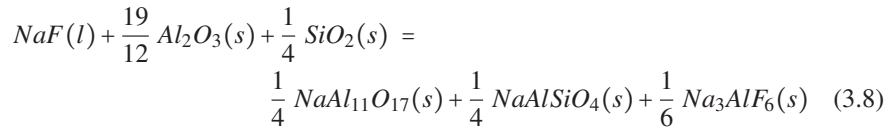




**Table 3.3:** Solidus temperatures of pure NaF, binary and ternary phase systems.

System	T <sub>S</sub> [°C]	Ref.
NaF	996	[76]
NaF-Na <sub>3</sub> AlF <sub>6</sub>	888	[77]
NaF-NaAlSiO <sub>4</sub>	970	[78]
NaF-NaAlSi <sub>3</sub> O <sub>8</sub>	868	[76]
NaF-Al <sub>6</sub> Si <sub>2</sub> O <sub>13</sub>	857	[18]
Na <sub>3</sub> AlF <sub>6</sub> -NaAlSiO <sub>4</sub>	952	[18]
Na <sub>3</sub> AlF <sub>6</sub> -NaAlSi <sub>3</sub> O <sub>8</sub>	897	[18]
NaF-Na <sub>3</sub> AlF <sub>6</sub> -β-Al <sub>2</sub> O <sub>3</sub>	881	[75]
NaF-Na <sub>3</sub> AlF <sub>6</sub> -NaAlSiO <sub>4</sub>	873	[18]
NaF-Na <sub>3</sub> AlF <sub>6</sub> -NaAlSi <sub>8</sub> O <sub>4</sub>	865	[18]

The combination of equations (3.5) and (3.7) to reaction (3.8)

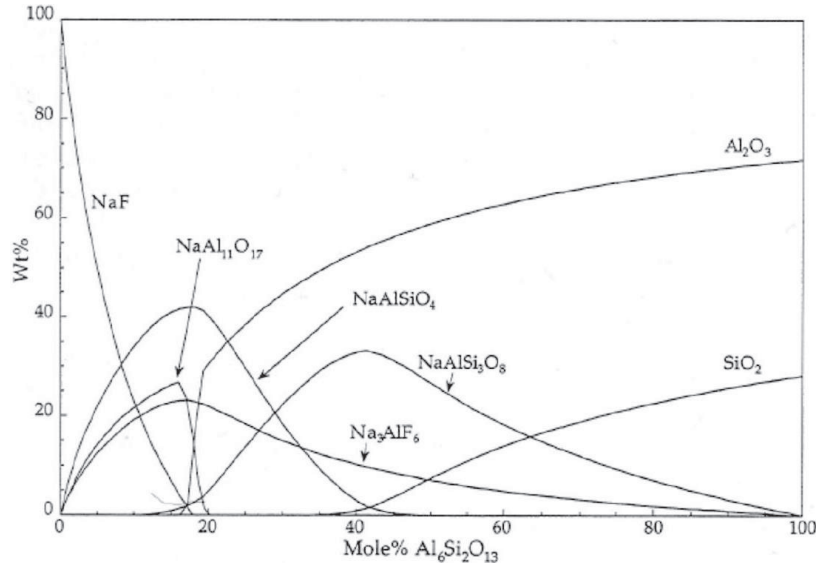


was confirmed by Rutlin and Grande [74]. Eq. 3.8 defines the borderline between two stability fields in the degradation map, see Fig. 3.9. The chemical reactions (3.5) and (3.7) are the endpoints of the line, respectively. The curvature is caused by adding both reactions with varying ratios. The formation of β-alumina (NaAl<sub>11</sub>O<sub>17</sub>) and nepheline (NaAlSiO<sub>4</sub>) shows that NaF is not coexisting with alumino-silicate refractories.

Cryolite is always present as a reaction product between NaF and the oxides. If the diffusion of volatile fluorides (NaAlF<sub>4</sub> and SiF<sub>4</sub>) [17] into the lining is neglected, Na<sub>3</sub>AlF<sub>6</sub> will not react with the firebrick material. Instead it will act as a solvent for NaF and oxide phases of the reacted material [10]. The solidus temperature for this quaternary system, including cryolite, nepheline, α- or β-alumina at an excess amount of NaF (> 82 mole%), is shown in Table 3.3. It is more than 100 °C below the operation temperature of the cell [10]. The quaternary eutectic melt is not viscous, since it mainly contains molten NaF-Na<sub>3</sub>AlF<sub>6</sub> with minor concentrations of alumina and nepheline [18].

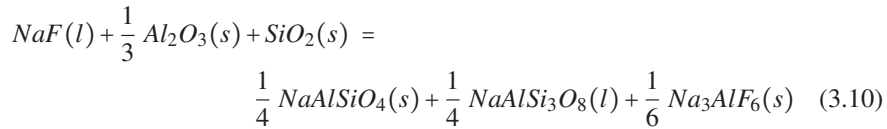
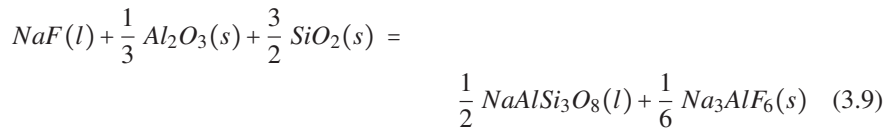
Near the reaction front an excess amount of refractory materials is present together with a deficiency of sodium fluoride. In this region β-alumina converts to α-alumina and a new phase, albite (NaAlSi<sub>3</sub>O<sub>8</sub>) appears due to the reaction of nepheline with silica. Albite is an excellent glass former and remains in the molten state together with

cryolite. The phase composition, including the new phases  $\beta/\alpha$ -alumina, nepheline and albite along the composition line NaF- $\text{Al}_6\text{Si}_2\text{O}_{13}$  was reported by Rutlin and Grande [74] and is depicted in Fig. 3.10.

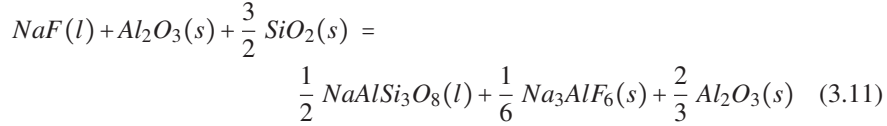


**Figure 3.10:** Estimated phase composition along the composition line NaF- $\text{Al}_6\text{Si}_2\text{O}_{13}$  (sodium fluoride-mullite) [74].

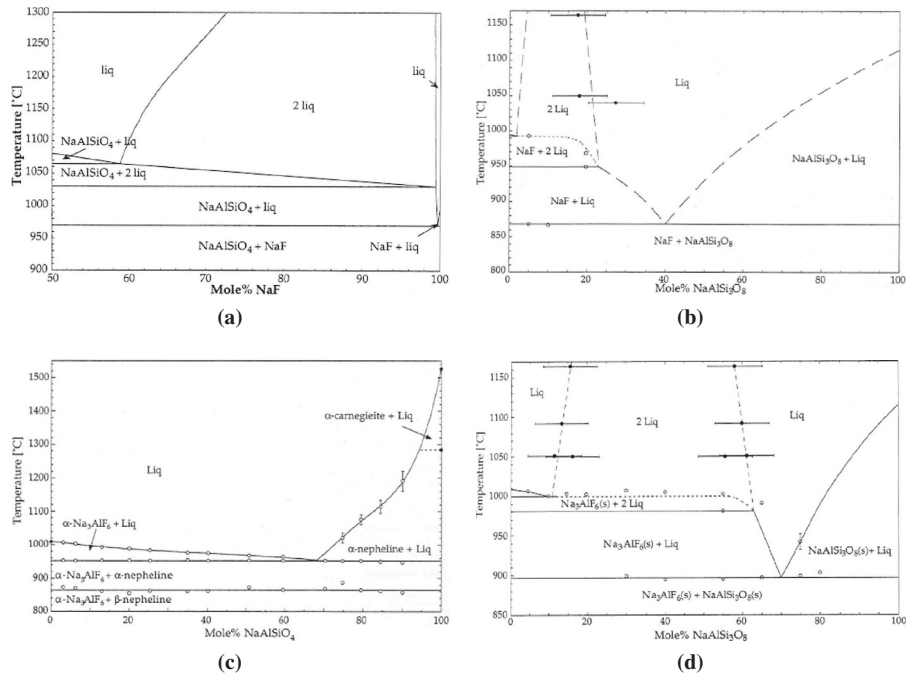
If the  $\text{SiO}_2$  content increases to more than 47 wt%, the  $\beta$ - $\text{Al}_2\text{O}_3$  phase is no longer present in the reaction zone [10] and nepheline as well as albite are formed according to equation (3.7), (3.9) and (3.10)



If the refractory lining is in surplus the mineral phase albite and additional alumina will be formed at the expense of nepheline and only silica will completely be converted as given in Eq. (3.11)



The reaction shows that alumina, silica, cryolite and albite are coexisting phases. Due to the  $\beta$ - $Al_2O_3$  deficiency at  $SiO_2 > 72$  wt% albite will form (Eq. (3.9)), instead of nepheline, see Eq. (3.10). The percolation of bath through the carbon cathode continues during the entire lifetime of the cell. Therefore, not only reaction between "fresh" refractory material and molten fluorides, but also reaction with the products need to be considered. Thus reactions of nepheline and albite with fluoride containing melts are important. Rutlin [18] investigated the ternary systems NaF- $Na_3AlF_6$ - $NaAlSiO_4$ , NaF- $Na_3AlF_6$ - $NaAlSi_3O_8$  including their pseudo-binary phase diagrams, which are shown in Fig. 3.11.



**Figure 3.11:** The pseudo-binary phase diagrams: (a) NaF- $Na_3AlF_6$ , (b) NaF- $NaAlSiO_4$ , (c)  $Na_3AlF_6$ - $NaAlSiO_4$  and (d)  $Na_3AlF_6$ - $NaAlSi_3O_8$  [18].

The solubility of albite in the fluoride is higher than nepheline. Cryolite is coexistent with the primary and secondary phases in the lining. The solidus temperatures in the phase diagrams are summarized in Table 3.3. It is shown that the solidus temperature does not significantly decrease with increasing silica content in the lining. The lowest values are observed in regions where sodium fluoride and cryolite are present

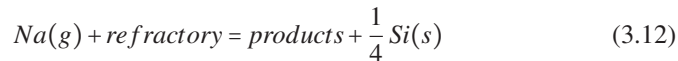
together [13]. Furthermore, the solidus temperature  $T_s$  of albite is 55 °C lower compared to nepheline (higher melting point) [13]. If albite is present in addition to sodium fluoride and cryolite the lowest solidus temperature of 865±5 °C is reported. Based on the solidus temperature albite should be avoided by keeping the alumina content in alumino-silicate refractories high [10].

A viscous melt and liquid-liquid phase separation between a fluoride-rich melt on the top and a silica-rich melt below has been observed by investigation of the cryolite resistance of alumino-silicate refractories using the cup-test (Section 3.2) [10]. The extent of the reaction and the thickness of the silica-rich melt has been observed to clearly depend on the silica content of the initial refractory brick as shown in Fig. 3.2. It was found that the cryolite resistance of alumino-silicate refractories increases with increasing silica content. Albite is present as the most important reaction product, see Fig. 3.9.

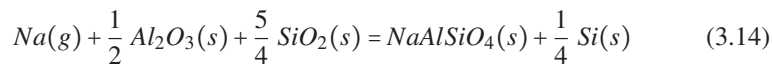
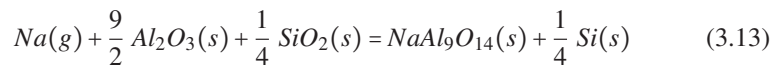
Rutlin and Grande [18, 79] have proposed that additions of albite or mixtures of albite and nepheline increase the viscosity of sodium fluoride and cryolite by several orders of magnitude. The oxyfluoride melt separates into a fluoride and alumino-silicate rich melt as shown in Fig. 3.2. The latter is the most dense phase and remain below the fluoride-rich melt due to gravity. It was therefore proposed that a higher silica content is beneficial due to the formation of a viscous barrier.

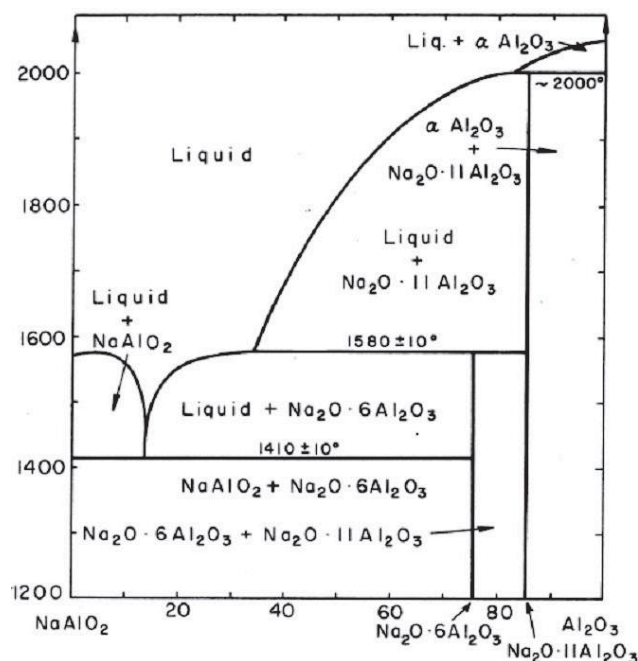
### 3.4.4 The Role of Sodium

Recently, Schønning et al. [12] have considered the chemical stability of some refractory materials in sodium-rich environments. The authors have studied the effect of sodium by using the cup-test and Na vapor test [10]. The important outcome was that both SiO<sub>2</sub> and Al<sub>2</sub>O<sub>3</sub> in the refractory materials are thermodynamically not stable in contact with metallic sodium since Na(g) works as strong reducing agent with respect to most oxides. The quasi-binary phase diagrams of Na<sub>2</sub>O-Al<sub>2</sub>O<sub>3</sub> and Na<sub>2</sub>O-SiO<sub>2</sub> are given in Figs. 3.12 and 3.13. Evidence for the reducing conditions in industrial cathodes was provided through autopsies of SPL [12]. Elemental silicon was found in the spent refractory layer, shown in Fig. 3.14, formed by the general equation

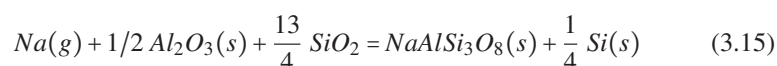


Alumino-silicate refractories, which are exposed to Na vapor form mainly  $\beta$ -alumina, nepheline, albite and silicon, according to following reactions (3.13)-(3.15)





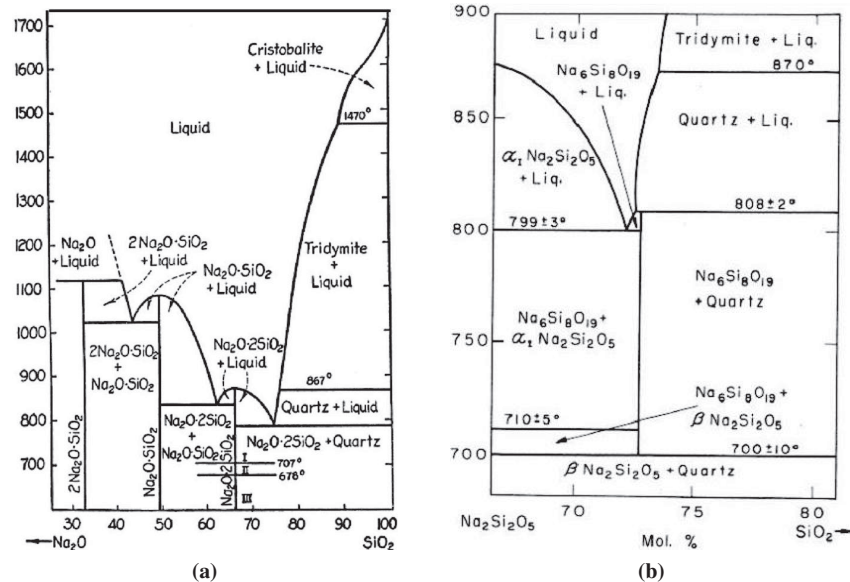
**Figure 3.12:** Equilibrium phase diagram of the system  $\text{NaAlO}_2\text{-Al}_2\text{O}_3$  proposed by Rolin and Thanh [80].



However, nepheline as well as albite are not stable in contact with sodium. Albite is more unstable than nepheline. The reduction of these minerals is disadvantageous, because it does not prevent further reactions with Na and will not act as a barrier.

### 3.4.5 Diffusion Barrier

Near the reaction front a layer of sodium alumino-silicates (mainly nepheline and albite) is present. During operation this silica-rich layer is a dense and highly viscous liquid acting as diffusion barrier. It is proposed to continuously slow down or retard further penetration and reaction by bath components. Rutlin and Grande [79] proposed that the formation of albite and its high solubility in  $\text{NaF-Na}_3\text{AlF}_6$  is the major explanation for the formation of a viscous layer. Furthermore, it was proposed that the higher the silica content the more viscous and thus effective is this barrier [10]. Fig. 3.15 shows how the viscosity of a silicate melt evolves by varying the  $\text{SiO}_2$  and/or the F<sup>-</sup> content. With decreasing silica as well as increasing fluoride content, the viscosity is decreasing and vice versa. Recently, based on an autopsy of a young cell, Tan [83] estimated the molten fraction underneath the carbon cathode block. Moreover,

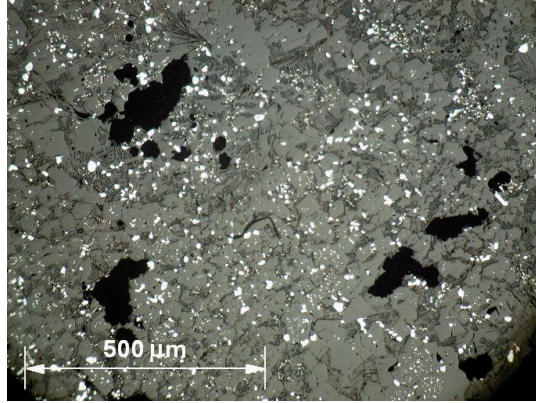


**Figure 3.13:** Equilibrium phase diagram of (a) the binary system Na<sub>2</sub>O-SiO<sub>2</sub> [81] and (b) the stability field of Na<sub>6</sub>Si<sub>8</sub>O<sub>19</sub> [82].

from literature data he discussed the viscosity and composition of the molten silicates forming the viscous barrier.

The percolating degradation agents react and destroy the lining material immediately after cell start-up. This attack continues relatively intensively during the early stage of operation. With increasing diffusion depth the penetration rate slows down. However, it proceeds the entire lifetime because "fresh" refractory material is continuously exposed to the degradation agents, which are percolated incessantly through the cathode [22]. The reaction rate is determined by the solubility of both the refractories as well as their reaction products in the percolating electrolyte. It is impossible to avoid a molten layer between the carbon cathode and the unreacted refractory material until the melt is saturated by reaction products, or the penetration depth increases until the temperature becomes too low and crystallization occurs [10].

Due to mineralogical transformations, the thermal conductivity of the materials rises since all the pores are filled with material. This will cause the movement of high temperature isotherms downwards, deeper into the lining. Thus the deterioration can proceed further on. An unstable thermal balance, accompanied by increased heat loss and energy consumption, is the consequence. This will increase the production costs for the aluminium industry. The movement of alkalis and bath constituents vertically through the lining toward or into the insulation, eventually results in the failure of the pot.



**Figure 3.14:** The presence of silicon droplets due to the reduction of  $\text{SiO}_2$  compounds in the refractory layer of a spent pot lining [12].

### 3.4.6 Sodium Diffusivity in the Refractory Lining

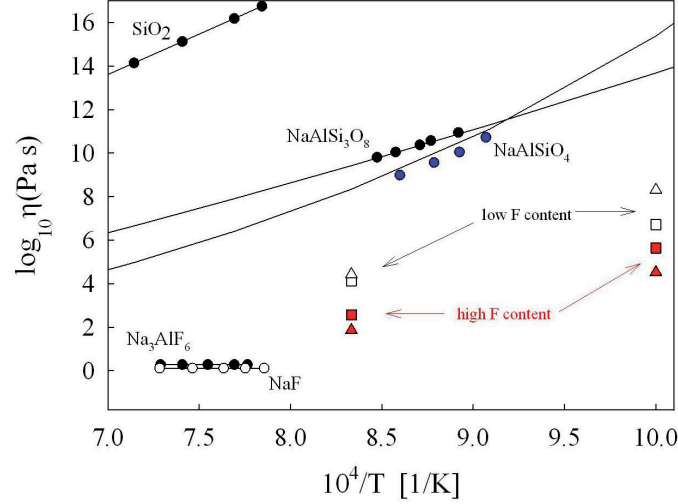
The diffusion of sodium in the cathode block was proven to be faster than the fluoride melts [60]. In the refractory layer the sequence has not been clarified so far. The possible attacking species (sodium or bath) and its diffusivity in the viscous barrier, made of aluminosilicates near the reaction front, is important to know. It enables the prediction of the diffusion mechanism and thus to determine a way to prevent the degradation of the refractory material. Sodium diffusivity data in the material in question is not available since the exact composition is unknown. However, it can be estimated based on viscosity data in related systems. In general, the diffusivity in a non-viscous liquid with known viscosity can be calculated using Stokes-Einstein relation (3.16)

$$D_\eta = \frac{k_B T}{6\pi r \eta} \quad (3.16)$$

where  $D_\eta$  is the viscous diffusivity [ $\frac{\text{m}^2}{\text{s}}$ ],  $k_B$  is the Boltzmann constant,  $\eta$  is the fluid viscosity [ $\text{Pa} \cdot \text{s}$ ],  $T$  is the temperature [ $\text{K}$ ] and  $r$  is the radius of the diffusing species [ $\text{m}$ ]. For molten silicates Eyring proposed a more appropriate Eq. (3.17)

$$D_\eta = \frac{k_B T}{\gamma \eta} \quad (3.17)$$

where  $\gamma$  is the distance between two equilibrium positions of an isometric sphere or so-called translation distance of the diffusion ion [ $\text{m}$ ]. It is well known that the diffusion barrier in the spent refractory material contains a sodium-silicate glass melt. The exact composition is not known, but albite has been suggested to be close to the composition [3]. A summary of viscosity data for several relevant compositions in



**Figure 3.15:** Viscosity data for relevant oxide and fluoride melts as a function of inverse temperature. The figure was redrawn from [18] including the authors measured data. The data for silica, aluminosilicates and fluorides were obtained from other authors [84–87].

the  $\text{Na}_2\text{O}-\text{Al}_2\text{O}_3-\text{SiO}_2$  system at elevated temperatures has been reported [85, 86, 88]. Some examples are given later in this section. The viscosity was fitted to the Eqs. (3.18) or (3.19)

$$\log_{10}\eta = -A_{Arr} + \frac{B_{Arr}}{T} \quad (3.18)$$

$$\log_{10}\eta = A_{VFT} + \frac{B_{VFT}}{T - T_0} \quad (3.19)$$

The Arrhenius relation (3.18) gives the logarithmic viscosity as a function of inverse temperature ( $T$ ) where  $A_{Arr}$  is a constant and  $B_{Arr}$  is the activation energy for viscous flow. In viscous melts this equation is insufficient to describe the temperature dependence of viscosity properly and the three-parameter Vogel-Fulcher-Tamann (VFT) Eq. (3.19) is used.

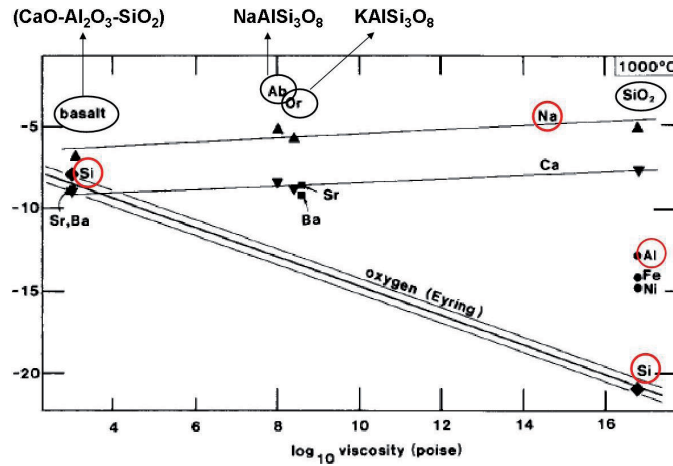
From previous investigations it is assumed that the viscous barrier is a glassy phase (estimated by albite). The alkali diffusion in alumino-silicate glass melts will be discussed in the next section.

The sodium ions are highly mobile and move relatively easily through silicate glasses compared to the lattice and covalent bonded elements such as silicon and oxygen [45, 89, 90]. Since the exact composition of the viscous or glassy phase (approximated by albite) is not well known [3], it is difficult to predict the diffusion constants for each ion involved. Differences in the diffusion coefficients of alkali ions, alkaline-earth ions and network formers in multicomponent melt systems have been studied by tracer



diffusion experiments [91–99]. Tracer diffusion, in contrast to chemical diffusion, occurs in the absence of a concentration gradient, which is usually assumed to be identical to self-diffusion.

Fig. 3.16 shows a comparison of tracer diffusions of different ions, dependent on melt viscosity in basalt, albite, orthoclase and pure SiO<sub>2</sub>. The diffusivity of Si follows the Eyring curve (Eq. (3.17)) for viscous diffusivity and reduces significantly as the viscosity increases. In SiO<sub>2</sub> melt Na<sup>+</sup> diffuses 16 orders of magnitude faster than Si<sup>4+</sup>. The glassy phase at the reaction front in SPL samples is approximated by albite. At this composition the sodium diffusivity reaches a value of approximately 2.5 · 10<sup>-6</sup> [cm<sup>2</sup>/s], which is still 7 orders of magnitude higher than the Si viscous diffusivity. Surprisingly, from Fig. 3.16 it can be seen that the Na diffusivity seems to be independent of the melt viscosity or the melt composition [93,99].



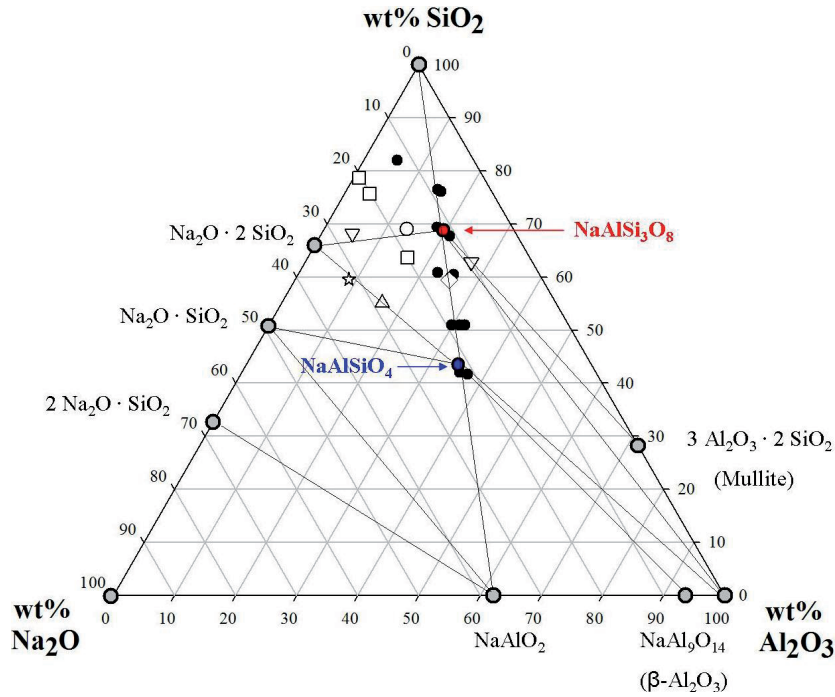
**Figure 3.16:** Tracer diffusivity data  $\log D$  [cm<sup>2</sup>/s] versus melt viscosity [P] for basalt, a Ca-Al-Si synthetic oxide melt, albite (Ab) and orthoclase (Or) melts, and SiO<sub>2</sub> melt at 1000 °C. The chemical formula were added by the author.

The diffusion of oxygen on the other side depends strongly on the melt viscosity. Here, the tracer diffusivity of oxygen is much lower than for sodium. The high Na diffusion coefficient compared to the viscous diffusivity were also observed by other authors. Moreover, other important factors like the initial Na concentration [45, 89], structural changes in the network [95], the thermal history [97] and the temperature [94] might influence the Na diffusivity. Furthermore, it was found that it is closely related to the conductive diffusivity. The conductivity diffusion coefficient  $D_\sigma$  of ions is linked to the dc ionic conductivity  $\sigma_{dc}$  [1/( $\omega \cdot \text{cm}$ )] via the Nernst-Einstein Eq. (3.20)

$$D_\eta = \frac{k_B \sigma_{dc} T}{q^2 N_{ion}} \quad (3.20)$$

Here,  $q$  is the charge,  $N$  is the number density of mobile Na<sup>+</sup> ions [ions/m<sup>3</sup>],  $k_B$  is

the Boltzmann's constant and  $T$  is the absolute temperature [K]. Available sodium diffusion and viscosity data for several melt compositions located in the  $\text{Na}_2\text{O}-\text{Al}_2\text{O}_3-\text{SiO}_2$  system are summarized in Fig. 3.17.



**Figure 3.17:** Review of melt compositions in the  $\text{Na}_2\text{O}-\text{Al}_2\text{O}_3-\text{SiO}_2$  system, where (1.) the viscosities of fourteen melts close to the  $\text{SiO}_2$ - $\text{NaAlO}_2$  join in the temperature range of  $700$ - $1650^\circ\text{C}$  were investigated [85] (black filled circles) and (2.) the sodium/fluorine diffusion coefficients are available. Here, most of the data were reviewed by [100]. The data used in this diagram are from [101] (white squares), [102] (white circle), [100, 103] (white triangle up), [104] (white triangle down), [105] (white star) and [91, 94] (white diamond).

The Arrhenius relationship was used to fit the temperature dependence of the measured diffusivity values, according to Eq. (3.21)

$$D = D_0 \exp\left(-\frac{Q}{RT}\right) \quad (3.21)$$

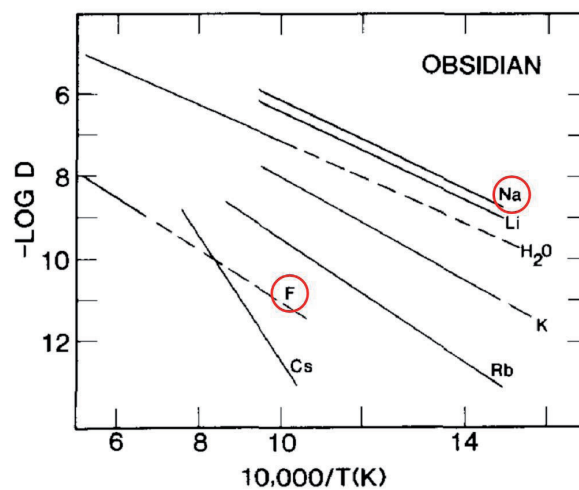
where  $D_0$  is the pre-exponential factor [ $\text{m}^2/\text{s}$ ],  $R$  is the gas constant  $8.314$  [ $\text{J}/(\text{K}\cdot\text{mol})$ ],  $T$  is the temperature in [K] and  $Q$  is the activation energy [ $\text{J}/\text{mol}$ ]. Sodium diffusion coefficients  $D_{\text{Na}}$  for compositions close to albite can be found in literature [91, 104]. The data are summarized in Table 3.4.

Dingwell [94] studied the transport of fluoride ions in silicate melts in the  $\text{Na}_2\text{O}-\text{Al}_2\text{O}_3-\text{SiO}_2$  system. The author compared the chemical diffusivities of  $\text{F}^-$  ions in albite (75 %  $\text{SiO}_2$  in  $\text{NaAlSi}_3\text{O}_8$ ) with tracer diffusivities of alkali in an obsidian melt

**Table 3.4:** Calculated pre-exponential factor  $D_0$ , activation energy  $Q$  and resulting sodium diffusion coefficient  $D_{Na}$  for compositions close to the albite.

Na <sub>2</sub> O [wt%]	Al <sub>2</sub> O <sub>3</sub> [wt%]	SiO <sub>2</sub> [wt%]	T [°C]	D <sub>0</sub> [cm <sup>2</sup> /s]	Q kcal/mole	D <sub>0</sub> cm <sup>2</sup> /s	Ref.
10.90 11.90	20.44 29.50	69.00 68.40	350-795	5.3·10 <sup>-3</sup>	13.5 ±3	2·10 <sup>-8</sup> -1·10 <sup>-6</sup>	[91]
10.90	18.00	70.6	352-716	5.02·10 <sup>-4</sup>	14.5 ±0.3	4·10 <sup>-8</sup> -4·10 <sup>-6</sup>	[104]

(natural glass with 70-75 % SiO<sub>2</sub> plus MgO, Fe<sub>2</sub>O<sub>4</sub>). The result is shown in Fig. 3.18. It was found that F<sup>-</sup> diffuses much slower than Na<sup>+</sup>. At a temperature of 1000 K the difference is around 6 and at 1100 K 5 orders of magnitude. Dingwell [94] proposed that the chemical diffusion of fluoride is decreasing with increasing SiO<sub>2</sub> content, which is probably due to a simple anionic exchange with oxygen.

**Figure 3.18:** Comparison of the chemical diffusivities of fluorine in albite melt and water in obsidian/ryolite melt with tracer diffusivities of alkalis in obsidian melt (data from [92,94,106]). Fluorine and sodium ions are marked with red circles.

### 3.5 Cathode heave

An often experienced phenomena in industrial cells during operation is the heaving of cathode blocks shown in Fig. 3.19. The heaving is detected as a lifting of the cathode blocks relative to the steel casing bottom [3], irrespective of any cathode abrasion or wear. One of the researchers, who first discussed the bottom heaving, was Waddington [107] in 1963. He suggested a "frost heave" analogy to describe the basic mechanisms, based on the shape of the bottom blocks. In the following years this

description has become the standard approximation to the problem [108]. During the last decades, several authors have worked more intensively with the topic of bottom heaving in aluminium electrolysis cells and new hypotheses aiming to explain this phenomena have been proposed [1, 3, 24, 69, 109–114].



**Figure 3.19:** Photographs of the cathode heave of a 585 days old pot [3].

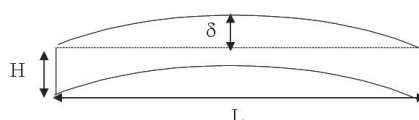
Most authors agree that the initial phase of cathode aging in Hall Héroult cells is due to the rapid penetration of sodium (Na) into the carbon block and subsequent penetration of the bath. Like mentioned earlier, the sodium content and sodium expansion are closely related. Thus every parameter that influences the former will influence the expansion. This is accompanied by the uneven thermal behaviour (expansion or contraction) of all the cell lining materials. Arching due to gradients in temperature and sodium concentration induces mechanical stresses. They basically arise when the expansion of the block is restrained by the outer steel shell. Both impacts are delayed in time, the thermal expansion occurs during the heat-up and start-up period of the cell (large temperature gradient) until operation temperature is reached. This is closely related to the cell design, the material properties and the accuracy of lining work. The sodium initiated expansion, in contrast, occurs during the first month of operation. Thus the generated stresses due to Na uptake arise on top of the cathode block before distributing through the whole bulk material [115]. Sodium absorption gives an expansion in the range of 0.1 to 1.5 % for commercial cathode materials [24] and thermal expansions can reach values up to 0.4 % [3]. Both are especially harmful, when vertical gradients are set up. It may result in heaving [3] and cracking.

The maximum heaving/deflection or so called arching ( $\delta$ ) [cm] of an unrestrained cathode block can be predicted by Eq. (3.22) with reference to Fig. 3.20 [24]

$$\delta = \frac{\alpha_{Na} \cdot L^2 \cdot \Delta C_{Na}}{8H} \quad (3.22)$$

where  $\alpha_{Na}$  is the sodium expansion coefficient [%] ,  $\Delta C_{Na}$  is the vertical sodium concentration gradient (assumed linear concentration gradient with maximum sodium swelling at the top and no sodium at the bottom),  $L$  is the length [cm] and  $H$  the height [cm] of the cathode block. The effect of thermal gradients is omitted in the equation.

Table 3.5 shows the calculated upward cathode bending for different cathode qualities with a varying graphite content by applying Eq. (3.22). The calculation demonstrates that the cathode heave decreases with increasing graphite content. If the cryolite ratio (CR) of the electrolyte in industrial cells decreases (lower sodium activity) and the counteracting compression pressure for restrained blocks are taken into consideration, the estimated bending is further reduced.



**Figure 3.20:** Principle of calculating upward bending of carbon cathode blocks due to sodium swelling [24].

Up to now it is believed that the arching is mainly formed due to the sodium uptake/swelling during the first few days of cell operation (up to 55 days) and is stable thereafter [3, 67, 108]. This might be true for anthracitic materials. Graphitized cathodes in contrast have a low chemical expansion of 0.1-0.20 %, which is lower than the thermal expansion. The resulting deflection is not enough to explain observed bottom heavings up to 20-30 cm [12]. Furthermore, a clear correlation between carbon quality, related sodium expansion and the final magnitude of cathode heaving (including collector bar bending) is not given yet.

**Table 3.5:** Calculated upward bending of cathode blocks due to sodium swelling using the nominal dimensions.

Material	Graphite cont. [%]	L [cm]	H [cm]	$\alpha_{Na}$ [%]	$\delta$ [cm]	Ref.
Anthracite	0	320	43	1.5	4.5	[108]
Anthracite	25	320	43	1.0	3.0	
Semi-graphite	90	320	43	0.5	1.5	
Graphitic	100	320	43	0.2	0.6	

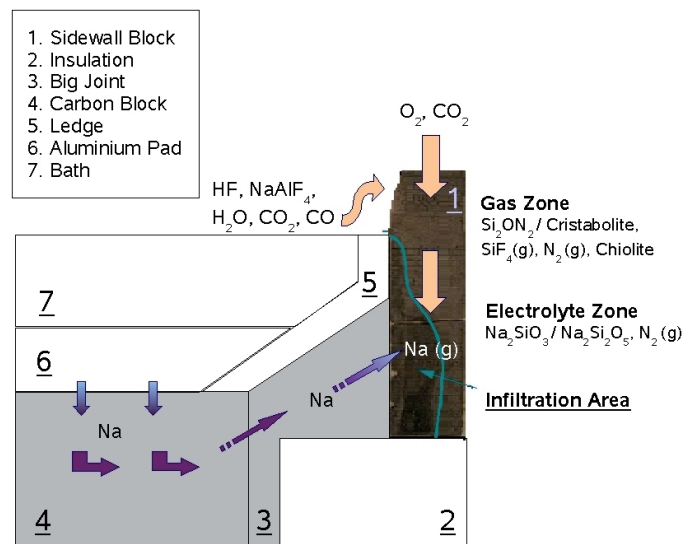
The slow second phase of ageing/heaving, which follows the initial bath penetration, is less well understood. This may lead to substantial upwards bending [116]. Some authors [3, 107, 116, 117] have discussed that the bottom heave is in some ways similar to the so called "frost heave", which normally deals with the transport and phase transition of pure water in soil which freezes. The temperature gradient alone is the reason for ice lens formation. In the case of the bottom lining in electrolysis cells, they refer to frozen "salt lenses" [118], found at the interface between the carbon block and the refractory material in SPL. However, the mechanism of the lens formation is not fully understood. Based on this hypothesis, the authors estimate that the penetrating bath in a carbon cathode is a supercooled melt and can therefore begin to freeze in capillary pores or below the carbon block. This gives a push-up effect upwards caused by the crystallization pressure, if it exceeds the strength of the porous material [3].

The experimental evidence to support this theory reached no final conclusion [116].

Like mentioned previously, the cathode heaving is a complex phenomena, which is still not well explained. It is possible that other mechanisms or reactions are involved. For instance the reactions between the percolating sodium and bath components and the lining materials lead to volume expansions. Weakening of the material strength through plastic deformations or upwards acting buoyancy forces are other possible reasons. In the end it is not possible to rule out new findings to explain the cathode heaving. Simulations by means of the finite element method [3, 119, 120] are used as an alternative tool to probe the cause of the cathode heave.

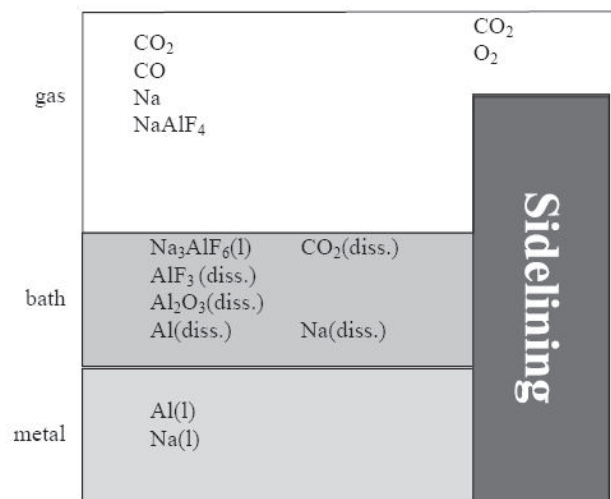
### 3.6 Chemical Degradation of Sidewall Blocks

Recently, efforts have been made to investigate the diffusion of sodium and resulting degradation of  $\text{Si}_3\text{N}_4$ -bonded SiC sidewall bricks. Wang et al. [27, 121] proposed that sodium diffuses as a gas inside the sidewall blocks due to its high temperature and the high equilibrium vapor pressure of the sodium. During normal operation the sideling block is most of the time covered by a ledge (frozen electrolyte layer) to prevent the direct exposure to the aluminium pad and the electrolyte. However, the sidewall block still deteriorates gradually over time due to the  $\text{Na(g)}$  diffusion and the accompanied reactions leading to deterioration [29]. Based on spent  $\text{Si}_3\text{N}_4$ -bonded SiC lining investigations Wang et al. [27, 29] proposed an overall diffusion path for  $\text{Na(g)}$  diffusion into the sideling as shown in Fig. 3.21.



**Figure 3.21:** A schematic overview of the proposed route of gas diffusion leading to the deterioration of SNBSC sidewalls (not in scale) [28].

They suggested that a reasonable assumption of the diffusivity of sodium might be  $10^{-7}$  [ $\text{m}^2/\text{s}$ ] [30]. It was found that the fine grained  $\text{Si}_3\text{N}_4$  binder phase is the weak and thus chemically degraded part. The attack of sidewall block material can be separated into three regions, dependent on position and prevailing chemical conditions, shown in Fig. 3.22. From top downwards the sequence is as follows: The gas zone (above the bath level), the electrolyte zone (between bath and metal level) and the aluminium zone (below the metal level). The main attacking agents are oxidizing gases ( $\text{O}_2$  or  $\text{CO}/\text{CO}_2$ ),  $\text{Na}(\text{g})$ , chiolite ( $\text{NaAlF}_4$ ), cryolite ( $\text{Na}_3\text{AlF}_6$ ) and aluminium. The three latter are present if the sidewall is less protected by the frozen ledge during operation [122]. The degradation of the upper part prefers the  $\alpha\text{-Si}_3\text{N}_4$  phase, results in the formation of  $\text{Si}_2\text{ON}_2$  due to the oxidizing gases [29]. The lower part is influenced by the presence of the oxidizing gas  $\text{Na}(\text{g})$ , forming  $\text{Na}_2\text{SiO}_3$ , which densifies this part. However, the thermal conductivity decreases due the appearance of the low conductive  $\text{Na}_2\text{SiO}_3$  phase. These properties (density, porosity or thermal conductivity) remain unchanged in the upper part [29].



**Figure 3.22:** A schematic representation of the chemical environment in the surroundings of a sideling without the presence of a frozen ledge [122].





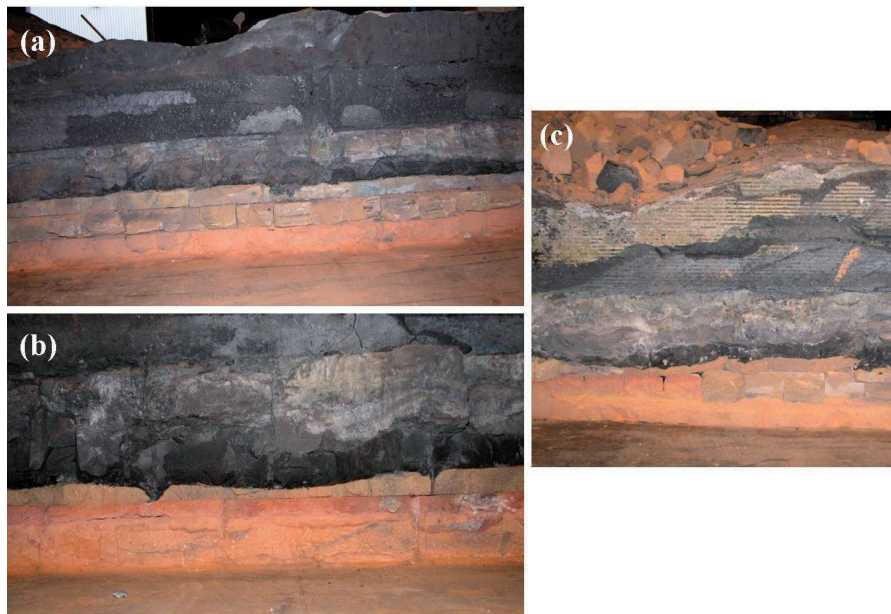
## **Part I**

### **Investigation of Spent Pot Lining (SPL)**

## 4 Experimental

### 4.1 Spent Cathode Lining Autopsies

In the course of the work, three autopsies were performed (1-3A) at two smelter locations of Hydro Aluminium. The spent pot lining (SPL) cross sections of different service life, shown in Fig. 4.1 were investigated in terms of chemical degradation and thermal properties. The cells were shut down at operation ages of 1569 (1A), 1767 (2A) and 2168 (3A) days respectively. The original pot lining design of the three cells was similar. It was build of a graphitized carbon cathode and a sequence of non-carbon materials. The thickness ratio of refractories and insulation materials was either 1:1 or 3:1. The specifications of the virgin materials are summarized in Table 4.1. The characterization methods applied to investigate the virgin carbon and refractory material as well as the 3 spent pot lining cross sections are summarized in Chapter 4.3.



**Figure 4.1:** Cathode bottom lining after (a) 1569, (b) 1767 and (c) 2168 days in operation. Refractory to insulation ratio: (b) 1:1; (a) and (c) 3:1.

**Table 4.1:** Chemical composition, bulk density, total porosity and apparent porosity of the lining materials [wt%] [123].

Specific.	Carbon block Graphitized	Collector bar S235JRG2	Refractory Chamotte	Insulation
SiO <sub>2</sub>			68	77
Al <sub>2</sub> O <sub>3</sub>			26	9
CaO				0.8
MgO				1.3
Fe <sub>2</sub> O <sub>3</sub>				7
Fe		99.83		
K <sub>2</sub> O				1.6
C	100	0.17		
<b>Bulk Density [kg/m<sup>3</sup>]</b>	1650	7850	2150	750
<b>Total Porosity [%]</b>	25.3			68
<b>App. Porosity [vol%]</b>			14	

## 4.2 Sampling

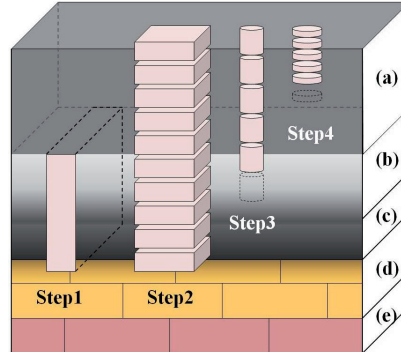
Sampling from the spent pot lining was carried out by hand. Analyses were performed on materials from the carbon cathode surface down to the lens build up and converted refractory bricks until the intact materials were reached.

### Chemical Properties

In order to investigate the chemical composition of the converted material the blocks from the first autopsy (1569 days old cell) were cut vertically through the entire cross section as shown in Fig. 4.2, Step1. These slices were cut continuously into approximately 2×2 cm cubes. The sawing was done with a diamond saw using water as cooling liquid. The samples were dried in between each step at 110 °C for 48 h and chilled in an exsiccator. For autopsies 2A (1767 days) and 3A (2168 days) the sampling procedure was slightly modified. The blocks were sliced horizontally by circular diamond saw as shown in Fig. 4.2, Step2. From each slice, cylinders were drilled in the gravitational direction (Fig. 4.2, Step3). Also here water was used as cooling liquid. Thus the samples were dried again at 110 °C for 48 h and chilled in an exsiccator to prevent further reaction with moisture. A smaller diamond saw performed tablets cutting as shown in Fig. 4.2, Step4. Isopropanol was applied as cooling media to prevent possible reactions during sawing in this case. All the length reported for the samples were measured by using a digital caliper.

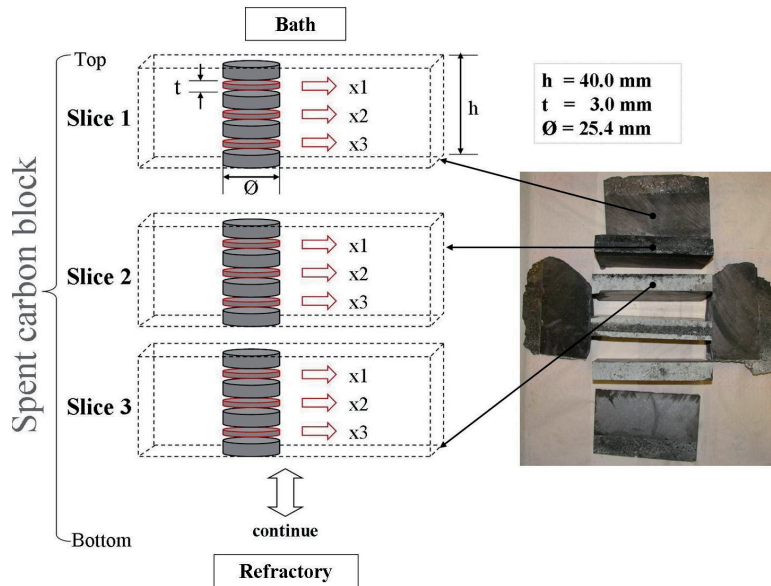
### Thermal Properties

The slice for the annealing test was cut in gravitational direction as shown in Fig. 4.2, Step1 and subsequently into 2×2 cm cubes. Cylinders with a diameter of 25.4

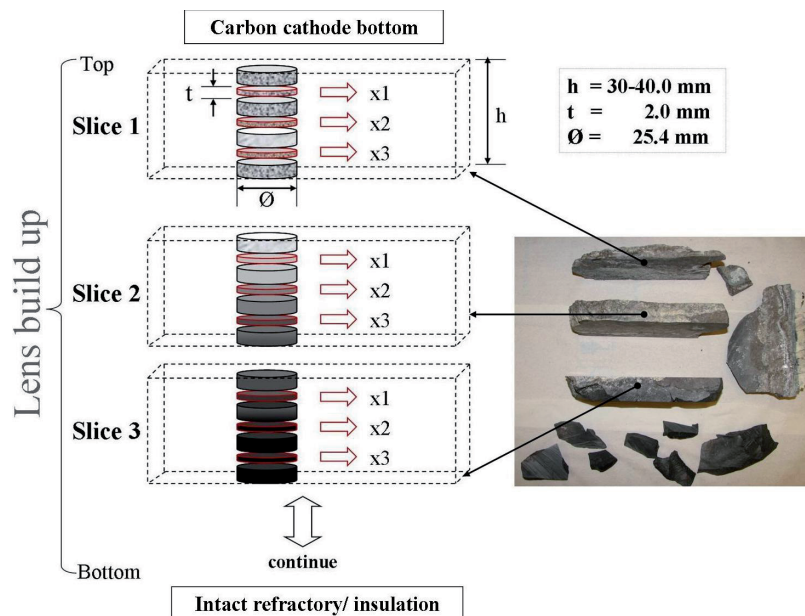


**Figure 4.2:** Sketch of sampling procedure through a SPL cross section: (a) infiltrated carbon block, (b) lens-build up, (c) reacted firebrick (d) intact firebrick, (e) insulation; Steps 1-4 are explained in the text.

mm were required for the thermal conductivity measurements. They were drilled parallel to the infiltration direction from each slice and dried in a furnace at 110 °C for 24 h. Further cutting of each cylinder into 2.0-5.0 mm thin tablets was performed with a smaller diamond saw. A schematic drawing of the sampling procedure and the subsequent labeling is shown in Fig. 4.3 for the spent carbon block and in Fig. 4.4 for the lens build up part. During the last sawing step isopropanol was used as cooling media to prevent possible reactions. All samples were dried again at 110 °C for 24 h and chilled in an exsiccator. The distances were measured by using a digital caliper.



**Figure 4.3:** Schematic drawing showing the labeling and sampling procedure of samples taken from spent carbon blocks.



**Figure 4.4:** Schematic drawing showing the labeling and sampling procedure of samples taken from lens build up part.

### 4.3 Characterization Methods

#### Annealing Test

Samples for annealing tests were placed on a thin layer of a fire brick. The furnace was equipped with 3 thermocouples placed in a row from the front opening to the back wall. The heating rate was 300 °C/hour. The relevant temperatures were taken from the thermo couple in the center position. Starting from 850 °C, each increment of 10 °C was held for 10 minutes until the maximum temperature of 950 °C was reached. At the end of each holding period, the furnace was opened and the samples were visually examined in order to investigate the presence of molten phases. The furnace was then heated up again, until the next dwell step was reached. The heating curve is shown in Fig. 4.5. After the last annealing at 950 °C, the samples were taken out and cooled down to room temperature.

#### Qualitative and Quantitative X-ray Diffraction

Samples originating from above the reaction front up to the carbon cathode surface were crushed in a ball mill (Retsh MM2000) for 2 min and sieved to < 63  $\mu\text{m}$ . The powder was then mounted in a silicon holder for X-ray diffraction analysis.

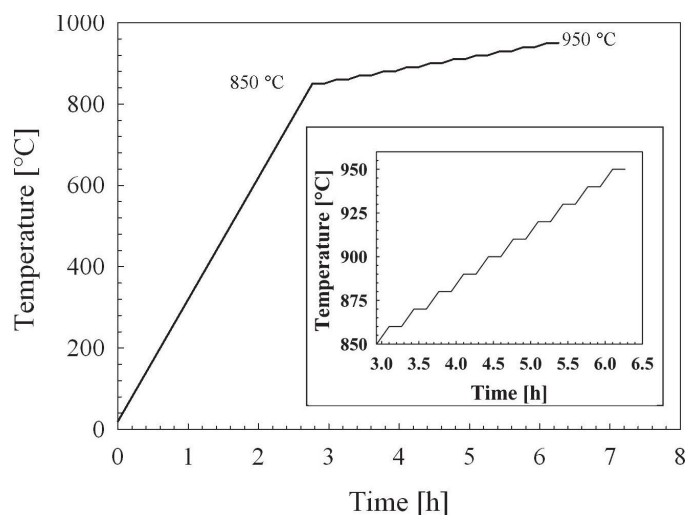


Figure 4.5: Heating curve for the annealing experiments.

Qualitative phase composition was investigated by powder X-ray diffraction using a Bruker AXS D8 Focus X-ray diffractometer with a LynxEye detector. The step size was  $0.02^\circ$  with a counting time of 0.5 s in the 2-Theta range of  $5^\circ$  to  $80^\circ$ . High resolution diffractograms for quantitative phase analysis were recorded using a Bruker AXS D8 Advance X-ray diffractometer with a Vântec-1 detector (step size of  $0.016^\circ$ ; counting time of 2.0 s; 2-Theta range  $6^\circ$  to  $120^\circ$ ).

The qualitative phase composition of the diffractograms were analyzed by *DIFFRAC<sup>plus</sup>* Evaluation software using the PDF database (powder diffraction file). The results were used to perform Rietveld refinements [124] with the *DIFFRAC<sup>plus</sup>* Topas software (Bruker AXS) version 4-1 to give the quantitative phase composition. The reference numbers for the PDF and structure files for the identified phases of the spent carbon cathode samples are summarized in Table 4.2. The absolute amount of the phases might be uncertain due to the polymorphism of the carbon (2H or 3R phase) and some overlapping reflections. The relative amount of the phases other than graphite in contrast is expected to be reliable. The relative amount is also considered to be more reliable in the analysis of the lens build up.

Due to the complexity of the multiphase system and some unidentified phases the lens build up zone was analyzed semi-quantitatively using the *DIFFRAC<sup>plus</sup>* Evaluation software. Later, this analysis was confirmed by the PW2400 X-ray fluorescence (XRF) spectrometer. With this data a quantitative phase analysis could be performed using the UniQuant<sup>®</sup> software. Both investigations were done at Hydro Aluminium-Primary Metal Technology in Årdal. Since the XRF device required more than 2 gram powder for each sample, the analysis was not performed exactly on the same powder. In addition, borate backing and the use of a binder phase (for brittle samples) were required.

**Table 4.2:** References for the phases used in the Rietveld Refinement for the spent carbon cathode cross section.

Composition	PDF File	Space Group	Ref.
Graphite (2H)	00-041-1487	P63/mc	[125]
Graphite (3R)	00-026-1079	R3m	[126]
Na <sub>3</sub> AlF <sub>6</sub>	00-025-0772	P21/c	[127]
NaF	00-036-1455	Fm3m	[128]
Na <sub>2</sub> Al <sub>11</sub> O <sub>22</sub>	01-076-0923	P63/mmc	[129]
CaF <sub>2</sub>	00-035-0816	Fm3m	[130]
Al <sub>4</sub> C <sub>3</sub>	01-079-1736	R3m	[131]

### Electron Microscopy

The microstructure and chemical analysis was performed by the LV-SEM S-3500N HITACHI scanning electron microscope. Line scan and mapping of the element composition were performed by electron probe micro analysis (EMPA) using a JXA-8500F Hyperprobe JOEL (EPMA/ WDS) apparatus. The reaction front samples were embedded into epoxy and polished by hand, to avoid further contact with liquids, which might react with the materials. Afterwards the samples were coated with carbon to reduce the problems with charging. The electron beam spot size was broadened to 30  $\mu\text{m}$  to avoid Na evaporation. The content of the major components Si, Al, O, F and Na and the minor elements Ca, K, Mg and Fe were recorded.

### Thermal Conductivity

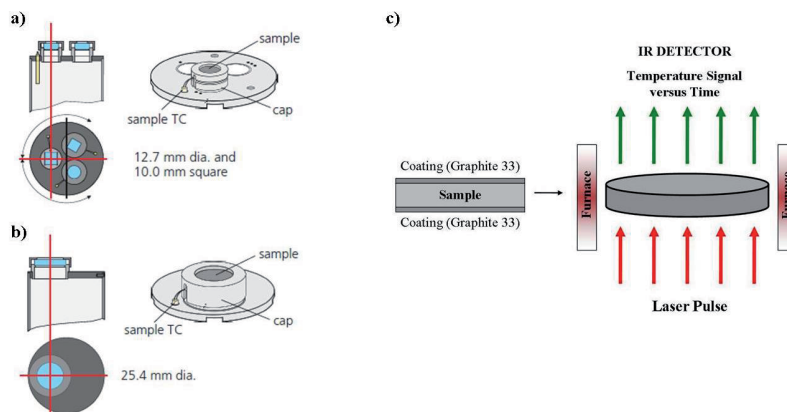
The laser flash technique [132] was used to determine the effective thermal conductivity by measuring the thermal diffusivity and specific heat of spent pot lining cross section samples as a function of temperature using Eq. (4.1)

$$\lambda(T) = \rho(T) \cdot c_p(T) \cdot a(T) \quad (4.1)$$

where  $\lambda$  is the thermal conductivity [W/(m·K)],  $a$  is the thermal diffusivity [ $\text{m}^2/\text{s}$ ],  $\rho$  is the density [ $\text{kg}/\text{m}^3$ ] and  $c_p$  is the heat capacity [J/(kg·K)]. Thermal diffusivity was measured, based on the transient heat flux principle [133] using the laser flash apparatus 457 MicroFlash™ from Netzsch. The thermal diffusivity was measured three times at each temperature to increase accuracy.

In order to compute the thermal conductivity, according to Eq. (4.1), the density  $\rho(T)$  as function of temperature was needed. For this purpose the measurement of the thermal expansion with a dilatometer was performed. The specific heat capacity was ascertained by a procedure of comparing measured to standard data. Thus every second

measurement was done with an  $\text{Al}_2\text{O}_3$  standard tablet (99.8 %, Netzsch, thickness 3.008 mm, diameter 25.37 mm) of similar thickness and under same conditions as for the samples.



**Figure 4.6:** Sketch of (a) a single sample arrangement with a tablet diameter of 25.4 mm, recommended for inhomogeneous materials and (b) a multiple sample arrangement with a tablet diameter of 12.7 mm. Sub-figure (c) is a sketch of the laser flash operation principle [134].

The SiC single-sample holder, see Fig. 4.6 (a) and two different heating rates were chosen, starting with 2 °C/min from 25 °C up to 100 °C and later 10 °C/min for temperatures  $\geq 100$  °C. The maximum temperature was set to 500 °C to avoid any damage to the instrument. This temperature was predetermined according to the chemical composition of the samples and by experimental evaluation. All samples were heated up to the maximum temperature.

The laser flash chamber was vacuumed, flushed and finally filled with nitrogen prior to the analysis to prevent the materials against possible reactions with oxygen in air. Before operation the sample geometry (thickness and diameter), density and the thermal expansions for each material/tablet in the desired temperature range were implemented into the Netzsch software. Figure 4.6 (c) shows the measurement principle. Finally, the thermal conductivity was calculated from the measured data by the Netzsch LFA Analysis software.

The success of the laser flash method depends strongly on the right sample preparation, described in the following four main steps:

1. The tablets were mechanically polished with SiC paper by hand and without any lubricant to receive two parallel surfaces. According to the apparatus description the accuracy is 0.01 mm.
2. The tablets were weighed and the thicknesses and diameters were measured. The thickness range of a sample is determined by the laser flash requirements. Recommended and used thicknesses are summarized in Table 4.3.
3. Specimens with large pores require additional sample preparation. The pores



should be filled with a paste made by e.g. SiC powder and water. This step was not considered with respect to the present samples, because only a few open pores were present.

4. All the test pieces were coated with graphite spray, to increase and smoothen the amount of energy absorption.

**Table 4.3:** Recommended thicknesses for LFA 457 Microflash apparatus [134]. The label "\*" indicates the thicknesses used for the measurements in this work.

Diffusivity	Example	Thickness [mm]
Low	Polymers	0.1-0.5
Medium	Ceramics	0.5-3.0 1.5-2.0 *
High	Cooper	2.0-3.0
Very high	Carbon	3.0 *-5.0

## Density

The sample preparation required no special effort because the density was measured on the same samples prepared for the thermal diffusivity measurement using the laser flash equipment. After testing by the laser flash method the graphite coating was removed with isopropanol and the samples were dried for 24h at 110 °C and cooled down to room temperature in an exsiccator.

The bulk density and apparent porosity were determined in accordance with the international standard description ISO 5017 based on Archimedes principle. Some exceptions have been made. The times for vessel evacuation, soaking in vacuum and soaking in air were extended by 15 minutes to ensure that all open pores were filled with liquid. For bulk density  $\rho_b$  [g/cm<sup>3</sup>] and apparent porosity  $\pi_a$  [%] calculation, according to Equations (4.2) and (4.3)

$$\rho_b = \frac{m_1}{m_3 - m_2} \cdot \rho_{liq} \quad (4.2)$$

$$\pi_a = \frac{m_3 - m_1}{m_3 - m_2} \cdot 100 \quad (4.3)$$

the following values are necessary and were achieved by weighing:

- ◆ Mass of the dry sample ( $m_1$ ) [g],
- ◆ Apparent mass when immersed in a liquid, which has been impregnated under vacuum ( $m_2$ ) [g],
- ◆ Mass in air; the test piece is soaked with the liquid ( $m_3$ ) [g].

Since the tested samples were sensitive to contact with water, the immersion liquid was isopropanol. The density of isopropanol at measured temperatures are shown in Table 4.4.

**Table 4.4:** Density of Isopropanol.

Temperature [°C]	Density [kg/(m <sup>3</sup> )]
20.0	786.125
21.0	785.213
21.2	785.030
22.4	783.933

The true density  $\rho_t$  [g/cm<sup>3</sup>] was measured with the 1-cm<sup>3</sup> AccuPyc 1330 Pycnometer. The apparatus determines the density and volume by measuring the pressure change of helium (99.995 % pure) in an calibrated volume. Helium penetrates into smallest pores and crevices and thus permits to approach the real volume. If the sample weight is specified the density is derived automatically. For this purpose the tablets were crushed in a ball mill (Retsh MM2000) and sieved to less than 63  $\mu$ m (ISO 565). The powder was dried at 110 °C for 24 h and chilled to room temperature in an exsiccator. After equipment calibration the sample holder was weighed and filled with sample powder to 2/3 of its volume. The filled cup was weighed again and the weight used as set-up parameter for the pycnometer. Four tablets used for bulk density measurements were investigated to compare the results and to find the maximum possible density.

Finally, the true  $\pi_t$  [%] and closed  $\pi_f$  [%] porosity was calculated from the true density, according to Equations 4.4 and 4.5

$$\pi_t = \frac{\rho_t - \rho_b}{\rho_t} \cdot 100 \quad (4.4)$$

$$\pi_f = \pi_t - \pi_a \quad (4.5)$$

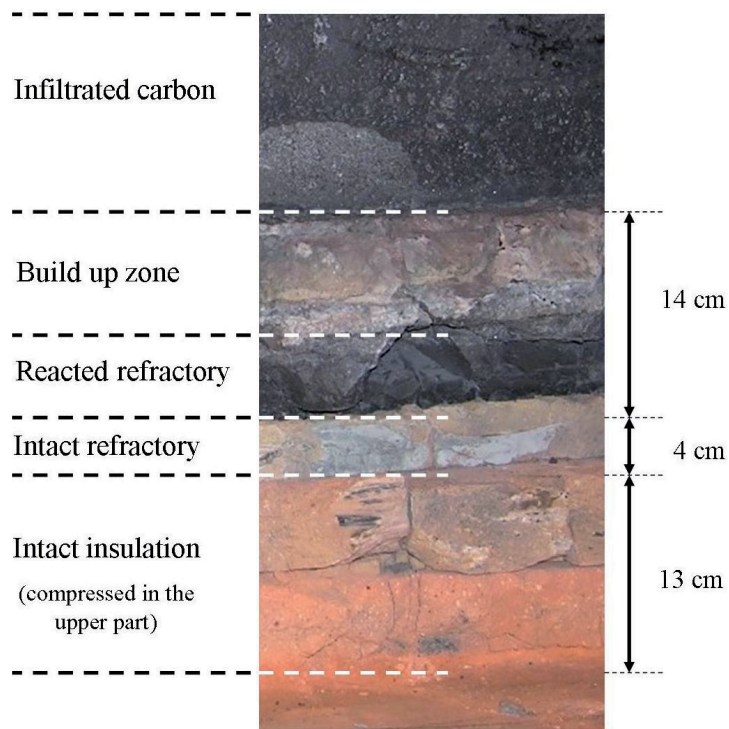
## Dilatometry

To determine the thermal expansion data bars were cut from the 2.0-3.0 mm slices made for the thermal conductivity measurements for carbon cathode cross sections as well as from the spent refractory lining using a Netzsch 402E dilatometer. Samples were in the range of 40-55 mm in length and up to 10 mm in diameter. Spacers made of alumina with known thermal expansion were used. The temperature range for measuring was between 25 and 530 °C. The upper temperature limit was set to prevent damage of the equipment due to reactions with the samples. Nitrogen gas was used as atmosphere to prevent reactions with oxygen in air. The heating and cooling rates were 2 °C/min and the holding time at maximum temperature was 5 min.

## 5 Results

### 5.1 Visual Observations

The cross sections of the three investigated spent pot linings displayed the typical layered structure, like described in Section 3.4.1. The different layers of the spent pot lining were visually distinguishable as shown in Fig. 5.1.



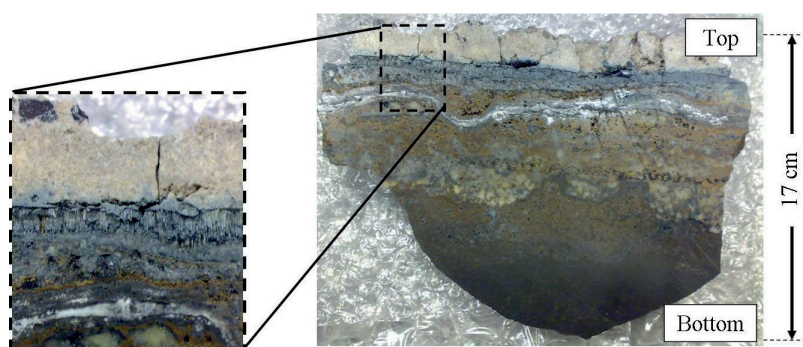
**Figure 5.1:** A typical cross section of spent pot lining from a 1569 days old cell.

Several main parts were identified: "Infiltrated carbon", "build-up", "reacted firebrick", and a sharp intersection towards the intact refractory layer, named "reaction front" was observed. The visual penetration depths were measured and summarized in Table 5.1. The design of the original lining below the carbon cathode is given by the ratio of refractory to insulation layers and their initial dimensions. In 1A and 3A, half of the second refractory layer was reacted. Due to the different design of the 1767 days old pot, only 1 cm of intact refractory material was left. In some places the upper part of the insulation layer was reacted. Common for all three autopsies was the observation

**Table 5.1:** Recorded penetration depth of all investigated spent pot lining cross sections.

Autopsy	Age [days]	Ratio	Design Total Height [cm]	Penetration Depth [cm]
1A	1569	3:1	19.2:6.4	15
2A	1767	1:1	12.8:12.8	11-13
3A	2168	3:1	19.2:6.4	16

of a continuous layer of large NaF crystals underneath the infiltrated carbon cathode block as shown in Fig. 5.2. They grew downwards in a needle-like shape.

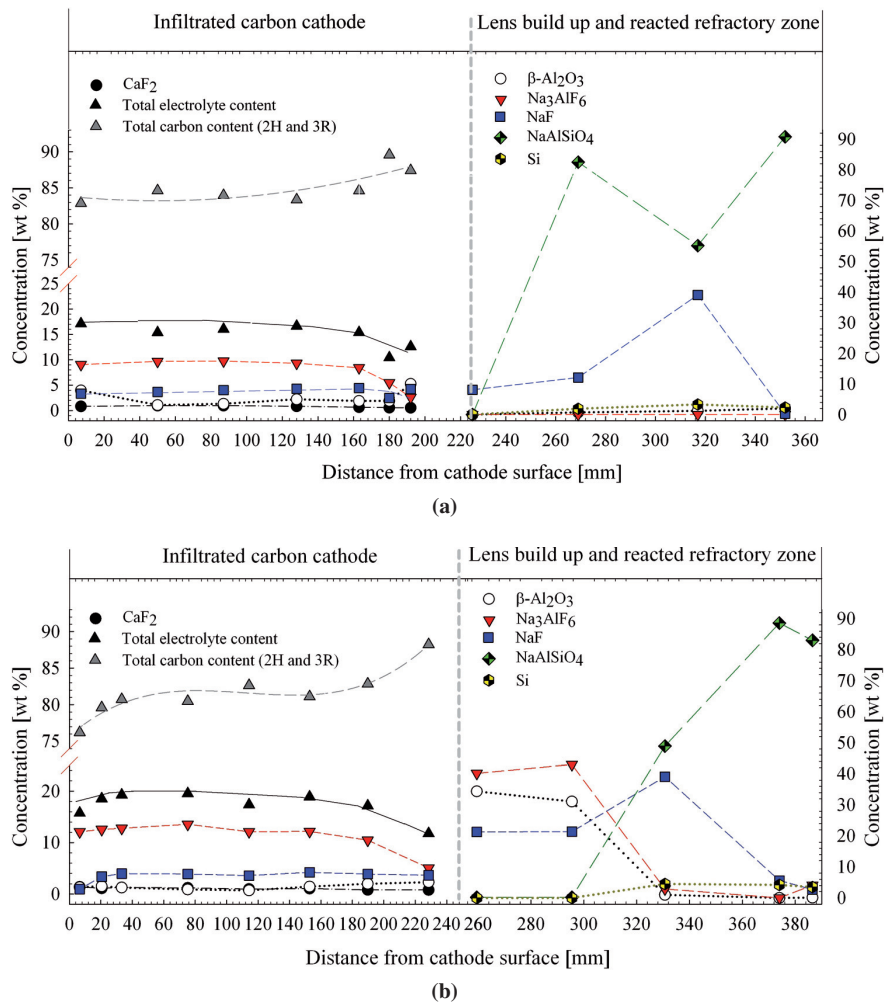


**Figure 5.2:** Layer of crystals grown downwards in a needle-like shape observed directly underneath the carbon cathode in SPL (1767 days old cell).

## 5.2 Mineralogical and Chemical Analysis

### 5.2.1 Spent Carbon Cathode Block

The phase composition of the three carbon cathodes was quite similar. A representative composition profile of two of the cathodes is shown in Fig. 5.3. The quantitative Rietveld refinement of the XRD diffractograms are summarized in Table 5.2. Several chemical species from the penetrating bath in addition to compounds formed in the cathode material namely,  $\text{Na}_3\text{AlF}_6$ , NaF,  $\text{CaF}_2$  and  $\beta\text{-Al}_2\text{O}_3$  were detected. The most interesting observation is the slight increase of the concentration of NaF and the  $\beta\text{-Al}_2\text{O}_3$  towards the cathode bottom, whereas at the same time the amount of cryolite decreases. The bath becomes more basic downwards in the cathode. Fig. 5.3 (left) shows that the  $\text{CaF}_2$  content fluctuates only slightly, the concentration lies between 0.5 and 1.0 wt%, which corresponds well with the  $\text{CaF}_2$  content in the bath.



**Figure 5.3:** Quantitative and semi-qualitative phase distribution in the SPL (2A and 3A): (a) 1767 and (b) 2168 days in operation.

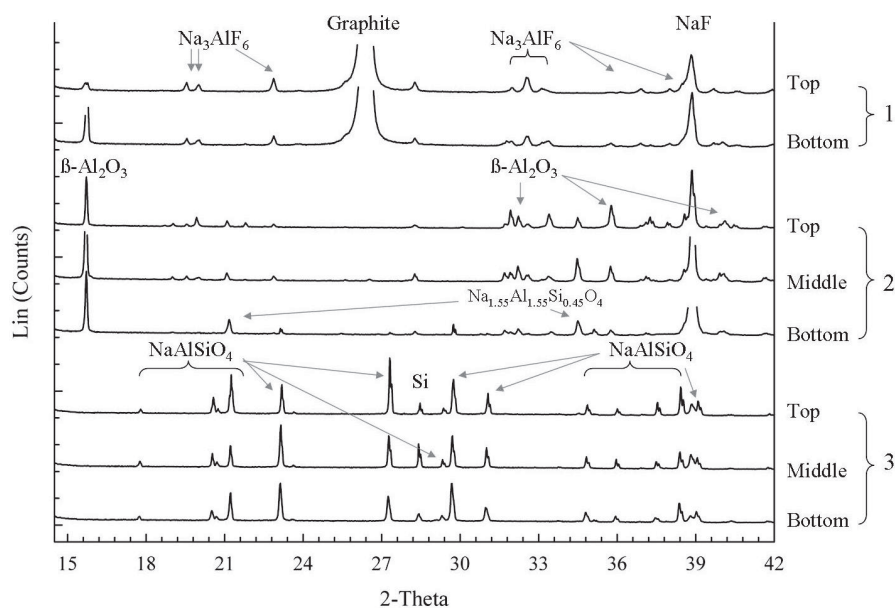
**Table 5.2:** Quantitative analysis (wt%) using the Rietveld refinement of samples from spent carbon cathode cross section. The position of the sample is relative to the cathode surface.

Sample Label	Position [mm]	CaF <sub>2</sub>	$\beta$ -Al <sub>2</sub> O <sub>3</sub>	Na <sub>3</sub> AlF <sub>6</sub>	NaF	Al <sub>4</sub> C <sub>3</sub>	2H	3R	Graphite	Melt Content
									$\Sigma(2H+3R)$	
<b>1A (1569 days)</b>										
Part 1	6	1.1	2.5	6.7	3.51	0	78.3	7.9	86.3	13.7
Part 9	122	0.7	0.9	7.1	2.76	0	79.4	9.2	88.6	11.4
Part 12	165	0.6	1.5	7.1	3.51	0	77.2	10.1	87.3	12.7
<b>2A (1767 days)</b>										
1 Slice x1	7	0.8	4.0	9.1	3.3	0	74.2	8.6	82.9	17.1
2 Slice x1	50	1.0	1.1	9.7	3.7	0	76.4	8.2	84.6	15.4
3 Slice x1	87	1.0	1.3	9.7	4.0	0	75.1	8.9	84.0	16.0
4 Slice x1	128	0.8	2.2	9.3	4.3	0	75.6	7.8	83.4	16.6
5 Slice x1	163	0.7	1.9	8.4	4.4	0	75.5	9.1	84.6	15.4
5 Slice x3	180	0.6	1.9	5.5	2.5	0	79.3	10.3	89.6	10.4
6 slice x1	192	0.6	5.2	2.6	4.2	0	77.8	9.6	87.4	12.6
<b>3A (2168 days)</b>										
1 Slice x1	228	0.8	2.3	5.1	3.6	0	78.6	9.7	88.2	11.8
2 Slice x1	190	0.8	2.0	10.5	3.9	0	74.7	8.1	82.9	17.2
3 Slice x1	153	1.8	1.4	12.2	4.2	0	72.0	9.1	81.1	18.9
4 Slice x1	114	1.0	0.7	12.1	3.6	0	73.1	9.5	82.6	17.4
5 Slice x1	75	1.2	0.9	13.6	3.9	0	71.4	9.1	80.5	19.5
6 Slice x1	33	1.3	1.3	12.8	4.0	0	70.4	10.3	80.7	19.3
7 Slice x2	21	1.1	1.5	12.6	3.4	1.9	71.1	8.5	79.6	18.5
7 Slice x1	7	1.4	1.3	12.1	1.0	8.1	65.4	10.8	76.2	15.8

### 5.2.2 Lens Build-Up and Reaction Front

Besides NaF and  $\text{Na}_3\text{AlF}_6$  the main secondary phases found by quantitative X-ray diffraction analysis in the SPL cross sections 2A and 3A were  $\text{NaAlSiO}_4$  and Si, as shown in Fig. 5.3. The quantitative and semi-quantitative phase analyses are summarized in Table 5.3. The same trend is observed in both autopsies. The qualitative analysis of the phases found by XRD in 1A is depicted in Fig. 5.4.

The formation of nepheline takes place according to reactions (3.7) and (3.14), when NaF/Na reacts with the refractory lining material. Depending on the composition of the refractory brick (ratio of  $\text{SiO}_2/\text{Al}_2\text{O}_3$ ),  $\beta\text{-Al}_2\text{O}_3$  and  $\text{NaAlSi}_3\text{O}_8$  are also possible products. The phase  $\beta\text{-Al}_2\text{O}_3$  was found in the spent linings with decreasing concentration towards the reaction front. Albite ( $\text{NaAlSi}_3\text{O}_8$ ) is a glassy phase and is not detectable by X-ray diffraction.



**Figure 5.4:** XRD profiles for samples from infiltrated cathode (1); lens build up (2) and reacted firebrick (3) of a 1569 days old shut down cell (1A). The infiltration direction is from top to bottom (1-3).

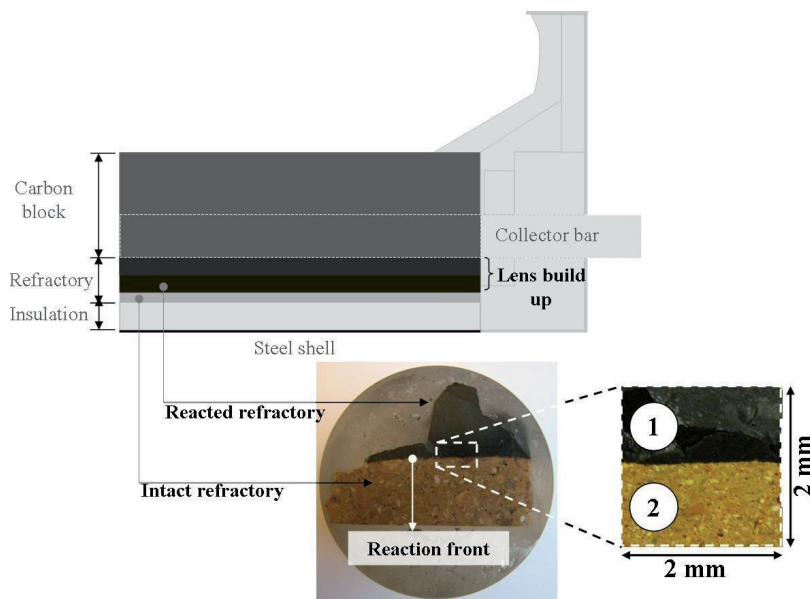
**Table 5.3:** Quantitative and semi-quantitative phase analysis of the X-ray diffraction patterns of two shut down cells with the age of 1767 and 2168 days. Unit of phase amount is wt%. The position of the sample is relative to the cathode bottom. <sup>1</sup>Sample 2A /Slice x1 contained carbon.

Method	Sample Label	Position [mm]	Na <sub>3</sub> AlF <sub>6</sub>	$\beta$ -Al <sub>2</sub> O <sub>3</sub>	NaF	NaAlSiO <sub>4</sub>	Si	Undefined
<b>2A (1767 days)</b>								
UniQuant	1 Slice x1	7	0	0	8.1	0	0	91.9 <sup>1</sup>
	2 Slice x1	53	0	0.7	12.1	82.5	1.9	2.8
	3 Slice x1	90	0	1.2	39.1	55.2	3.3	1.2
	4 Slice x1	138	0	2.0	0.3	90.8	2.3	4.6
EVA	1 Slice x1	7	0	0	21.0	0	0	79.0
	2 Slice x2	32	0	0.2	20.0	51.0	0	26.0
	3 Slice x1	53	0	0	14.0	83.0	3.0	0
	4 Slice x1	90	0	0	61.0	36.0	3.0	0
	5 Slice x1	138	0	0	0	97.0	3.0	0
<b>3A (2168 days)</b>								
UniQuant	1 Slice x1	4	40.2	34.4	21.3	0.2	0	3.9
	2 Slice x1	40	43.0	31.1	21.4	0.2	0	4.3
	3 Slice x1	75	2.9	1.0	39.1	48.9	4.5	3.6
	4 Slice x1	118	0	0	5.6	88.6	4.2	1.6
	5 Slice x1	131	4.1	0.1	2.7	83.0	3.5	6.6
EVA	1 Slice x1	4	29.5	54.0	16.0	0	0.9	0
	2 Slice x1	40	32.0	51.0	17.0	0	1.0	0
	3 Slice x1	75	0	2.0	53.0	40.0	5.0	0
	4 Slice x1	118	0	0	8.0	88.0	4.0	0
	5 Slice x1	131	0	0	0	95.0	5.0	0



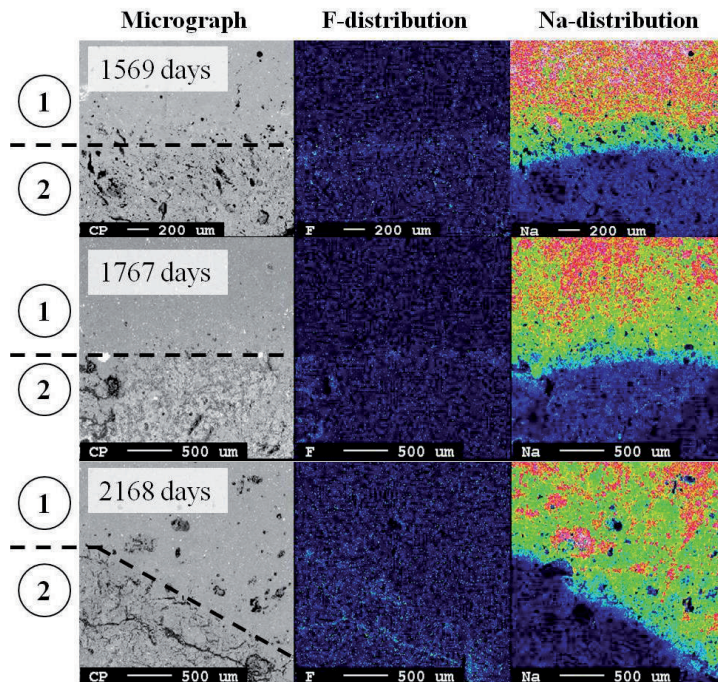
Common for all three autopsies are the following two main observations. First, nepheline ( $\text{NaAlSiO}_4$ ) appears at a certain distance and increases while moving downwards from the carbon blocks. Secondly,  $\text{NaF}$  disappears at a lower level than  $\text{Na}_3\text{AlF}_6$ . The amounts of the phases depend on the sampling position and can vary between different autopsies since the lens build up and reacted refractory zones are heterogeneous. The phases and sequences detected were in line with reported findings [13–16].

Line scans and area mappings across the reaction front from three different cells were measured by EPMA. An optical image of a sample showing clearly the reaction front is depicted in Fig. 5.5. The reaction front was determined from the specific micrograph as shown in Fig. 5.6. An area scan analysis of  $2 \times 2$  mm at this section was performed. Fig. 5.6 comprises the elemental distribution images of F and Na across the reaction front in the three different SPLs. The area map is scaled and the lighter the colour the higher is the content. The area mapping demonstrates that no F is present at the interface to the unreacted material. In contrast it is evident from the area mapping that the sodium content decreases sharply towards the reaction front. This shows that only sodium is present at the reaction front.



**Figure 5.5:** Optical image of the reaction front of a 1569 days old cell including the sample position for area mapping and line scan; (1) reacted firebrick and (2) intact firebrick.

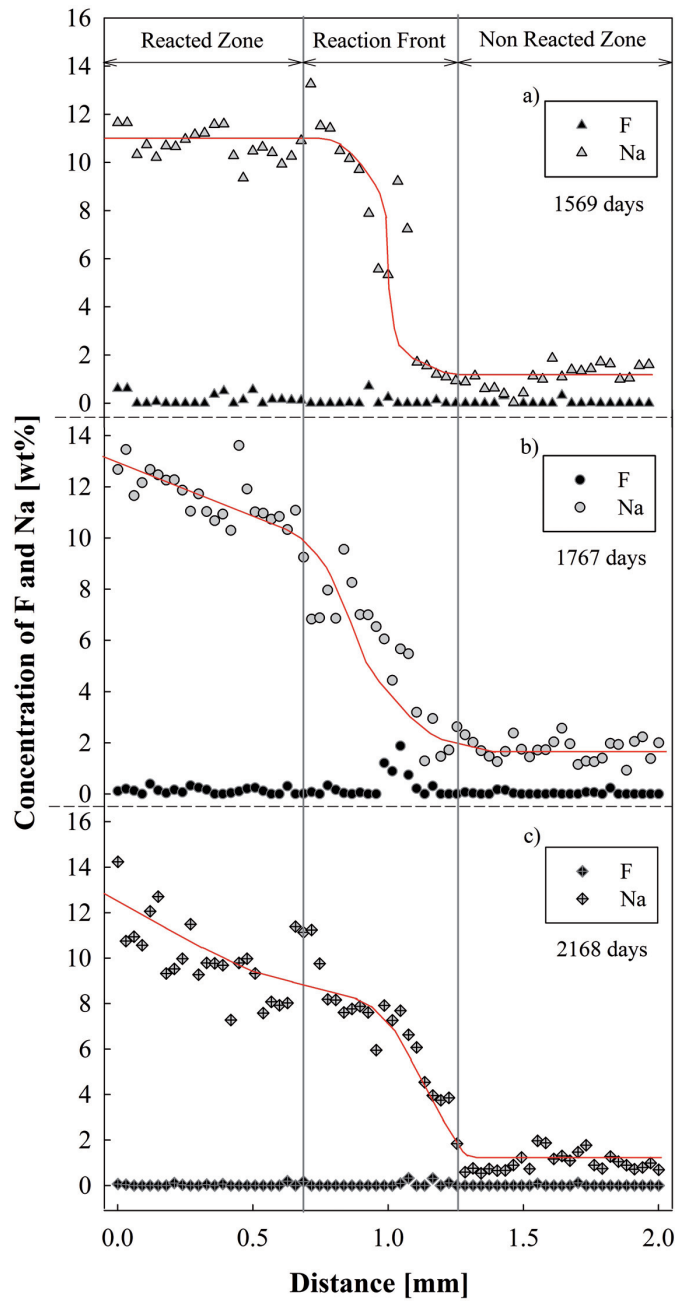
The line scans, depicted in Fig. 5.7, show the content of Na and F in wt% over a distance of 2 mm across the intersection. The concentration gradient of sodium is clearly evident in all three linings. At the reaction front the sodium gradient is particularly steep and the sodium content decreases rapidly from 10-14 wt% to approximately 1-2 wt%. This corresponds to the initial impurity level in the refractory



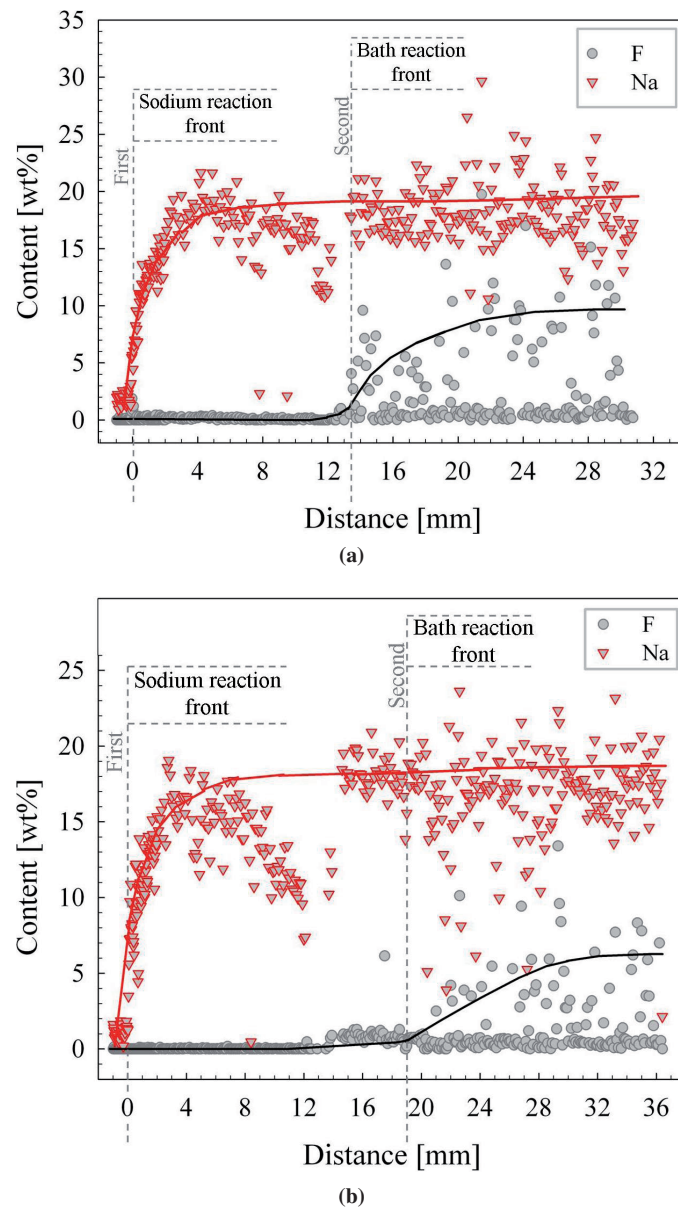
**Figure 5.6:** Micrograph of the reaction front indicated by the black dashed line and the element distributions of Na and F (right) of three different spent pot linings.

materials. Interestingly, there is no gradient in the fluoride content across the reaction front, and the F concentration is almost zero across the entire reaction zone. This confirms and support the results of the area mapping, that only sodium is present at the reaction front, which is in the following is called the "first reaction front".

Line scans in the region above the reaction front were carried out in order to find the location where fluoride from the percolated bath appears. The F content versus distance is shown in Fig. 5.8 for two different autopsies. The fluoride appears between 13-14 mm (2A) and 17-19 mm (3A) above the intersection of reacted and virgin refractory material. For the location of the penetrating bath the term "second reaction front" is used. Further away, the F content increases up to 20 wt% for 2A and 15 wt% for 3A. The Na content is distributed homogeneously, whereas the F content appears to be enriched in spots. This demonstrates that the fluoride crystals accumulate in certain areas during cooling of the lining.

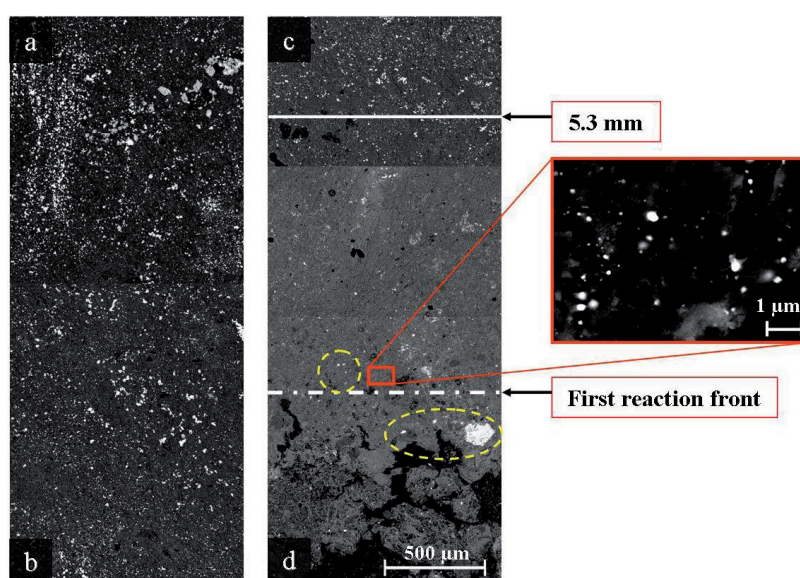


**Figure 5.7:** The chemical analysis (line scans) across the interface between reacted and intact firebrick of 3 different pot ages: (a) 1569 days, (b) 1767 days, (c) 2168 days.



**Figure 5.8:** Chemical analysis (line scans) across the two reaction fronts and upwards in the lining,  $x=0$  indicates the intersection between reacted and intact firebrick material of two pot ages: (a) 1769 days and (b) 2168 days. The reaction front in the two linings are marked with grey dashed line. The drop of the Na content at around 10-12 mm is due to the fact that this part is the intersection between the physically separated part of the SPL samples. For this reason the actual course of the Na and F content was highlighted by solid lines.

The microstructure of the materials was evaluated by a continuous set of SEM images from the reaction front and upwards in the lining (Fig. 5.9). Quite a few white spots were located and identified as Si by EDS. The presence of Si demonstrates that the chemical conditions below the carbon cathode are reductive in nature. The refractory material will be reduced by sodium metal according to Eq. (3.12). The Si particles are distributed over the entire reaction front layer, but a size gradient is clearly visible. In the first few millimeters above the reaction front tiny white droplets appeared. They were too small for a precise chemical analysis by EDS, but they clearly contained Si. Away from the reaction front, the Si grains become larger and the composition could be confirmed by EDS.

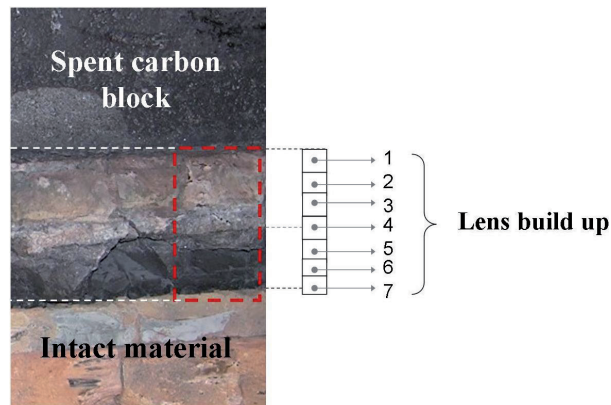


**Figure 5.9:** Microstructure showing the place of reduction reaction leading to Si metal formation. The infiltration direction is from (a) to (d). The yellow dashed circles show the remaining  $\text{SiO}_2$  and  $\text{Al}_2\text{O}_3$  particles from the virgin refractory material. The red framed spot is a high resolution image, showing the upcoming tiny Si spots. The mark at 5.3 mm indicates the size gradient of the spots.

### 5.3 Annealing Test

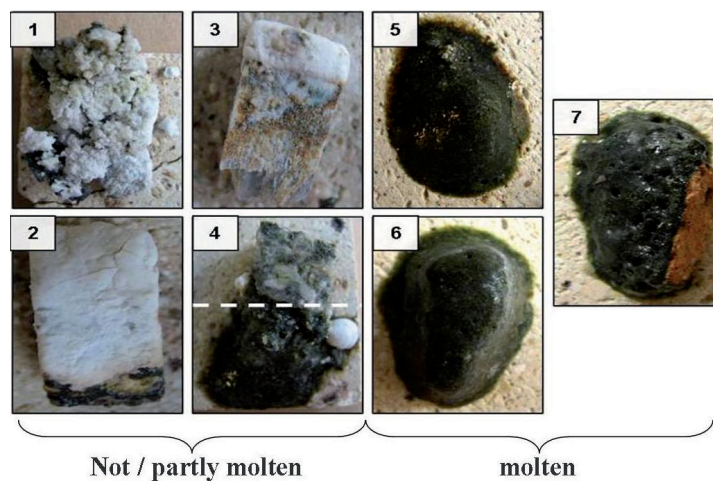
Thermal annealing of samples from the spent pot linings was performed in order to investigate the possible presence of molten phases at elevated temperatures. Photographs of sample position and the annealed samples are shown in Figs. 5.10 and 5.11, respectively.

Softening of samples 7, 6 and 5 occurred at 840 °C and at 900 °C all of these were clearly partly or fully melted. Sample 4 was partly molten at 930 °C, representing



**Figure 5.10:** Sample position of the materials annealed at elevated temperatures.

the boarder between the reacted firebricks (samples 5-7) and the build-up or lens material. Samples 3, 2 and 1 did not show any sign of softening up to 950 °C, which is higher than the temperature present below the cathode during operation. Consequently there is no molten phase in the vicinity of the cathode, but the black part in the lining clearly contained molten phase. These observations demonstrate that the sequence of materials in the lining reflects crystallization during cooling of the partly molten layer below the carbon cathode.



**Figure 5.11:** Images of the annealing test samples: (1), (2) and (3) are from the "lens build up" zone, (4) is the intersection to the samples (5) and (6), originate from the "reacted firebrick" zone and sample (7) contains the "reaction front" and "intact refractory" material (the exact positions in the cell are illustrated in Fig. 5.1).

## 5.4 Density and Thermal Expansion

### 5.4.1 Spent Carbon Cathode Block

#### Density and Apparent Porosity

The apparent porosity of the virgin carbon cathode material was around 19 % and the bulk density was around 1.67 g/cm<sup>3</sup>. A summary of the bulk density and porosity of the spent carbon cathodes are given in Table 5.4. Bath infiltration and reaction products fill the pores, which causes a decrease in the apparent porosity and an increase in the density. The density variation of samples across the spent carbon cathode was small and similar for both cathodes. This is caused by the relatively homogeneous chemical composition. Typical values are in the range of 2.0 to 2.2 [g/cm<sup>3</sup>], influenced by the amount of the main phases  $\beta$ -Al<sub>2</sub>O<sub>3</sub> (3.30 g/cm<sup>3</sup>), Na<sub>3</sub>AlF<sub>6</sub> (2.97 g/cm<sup>3</sup>) and NaF (2.56 g/cm<sup>3</sup>).

**Table 5.4:** Ambient bulk density, apparent porosity and distance to the top of the carbon block for 2A (1569 days) and 3A (1767 days) spent carbon cathode samples. GC is the abbreviation for graphitized carbon.

Sample	Position [mm]	Bulk Density [g/cm <sup>3</sup> ]	Apparent Porosity [%]
Virgin block (GC)	-	1.67	19.13
	19.00	1.95	7.69
	65.35	2.01	5.49
2A	101.85	2.06	2.75
	144.60	2.07	2.15
	175.50	2.05	3.44
	53.12	2.16	2.25
3A	75.56	2.17	2.07
	121.34	2.05	1.42
	163.75	2.10	3.53
	200.25	2.15	1.47
	247.88	2.05	5.80

#### Thermal Expansion

The thermal expansion of the virgin and the spent carbon cathode is shown in Fig. 5.12. Due to bath infiltration the thermal expansion of the spent materials is higher than the corresponding value for the virgin material. There is a slight difference between the bottom and top part of the cathode. This mismatch is caused by the difference in chemical composition, porosity and density, shown in Table 5.4.

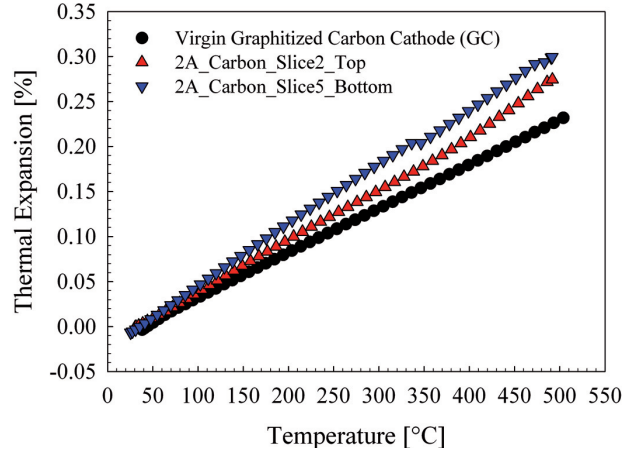


Figure 5.12: The thermal expansion of the spent carbon block (1767 days).

## 5.4.2 Lens Build-Up and Reaction Front

### Density and Apparent Porosity

The apparent porosity of the virgin refractory material is approximately 16 % and the bulk density is  $2.15 \text{ g/cm}^3$ . The bulk density and apparent porosity of the spent refractory lining are summarized in Table 5.5.

Table 5.5: Ambient bulk density, apparent porosity and position of the samples of the carbon block for 2A (1569 days) and 3A (1767 days) build up and reacted firebrick samples.

Sample	Position [mm]	Bulk Density [ $\text{g/cm}^3$ ]	Apparent Porosity [%]
Virgin brick (Chamotte)	-	2.15	16.09
	14.30	2.19	4.46
2A	56.65	2.63	1.97
	104.60	2.53	2.92
	139.63	2.62	0.82
	8.82	2.90	7.60
3A	36.50	2.89	2.73
	98.25	2.84	3.67
	121.00	2.61	1.48
	153.53	2.50	1.20

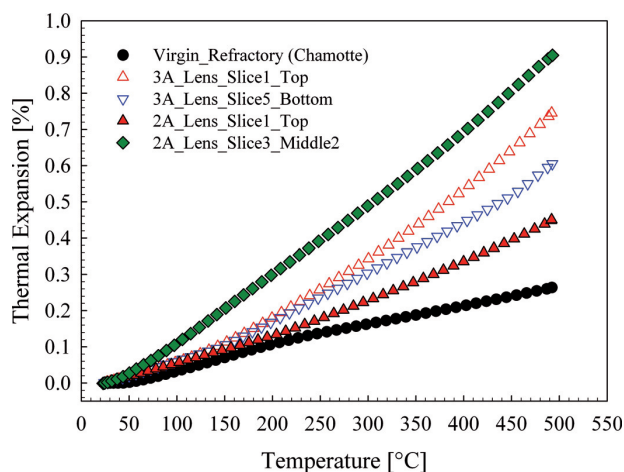
The degradation process leads to mineralogical transformation and filling of pores, which changes the apparent porosity and density correspondingly. The apparent porosity, decreases down to approximately 1 % near the reaction front compared to the virgin material and the bulk density increases to  $2.5\text{-}2.6 \text{ g/cm}^3$ . In general, dense phases like  $\beta\text{-Al}_2\text{O}_3$  ( $3.3 \text{ g/cm}^3$ ) and  $\text{Na}_3\text{AlF}_6$  ( $3.0 \text{ g/cm}^3$ ) are dominating the overall density of the top part and glassy phases with comparatively low densities



of  $2.6 \text{ g/cm}^3$  are responsible for the lower density at the bottom. Sodium fluoride and nepheline have also lower densities of  $2.56 \text{ g/cm}^3$  and  $2.6 \text{ g/cm}^3$  respectively. The reproducibility especially of the top part (build up zone) is low because of the inhomogeneous chemical composition, which is dependent on the sampling position and cooling conditions. The results given here are representing the cooling history of the spent pot shell. This will be further discussed below. The data were confirmed and reproduced using larger samples.

### Thermal Expansion

The thermal expansions of the SPL, shown in Fig. 5.13, are significantly higher than values for the virgin refractory material. The difference between top and bottom part for 3A is relatively small, whereas the difference between the top and lower part of the 2A samples is approximately 50 % at  $500 \text{ }^\circ\text{C}$ .



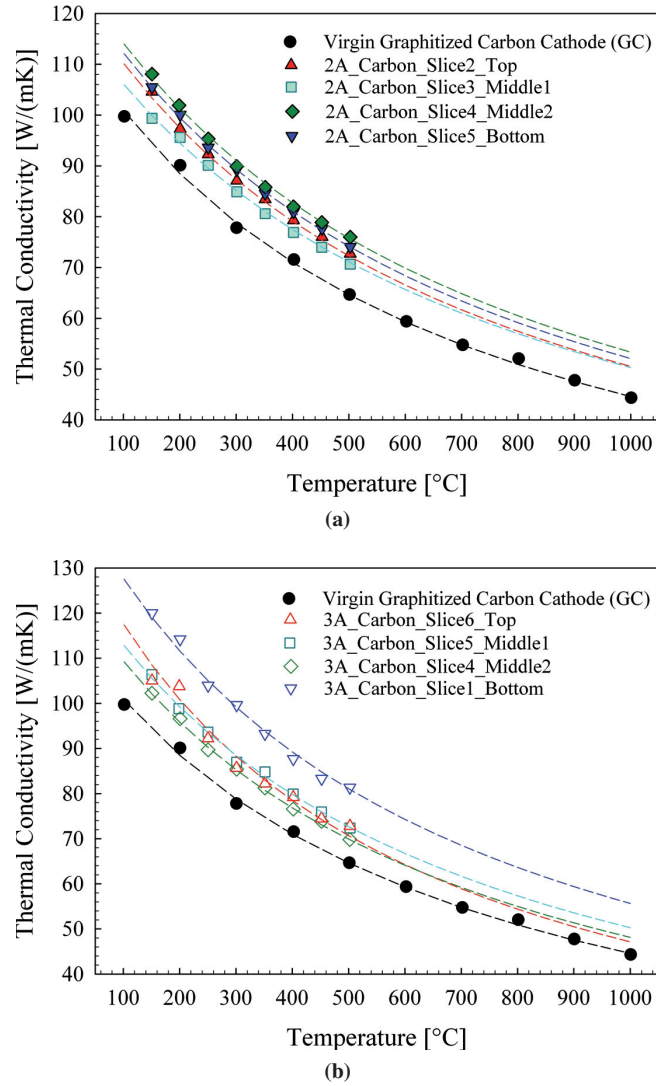
**Figure 5.13:** The thermal expansion of the lens build up and reacted refractory part of spent cathode lining with 1767 and 2168 days age.

## 5.5 Thermal Conductivity

### 5.5.1 Spent Carbon Cathode Block

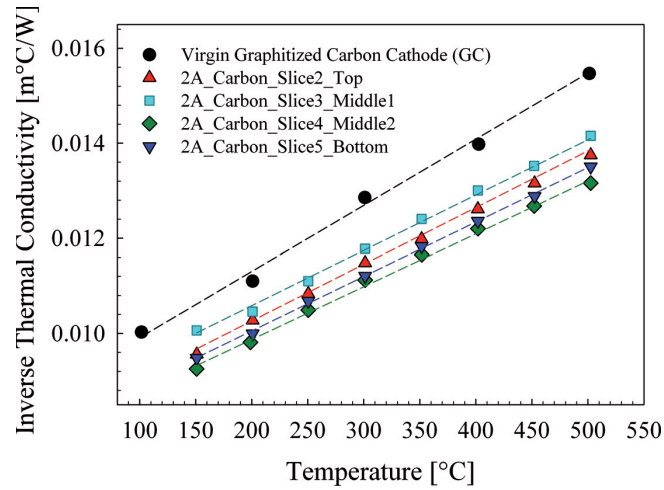
The thermal conductivity of the spent pot lining samples compared with the respective virgin material are compared in Figs. 5.14 (a) and (b). The tabulated values for thermal conductivity and heat capacity are given in the Appendix A. The data were fitted to Eq. (5.1)

$$\lambda = \frac{1}{aT + b} \quad (5.1)$$

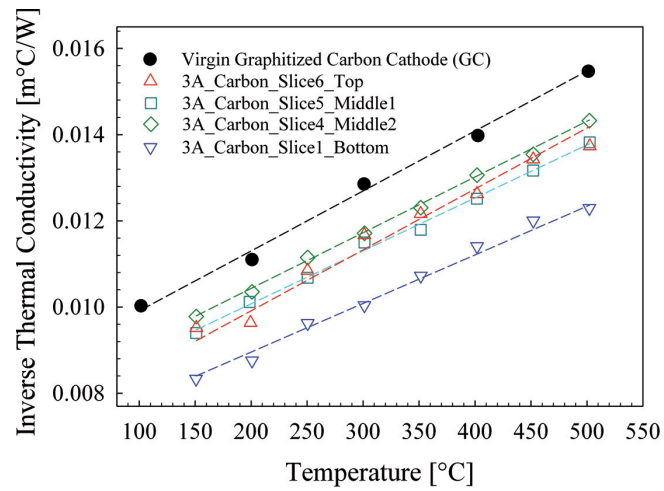


**Figure 5.14:** The thermal conductivity of spent carbon block (with the age of (a) 1767 and (b) 2168 days) up to 500 °C. The dashed lines are curves fitted to the measured data (open and closed symbols) up to 1000 °C using the Eq. (5.1) and Fig. 5.15.

where  $y$  is the thermal conductivity [W/m°C] and  $T$  is the temperature [°C]. The constants  $a$  and  $b$  are the slope and the intersection with the y-axis, respectively. The dashed lines in Fig. 5.15 (a) and (b) are the regression lines used to extrapolate the thermal conductivity above 500 °C. A significant increase in the thermal conductivity relative to the virgin material were observed for the SPL materials. The thermal conductivity is strongly temperature dependent, and the relative difference between the virgin and SPL materials increases with increasing temperature.



(a)

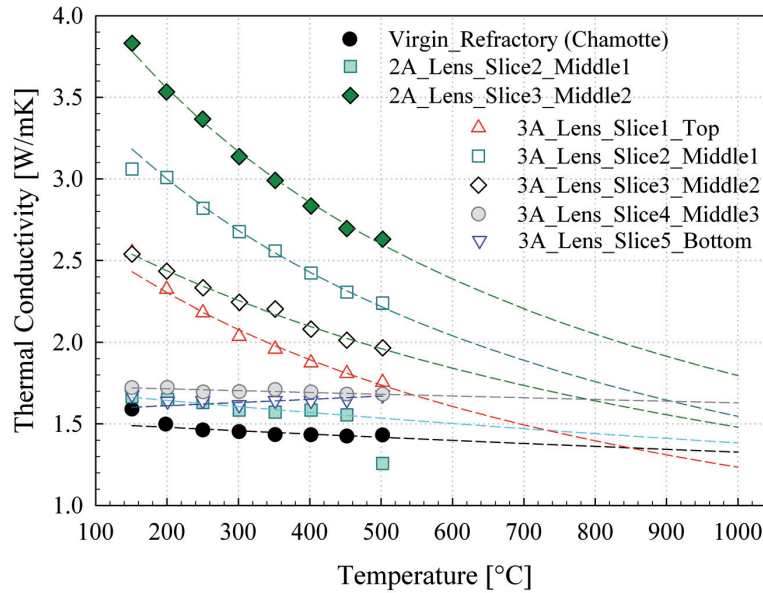


(b)

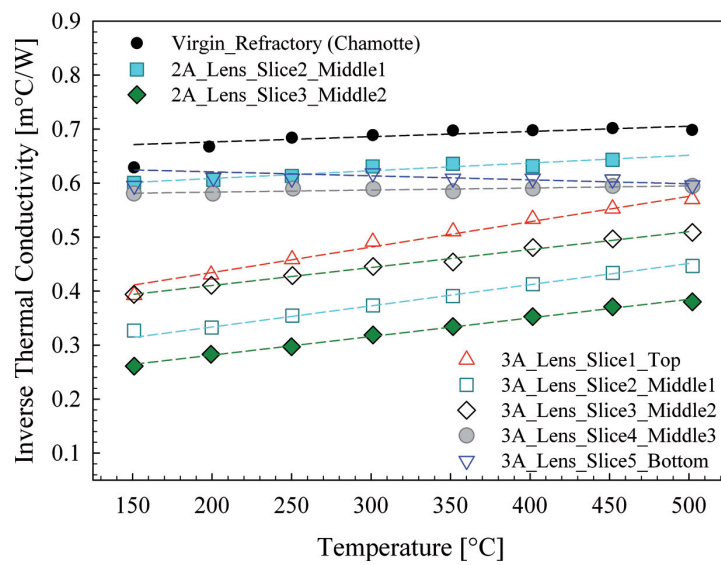
**Figure 5.15:** Inverse of the thermal conductivity versus temperature to extrapolate the data in Fig. 5.14. The symbols represent the inverse of the measured thermal conductivity data of spent carbon block with the age of (a) 1767 and (b) 2168 days. The designated constants  $a$  and  $b$  of the dashed straight lines were used to interpolated the values in Fig. 5.14.

### 5.5.2 Lens Build-Up and Reaction Front

The thermal conductivity of the SPL samples compared with the virgin material are shown in Fig. 5.16. The measured data for thermal conductivity and heat capacity are tabulated in the Appendix A. Samples from 2A and 3A were characterized. The data were fitted to the Eq. (5.1) and extrapolated above 500 °C using the inverse of the thermal conductivity versus temperature (Fig. 5.15). The thermal conductivity of the lens build-up is significantly higher than the virgin refractory material. This is expected since both the phase content, density and microstructure are quite different from the virgin material.



**Figure 5.16:** The thermal conductivity of the lens build-up with the age of 1767 (2A) and 2168 days (3A) up to 500 °C. The dashed lines are curve fitted to the measured data (open and closed symbols) up to 1000 °C using the Eq. (5.1) and Fig. 5.17.



**Figure 5.17:** Inverse of the thermal conductivity versus temperature to extrapolate the data in Fig. 5.16. The symbols represent the inverse of the measured thermal conductivity data of the lens build-up with the age of (a) 1767 and (b) 2168 days. The designated constants  $a$  and  $b$  of the dashed straight lines were used to interpolated the values in Fig. 5.16.

## 6 Discussion

### 6.1 Two Reaction Fronts in the Refractory Lining

#### 6.1.1 Diffusion Mechanism of Attacking Agent at Reaction Front

The present observations in terms of the phases found in the spent pot lining are in line with the findings reported by previous investigations [16, 72]. It has been shown previously, that the diffusion of Na into the carbon cathode blocks occurs early after cell start up [12, 60]. The percolation of bath will follow after the infiltration of Na since the bath wets the cathode only after Na-infiltration as shown in Fig. 3.3 [3, 12, 60]. This points to the fact that Na will diffuse into the refractory lining first and that the bath will arrive at the interface between the carbon cathode and the refractory lining at a later stage in the cell life. Thus the chemical degradation of the refractory lining is governed first by the diffusion of Na(g) and second the infiltration/diffusion of bath components/fluoride melt (mainly NaF). In general, both attacking agents cause material transformations. It has not been established if the reaction pattern taking place in the carbon block remains the same during the entire lifetime of the cell and how the degradation at the reaction front in the refractory lining evolves over time.

The presence of only Na and no bath components at the "first reaction front" (Figs. 5.6 and 5.7) clearly demonstrates that this scenario is maintained during the life time of the cell. The fluoride or "second reaction front" was detected in some distance to the sodium or "first reaction front", shown in Fig. 5.8. The first reaction front in the refractory lining is therefore indeed an attack by sodium only. What is then the diffusion mechanism of Na at the first reaction front? At an early state in the cell operation, sodium penetrates and reacts with the virgin refractory material (20 vol% porosity). The first secondary phase, which forms is a viscous or glassy melt. Therefore, Na diffusion in oxide glasses, which always occurs as ionic conduction [89], is further considered.

Three hypotheses for the diffusion of Na at the first reaction front are presented in Fig. 6.1. Hypothesis 1 (*H1*) states that sodium diffuses together with fluoride as NaF. In hypothesis 2 (*H2*) it is proposed that the transport of sodium ions is compensated by the transport of oxygen ions resulting in transport of Na<sub>2</sub>O. Finally, in hypothesis 3 (*H3*) it is also proposed that sodium is oxidized to Na<sup>+</sup>. The transport of sodium is by ionic diffusion as in *H1* and *H2*. However, the charge transfer in this case is compensated by the transport of electrons. In the following discussion all three hypotheses are discussed in relation to the experimental observations and data on the diffusion of ions in oxide melts.

The experimental evidence for the separation of sodium and the fluoride bath (fluorine ions) demonstrates clearly that *H1* is not supported by the experimental observations.

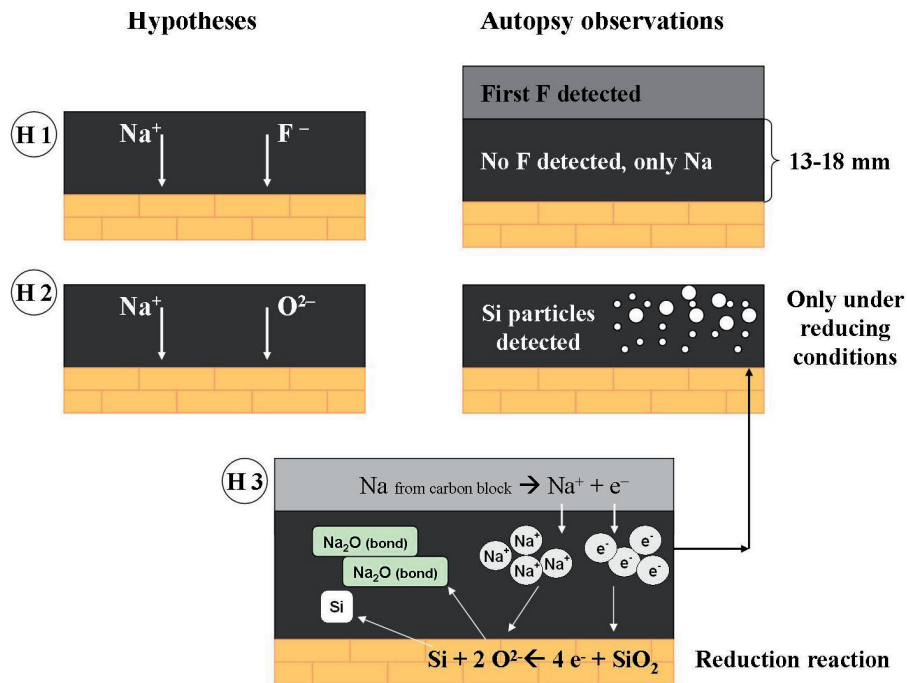


Figure 6.1: Three possible transport mechanisms for Na in the refractory lining.

The percolation of bath through the refractory lining will also take place, but in a certain distance behind the first reaction front. This will result in further reactions with the bath components. In this case the reaction is not necessarily with the pristine refractory materials, it may also react with the secondary phases formed due to the reaction with Na. The interaction of attacking species with the refractory material is strongly effected by diffusion. It is well known that sodium ions are highly mobile compared to the lattice elements, such as silicon and oxygen. Sodium aluminosilicate glasses and Na diffusion in these systems were discussed in Sections 2.3 and 3.4.6. Different to other cations Na exhibits only a slight increase in diffusivity with increasing silica content [93,99] and is thus relatively unaffected by viscosity changes. Dingwell [93] has shown that the tracer diffusion of oxygen is much lower than compared to sodium. The former depends strongly on the melt viscosity. Dingwell [94] also found that  $\text{F}^-$  diffuses much slower than  $\text{Na}^+$ . The chemical diffusion of fluoride ions are decreasing with increasing  $\text{SiO}_2$  content, which is probably due to a simple anionic exchange with oxygen. The change in the viscosity with variations in the  $\text{SiO}_2$  and/or the F content was shown in Fig. 3.18. The significant difference in the mobility of  $\text{Na}^+$  and  $\text{F}^-$  explains why the fluoride bath never reaches the sodium reaction front.

The phase content of spent refractory samples displayed that the concentration of NaF decreases/disappears deeper in the lining (at a later stage than cryolite) due to the formation of  $\text{NaAlSiO}_4$ . Thus we can predict that the second reaction front is

less viscous than the first reaction front containing only oxides. The sodium aluminosilicates formed in the reaction between Na and the refractory layer are most likely a viscous liquid, which is not necessarily completely miscible with the fluoride melt [18]. Thus the oxygen diffusion limits the fluorine diffusion, where the former depends on the viscosity and thus on the SiO<sub>2</sub> content. This again revokes hypothesis *H1*, but in the same time also *H2*, since diffusion of sodium ions are not affected by viscosity changes.

The fluoride melt is far less viscous than the oxides. Hence diffusion/convection of the electrolyte components will slow down, when they come into contact with the viscous layer. This scenario gives a possible explanation for why bath components are hindered to reach the first reaction front (Fig. 5.8). Right below the carbon cathode mainly NaF, Na<sub>3</sub>AlF<sub>6</sub> and β-Al<sub>2</sub>O<sub>3</sub> were present. Attack by Na-vapour results in the formation of sodium aluminosilicates (NaAlSiO<sub>4</sub> and NaAlSi<sub>3</sub>O<sub>8</sub>), β-Al<sub>2</sub>O<sub>3</sub> and Si, see Figs. 5.3 and 5.4. Moreover, the presence of Si(s) evidences that the attack is strongly reductive in nature (Fig. 5.9). This is the case through the entire reaction front layer, shown by the uniform black colour and the presence of white Si spots, as shown in Fig. 5.9. The presence of Si at the reaction front demonstrates that *H2* can not explain the transport of Na to the reaction front. Otherwise reaction 6.1 would take place in some distance to the reaction front and no elemental Si should be detected, which was not the case.



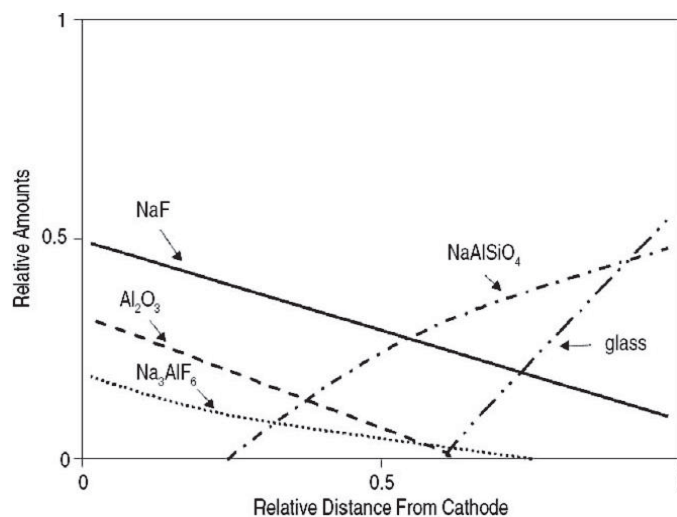
In hypothesis *H3* a plausible route for sodium transfer at the first reaction front and possibly also further up is proposed. The presence of Si demonstrates that the oxidation of sodium takes place below the build-up. Above, Na(g) is transported through the bath (sodium is soluble in the electrolyte [135]). Na(g) transforms into a Na<sup>+</sup> ion by the loss of an electron. The Na<sup>+</sup> diffuses together with the e<sup>-</sup> through the viscous melt. It attacks the intact refractory material, by reducing the SiO<sub>2</sub> to Si metal and to oxygen ions. The degradation proceeds by diffusion of Na<sup>+</sup> from the place where the reduction takes place and further into the non-reacted lining. It is supposed that the degradation reaction is faster than diffusion. Thus the rate limiting step is not the diffusion of Na<sup>+</sup> but the mobility of the charge compensating O<sup>2-</sup> ions. The viscous barrier is therefore a barrier for the diffusion of O<sup>2-</sup> and also F<sup>-</sup>.

The reaction front has always a low concentration of Na<sup>+</sup>. The concentration gradient of Na is the driving force for further sodium diffusion. As the sodium content increases, the viscosity of the glassy melt is lowered. Here, it is proposed that the silicate melt formed at the reaction front becomes electrical conductive enhancing the transport of Na. Attempts to support the change in electrical conductivity between virgin refractory material and the first 10 mm of the reaction front were performed. Due to the brittle behaviour of this part and the lack of appropriate samples this hypothesis could not be supported by experimental evidence. The black colour of the material does however support the possibility for electrical conductivity.



### 6.1.2 The Importance of the Thermal History of SPL

Siljan et al [16] reported a qualitative representation of how the content of phases changes with distance from the carbon cathode blocks downwards in the lining, see Fig. 6.2. The general trend shown in the figure is consistent with the present investigations (Fig. 5.3). Minor variations can be explained by the inhomogeneous appearance of the spent lining, shown by the layered structure in Fig. 5.1. Thus sampling position and preparation may become important issues. The overall appearance of the spent cross section strongly depends on another major aspect, the cooling history. A large number of autopsies have been performed [3], which is the most frequent method to investigate the spent bottom lining. To the author's knowledge, previous analyses have been based on the idea that the physical appearance or so called layered structure of the spent lining reflects the conditions at the operation temperature before the shut down of the cell. Here it is shown by the simple annealing experiments of the samples from the spent pot lining that this is indeed not the case. The layered structure of the cross section samples of SPL are clearly visible (Fig. 5.1), but the formation and conditions are proposed to be of complex nature.



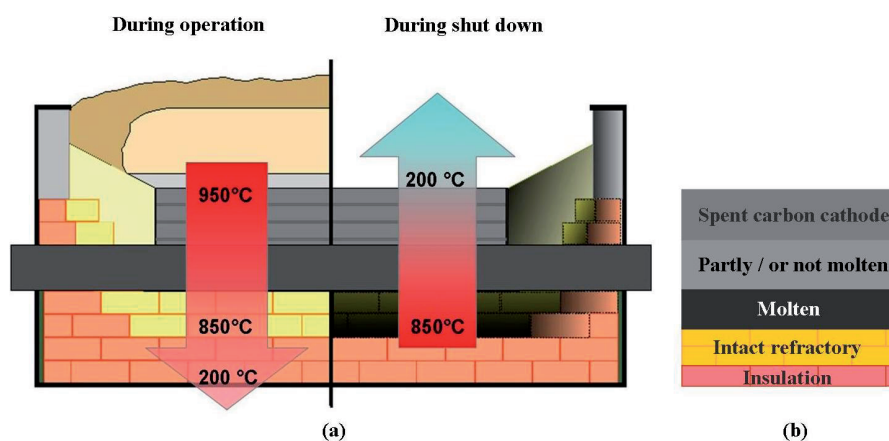
**Figure 6.2:** Relative amounts of the major mineral phases as function of distance from the cathode blocks observed in real aluminium electrolysis cell linings. Data are based on XRD semi-quantitative analysis of reacted materials [16].

It is proposed based on the annealing experiments that there is a significant amount of molten phase present below the carbon block during operation. This molten phase consists mainly of bath components and is therefore of non-viscous nature. Solid particles originating from the pristine material or precipitated reaction products may also be present in the melt. The main components in the molten phase will start to precipitate/crystallize during cooling, and crystallization will start in the region with the lowest temperature. Since the cell is well insulated at the bottom, the main heat

loss is proposed to occur upwards during the cooling of the cell, which takes around 4 days for a common shut down cell. It is therefore likely to find nearly pure NaF and  $\beta$ -alumina crystallized from the carbon cathode interface and downwards, which is in line with the autopsy results.

Two observations support the influence of the thermal history. First, it was found needle-like crystals, shown in Fig. 5.2, growing downwards below the cathode block. These samples did not show any evidence of melting during the annealing experiments (Fig. 5.11). Secondly, the lens build up zone (samples 1, 2, 3 as well as a part of sample 4) was not molten even at 950°C. The operation temperature of a common cell is 950-965°C [3]. The qualitative X-ray analysis has shown that these samples mainly contain the secondary phases  $\beta$ -Al<sub>2</sub>O<sub>3</sub> and NaF. Moreover, the samples near the reaction front gave clear evidence of the presence of molten phases below the carbon cathode and they were not found close to the carbon cathode. These facts support that crystallization initiates from the top and propagates in downwards direction during cooling. As the concentration of NaF and  $\beta$ -alumina are reduced due to crystallization, the molten phase becomes enriched in other components such as sodium aluminosilicates. The viscosity of the molten phase will therefore increase due to the increasing oxide content and reducing temperature. The growth of needle like crystals of NaF and  $\beta$ -alumina will eventually stop, and mass transport by convection will be inhibited due to higher viscosity and increased concentration of solid particles in the melt.

According to the scenario described above, the thermal gradient in the refractory lining during the operation and the period of cooling after a shut down is reversed. An illustration of the thermal history is shown in Fig. 6.3.

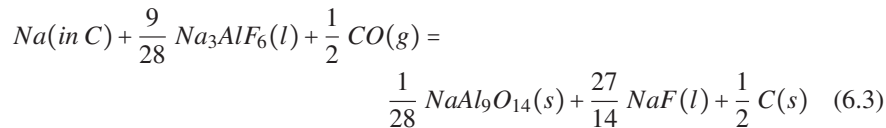
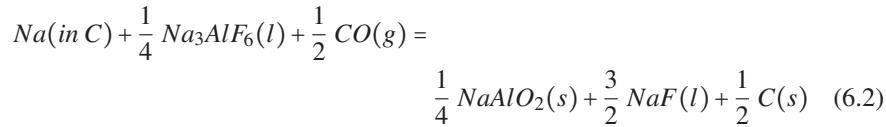


**Figure 6.3:** (a) An illustration of the effect of the thermal history from a situation during operation of the cell to a situation during cooling. (b) Sequence of materials in the lining during cooling found by the annealing experiments.

## 6.2 Carbon Cathode

In general the investigations in this work have shown that the overall chemical composition of the three spent carbon cathodes was quite similar and in line with expectations. The melt in the carbon cathode blocks, with more than 800 days of operation changes gradually to a electrolyte-like composition over time [62]. The cells investigated here are high in age and more than 1500 days. Thus in agreement to Lossius and Øye [62] the phases found were  $\text{CaF}_2$ ,  $\beta\text{-Al}_2\text{O}_3$ ,  $\text{Na}_3\text{AlF}_6$  and  $\text{NaF}$  (Fig. 5.3). The  $\text{CaF}_2$  content in electrolytes is suited between 4-6 wt%. Therefore an electrolyte content of 10-20 wt% in the SPL implies a  $\text{CaF}_2$  level of 0.5–1 wt%, which is in agreement with our investigations.  $\text{CaF}_2$  is not reacting while diffusing through the cathode block. More interesting is the fact that the penetrated melt becomes more basic towards the lower surface. A basic melt has a higher ratio between sodium fluoride ( $\text{NaF}$ ) and cryolite ( $\text{Na}_3\text{AlF}_6$ ) in addition to the added excess of typically 6-13 mass%  $\text{AlF}_3$ . The melt becomes more basic because of reactions inside the carbon cathode blocks as described by Brilliot et al. [61] and Shamsili et al. [136]. Besides the fact that the refractory material underneath is attacked by a basic melt, there is no obvious explanation why the  $\text{Na}_3\text{AlF}_6$  content suddenly decreases, while the amount of  $\beta\text{-Al}_2\text{O}_3$  increases at the cathode bottom. Here again, the cooling of the cathode after shut down may be relevant for the composition profile.

During cooling, the heat is transferred in the reversed direction as shown in Fig. 6.3 (a). As the carbon cathode cools down the melt inside the porous structure crystallizes from the top to the bottom. The cryolite, which is the main component in the melt, starts to precipitate first. The remaining melt becomes enriched in  $\text{NaF}$  and  $\beta$ -alumina. According to Lossius and Øye [62],  $\beta$ -alumina starts to precipitate at  $\text{CR} > 3$ . Another, but less likely explanation, could be the reaction of melt components with gaseous carbon monoxide, shown by Eqs. (6.2) and (6.3)

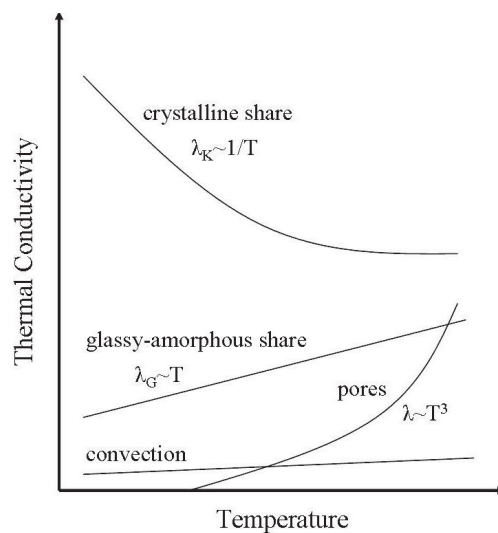


Both reactions are thermodynamically possible ( $\Delta G < 0$ ), but it is not very likely that significant amounts of oxygen in form of  $\text{CO}$  are present in the cathode.

### 6.3 Thermal Conductivity

The pristine refractory and carbon bricks are heterogeneous materials. Thus porosity, pore distribution, orientation of grains, grain size distribution, binder matrix, content of impurities, structural defects and cracks influence the thermal conductivity as well as the grade of graphitization for carbon cathode materials [3, 8, 31]. The measured thermal conductivity of the virgin materials were in accordance with the manufacturer's specifications.

The pristine refractory material shows a maximum in the thermal conductivity at 150 °C. The temperature dependency corresponds to what is expected for a mixture of a crystalline and an amorphous material [41]. This is not surprising because chamotte bricks are based on alumino-silicates. Beside mullite and cristobalite, they contain a silica-rich amorphous phase. SPL materials have undergone a mineralogical transformation, where new phases appeared at the same time as pores are filled. The top part samples contain mainly crystalline phases (e.g.  $\beta$ -Al<sub>2</sub>O<sub>3</sub>, NaF and Na<sub>3</sub>AlF<sub>6</sub>) resulting in a temperature dependence of the thermal conductivity typical for crystalline materials (Fig. 6.4).



**Figure 6.4:** Qualitative progression of the thermal conductivity of the components of a refractory material (redrawn from [41]).

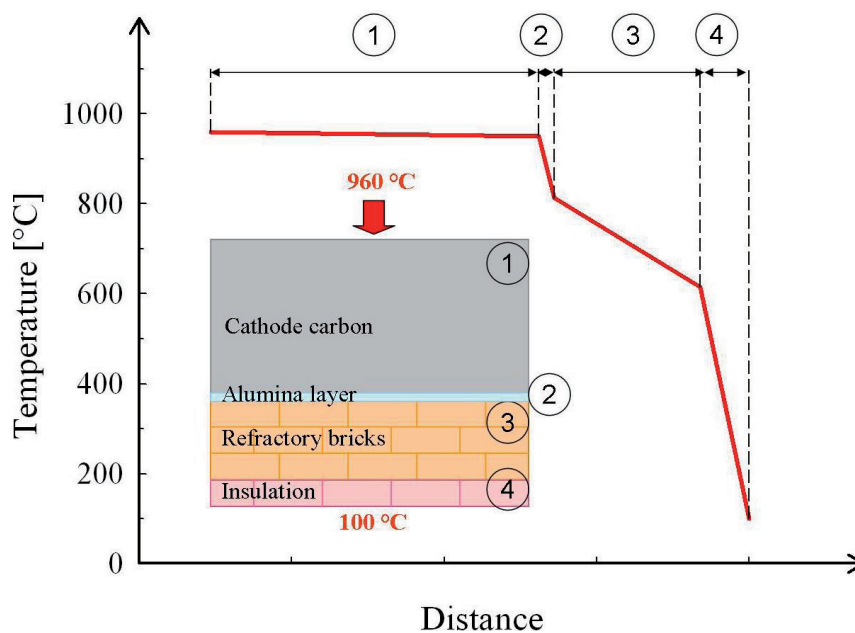
Samples from the bottom part of the lens build-up, consist of a glassy phase (e.g. albite) and the thermal conductivity behaves as expected for amorphous materials. The thermal conductivity is proposed to continue to increase above 500 °C. This becomes important for the thermal stability of the entire non-carbon cathode bottom lining, since it is proposed that there is a significant amount of molten phase between cathode block and the intact refractory/insulation layers. From the measured data it is shown that the thermal conductivity of the SPL samples is increasing in the measured

temperature range in the following order:

top part (with some pores, crystalline phases) > bottom part (no or very few pores, but glassy phases) > pristine material (crystalline + amorphous phases, many pores).

The thermal conductivity of the pristine graphitized carbon material decreases with increasing temperature. The temperature dependence is typical for crystalline materials [41] (Fig. 6.4), where lattice vibrations are the primary mechanism for heat conduction. The thermal conductivity for the spent samples, penetrated by sodium and bath components, is in general significantly higher than for the original graphitized block. This is mainly caused by filling the pores with bath components. The temperature dependence of the thermal conductivity is still comparable to pristine and thus typical for crystalline materials.

To illustrate the consequences of the changes in the thermal conductivity of the lining materials, a simple heat transfer model was employed. The different scenarios and the resulting thermal profiles are shown in Figs. 6.5, 6.6 and 6.7. The material data for the virgin lining *model 1* was taken from the suppliers specifications and compared with the spent lining *model 2* by using the measured data reported here.



**Figure 6.5:** Temperature profile through the virgin carbon cathode and the virgin bottom lining (*model 1*).

The data used in the calculations are given in Table 6.1. SPL materials demonstrate an overall increase of the thermal conductivity compared to the virgin materials. Consequently, an increase in heat loss is expected. This is balanced by the continuous reduction of the cathode carbon block thickness because of the erosion during opera-

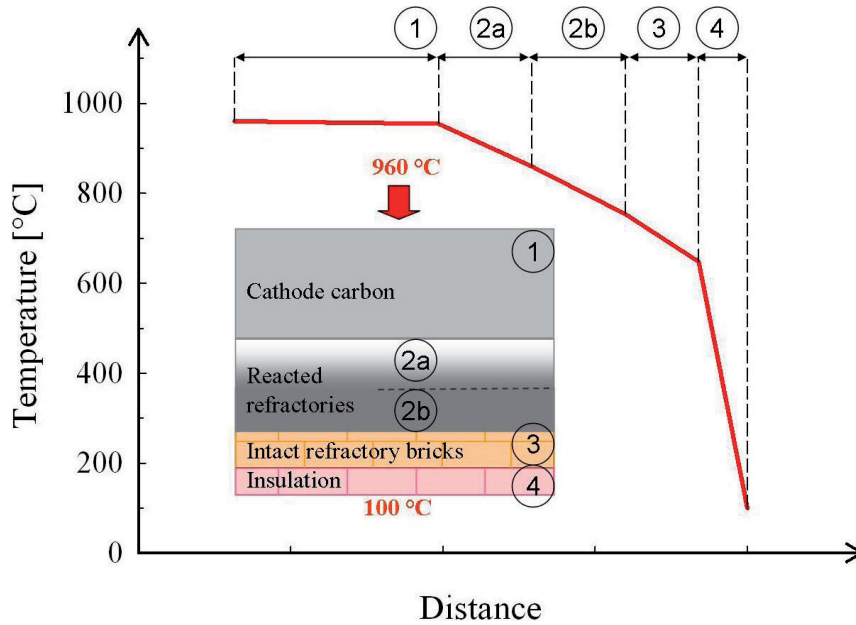
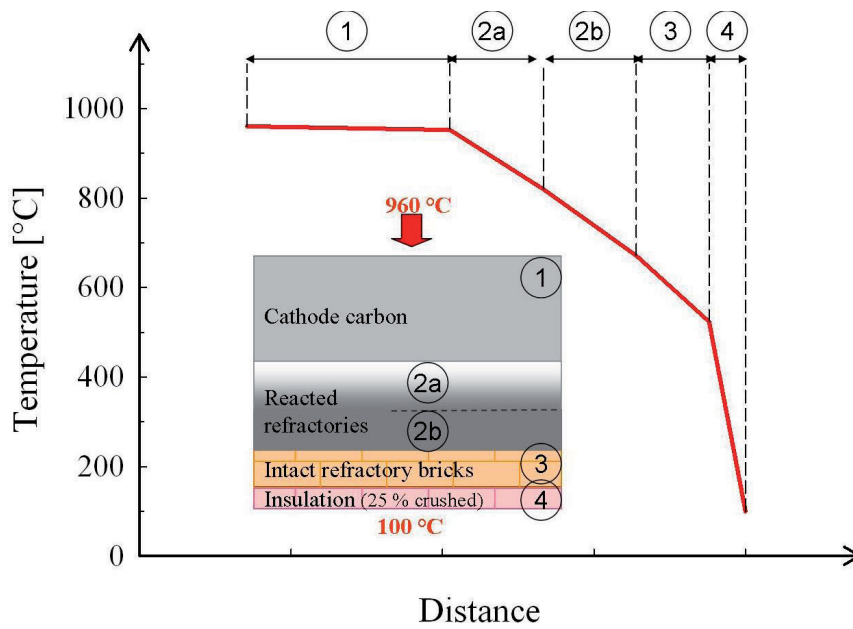


Figure 6.6: Temperature profile through the spent cathode lining materials (*model 2*).

tion [3], and the successive build up of a lens layer with a low thermal conductivity as compared to the spent carbon material. This leads only to a slight increase in the total heat flux, shown in Table 6.1, which depends on the ratio between spent carbon block and lens build up layer. A different situation can be predicted when the insulation layer is crushed during operation [3] (Fig. 6.7 *model 3*). Here a reduction of the insulation layer thickness of 25 % was assumed, associated by an increase in the thermal conductivity [137]. The heat flux through the bottom increases significantly (Table 6.1). An additional increase of 25 % of the thermal conductivity of the reacted layers (lens build up and reacted refractory part) effects the heat flux as well. However, it is not influenced to the same extend as by the crushed insulation layer (Table 6.1 *model 4*). To conclude the following points can be summarized:

1. The cathode lining becomes more dense due to the infiltration and the reaction with sodium and the bath components, and the thermal conductivity of the carbon cathode, refractory and insulation materials increases compared to the virgin materials.
2. The overall heat loss of the cathode bottom lining increases, but the effect is damped by the thickness decrease of the carbon cathode and thickness increase of the lens build up material.
3. The insulation layer at the bottom of the cathode lining is the most important part for the thermal balance of the cell, and a compression of the insulating layer effects the heat loss significantly.



**Figure 6.7:** Temperature profile through the spent cathode lining materials with crushed insulation layer (model 3).

**Table 6.1:** Data used in the heat flux  $q$  calculation with the thickness  $t$  and the thermal conductivity  $\lambda$  for each material. The ratio between refractory and insulation material is 3:1. The numbers were rounded up.

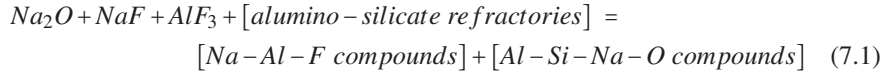
	Specification	$t$ [m]	$\lambda$ [W/(m·K)]	$q$ [W/m <sup>2</sup> ]
<b>Model 1:</b> New lining (suppliers data)	Carbon block (incl. collector bar)	0.43	65	
	Alumina (leveling layer)	0.02	0.21	1447 (initial value)
	Refractory	0.19	1.40	
	Insulation	0.06	0.18	
<b>Model 2:</b> Spent lining (measured data)	Spent carbon block (incl. collector bar)	0.27	74	
	Lens build up (top)	0.12	2.0	
	Lens build up (bottom)	0.12	1.78	1541 (↑ of 6.5 %)
	Intact refractory	0.10	1.40	
	Intact insulation	0.06	0.18	
<b>Model 3:</b> Crushed insulation (25 %)	Crushed insulation	0.05	0.24	2153 (↑ of 49 %)
<b>Model 4:</b> Increase of $\lambda$ (25 %)	Lens build up (top)	0.12	2.50	
	Lens build up (bottom)	0.12	2.22	1616 (↑ of 11.7 %)
Temperature at the carbon surface = 960 °C				
Temperature at the insulation bottom = 100 °C				



## 7 Degradation Map for the Sodium Attack

### 7.1 Introduction

A unified approach, also referred to as degradation map taking both reacting agents (molten NaF and metallic Na) on alumino-silicates into account was proposed by Pelletier et al. [22,23]. They assumed that all the sodium was oxidized atmospherically to Na<sub>2</sub>O. The unified pattern is illustrated by Eq. (7.1)

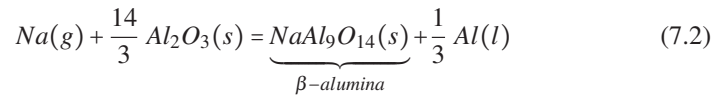


The prediction can be visualized by drawing a degradation map. The degradation path will vary dependent on the NaF: Na<sub>2</sub>O ratio. The complete oxidation of sodium is questionable since the elemental silicon droplets found in the reaction front demonstrate clearly that the deterioration takes place at reducing conditions. Sodium metal reduces silica in the lining to Na<sub>2</sub>O(bonded) and Si metal, see Section 5.2.2. According to thermodynamics, sodium works as a strong reducing agent with respect to most oxides. The predominance phase diagram or degradation map of sodium attack was established to show the stable compounds formed during degradation of alumino-silicate refractories by sodium vapor.

### 7.2 Thermodynamic Calculations

The map was constructed based on the reactions (7.2) to (7.13). These reactions represent equilibrium reaction and minimization of Gibbs energy as shown in Table 7.1. The calculations were supported by the use of phase diagrams and relevant thermochemical software FactSage™ 5.2. Only scenarios at equilibrium conditions are considered and informations about the kinetics of the reactions are not given.

As for the pure NaF attack, the focus is first on chemical reactions between pure alumina refractories and sodium vapor. The only reaction is the formation of  $\beta$ -alumina, according to reaction 7.2



Despite extensive efforts, the phase diagram of the quasi-binary system Na<sub>2</sub>O-Al<sub>2</sub>O<sub>3</sub> is not well established. Several versions of the phase diagram have been proposed [138].

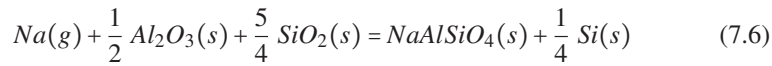
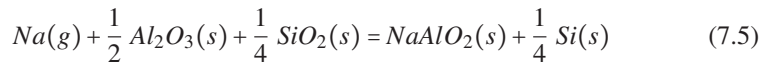
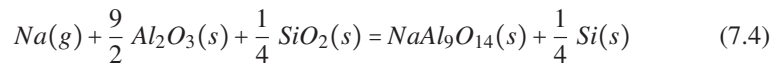
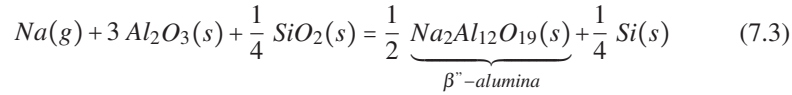
**Table 7.1:** Gibbs energies for equations (7.2)-(7.13) from FactSage™ 5.2.

Eq. nr.	$\Delta G_K^\circ_{1100K}$ [kJ]	Eq. nr.	$\Delta G_K^\circ_{1100K}$ [kJ]
(7.2)	-28.00	(7.8)	-135.54
(7.3)	-60.74	(7.9)	-67.60
(7.4)	-71.16	(7.10)	-48.23
(7.5)	-34.46	(7.11)	-73.40
(7.6)	-120.08	(7.12)	-81.06
(7.7)	-9.17	(7.13)	-81.63

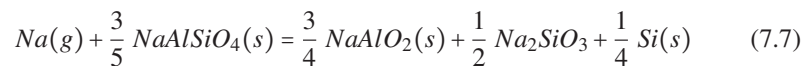
Rolin and Thanh [80] identified three sodium aluminate phases:  $\text{NaAlO}_2$ ,  $\beta$ -alumina ( $\text{NaAl}_{11}\text{O}_{17}$ ) and  $\beta''$ -alumina ( $\text{Na}_2\text{Al}_{12}\text{O}_{19}$ ). Their phase diagram was given in Section 3.4.4 (Fig. 3.12). Later this version has been critically reviewed by DeVries and Roth [139]. They observed the same phases, but found discrepancies in their exact composition and temperature.

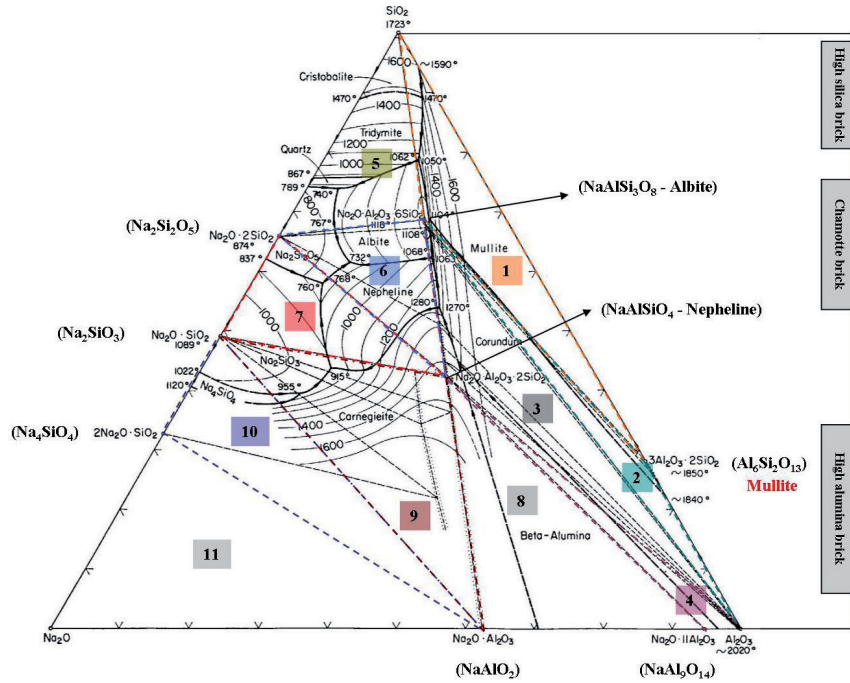
If silica is present sodium reacts and reduces both the refractory oxides. The quasi-ternary system  $\text{Na}_2\text{O-Al}_2\text{O}_3\text{-SiO}_2$  illustrates the thermochemical relationships between these three oxides. It has been investigated and published by Schairer and Bowen [140]. In 1960, Osborn and Muan [141] revised the system, because of new data in the  $\text{Na}_2\text{O-Al}_2\text{O}_3$  system. Their version is depicted in Fig. 7.1.

Due to the reactions with sodium and the presence of silica, high alumina bricks convert to sodium aluminates, nepheline and silicon, according to Eqs. (7.3)-(7.6)

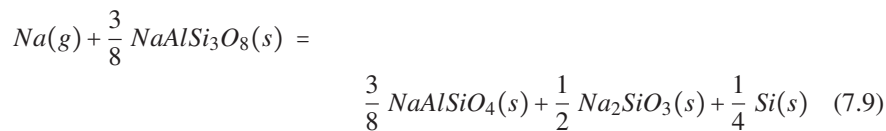
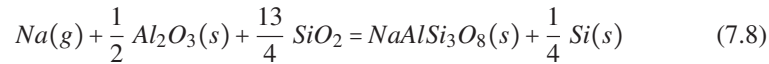


At higher  $\text{SiO}_2$  content, albite ( $\text{NaAlSi}_3\text{O}_8$ ) will be produced at the expense of nepheline ( $\text{NaAlSiO}_4$ ), see Eq. (7.8). Since both of these two reaction products are not stable in contact with sodium, they can further react with sodium according to reactions (7.7) and (7.9)



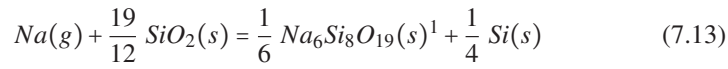
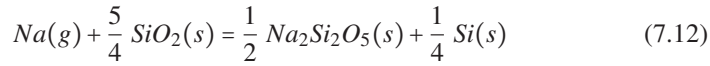
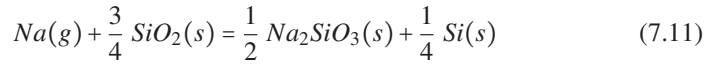
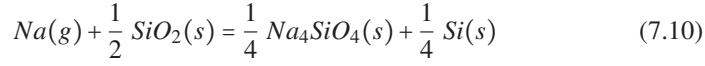


**Figure 7.1:** Original Na<sub>2</sub>O-Al<sub>2</sub>O<sub>3</sub>-SiO<sub>2</sub> system [141]. The numbers 1-11 represent Alkemade triangles. The corners are the coexisting phases.



Albite is more unstable than nepheline. The reduction of these reaction products in the deteriorated lining is disadvantageous with respect to maintaining a viscous penetration barrier, which retards further penetration. The silicon precipitates as small accumulations in the reacted refractory layer. They appear as bright spots or droplets as shown in Fig. 3.14 and spread down to the reaction front as seen in Fig. 5.9.

Sodium attack on pure silica results in sodium silicate compounds and elemental silicon, according to Eq. (7.10)-(7.13). The quasi-binary system of Na<sub>2</sub>O-SiO<sub>2</sub> was studied by Morey and Bowen [142] and was later extended by Kracek [81]. His version and the work of Williamson and Glaser [82] were shown in Section 3.4.4 (Fig. 3.13)



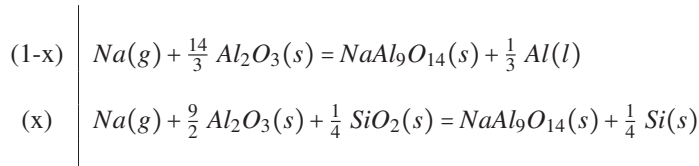
### 7.3 Boundaries of Stability Fields

The basis for all equilibrium considerations in heterogeneous systems and the representation of equilibria in form of phase diagrams is the Gibbs phase rule (7.14)

$$P + F = C + 2 \quad (7.14)$$

It is applied to determine the number of coexisting phases under given conditions, where  $P$  is the number of phases,  $F$  is the degree of freedom,  $C$  is the number of components and two denotes the variables pressure and temperature. To construct the degradation map, the boundaries of the stability field of coexisting phases need to be identified. The system Na-Al-Si-O is a four component system. If the temperature and pressure are chosen to be constant, a maximum of four phases may coexist. The phases are represented by the compounds found in the reaction front. Here, the boundaries have been identified by combining reactions giving the total number of three new compounds. The following description shows one example of the determination of a boundary between two stability fields.

First, the reactants side (left side) of the reaction in question, (7.2) and (7.4), are reformulated into equations, see Eq. (7.15)-(7.16)



<sup>1</sup>With reference to the degradation map in Fig. 7.2, the phase  $Na_6Si_8O_{19}$  is not present in the original  $Na_2O-Al_2O_3-SiO_2$  system, see Fig. 7.1. In the  $Na_2Si_2O_5-SiO_2$  binary system, shown in Fig. 3.13 (b)  $Na_6Si_8O_{19}$  is only stable in a very narrow crystallization region and temperature window.

$$W(\text{SiO}_2) = \frac{x \cdot m_{\text{SiO}_2}}{(x \cdot m_{\text{SiO}_2} + x \cdot m_{\text{Al}_2\text{O}_3} + (1-x) \cdot m_{\text{Al}_2\text{O}_3})} \quad (7.15)$$

$$W(\text{Na}) = \frac{x \cdot m_{\text{Na}} + (1-x) \cdot m_{\text{Na}}}{x \cdot m_{\text{Na}} + (1-x) \cdot m_{\text{Na}} + x \cdot m_{\text{SiO}_2} + x \cdot m_{\text{Al}_2\text{O}_3} + (1-x) \cdot m_{\text{Al}_2\text{O}_3}} \quad (7.16)$$

Here,  $x$  denotes the ratio between both equations, varying from 0 to 1 and  $m$  is the mass of the respective species. The latter is assembled by  $n$  and  $M$ , which are the number of mols as well as the molecular weight [g/mol] of each chemical involved. The results are the weight fractions of  $\text{SiO}_2$  and  $\text{Na(g)}$ , which correspond to two variables in the degradation map. The example given here, describes the line, which separates region  $a$  and  $b$  in Fig. 7.2, shown in the following section. The other boundary lines are determined in a similar manner.

## 7.4 Degradation Map

Using the Gibbs phase rule and following the description in Section 7.3 for all involved reactions, the complete degradation map of "dry" attack can be constructed, as illustrated in Fig. 7.2. It shows the behaviour of all alumino-silicate refractories under pure Na attack. This map is significantly more complex than the map for pure NaF attack (Section 3.4.3) with quite a few stability regions. Each stability field includes four coexisting phases.

The number and shape of the stability regions is controlled by one important factor:  $W(\text{Na})$ . This parameter is the weight fraction of the attacking agent sodium, introduced as a vapor species (y-axis) and as a function of the silica content of the refractory (x-axis).

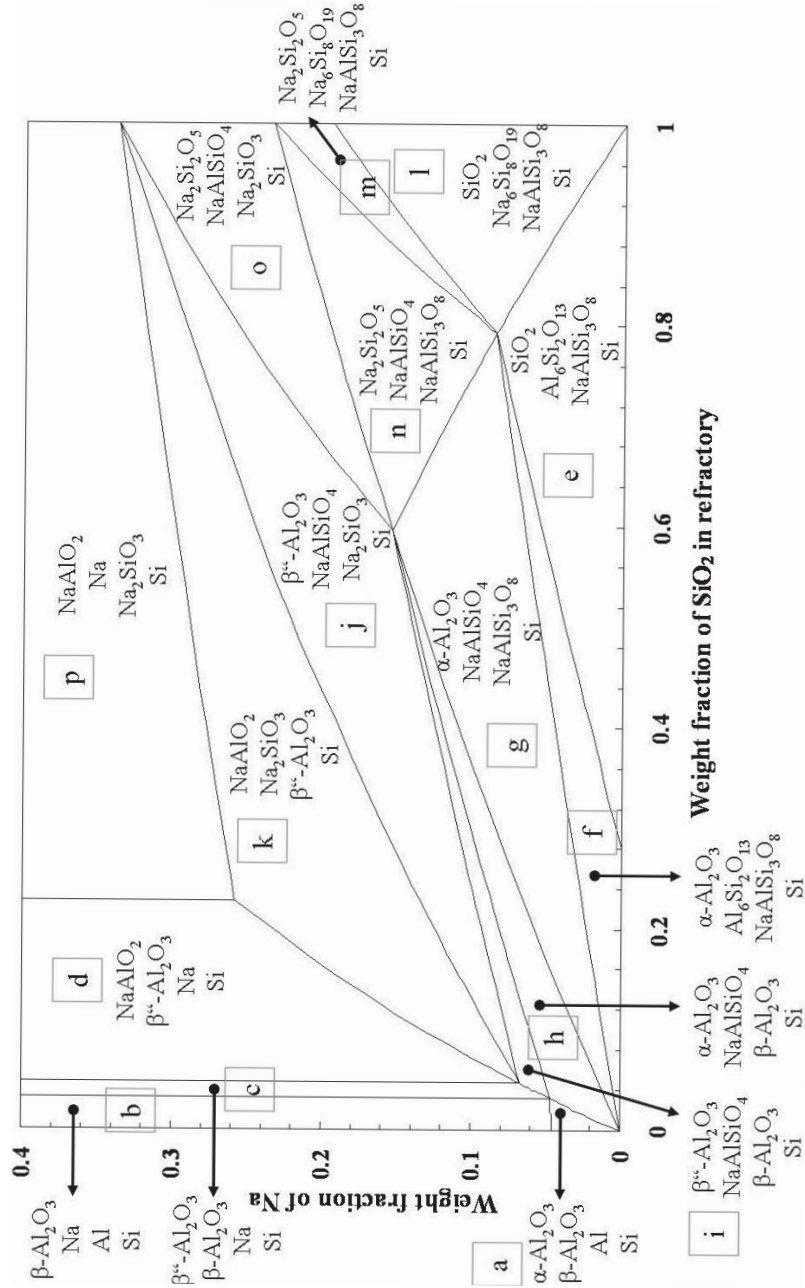


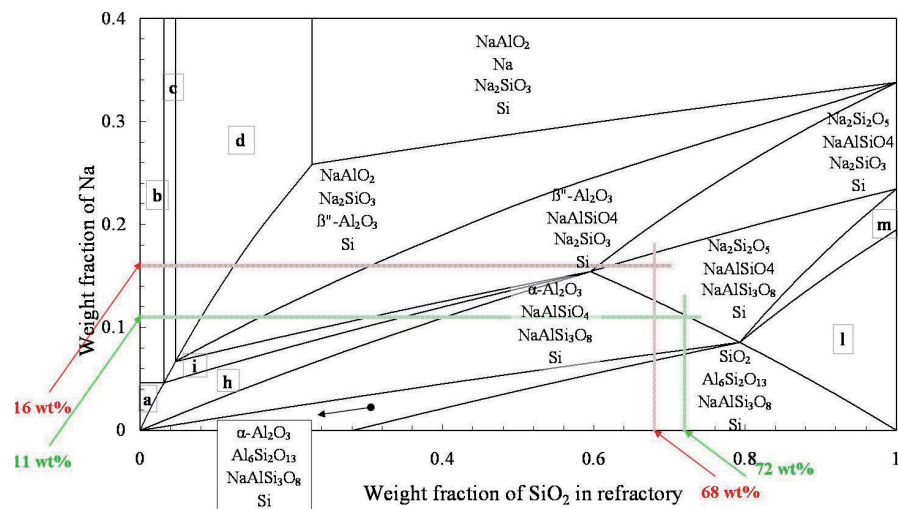
Figure 7.2: Phase compositions due to chemical reaction between aluminosilicate materials and sodium vapor. The phase composition is given as a function of the silica content in the refractory material and the weight fraction of Na(g) relative to the amount of aluminosilicate material.

## 7.5 Application of the Degradation Map

### 7.5.1 Analyses of SPL

The degradation map can be used to predict and interpret experimental investigations of spent pot lining. The starting point in the map is the initial lining composition. In principle, only the silica content is required and trace amounts of other oxides in the lining are neglected.

As an example, a common chamotte brick contains 68 wt%  $\text{SiO}_2$  and 26 wt%  $\text{Al}_2\text{O}_3$  (molar ratio is 4.43:1). This gives a normalized weight ratio of 72:28. Thus the initial composition of the lining corresponds to 72 wt%  $\text{SiO}_2$  and 28 wt%  $\text{Al}_2\text{O}_3$ . A second lining composition of 68 wt%  $\text{SiO}_2$  and 32 wt%  $\text{Al}_2\text{O}_3$  is also used for comparison. The two lining compositions are marked as vertical lines in Fig. 7.3.



**Figure 7.3:** Redrawn from Fig. 7.2 including two examples of initial refractory material composition and corresponding  $\text{Na(g)}$  contents. The remaining labels (a-d), (h), (i), (l) and (m) can either be read from Fig. 7.2 directly or are available in tables [143].

The sodium content in the spent pot lining can be found by chemical analysis. Here, the results from Section 5.2.2 are used. A mean  $\text{Na}$  content of 11 wt% was found near the reaction front in Fig. 5.7. This sodium content is marked by the green horizontal line in Fig. 7.3. A second value of 16 wt% (red horizontal line) was chosen for comparison. This value corresponds to the upper limit of the  $\text{Na}$  content detected in this work. The intersection between 11 wt% sodium and 72 wt% silica predicts the phase composition of the attacked lining. Its point is located in the stability region (g) in Fig. 7.3, where  $\alpha\text{-Al}_2\text{O}_3$ , nepheline ( $\text{NaAlSiO}_4$ ), albite ( $\text{NaAlSi}_3\text{O}_8$ ) and elemental  $\text{Si}$  are the coexisting phases<sup>2</sup>.

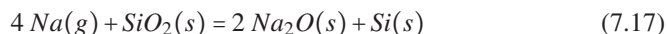
The prediction based on the map can be compared with the phase composition of

the reaction front from Chapter 5.2.2. As expected, neither albite nor  $\alpha$ - $\text{Al}_2\text{O}_3$  were detected by X-ray diffraction, since the former mineral normally does not crystallize and the latter is dissolved in the glass. Albite was present as amorphous or glassy phase in reacted refractory layers of shut down cells.  $\text{NaAlSiO}_4$  and Si were the only detected crystalline phases. This shows a good agreement between autopsy results and the proposed phase composition predicted by the map.

### 7.5.2 Reaction Path in the $\text{Na}_2\text{O}$ - $\text{Al}_2\text{O}_3$ - $\text{SiO}_2$ Phase Diagram

The reaction scheme of the degradation map can also be estimated by using the ternary phase diagram of the system  $\text{Na}_2\text{O}$ - $\text{Al}_2\text{O}_3$ - $\text{SiO}_2$  as shown in Fig. 7.1.

The 11 Alkemade triangles represent the possible three coexisting compounds. Since this diagram is made of oxides, the Na content has to be converted into  $\text{Na}_2\text{O}$  according to Eq. (7.17)

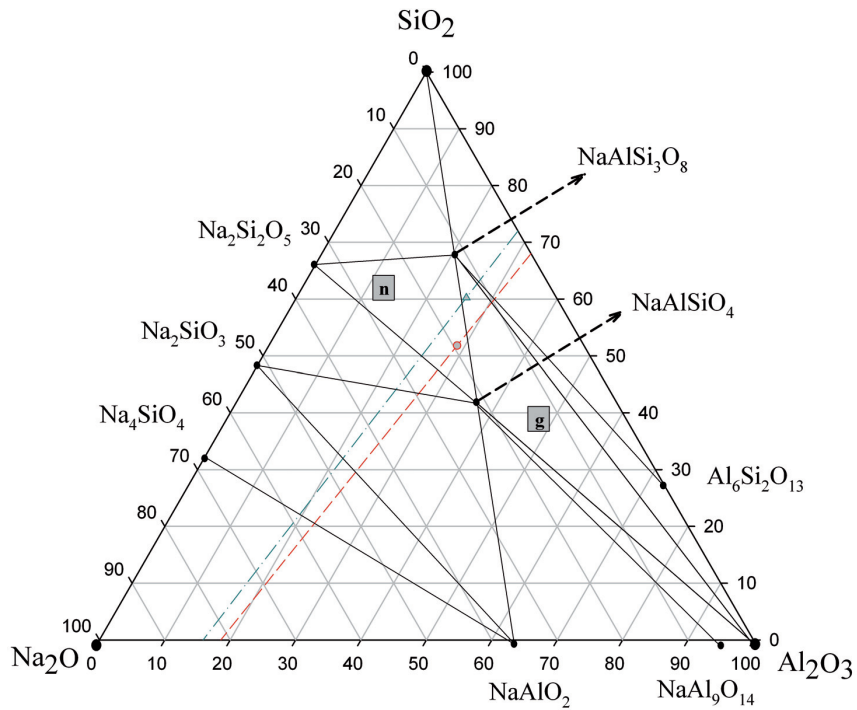


$\text{SiO}_2$  will be reduced by Na to form  $\text{Na}_2\text{O}$  and Si. This conversion is valid for regions in the degradation map where Si metal is produced (*c-p*). In region (*a*) and (*b*) Al as well as Na metal are produced in addition to Si. Refractory compositions with silica contents up to 4.6 wt% are not common. Therefore the focus will be on reaction (7.17). The ternary diagram in question is redrawn in Fig. 7.4 to simplify the illustration of reaction (7.17).

Let us start with the composition of 72 wt%  $\text{SiO}_2$  and 28 wt%  $\text{Al}_2\text{O}_3$ . The experimentally determined content of Na is then used to convert the amount of silica to sodium oxide according to reaction (7.17). The particular composition in the ternary phase diagram is given by the initial alumina content, the produced sodium oxide and on the basis of mass balance of the remaining  $\text{SiO}_2$ . The pristine refractory composition is located at the  $\text{SiO}_2$ - $\text{Al}_2\text{O}_3$  side and the  $\text{Na}_2\text{O}$ - $\text{Al}_2\text{O}_3$  join represents the products, when all silica is consumed. The straight line between the two points represents the path of the sodium attack. Here, 72 wt%  $\text{SiO}_2$  can be fully converted into 84.13 wt%  $\text{Na}_2\text{O}$  and 15.87 wt%  $\text{Al}_2\text{O}_3$ , shown in the  $\text{Na}_2\text{O}$ - $\text{Al}_2\text{O}_3$ - $\text{SiO}_2$  phase diagram in Fig. 7.4 (green line). Dependent on the  $\text{SiO}_2/\text{Al}_2\text{O}_3$  ratio of the raw refractory material the path will shift, as shown by the red line, for the case of 68 wt%  $\text{SiO}_2$  and 32 wt%  $\text{Al}_2\text{O}_3$ . The reactions during Na attack can be found by following the path, which crosses successive Alkemade triangles. The resulting reactions correspond to the reactions summarized above. The intersection of the vertical lines (72 wt% or 68 wt%  $\text{SiO}_2$ ) with the horizontal line of 11 wt% in region (*g*) or with 16 wt% in region (*n*) in Figs. 7.2 and 7.3 can be found as the points shown in Fig. 7.4. Here, equation

<sup>2</sup>The other intersection point between 16 wt% sodium and 68 wt% silica lies in the stability field *g*, where the phase sodium disilicate ( $\text{Na}_2\text{Si}_2\text{O}_5$ ) is present in addition to nepheline, albite and silicon. Like albite, sodium disilicate remains as a glassy phase, which is unlikely to be detected by XRD.





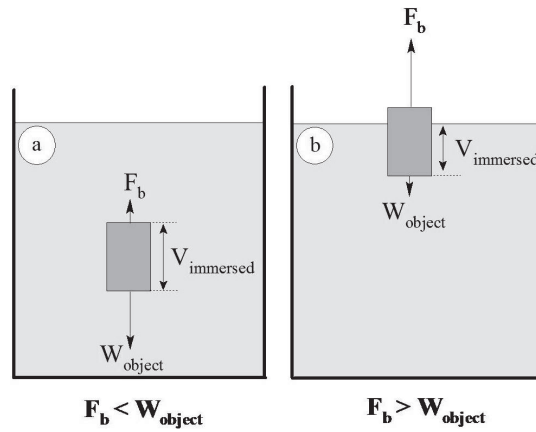
**Figure 7.4:** Redrawn  $\text{Na}_2\text{O}-\text{Al}_2\text{O}_3-\text{SiO}_2$  system from Fig. 7.1 for easier implementation of the degradation path and results from the degradation map.

(7.17) was used to convert Na into  $\text{Na}_2\text{O}$ . It is evident, that both points appear in the appropriate Alkemade triangle. The coexisting products correspond to the ones predicted by the degradation map for sodium attack.

## 8 Cathode Heave Phenomena

### 8.1 Consideration of Buoyancy Force

In this work it is proposed that there is a liquid phase below the cathode carbon, and the typical layering of SPL arises as a combination of operation conditions and cooling period after cell shut down. Thus the cathode heave due to crystallization pressure is not very likely. Buoyancy force has also been suggested as a possible explanation. According to the Archimedes principle, every object immersed in a fluid is buoyed up by a force equal to the weight of the displaced fluid. This phenomenon provides a so-called buoyancy force, which is acting upwards in vertical direction.



**Figure 8.1:** Buoyancy force model: (a) the object is sinking, (b) the object is rising.

The principle is visualized in Fig. 8.1. Considering an object of known density immersed in a liquid. The volume of the object is given by multiplying its length, width and height. Therefore it is possible to calculate the weight of the body  $W_{object}$  [N] by Eq. (8.1)

$$W_{object} = \rho_{object} \cdot V_{object} \cdot g \quad (8.1)$$

This weight is the force acting downwards in vertical direction due to gravity, where  $g$  is the gravitational force (acting vertical, downwards) [ $m/s^2$ ],  $\rho_{object}$  is the density [ $kg/m^3$ ] and  $V_{object}$  is the volume of the object [ $m^3$ ]. The upward or buoyant force  $F_b$  [N] that can be applied by a liquid is calculated by Eq. (8.2)

$$F_b = \rho_{liquid} \cdot V_{immersed} \cdot g \quad (8.2)$$

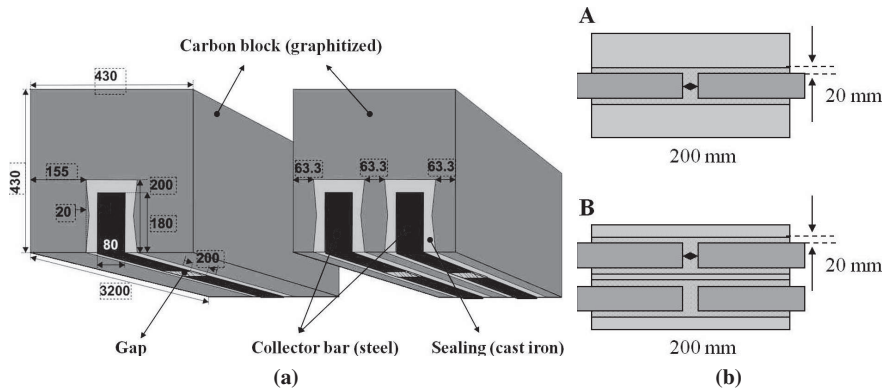
where  $\rho_{liquid}$  is the density of the liquid [ $\text{kg}/\text{m}^3$ ],  $V_{immersed}$  is the volume of a body immersed in the liquid [ $\text{m}^3$ ] and  $g$  is the gravitational force [ $\text{m}/\text{s}^2$ ]. The difference between the two body forces  $W_{object}$  and  $F_b$  is the so called net force  $F_{net,object}$  [N] (Eq. (8.3))

$$F_{net,object} = F_b - W_{object} \quad (8.3)$$

The ratio of the two forces gives information about whether the object will rise ( $F_{net,object} > 0$ ), float ( $F_{net,object} = 0$ ) or sink ( $F_{net,object} < 0$ ).

## 8.2 The Buoyancy Force Acting on the Cathode Block

Depending on the particular cell design the carbon blocks are installed with one or two slots. The full length or split steel collector bars are embedded and sealed with cast iron or ramming paste. Further calculations are based on two common variations, which are denoted as "composite material" illustrated in Figure 8.2.



**Figure 8.2:** Illustration of "composite" material with one and two embedded collector bars, including the dimensions used for the buoyancy force calculation: (a) front view (b) bottom view.

Both cathode blocks are made of graphitized carbon, cast iron sealing and the steel collector bar(s) is/are split with an "empty" gap in between. Material dimensions and densities used in the calculation are listed in Table 8.1. Furthermore, it is assumed that the "composite material" is unrestricted and fully submerged into the liquid bath, which has penetrated through the cathode block during the first days of operation. Here, Eq. (8.3) simplifies to Eq. (8.4) by equating the immersed volume with the volume of the object ( $V_{object} = V_{immersed}$ )

$$F_{net,object} = V_{immersed} \cdot g \cdot (\rho_{liquid}) - \rho_{object} \quad (8.4)$$

The density of the object ( $\rho_{object}$ ) is given by Eq. (8.5)

$$\rho_{object} = \rho_{CC} \cdot X_{CC} + \rho_{CIS} \cdot X_{CIS} + \rho_{SCB} \cdot X_{SCB} \quad (8.5)$$

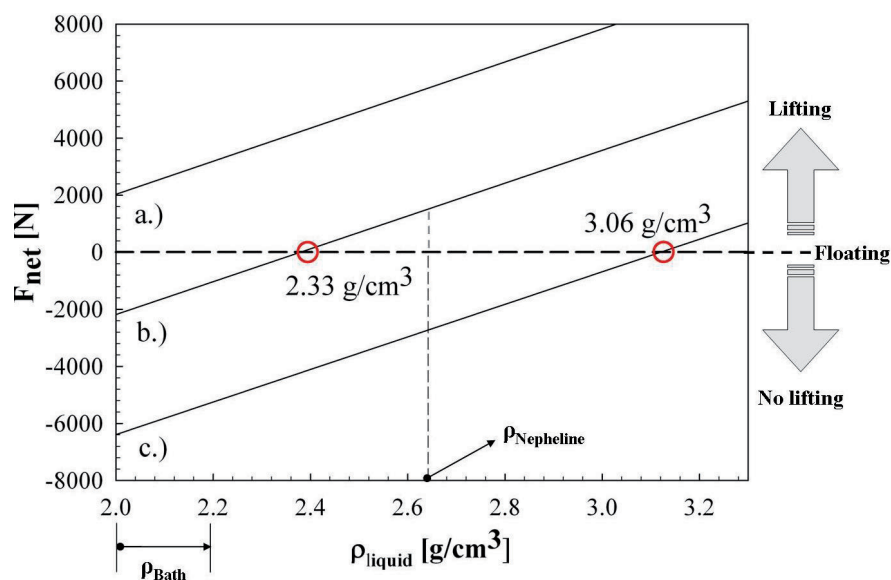
In this equation  $X$  is the volume fraction of the "composite material" given as  $V_{material(CC,CIS,SCB)}/V_{immersed}$ , where the abbreviations CC, CIS and SCB stand for the carbon cathode, the cast iron sealing and the steel collector bar, respectively. The immersed volume and the average densities for the one or the two collector bar case is given in Table 8.1.

**Table 8.1:** Material dimensions and densities used to calculate buoyancy force.

Material	$\rho$ [g/cm <sup>3</sup> ]	$V_{object}$ in [m <sup>3</sup> ]
Carbon Cathode (CC) - for one bar	1.65	0.51
Carbon Cathode (CC) - for two bars	1.65	0.44
Cast Iron Sealing (CIS) - for one bar	7.20	0.03
Cast Iron Sealing (CIS) - for two bars	7.20	0.06
Steel Collector Bar (SCB) (1)	7.85	0.02
Steel Collector Bar (SCB) (2)	7.85	0.09
$V_{immersed}$ for one bar case	2.51	0.59
$V_{immersed}$ for two bar case	3.22	0.58

The calculation based on Eq. (8.4) as function of liquid density is illustrated in Fig. 8.3 and summarized in Table 8.2. The lifting depends on the density of the materials and the density of the liquid. The typical bath density is between 2.00 and 2.20 g/cm<sup>3</sup> at operation temperatures of 1000 °C [1]. They provide upward forces high enough to lift the pure graphitized carbon block as shown in Table 8.2. However, the buoyancy force alone is not sufficient to lift the unrestricted "composite material" with one or two collector bars. An upwards force on the composition material is predicted. The "composite" material is lifted once the liquid density is higher than 2.33 g/cm<sup>3</sup> (one collector bar case) or 3.06 g/cm<sup>3</sup> (two collector bar case). Based on the calculations shown in Table 8.2 there is a lack of at least 0.75–1.58 kN/m<sup>2</sup> (one collector bar) and 3.81–4.64 kN/m<sup>2</sup> (two collector bars) in the net lifting force.

Samples from autopsies were used to measure the density below the cathode as shown in Section 5.4.2 (Table 5.5). A maximum density of 2.9 g/cm<sup>3</sup> was measured. In theory this provides a lifting force of 12.13 kN/m<sup>2</sup> for the one bar case and 12.03 kN/m<sup>2</sup> for the two bar case. Compared with the required numbers in Table 8.2 there is a positive difference of 2.18 kN/m<sup>2</sup> for the cathode with one collector bar, which results in a lifting effect. Common for industrial cells are two collector bars, embedded in the carbon block. There is still a lack of 0.91 kN/m<sup>2</sup>. Thus the force is too little to lift the carbon block alone. FEM simulations were performed in order to analyse the stress level acting on the collector bars and to identify possible forces leading to the observed deformations as shown in Fig. 3.19.



**Figure 8.3:** Estimated force acting on the cathode block as a function of the density of the electrolyte: (a) pure graphitized cathode carbon block with  $\rho = 1.65 \text{ g/cm}^3$ , (b) "composite material" with one collector bar, (c) "composite material" with two collector bars.

**Table 8.2:** Comparison of forces per area resulting from different bath densities.

Composite Material	V [m <sup>3</sup> ]	A [m <sup>2</sup> ]	$\rho_{bath}[\text{g/cm}^3]$	$\sigma$ [kN/m <sup>2</sup> ]
<b>without collector bar</b>	no slot	0.592	2.00	6.96
	one slot	0.586	1.38	6.90
	two slot	0.582	2.20	6.85
<b>one collector bar</b>		0.586	1.38	8.37
			2.20	9.20
at least required			2.33	9.95
<b>two collector bars</b>		0.582	1.38	8.30
			2.20	9.13
at least required			3.06	12.94

## 9 Conclusion Part I

In the first part of the work the deterioration of refractory linings during operation was investigated by means of experimental investigations and construction of a degradation map.

It was shown that the chemical degradation of the refractory lining is initiated by infiltration of sodium into the refractory lining. Two reaction fronts, separated by a distance of 13-19 mm, were identified by line scans using EMPA. The "first reaction front" consisted of only sodium as an attacking species, which is followed by the "second reaction front" made of the bath components. The strong reductive nature of sodium was demonstrated by the presence of Si(s) precipitates in the spent pot lining down to the reaction front. The fact that Si(s) was found down to the reaction front provided an explanation of the nature of sodium transportation in this layer. It was proposed that sodium is transported by ionic diffusion together with charge compensating electrons. The discussion revealed that the viscous diffusion barrier retards the diffusion of  $O^{2-}$  and  $F^{-}$  instead of  $Na^{+}$ , which influences the rate and slows down the deterioration of the refractory material. This is in contrary to earlier explanations where a viscous barrier has been proposed to slow down the degradation due to slow diffusion of sodium.

The sodium is the first attacking agent at the reaction front thus a degradation map of sodium attack was established, inspired by the work of Schøning et al. [11]. This map is significantly more complex with several stability regions. The map provides a qualitative representation of the chemical reactions between alumino-silicate refractories and sodium. This predominance phase diagram was constructed based on the possible reactions predicted from thermodynamics. The degradation map identifies the stable compounds present as a function of  $SiO_2/Al_2O_3$  ratio in the refractory lining and the amount of sodium infiltrated in the lining. The calculation was verified by a comparison with experimental findings. The map is a useful tool to evaluate autopsies and to predict mineralogical changes in the reaction front in SPL.

Simple annealing experiments demonstrated that the layered structure found in autopsies of shut down cells does not only reflect the conditions before the pot was taken out of service. The physical appearance is more likely a combination of operation and crystallization of molten constituents present below the cathode during operation. The thermal gradient in the refractory lining is proposed to be reversed during cooling due to the insulation layer below the refractory layer. This fact is supported through the observation of the melting behaviour of SPL specimens and the needle like shaped NaF crystals grown in gravitational direction from the cathode. Thus crystallization occurs from interface of the cathode lining and downwards. The main secondary phases ( $\beta$ -alumina, nepheline, NaF and Si) were detected by X-ray diffraction and evaluated through Rietveld refinements both in the carbon and lens build-up cross

section of SPL. The results were in line with previous observations.

The thermal conductivity of the SPL was determined by Laser Flash measurements up to 500 °C, and the thermal conductivity data were interpolated to 900 °C using the linear relationship between temperature and inverse thermal conductivity. The measurements revealed that the thermal conductivity decreases with temperature. The thermal conductivity of SPL was increased compared to the virgin material, which reflects the change in density and phase composition, particularly the content of crystalline and amorphous phases. This was also reflected by the measurements of the top and bottom part of the lens build up. The top and the bottom part of the infiltrated carbon block showed minor difference in thermal conductivity, but was significantly higher than the virgin materials. The influence of the increased thermal conductivity of SPL was investigated by simulations of the heat transfer through the lining. The simulations revealed that the overall heat loss of the cathode bottom lining increases but the reduction of the cathode block and the growth of the build-up layer counteract the effect. Moreover, it was also shown that the insulation layer is the most important part for the thermal balance in line with expectations.





## **Part II**

# **Thermo-Mechanical Model of the Cathode Lining**

## 10 The Finite Element Methods

### 10.1 Introduction

The development of the finite element method (FEM) started in the 1950s. It was first used for airframe and structural analysis at the University in Stuttgart (Germany) [144]. Clough was one of the founders of the FEM and he probably coined the term "finite elements" in an article in 1960 [145]. Nowadays, it is a widely used method in science and engineering to model complex phenomena [146].

Partial differential equations (PDE) are applied to describe physical phenomena, but usually the problems addressed are too complex to be solved by the classical analytical method. Therefore, the finite element method (FEM) is used. FEM is nowadays one of the most powerful numerical methods to solve arbitrary PDE in an approximated manner. It is used to evaluate a wide variety of complex chemical and physical engineering problems, such as structural mechanics, heat transfer, fluid dynamics, diffusion, biological and geological processes. The differential or governing equations, which describe the physical problem in question, are assumed to hold over a certain region (in 1D, 2D or 3D). In general, the characteristic feature of the finite element approach is to seek an approximation  $U_N$  to the exact solution  $u$  that satisfies the governing PDE, in the form of Eq. (10.1)

$$u \approx U_N = \sum_{j=1}^n u_j \psi_j + \sum_{j=1}^m c_j \phi_j \quad (10.1)$$

where  $u_j$  are the values of  $U_N$  at the element nodes and  $\psi_j$  are the interpolation functions [146]. The approximation  $U_N$  is a linear combination of the unknown parameters  $c_j$ , which are not associated with the nodes and the known or associated approximation functions  $\phi_j$ .

The advantage and basic idea of FEM to find an approximate solution can be described with three distinct features [146, 147]. First, the physical problem and its governing equation need to be identified. The strong form of the differential equation in question is reformulated into a lower order or so called *weak form*. Afterwards the domain of interest is subdivided into simple shaped and geometrically smaller parts as illustrated in Fig. 10.1. Each part is either called subdomain or finite element. In this context, the term subdomain can have a different meaning. This will be discussed later. The collection of all elements is called a *finite element mesh*, which represents the original geometry and the solution of the problem.

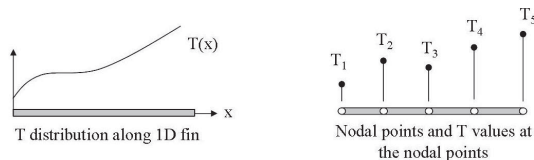


Figure 10.1: Temperature distribution and nodal points along 1D fin, redrawn from [147].

Second, each finite element is treated as an independent domain by itself over which the relations among the field variables are solved or interpolated by the adoption of a rather simple approximation as illustrated in Fig. 10.2. The approximation is usually a polynomial [147] with a finite number of parameters, the so called degrees of freedom (DOF's). This assumes that some of the variables are known at certain points. They are usually located at the boundary of each element and are called *nodal points*. Inserting the approximation into the weak form of the equation generates a system of equations (stiffness matrix form) for the DOF's. Once one element is approximated by the equations used, the corresponding behaviour of each element can then be determined. This can be performed because the approximation made over each element is fairly simple [147] (linear, quadratic, cubic ect.).

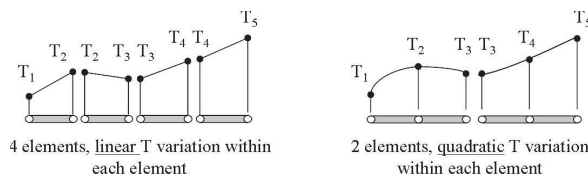


Figure 10.2: The 1D fin is split into elements with either linear or quadratic temperature variation, redrawn from [147].

Third, having determined the behaviour of all elements, the element equations are reconnected or assembled at the nodes using some specific rules (e.g. continuity) as if nodes were pins or drops of glue that hold the entire domain together, shown in Fig. 10.3. This provides the approximated solution to the object's behaviour. Even if the variables vary in a highly non-linear manner over the entire structure, the finite element method assumes a linear variation over each element. Thus the main advantage of this procedure is the simplification of complex functions through a set of simple polynomials.

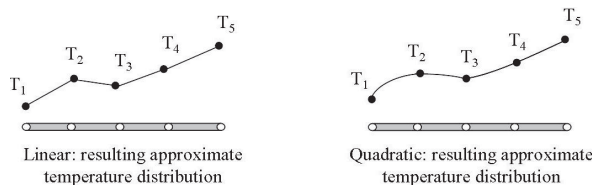
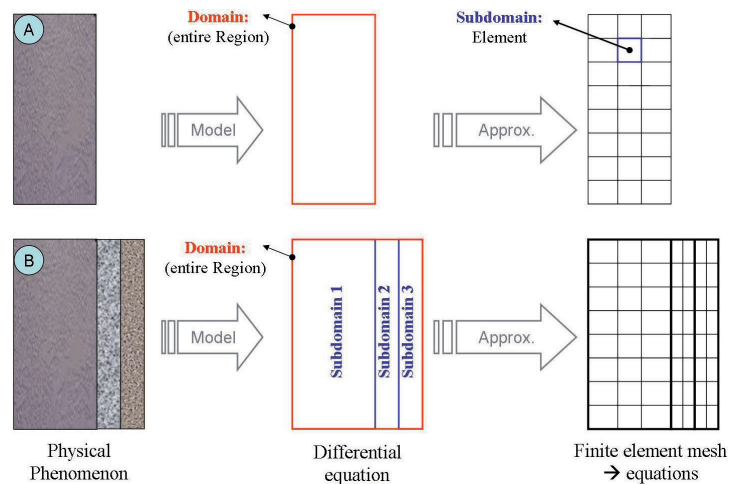


Figure 10.3: Resulting approximate temperature distribution along the 1D fin, redrawn from [147].

As mentioned before the term subdomain has a twofold definition and should not be misinterpreted as shown in Fig. 10.4. The definition under *B* in this figure is preferred. Most systems considered in engineering fields involve a tremendous number of unknowns and they cannot be solved analytically. Therefore, the FEM relies entirely on the availability of efficient computers and suitable software.



**Figure 10.4:** Illustration of modelling steps in engineering mechanics analysis. The term subdomain is referred to A: the elements in the mesh, B: the different parts/materials of the physical problem/geometry, the mesh is an independent term.

## 10.2 COMSOL - A Software Based on FEM

COMSOL (formerly FEMLAB) is a powerful engineering tool that performs equation-based multiphysics modelling in an interactive environment. It is designed to model and solve all kinds of scientific and engineering problems based on partial differential equations (PDE) [148]. The software provides built-in physics modes to build models by means of defining the relevant physical quantities (e.g. material properties, loads and constraints) rather than by writing the underlying equations directly. COMSOL then internally compiles a set of PDE representing the entire problem. It also allows to create equation-based models. By providing these multiple modeling approaches the software power can be accessed in two ways. Either through a flexible self-containing graphical user interface or from scripting in MATLAB language via Live-link™ [148].

The underlying mathematical structure of COMSOL is a system of partial differential equations. The PDE can be entered directly as coefficient form (linear or nearly linear problems), general form (nonlinear problems) or weak form. The capability of the COMSOL Multiphysics basic version can be expanded by 12 add-on and 2 support modules [149]. Each add-on tool or module, which represents an area in physics, consists of predefined templates and a user interface already set up with specific

equations and variables. By combining any number of these application tools into a single problem description, it is possible to model a multi-physics problem. When solving the PDE that describe a model, COMSOL applies the proven finite element method (FEM). It runs this method together with adaptive meshing and error control as well as with a variety of numerical solvers [148]. COMSOL Multiphysics version 3.5a is used in the present work in combination to the following two application modes:

- ◆ Structural Mechanics Module
- ◆ Heat Transfer Module

### 10.3 Calculation of the Thermal Field

#### 10.3.1 Governing Equation

The heat transfer is commonly described as the movement of energy from a higher-temperature to a lower-temperature object due to a temperature difference until thermal equilibrium is reached. Heat transfer can occur by conduction, convection and radiation. For the 2D thermal field simulation the transient, general heat transfer module in COMSOL (3.5a) was used embedded in the add-on Heat Transfer application.

The partial differential or governing Eq. (10.2) for pure conductive heat transfer in a solid is valid over the whole domain if the velocity is set to zero

$$\rho C_p \frac{\partial T}{\partial t} + \nabla \cdot (-k \cdot \nabla T) = Q \quad (10.2)$$

Here,  $\rho$  is the material density [ $\text{kg}/\text{m}^3$ ],  $C_p$  is the heat capacity at constant pressure [ $\text{J}/(\text{kg}\cdot\text{K})$ ],  $T$  is the absolute temperature [ $\text{K}$ ],  $t$  is time [ $\text{s}$ ],  $\partial T/\partial t$  is the partial derivative with respect to time,  $k$  is the thermal conductivity [ $\text{W}/(\text{m}\cdot\text{K})$ ],  $\nabla$  is the nabla-operator,  $\nabla T$  is the temperature gradient [ $\text{K}/\text{m}$ ] and  $Q$  is the inner heat-generation [ $\text{W}/\text{m}^3$ ]. According to the definition of the nabla-operator Eq. (10.2) in 2D takes the form

$$\rho C_p \frac{\partial T}{\partial t} = - \left( \frac{\partial q_x}{\partial x} + \frac{\partial q_y}{\partial y} \right) + Q \quad (10.3)$$

where  $q_x$  and  $q_y$  are the components of heat flow [ $\text{W}/\text{m}^2$ ]. The components are expressed by Fourier's law of heat conduction Eq. (10.4)

$$\left. \begin{array}{l} q_x = -k \frac{\partial T}{\partial x} \\ q_y = -k \frac{\partial T}{\partial y} \end{array} \right\} q = -k \nabla T \quad (10.4)$$

where  $\partial T/\partial x$  and  $\partial T/\partial y$  are the temperature gradients [K/m] and  $k_x$  and  $k_y$  the thermal conductivities [W/(m·K)] in x- and y-direction, respectively. If no inner heat is generated Eq. (10.3) can be simplified to Eq. (10.5)

$$\rho C_p \frac{\partial T}{\partial t} = \frac{\partial}{\partial x} \left( k_x \frac{\partial T}{\partial x} \right) + \frac{\partial}{\partial y} \left( k_y \frac{\partial T}{\partial y} \right) \quad (10.5)$$

In this module the Lagrange-quadratic element type and the linear system solver (UMFPACK direct) were chosen.

### 10.3.2 Subdomain Settings

In the subdomain settings the material properties such as the density, heat capacity and thermal conductivity were specified. The thermal conductivity  $k$  describes the relationship between heat flux vector  $q$  and the temperature gradient  $\nabla T$  shown by Eq. (10.4). The density, thermal conductivity and the heat capacity can be imported either as constants or temperature dependent functions. It is necessary to specify initial and boundary conditions to get a unique temperature distribution. The initial condition describes a temperature field  $T=f_{x,y,z}$ , when the time is equal to 0.

### 10.3.3 Boundary Conditions

In COMSOL Multiphysics only one generalized boundary condition for general, convective and radiative heat flux exists as given in Eq. 10.6

$$n \cdot (k \nabla T) = q_0 + \underbrace{h(T_{\text{inf}} - T)}_{\text{convection}} + \underbrace{\varepsilon \sigma (T_{\text{amb}}^4 - T^4)}_{\text{radiation}} \quad (10.6)$$

where  $q_0$  is the inward heat flux [W/m<sup>2</sup>],  $h$  is the heat transfer coefficient [W/(m<sup>2</sup>·K)],  $T_{\text{inf}}$  is the reference or external temperature [K],  $T_{\text{amb}}$  is the ambient temperature [K],  $\varepsilon$  is the emission coefficient, which is a dimensionless number in the range of  $0 \leq \varepsilon \leq 1$  and  $\sigma$  is the Stefan-Boltzmann constant [W/(m<sup>2</sup>·K<sup>4</sup>)].

The boundary condition can be divided into two fundamental types. The first one is of Dirichlet type and is called specified temperature, which defines a temperature at the boundary ( $T=T_0$ ). The second boundary type is called Neumann condition and defines the inward heat flux  $q_0$  [W/m<sup>2</sup>] normal to the boundary. It originates from external sources and is defined as the inner product of the conductive heat flux vector  $q$  [W/m<sup>2</sup>] shown in Eq. (10.7) and the normal vector  $n$  of the boundary (points out from the domain). As mentioned before the velocity is set to 0, thus the second term in Eq. (10.7) disappears

$$q = -k \nabla T + \rho C_p u T \quad (10.7)$$

### Insulation/Symmetry

The condition  $n \cdot (k \nabla T) = 0$  or  $q_0 = 0$  is called thermal insulation or symmetry. The latter is introduced to reduce the model size. It specifies that the gradient across the boundary must be zero. To fulfill that requirement, the temperature must be equal on both sides of the boundary in question. No heat can be transferred because there is no temperature difference.

### Heat Flux

The inward heat flux  $q_0$  is normally described as the sum of the different heat transfer processes. Thus it is convenient to split Eq. (10.6) to (10.8) [150]

$$-n \cdot q = q_0 + q_r + q_s + h(T_{\text{inf}} - T) \text{ on } \partial\Omega \quad (10.8)$$

Selecting the heat flux boundary condition gives access to all the terms in Eq. (10.8). The parameter  $q_r$  represents the net influx from radiation [ $\text{W}/\text{m}^2$ ] and  $q_s$  is devoted to the energy transferred from other parts of the boundary through a thin highly conductive shell [ $\text{W}/\text{m}^2$ ] in contact with the boundary. The last term is a product of the heat transfer coefficient  $h$  [ $\text{W}/(\text{m}^2 \cdot \text{K})$ ] and the difference between the surface temperature  $T$  [ $\text{K}$ ] and a reference bulk temperature  $T_{\text{inf}}$  [ $\text{K}$ ].

COMSOL provides a material library of predefined heat transfer coefficients  $h$  for common flow and geometrical situations. The library covers all categories of convection: Laminar and turbulent flow, natural and forced type of convection and dependent on the geometrical conditions the internal or external convection. The Heat Transfer Module allows two different settings for the radiosity: *Surface-to-ambient radiation* and *surface-to-surface radiation* [151].

### Continuity

The default setting for the interior boundaries, between subdomains (inside the structure) is *continuity*. If no heat source (or sink)  $Q$  is present, condition  $-n_1 \cdot (q_1 - q_2)$  becomes 0. In this case the heat flux in normal direction is continuous across the boundaries. The temperature is always continuous due to the continuity of the finite element field.

## 10.4 Calculation of the Thermal-Stress Field

### 10.4.1 Governing Equation

The analysis of thermal stresses in general includes two steps. One is the time-dependent heat transfer, where the temperature distribution at various time stages is

calculated. The other is the thermal stress analysis, which uses the results obtained from the first step to carry out the stress analysis. Since the temperature is time-dependent, the thermal stress is time-dependent as well. Coupled heat transfer and thermal stress simulations were performed in 2D, using the transient, plain strain module in COMSOL (3.5a), which is embedded in the add-on application named structural mechanics.

In general, the stress on an object is the measure of force per unit area. In 2D it is described by the stress tensor  $\sigma$  with normal ( $\sigma_{xx}$ ,  $\sigma_{yy}$ ) and shear  $\tau_{xy}$  stresses, defined in Eq. (10.9)

$$\sigma = \begin{bmatrix} \sigma_{xx} & \tau_{xy} \\ \tau_{yx} & \sigma_{yy} \end{bmatrix} \quad \tau_{xy} = \tau_{yx} \quad (10.9)$$

where the stress is typically expressed in [Pa].

### Strain-Displacement Relationship

Stress transfer takes place within and on the boundaries of a solid object. Besides the stress in a body also its deformation needs to be considered. In the finite element methods, it is possible to describe the strain conditions by components of the displacement vector  $\mathbf{u}$ , which are the primary unknowns. They vary over space and are denoted as  $(u, v)$  in x, y-directions respectively as shown in Eq. (10.10)

$$\epsilon_x = \frac{\partial u}{\partial x} \quad \epsilon_y = \frac{\partial v}{\partial y} \quad (10.10)$$

where  $\epsilon_x$  and  $\epsilon_y$  are the normal strain in x- and y-direction, respectively. Their derivatives  $\partial u/\partial x$  and  $\partial v/\partial y$  or so called displacement gradients are dimensionless quantities, often expressed as [m/m]. Having obtained a description of stresses in a body, the multiple components of the displacement gradients are combined into alternate forms called *shear strains*, according to Eq. (10.11)

$$\epsilon_{xy} = \frac{\gamma_{xy}}{2} = \frac{1}{2} \left( \frac{\partial u}{\partial y} + \frac{\partial v}{\partial x} \right) \quad (10.11)$$

Strain, often referred as the effect of stress, is defined as the change in dimension per unit length. In 1D the normal strain is a ratio of change in length over the original length. In 2D, both normal and the shear strain components exists, given from the deformation [152]. The former involves only the part of the gradient terms parallel to the displacement component as shown in Eq. (10.10). The shear strain causes a change in shape and involves a combination of the gradient components that are perpendicular to the displacement components, shown in Eq. (10.11). In brief, to express the shear strain in 2D, either the tensor ( $\epsilon_{xy}$ ) or engineering ( $\gamma_{xy}$ ) form, see (10.12) is applied. The plane strain application mode assumes that  $\epsilon_z$ ,  $\epsilon_{yz}$  and  $\epsilon_{xz}$  components of the strain tensor are zero [153]



$$\boldsymbol{\varepsilon} = \begin{bmatrix} \varepsilon_{xx} & \gamma_{xy} \\ \gamma_{yx} & \varepsilon_{yy} \end{bmatrix} \quad \gamma_{xy} = \gamma_{yx} \quad (10.12)$$

The total strain in a thermal stress analysis includes three main parts: The thermal strain, the elastic, plastic or classical creep strain and the initial strain. They are caused by the change in temperature, microstructure or chemical composition and by applying an external stress, respectively. The free thermal strain  $\boldsymbol{\varepsilon}_0$  is expressed by a linear function of temperature and thermal expansion coefficient  $\alpha$  [1/K], defined in Eq. (10.13)

$$\boldsymbol{\varepsilon}_{th} = \alpha \underbrace{(T - T_0)}_{\Delta T} \quad (10.13)$$

where  $T_0$  defines the initial temperature [K]. COMSOL uses the term  $Temp_{ref}$ . The creep strain, unlike to the free thermal strain, is also a function of stress and time. COMSOL does not provide a build-in function to describe creep. By establishing a self written PDE formulation for thermally induced creep stresses it is possible to insert creep using the PDE mode of COMSOL Multiphysics.

### Stress-strain relationship

Like in the general heat transfer case the strains need to be multiplied by a material property to define the physical quantity the stress. In general, the relation between stress and strain for linear conditions, in presence of external forces is described by the Hook's law, known as Eq. (10.14)

$$\boldsymbol{\sigma} = \mathbf{E} \cdot \boldsymbol{\varepsilon} \quad (10.14)$$

The term  $\mathbf{E}$  is the square material matrix, which contains the elastic modulus  $E$  or Young's modulus and  $\nu$ , which is the contraction in perpendicular direction, known as Poisson's ratio of the material. For  $\mathbf{E}$  the expression elasticity matrix  $\mathbf{D}$  and the more basic inverse flexibility or compliance matrix  $\mathbf{D}^{-1}$  is used in COMSOL. It is defined differently for isotropic, orthotropic and anisotropic materials. The theory can be found in [152, 153]. Here, isotropic material behaviour will be in focus. The stress-strain relationship or Hook's law is given in compliance (Eq. 10.15) and in elasticity or so-called stiffness form (10.16)

$$\begin{bmatrix} \varepsilon_{xx} \\ \varepsilon_{yy} \\ \gamma_{xy} \end{bmatrix} = \underbrace{\frac{1}{E} \begin{bmatrix} 1 & -\nu & 0 \\ -\nu & 1 & 0 \\ 0 & 0 & 2(1+\nu) \end{bmatrix}}_{\mathbf{D}^{-1}} \begin{bmatrix} \sigma_{xx} \\ \sigma_{yy} \\ \tau_{xy} \end{bmatrix} \quad (10.15)$$

$$\begin{bmatrix} \varepsilon_{xx} \\ \varepsilon_{yy} \\ \gamma_{xy} \end{bmatrix} = \underbrace{\frac{E}{(1+\nu)(1-2\nu)}}_D \begin{bmatrix} 1-\nu & \nu & 0 \\ \nu & 1-\nu & 0 \\ 0 & 0 & \frac{1-2\nu}{2} \end{bmatrix} \begin{bmatrix} \sigma_{xx} \\ \sigma_{yy} \\ \tau_{xy} \end{bmatrix} \quad (10.16)$$

The two dimensional equations for isotropic materials including the free thermal expansion are denoted as Eqs. 10.17, 10.18 and 10.19

$$\varepsilon_x = \frac{1}{E}\sigma_x - \frac{\nu}{E}\sigma_y + \alpha_{th}\Delta T \quad (10.17)$$

$$\varepsilon_y = -\frac{\nu}{E}\sigma_x + \frac{1}{E}\sigma_y + \alpha_{th}\Delta T \quad (10.18)$$

$$\gamma_{xy} = -\frac{2(1+\nu)}{E}\tau_{xy} \quad (10.19)$$

where  $\alpha_{th}$  is the thermal expansion coefficient and  $\Delta T$  is the temperature change (in COMSOL written as  $\Delta T = T - Temp_{ref}$ ).

### Isotropic, Linear Elastic and Non-linear Elasto-Plastic Material Models

In COMSOL the stress-strain relationship or so called constitutive equation for linear conditions can be expressed by Eq. (10.20)

$$\boldsymbol{\sigma} = D\boldsymbol{\varepsilon}_{el} + \boldsymbol{\sigma}_0 - lp_i \quad (10.20)$$

where  $\boldsymbol{\sigma}_0$  and  $p_i$  denotes the initial states of stress and pressure. The total strain  $\boldsymbol{\varepsilon}$  contains an elastic ( $\boldsymbol{\varepsilon}_{el}$ ), a thermal ( $\boldsymbol{\varepsilon}_{th}$ ) and an initial ( $\boldsymbol{\varepsilon}_0$ ) part. For non-linear elasto-plastic materials, Eq. (10.21) is extended with a fourth term, the plastic strain ( $\boldsymbol{\varepsilon}_{pl}$ )

$$\boldsymbol{\varepsilon} = \boldsymbol{\varepsilon}_{el} + \boldsymbol{\varepsilon}_{th} + \boldsymbol{\varepsilon}_0 + \boldsymbol{\varepsilon}_{pl} \Rightarrow \boldsymbol{\varepsilon}_{el} = \boldsymbol{\varepsilon} - \boldsymbol{\varepsilon}_{th} - \boldsymbol{\varepsilon}_0 - \boldsymbol{\varepsilon}_{pl} \quad (10.21)$$

Equation (10.20) and (10.21) can be combined to Eq. 10.22

$$\boldsymbol{\sigma} = D \cdot (\boldsymbol{\varepsilon} - \boldsymbol{\varepsilon}_{th} - \boldsymbol{\varepsilon}_0 - \boldsymbol{\varepsilon}_{pl}) + \boldsymbol{\sigma}_0 - lp_i \quad (10.22)$$

Like mentioned above the square elasticity matrix  $D$  changes according to the different material properties available. The stress and strain are given in the form of columnar vectors, see Eqs. 10.15 and 10.16. The difference between the nonlinear and the linear models is the variable  $\boldsymbol{\varepsilon}_{pl}$  and a vector  $\boldsymbol{\kappa}$  of state parameters, which describes the state of a plastic deformation. This vector is defined differently depending on the material.

The mathematical treatment according to the different material properties will not be given here and can be consulted in [153].

### Von Mises Stress

At any point within the body there are stresses acting in different directions, and the direction and magnitude of stresses changes from point to point. The Von Mises criterion is a formula to calculate whether the stress combination at a given point will cause deformation [153]. There are two *principal stresses* that can be calculated at any point, acting in the x and y directions, which are the principal axes. *Von Mises* stated that, even though none of the principal stresses exceeds the yield stress of the material, it is possible to overcome the yield stress as a result from the combination of stresses. Thus the *Von Mises* criteria is a formula for combining the two stresses into an equivalent or so-called *Von Mises stress* [154]. Basically it is not really a stress. It is considered to be an index, which can be used as comparison to the yield stress of the material. The yield stress is a known material property, which is usually considered to be the failure stress. If the "Von Mises Stress" exceeds the yield stress, then the material is considered to be at failure condition or under deformation.

### 10.4.2 Subdomain Settings

The material properties, their variations, initial constraints and loads (force applied to the structure) can be specified more precisely by using the incorporated subdomain settings dialog box. For thermal stress analysis in addition to the density, the thermal expansion coefficient [1/K], the Poisson's ratio and the Young's modulus [Pa] are necessary material characteristics.

An additional feature of the load tab is to enable the thermal expansion. This requires the coupling of the general heat transfer and the plane strain module by setting the strain temperature  $T = T_{thermal\ model}$ , as shown in Eqs. (10.17) and (10.18).

### 10.4.3 Boundary Conditions

An important aspect of the structural analysis is the formulation of applied forces ( $F_x$  and  $F_y$  in  $[N/m]$  or  $[N/m^2]$ ) and proper constraints. Together they form the boundary conditions of a model. Symmetry is used in many cases, which greatly reduces the model size and hence the memory requirements. This follows the same principle like in the thermal model. The Structural Mechanics Module provides various types of predefined constraints, such as free, fixed, prescribed displacements, ect. [152].

## 10.5 Implementation of Chemical Expansion

COMSOL provides no predefined tool for implementing chemical expansion. Thus to simulate the thermal and sodium expansion of the carbon cathode, the two dimensional

equations for isotropic material (discussed in Section 10.4.1) were expanded by the term  $\alpha_{ch}\Delta C$  as shown in Eq. (10.23) and (10.24)

$$\varepsilon_x = \frac{1}{E}\sigma_x - \frac{\nu}{E}\sigma_y + \alpha_{th}\Delta T + \alpha_{ch}\Delta C \quad (10.23)$$

$$\varepsilon_y = -\frac{\nu}{E}\sigma_x + \frac{1}{E}\sigma_y + \alpha_{th}\Delta T + \alpha_{ch}\Delta C \quad (10.24)$$

where  $\alpha_{ch}$  is the chemical or sodium expansion coefficient [ $\text{m}^3/\text{mol}$ ] and  $\Delta C$  is the difference between initial  $C_{0,Na}$  and the saturation concentration  $C_{Sat,Na}$  of sodium in carbon [ $\text{mol}/\text{m}^3$ ]. The COMSOL code was rewritten<sup>1</sup> by introducing the second term in Eq. (10.25)

$$p = -K \cdot (evol) - \left[ 3 \cdot \alpha_{th}(\Delta T) \quad \underbrace{+ 3 \cdot \alpha_{ch}(\Delta C)}_{\left( (C_{Na} \text{ as } f(t) \text{ until } C_{Sat,Na}) - C_{0,Na} \right)} \right] \quad (10.25)$$

where  $p$  is the pressure [Pa],  $evol$  is the volumetric strain [m/m], defined in Eq. (10.23) and  $K$  is the bulk modulus [Pa]

$$evol = \varepsilon_x - \varepsilon_y \quad (10.26)$$

The bulk modulus of an object measures the object's resistance to uniform compression. In general it is defined as the pressure increase needed to cause a decrease in volume, see Eq. (10.27)

$$K = \frac{E}{3(1-2\nu)} \quad (10.27)$$

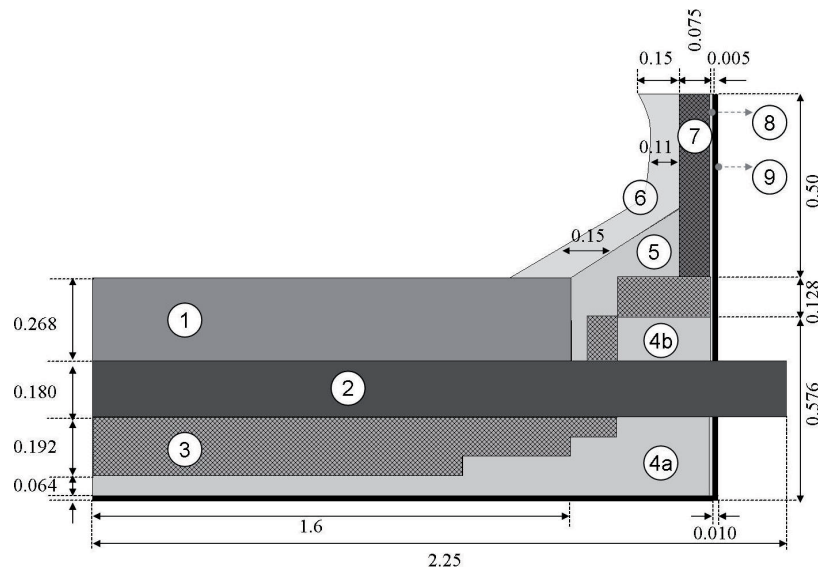
---

<sup>1</sup>For completeness the expression for the entropy  $Ent$  [ $\text{J}/(\text{m}^3 \cdot \text{K})$ ] was reformulated as shown in the Appendix B.1 Eq. (1). This had no influence to the simulation described here. The meaning of  $imag(E)$  is important in the frequency dependent analysis, when losses need to be included in the Young's modulus [155].

# 11 FEM Simulation of Cathode Lining

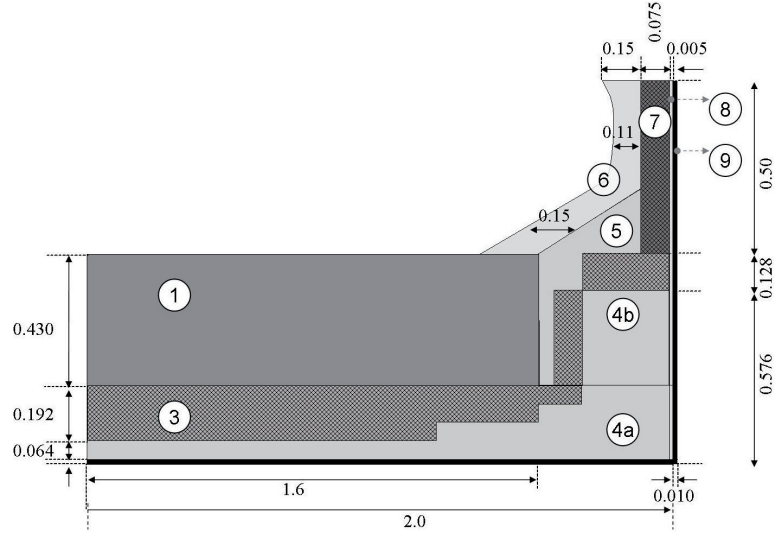
## 11.1 The Cell Model

A common potshell dimension of an aluminium electrolysis cell is 4 x 12 m. Fig. 11.1 shows a schematic 2-dimensional drawing of the cross section of the short side. Due to symmetry it was not necessary to model the entire geometry and only half of the cross section is shown.



**Figure 11.1:** 2D half cell of a common cathode lining in aluminium reduction cells. The dimensions are given in [m]. This includes: (1) cathode block (GC), (2) steel collector bar (S235JRG2), (3) refractory (chamotte), (4) insulation with two qualities (4a) and (4b), (5) ramming paste, (6) sideledge, (7) SiC sidewall block, (8) mortar, (9) steel shell

The present cell design included the carbon cathode block, the collector bar, the refractory and the insulation materials, the ramming paste, the side crust or ledge and finally the sideling. The entire structure is constrained in a steel shell. All dimensions were related to industrial norms except the carbon cathode block (in reality y direction = 0.450 m), like shown in Fig. 11.1. This is because a 2-dimensional model has the weakness that structural details cannot be modelled. Therefore, the collector bar is often not included [119]. Here, the cathode lining in two 2D models were studied. One included the collector bar (Fig. 11.1) and the other was without (Fig. 11.2).



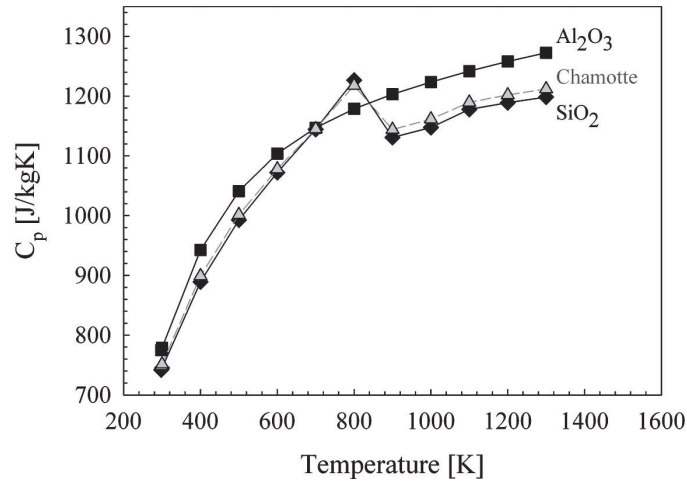
**Figure 11.2:** 2D half cell of a common cathode lining in aluminium reduction cells without the steel collector bar (2) shown in Fig. 11.1. The dimensions are given in [m]. This includes: (1) cathode block (GC), (3) refractory (chamotte), (4) insulation with two qualities (4a) and (4b), (5) ramming paste, (6) sideledge, (7) SiC sidewall block, (8) mortar, (9) steel shell

## 11.2 Material Properties

The thermal expansion and heat capacity used in the model are listed in Table B.20 and B.21 [76, 156] in Appendix B. The chemical composition, as shown in Table B.18 in Appendix B was used to calculate the heat capacity  $C_p$  of each material according to Eq. (11.1)

$$C_p(T) = X_A \cdot C_{pA}(T) + X_B \cdot C_{pB}(T) + \dots \quad (11.1)$$

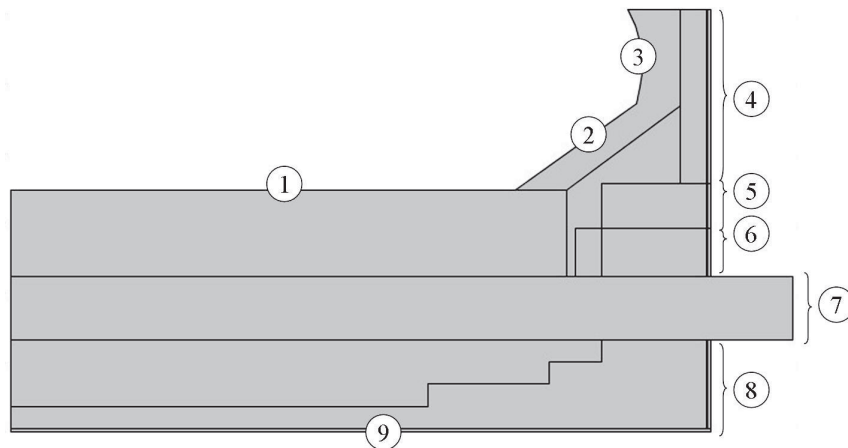
where  $X_{A,B}$  denotes the mole fraction and  $C_{pA,B}$  [J/(kg·K)] thermal conductivity of each component involved. The refractory material in Fig. 11.3 was chosen as an example. The thermal conductivity and the heat capacity were imported as temperature dependent functions. The density was kept constant and independent of temperature. The temperature-dependent material constants, like the heat capacity and the thermal conductivity for most of the materials in the heat transfer module were accessed from literature. In contrast the physical properties required for the transient thermal stress analysis, such as thermal expansion coefficient, Poisson's ratio and Young's modulus were allowed to vary with temperature only if the data was available. The thermal expansion coefficient, Poisson's ratio and Young's modulus are listed in Table B.23 and B.24 in Appendix B for each material.



**Figure 11.3:** Calculation of the heat capacity of chamotte containing mainly 68 wt% SiO<sub>2</sub> and 26 wt% Al<sub>2</sub>O<sub>3</sub>. The data was taken from [76].

### 11.3 Constraints and Simplifications

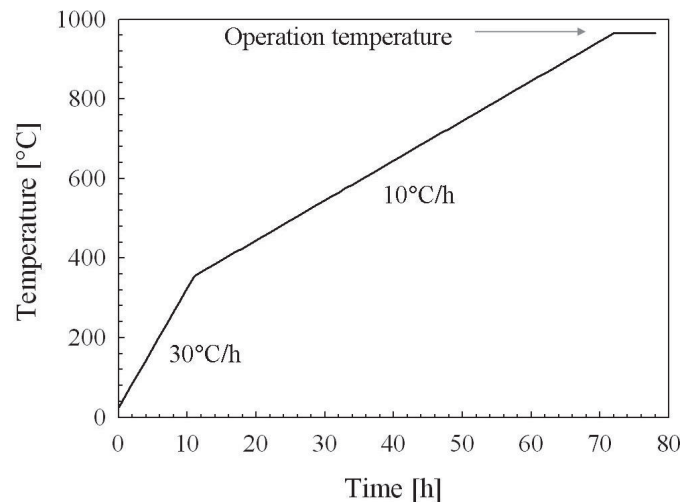
To establish the models the following simplifications and constraints were introduced. Some of these involve boundary and material settings and others the restrictions of the model. The numbering and position of the boundaries in question are shown in Fig. 11.4.



**Figure 11.4:** Numbering of outer boundaries.

## Thermal Model

- ◆ Each layer in the cathode lining was made of a homogeneous and isotropic material.
- ◆ Inside the cell the heat transfer was only allowed by conduction only.
- ◆ The physical properties of each material, such as the thermal conductivity and the specific heat, were dependent on temperature.
- ◆ The material densities were constant and independent of the temperature.
- ◆ Insulation/symmetry condition was set at the symmetry plane of the half cell model and at the top of the sidewall block.
- ◆ The initial temperature conditions were set to 298.15 K which describes a temperature field  $T=f_{x,y,z}$  at room temperature, when the time is equal to 0.
- ◆ In industrial cells the outer surfaces of the steel shell and collector bar ends are surrounded by the cooling fluid air. The heat transfer at the bottom and the sidewall surface with the surrounding was therefore described as air convection with the steel shell and radiation. The heat transfer coefficient  $h$  for *external* and *natural convection with air* along vertical and horizontal planes with defined convection length scale [150] was chosen for the outer boundaries 4-9 in Fig. 11.4. The surface emissivity  $\varepsilon$  and the ambient temperature were set to 0.8 and 298.15 K, respectively. The outside air temperature was assumed to be constant.
- ◆ The temperatures at the carbon block and the sideledge surface followed a preheating curve, shown in Fig. 11.5, until a uniform operation temperature of 960 °C at the sideledge (boundaries 2 and 3 in Fig. 11.4) and 965 °C at the cathode surface were reached (boundary 1 in Fig. 11.4).



**Figure 11.5:** Preheating curve used in the two models for the boundaries 1-3 shown in Fig. 11.4.



## Thermal-Stress Model

- ◆ The physical properties, such as thermal expansion coefficient and the E-modulus of each material were allowed to vary with temperature if data was available.
- ◆ The Young's modulus of the collector bar at room temperature (Table B.24 in Appendix B) was chosen.
- ◆ Creep was not considered.
- ◆ The outer boundaries 4-9 in Fig. 11.4 were either fixed or were allowed to move/deform.
- ◆ The weight of 20 cm bath in addition to 20 cm metal pad, a maximum bath density of 2.2 g/cm<sup>3</sup> [1] and the metal pad density of 2.7 g/cm<sup>3</sup> [5] were used to calculate the force of 9600 N/m<sup>2</sup> acting on the cathode surface or boundary 1 (Fig. 11.4) in the gravitational direction. The same principle was applied at the side crust/ramming paste surface or boundary 2 in Fig. 11.4. Here, only 20 cm bath were used to receive a force of 4300 N/m<sup>2</sup>. The dimensions used to estimate the gravitational forces are shown in Figs. B.14 and B.15 in Appendix B.
- ◆ COMSOL Multiphysics automatically connects the geometry, mesh, and physics at the interior interfaces (intersection between the different materials or subdomains). This setting was chosen for the present simulation because a manual connection required the knowledge of all properties at the interior boundaries. The disadvantage of this approach is that the cell design is a composite geometry, meaning the different materials act like one material or block.

## Implementation of Chemical Expansion

In addition to the thermal expansion, the carbon blocks will expand due to the absorption of sodium. As shown in Chapter 10.5 modifications of the already built-in strain equations were performed to simulate the chemical expansion. Due to computational limitations the following simplifications concerning the cathode material behaviour and sodium uptake were required:

- ◆ The graphitized cathode material was considered to be isotropic [157]
- ◆ The swelling of the carbon was proportional to the sodium content [3]
- ◆ Creep deformation of the carbon material was neglected

Data used for implementing the chemical expansion in the present model for graphitized carbon material are summarized in Table 11.1. The expansion at the saturation concentration  $\epsilon_{C_{Sat,Na}}$  is based on reported data for graphitized material [8]. The amount of sodium in carbon [mol/m<sup>3</sup>] at saturation concentration ( $C_{Sat,Na}$ ) of 2 wt% was calculated for a common carbon block dimension of 43×43 cm, which was also used for diffusion simulations performed by Wang et al. [30]. The time to reach sodium

saturation ( $t_{C_{Sat,Na}}$ ) was set arbitrarily, since the influence of creep in the cathode and collector bar material were neglected. From the data in Table 11.1 the chemical expansion coefficient  $\alpha_{ch}$  turned out to be  $2 \cdot 10^{-6}$  [8].

**Table 11.1:** Data used for chemical expansion calculation [8].

Carbon quality	$C_{0,Na}$ [mol/m <sup>3</sup> ]	$C_{Sat,Na}$ [wt%]	$C_{Sat,Na}$ [mol/m <sup>3</sup> ]	$\epsilon_{C_{Sat,Na}}$ [%]	$t_{C_{Sat,Na}}$ [days]
Graphitized	0	2	1435	0.25	25

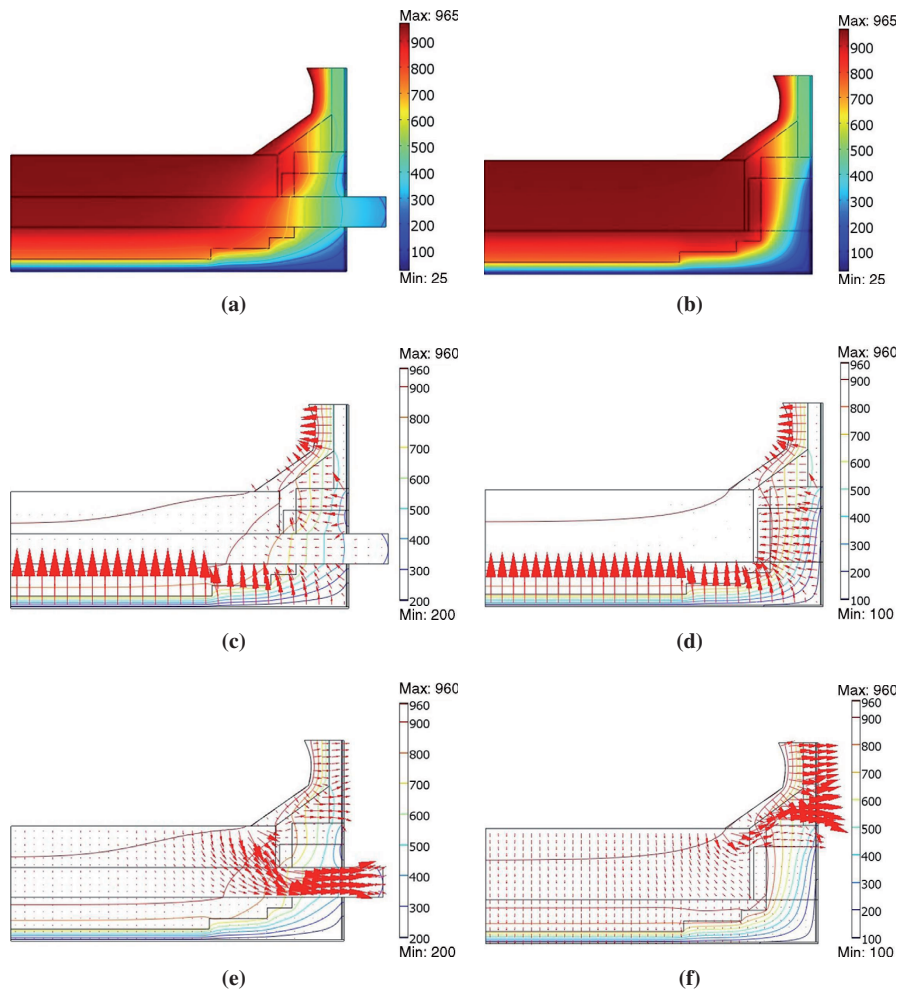
## 11.4 Results

### 11.4.1 The Thermal Gradient in the Cathode

The simulations of the general heat transfer from the preheating period to the operation conditions of the two half cells (with and without collector bar) were performed by the time-dependent solver in COMSOL. A comparison of both models in terms of the temperature distributions, given as surface and contour plots at the steady state conditions, are shown in the Figs. 11.6 (a) and (b). The maximum temperature is in the middle part of the cell and decreases towards the bottom and towards the sidewall. Temperature differences between the carbon block, the refractory, the insulation surfaces and the outer steel shell for both cell models at different positions are summarized in Table B.22 in Appendix B. The temperature at the top part of the sidewall block is approximately 20 °C lower than the bottom part.

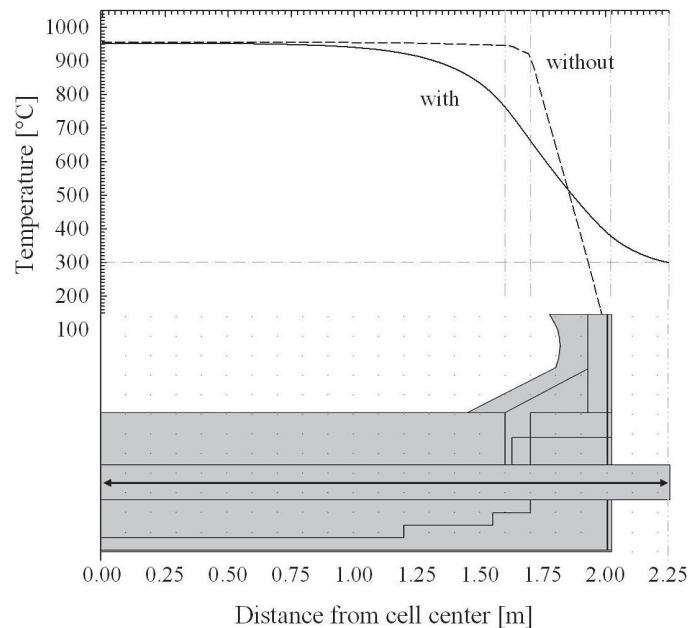
The temperature gradients in the two models are shown in Fig. 11.6 (c) and (d). The arrow points towards regions with higher temperature. The gradient is displayed by the length and visibility of the arrows relative to each other. It is shown that the vertical temperature gradient within the graphitized cathode block, followed by the SiC sidewall block are the lowest because of their high thermal conductivity. The largest inward and upward temperature gradients can be found in the most insulating parts of the cell, which are the sideledge and bottom insulation layer, respectively.

The heat fluxes, their direction and intensity are displayed as an arrow plot in Figs. 11.6 (e) and (f). Here, the material or position in the cell with the highest heat flux is quite different in the two models. In model (e) the heat, which comes from the cathode block, is mainly conducted through the collector bar. Model (f) in contrast conducts the heat mainly through the ramming paste and the sidewall block.



**Figure 11.6:** Comparison of the half cells with (left) and without (right) a collector bar, in terms of: (a,b) temperature distribution [ $^{\circ}\text{C}$ ]; (c,d) temperature gradient and (e,f) total heat flux [ $\text{W}/(\text{m} \cdot \text{K})$ ]. The arrows gives the direction and magnitude of the thermal gradient and heat flux respectively; the Figs. (c-f) include contour plots, showing the temperature distribution [ $^{\circ}\text{C}$ ].

The temperature distribution in the two models along the x-axis of the collector bar is compared in Fig. 11.7. The label **with** refers to the model with embedded collector bar, see Fig.11.6 (a), whereas the label **without** shows the temperature distribution at the same position, but without the collector bar itself, as seen in Fig. 11.6 (b).



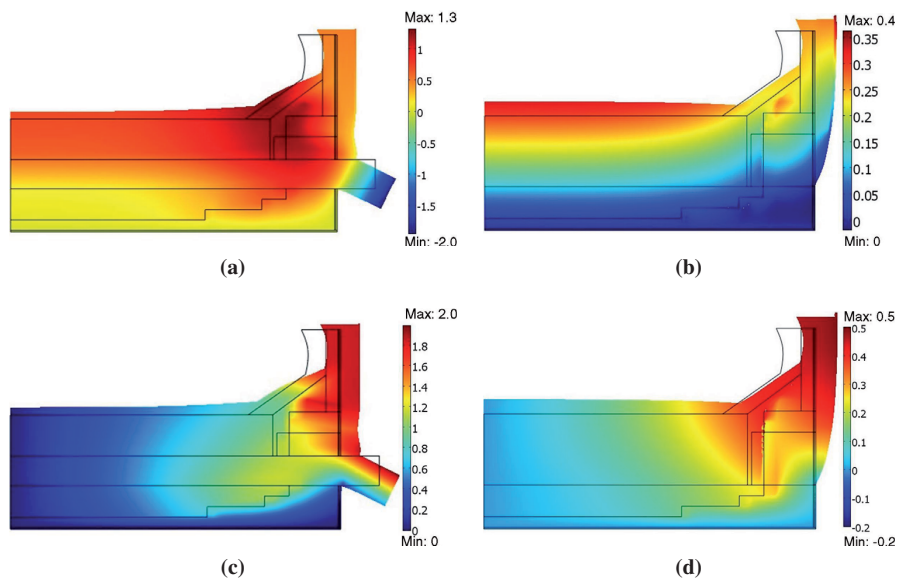
**Figure 11.7:** Temperature distribution along the position (black arrow) of the collector bar: **with** and **without** insertion of the collector bar at steady state conditions.

The temperature gradients of the models are significantly different. The model **with** embedded collector bar demonstrates that the strongest temperature gradient ( $\partial T/\partial x$ ) can be found at the intersection between the carbon block and the ramming paste/refractory material. This intersection is therefore the area where changes are most likely to occur.

The passage between the steel shell and the collector bar ends implies the lowest  $\partial T/\partial x$ . A temperature of 300 °C at the outer boundary of the collector bar coincides with the measurements from the aluminium industry [158]. The transition region between the cathode block and the ramming paste/refractory material for the other simulation (**without** collector bar) displays a flat, hardly noticeable drop in temperature. The largest temperature drop (also between both models) appears in the refractory and insulation material, towards the sidewall of the cell. The influence of the thermal field on the stress build up in the lining was further studied.

### 11.4.2 Thermal Stress Model

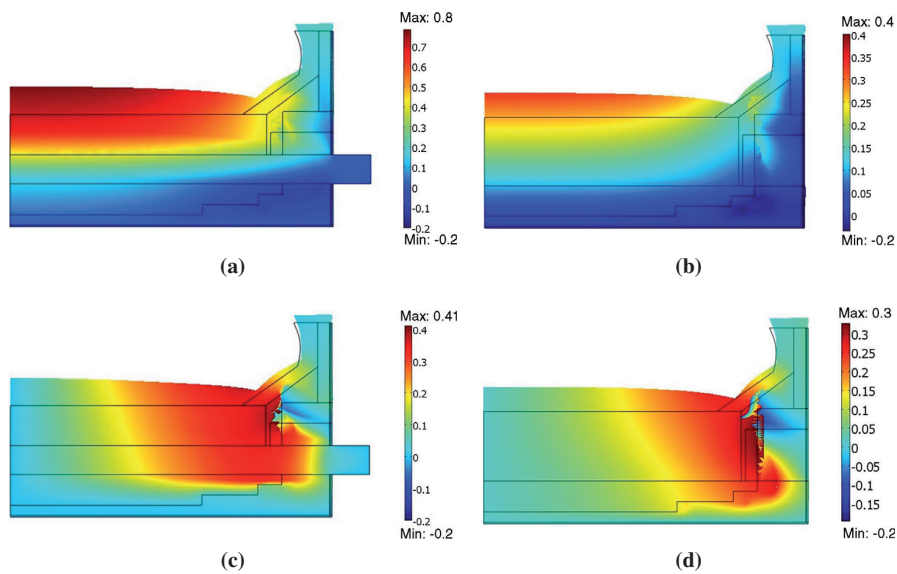
The influence of free and fixed constraints at the outer boundaries 4-7 for both models are depicted in Figs. 11.8 and 11.9. The displacement in x- and y-direction [cm] as well as the stress distribution [Pa] were considered. For better visualization of the deformation, the deformed plot feature of COMSOL Multiphysics was used. It should be noticed that the deformed shape is primarily intended for visualizing x- and y-displacements (u and v). Thus in each case it reflects the total deformation and not the individual components. By default this method automatically scales the deformation to 10 % of the initial cell dimension. Figs. 11.8 (a) and (b) demonstrate that the y-direction displacement on the top of the carbon is larger than on the bottom, which is due to the temperature gradient. Here, the minus "-" sign means negative direction or downwards movement and plus "+" means positive direction, namely upwards. For model (a), the largest upwards displacement is concentrated in the intersection region between the carbon block and the ramming paste. In model (b) the y-displacement is more regularly distributed along the cathode surface. Thus the maximum deflection in (b) is lower compared to (a), which is due to the collector bar. The exact values and their comparison are summarized in Table 11.2.



**Figure 11.8:** Comparison of the half cells **with** (a,c) and **without** (b,d) a collector bar, in terms of: (a,b) y-direction displacement [cm] and (c,d) x-direction displacement [cm], the colours indicate the intensity and can be compared to the specific scale bar. Note that the scale bars between the figures are different. The Figs. (a-d) are presented as deformed-shape plots to give additional information about the resulting geometrical shape. Note this implies the total deformation only. The constraints for boundaries 4-7 = free, Fig. 11.4.

The x-direction displacements are compared in Fig. 11.8 (c) and (d). The minus "-" sign means left direction and plus "+" means right direction movement. In both simulations the main deformation in the x-direction or outwards takes place in the upper sidewall region of the cell. The difference between model (c) and (d) is significant as shown in Table 11.2.

The influence of fixed constraints at the outer boundaries 4-7 for both models are depicted in Figs. 11.9. The change from free to fixed boundary conditions influences the deformations, especially the one **with** the collector bar significantly. In Fig. 11.9 (a) the position of the maximum y-deflection ("+" sign) moved towards the symmetry plane. In a real cell this corresponds to the middle of the carbon cathode. Both maximum y-displacements are lower compared to the free boundary condition models in Fig. 11.8. Model (a) shows in addition that the thermal expansion of the interacting materials is partly compensated by a downwards movement ("-") sign). This is particularly the case right below the collector bar and in the insulation. Compressed insulation layers are typical observations in autopsies of SPL [3].



**Figure 11.9:** Comparison of the half cells **with** (a,c) and **without** (b,d) a collector bar, in terms of: (a,b) y-direction displacement [cm] and (c,d) x-direction displacement [cm], the colours indicate the intensity and can be compared to the specific scale bar. Figs. (a-d) are presented as deformed-shape plots to give additional information about the resulting geometrical shape. Note this implies the total deformation only. The constraints for boundaries 4-7 = fixed, Fig. 11.4.

The x-direction displacement is compared in Figs. 11.9 (c) and (d). The minus "-" sign means left direction and plus "+" means right direction movement. In both simulations the main deformation in the x-direction moved to the intersection region

between the cathode block and the ramming paste/refractory material. The expansion is compensated by a compression of the upper ramming paste and the refractory material. The exact values, their comparison and a summary of the positions with maximum deformation are collected in Table 11.2.

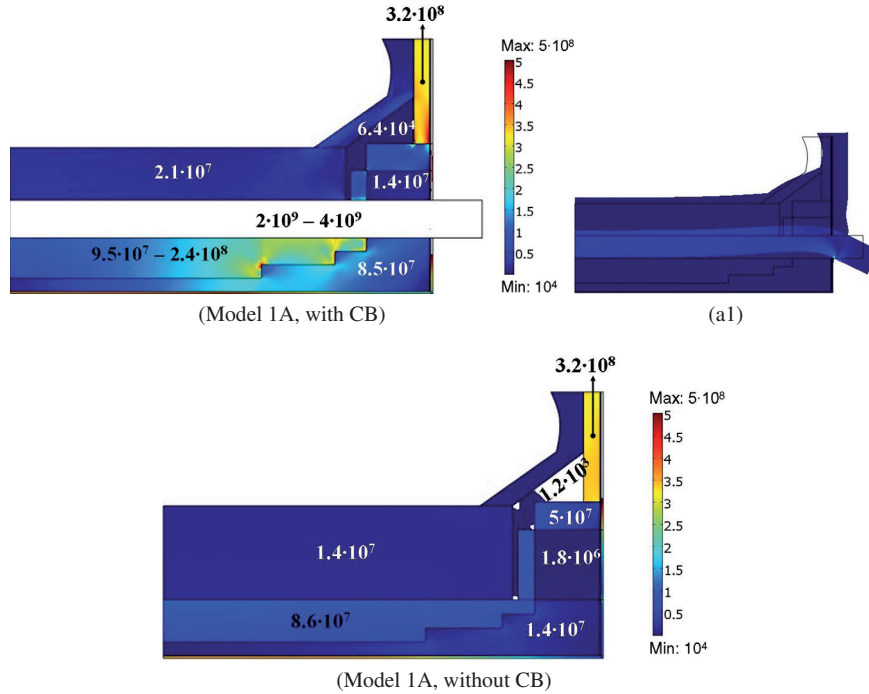
**Table 11.2:** Comparison of maximum x- and y-deflections  $\delta_{max}$  of *Model 1A* (constraints for boundaries 4-7 = free) and *Model 2A* (constraints for boundaries 4-7 = fixed). The labels a-d are provided in the respective images 11.8 and 11.9. CB, RP, R, SW, SP and Inters. are the abbreviations for cathode block, ramming paste, refractory, sidewall, symmetry plane and intersection.

Model	$\delta_{max}$ [cm]	Position of $\delta_{max}$	Model	$\delta_{max}$ [cm]	Position of $\delta_{max}$	$\Delta$ [%]
1A(a)	1.31	Inters. CB/RP/R	2A(a)	0.78	CB SP	41
1A(b)	0.36	CB surface	2A(b)	0.33	CB SP	9
$\Delta$ [%]	72			58		
1A(c)	1.99	Upper SW	2A(c)	0.41	Inters. CB/RP/R	79
1A(d)	0.50	Upper SW	2A(d)	0.32	Inters. CB/RP/R	37
$\Delta$ [%]	75			23		

### Von Mises Stress Distribution

Figs. 11.10 and 11.11 show the *Von Mises stress* distribution in [Pa] of the two simulations with either free or restricted boundaries 4-7 (Fig. 11.4). Since the original scale range is too broad it was limited to values of  $10^4$ - $5 \cdot 10^8$  Pa, where most of the stress in the materials could be included. The materials with stresses out of range appear white. The sub-figures (a1) and (b1) show the corresponding total deformation profile of the collector bar.

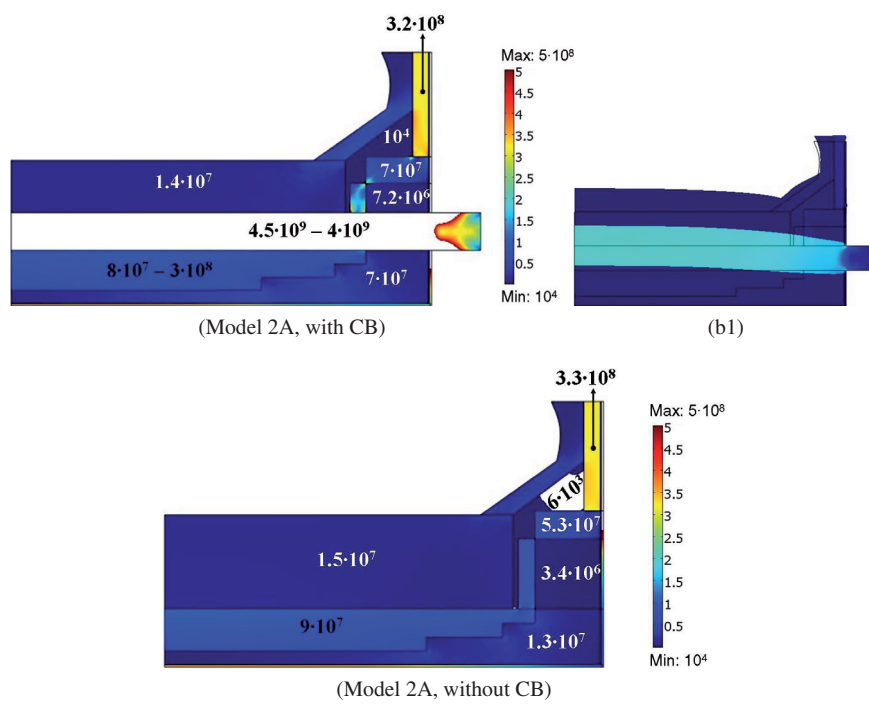
From Figs. 11.10 and 11.11 it is shown that the stresses observed in the graphitized carbon block reach and even become higher than the materials bending strength of  $1.3 \cdot 10^7$  Pa, but the stress does not reach the crushing strength of  $3.2 \cdot 10^7$  Pa at room temperature [159]. The largest stresses in the order of  $10^9$  Pa appear along the collector bar. They are high enough to exceed the collector bar's yield strength  $\sigma_y$  of  $2.35 \cdot 10^8$  Pa at room temperature. The  $\sigma_y$  of a material is the level of stress necessary to cause permanent deformations. This becomes even more likely at elevated temperatures where the yield strength is significantly lower and creep may occur. Creep was not considered in the present simulations. The collector bar ends in turn have lower stress, because they are not restricted and are lower in temperature. Moreover, the stress inside the collector bar increases with increasing rigidity of the steel shell as shown



**Figure 11.10:** Von Mises Stress distribution of the half cell simulation **with** and **without** collector bar (CB): (Model 1A) boundaries 4-7 = free, Fig. 11.4, (a1) corresponding deformation profile of the collector bar. Materials, which are not in scale appear white. The numbers were added to show the approximate magnitude of the prevailing stress.

in Fig. 11.11 (Model 2A). The highest values were obtained where the collector bar leaves the cathode block. This results in a strong deformation or upward bending at the intersection between the cathode block and the ramming paste/refractory material, which is indicated in Figs. 11.10 (a1) and 11.11 (b1). From Fig. 11.10 it is shown that the stress in the carbon block is lower compared to the model in Fig. 11.11. No uniform stress gradient was observed in the carbon cathode. The carbon block releases its stress in the directions where deformations are possible. Thus from Fig. 11.8 and 11.9 it is shown that the block bends upwards near the symmetry plane and compresses the material in the intersection between the carbon block and the ramming paste/refractory or insulation material.

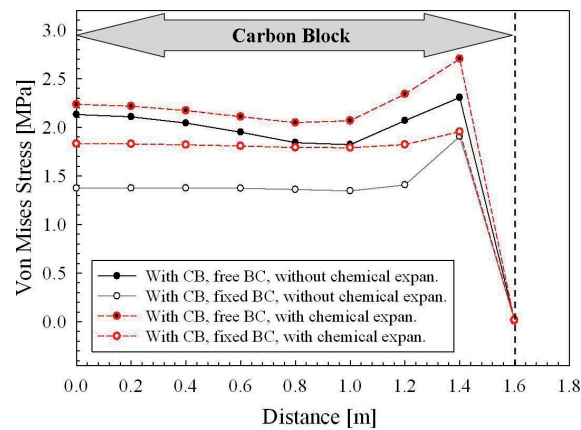




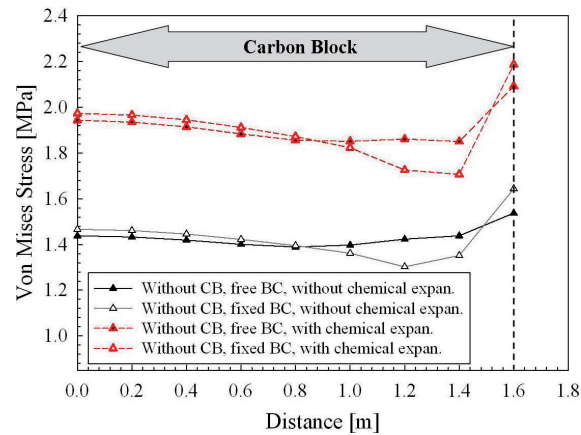
**Figure 11.11:** Von Mises Stress distribution of the half cell simulation **with** and **without** collector bar (CB): (Model 2A) boundaries 4-7 = fixed, Fig. 11.4, (b1) corresponding deformation profile of the collector bar. Materials, which are not in scale appear white. The numbers were added to show the approximate magnitude of the prevailing stress.

### 11.4.3 Influence of Sodium Expansion

By including the sodium expansion for graphitized carbon material, the situation has not been changed to the extent as expected from previous investigations [3, 119, 120]. It should be noted that the sodium expansion coefficient in graphitized carbon materials is lower than the thermal expansion coefficient, which in turn is different in non-graphitized materials [8]. The *Von Mises stress* distribution with and without the addition of sodium expansion are compared in Figs. 11.12 and 11.13.



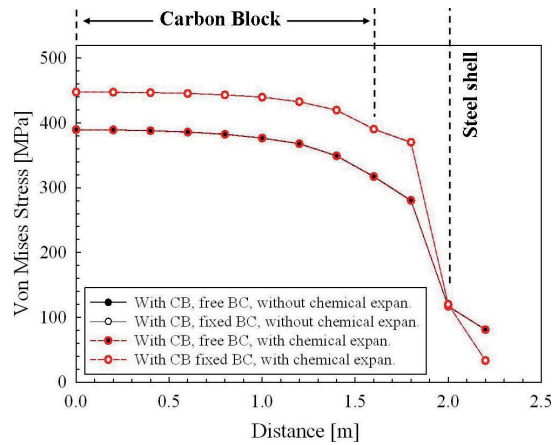
(a)



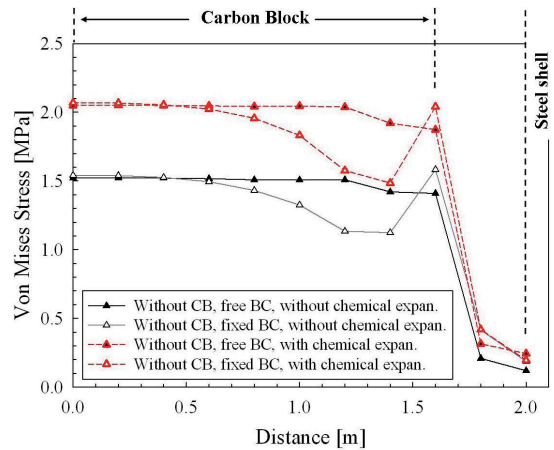
(b)

**Figure 11.12:** Influence of sodium uptake on the *Von Mises Stress* distribution along the carbon block middle axis in x-direction from symmetry plane towards the steel shell for (a) Model 1A, 2A **with** collector bar (CB), (b) Model 1A, 2A **without** collector bar (CB), both are compared to Model 1B, 2B (with chemical expansion). BC means boundary condition.

The sodium expansion causes an increase of stresses in the cathode block, particularly at the cathode ends towards the ramming paste/refractory material of the cell. Higher stress values are in general obtained in simulations in which the collector bar is absent and replaced by the carbon materials as shown in Fig. 11.13 (b). The sodium expansion has no significant influence at the collector bar stress level as shown in Fig. 11.13 (a).



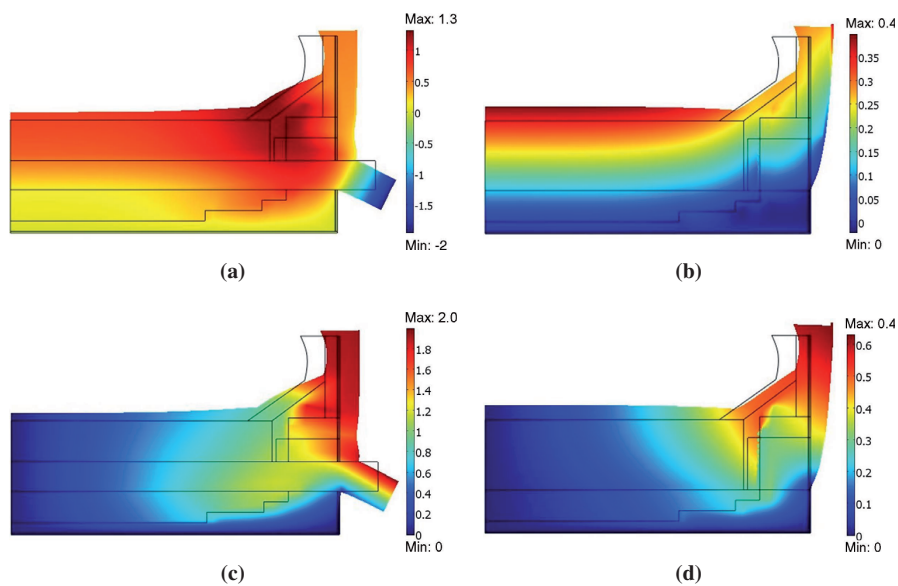
(a)



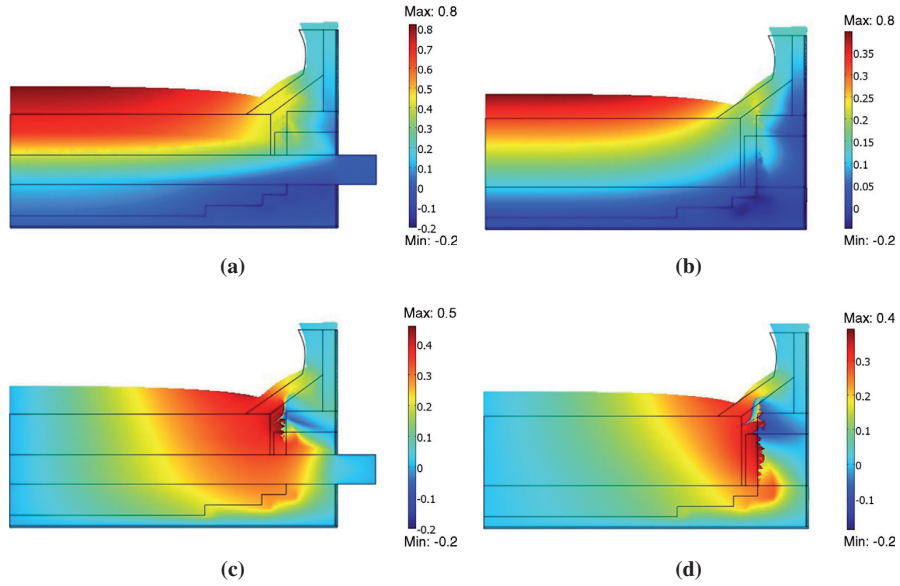
(b)

**Figure 11.13:** Influence of sodium uptake on the *Von Mises Stress* distribution along the collector bar middle axis in x-direction from symmetry plane towards the steel shell for (a) Model 1A, 2A **with** collector bar (CB), b) Model 1A, 2A **without** collector bar (CB), both are compared to Model 1B, 2B (with chemical expansion). BC means boundary condition.

The resulting deformations reflected by the x- and y-direction displacements are shown in Fig. 11.14 and in Fig. 11.15 (boundaries 4-7 = free or fixed, Fig. 11.4). The maximum deflections are summarized and compared to the previous simulations (without chemical expansion) in Table 11.3. The influence of the sodium expansion is shown by a slight increase of  $\delta_{max}$  in the y-direction. The reason is that the sodium uptake causes only the carbon block to expand. In Fig. 11.14 and 11.15 (b,d) the collector bar is absent. This explains the higher values obtained. It is also evident that the entire x-direction displacement is more effected, especially in the cathode carbon block and the intersection between the carbon block and the ramming paste/refractory material. Moreover, the stresses within the cell in the x- or y-direction increase with the rigidity of the steel shell.



**Figure 11.14:** Comparison of the half cells **with** (left) and **without** (right) a collector bar and the influence of chemical expansion in terms of: (a,b) y-direction displacement [cm] and (c,d) x-direction displacement [cm], the colours indicate the intensity and can be compared to the specific scale bar. Figs. (a-d) are presented as deformed-shape plots to give additional information about the resulting geometrical shape. Note this implies the total deformation only. The constraints for boundaries 4-7 = free, Fig. 11.4.



**Figure 11.15:** Comparison of the half cells **with** (left) and **without** (right) a collector bar and the influence of chemical expansion in terms of: (a,b) y-direction displacement [cm] and (c,d) x-direction displacement [cm], the colours indicate the intensity and can be compared to the specific scale bar. Figs. (a-d) are presented as deformed-shape plots to give additional information about the resulting geometrical shape. Note this implies the total deformation only. The constraints for boundaries 4-7 = fixed, Fig. 11.4.

**Table 11.3:** Comparison of the influence of chemical expansion Model 1B and 2B on the maximum x- and y-deflections of Model 1A and Model 2A from Table 11.2. The labels a-d are provided in the respective images 11.8 and 11.9. In Model 1B the constraints for boundaries 4-7 = free and for Model 2B boundaries 4-7 = fixed, Fig. 11.4. The labels a-d are provided in the respective images 11.14 and 11.15.

$\delta_{Direct.}$		$\delta_{max}$ [cm]			$\delta_{max}$ [cm]		
		Model 1B	Model 1A	$\Delta_{max}$ [%]	Model 2B	Model 2A	$\Delta$ [%]
Y	(a)	1.32	1.31	0.15	0.82	0.78	5
	(b)	0.4	0.36	8.82	0.40	0.33	17
$\Delta$ [%]		70			51		
X	(c)	1.991	1.99	0.10	0.46	0.41	10
	(d)	0.63	0.50	20.48	0.39	0.32	19
$\Delta$ [%]		68			15		

## 11.5 Discussion

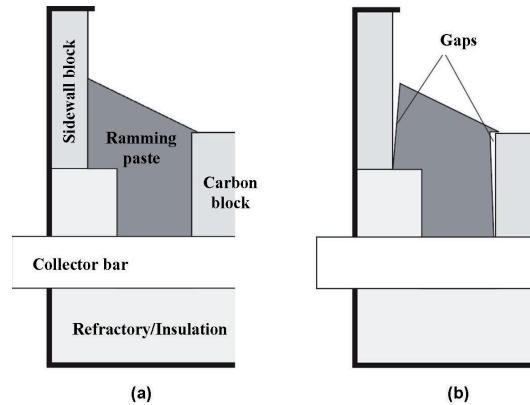
The thermal model was established to identify the temperature distribution and thermal gradients in the cathode lining. From the simulation and Fig. 11.7 it was shown that the largest temperature gradient appeared where the collector bar leaves the carbon block into the ramming paste/refractory material. Moreover, it is important to notice that the main heat flux is going through the ramming paste and not the sideledge. This might explain the shape differences and the chemical degradation profile as reported by Wang [121]. It also reflects the vertical temperature gradient  $T_{\text{Top}} \leq T_{\text{Bottom}}$  inside the SiC sidewall block. Here, it should be mentioned that the position of the heat flux in both models is somewhat overestimated. In Fig. 11.6 (f) the collector bar itself is absent, whereas in simulation (e) the bar is a steel plate.

Furthermore the simulation revealed the influence of the thermal field on the stress build up in the lining. The stress distribution in the simulations are influenced by certain conditions. The main factors are the material properties, constrains and the restrictions of the model. The constrains lead to a stress increase whereas the unrestricted or compressible parts are able to release their stress due to deformations. In Figs. 11.10 and 11.11 it was demonstrated that the stresses were sufficient to exceed the materials strength especially of the carbon block and collector bar. This in turn facilitates their deformation. The maximum upwards deflection was identified at the intersection between carbon block and ramming paste/refractory material. This is exactly the same position where the largest temperature gradient in the thermal model occurred. As the stiffness of the steel shell increases the maximum deflection moved to the center part of the carbon block towards the symmetry plane. The stresses were also released due to compressions of the insulation material.

Taking the sodium expansion of graphitized carbon cathodes into account evidenced that the sodium uptake has less influence on the cathode heave. The main force is the thermal expansion caused by the temperature gradients inside the cell. The sodium expansion only strengthens the effect of the thermal expansion.

Sørli and Øye [3] described the rammed parts to be the weak link in a lining. Between installation and preheat or early operation stage the ramming paste undergoes physical, chemical and thermomechanical changes from a plastic to a baked and solid form [8]. The combination of paste quality, installation, heating and baking rate influences the extent of the dimensional changes. In the worst case too intensive shrinkage can cause cracks or gaps against the bottom or sidewall blocks as illustrated in Fig. 11.16.

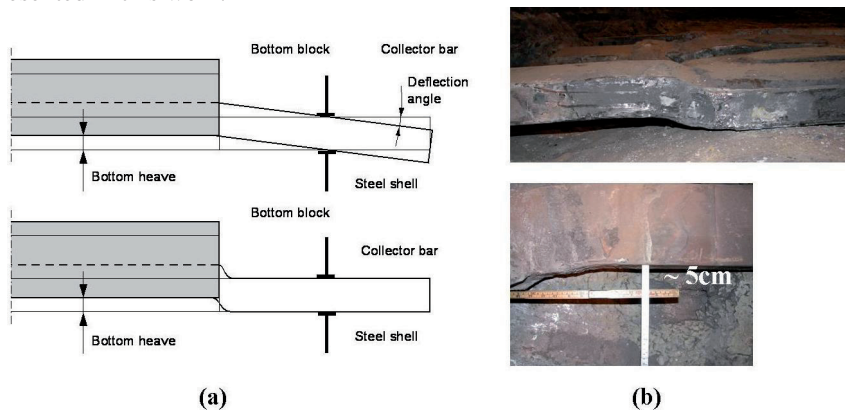
Moreover, from autopsies it was possible to study the deformation profile of the collector bar [3]. The vertical movements of the collector bar are restrained either by the portholes through the steel shell or the surrounding refractory material. Therefore the cathode heaving induces a considerable deformation of the collector bar, as shown Fig. 11.17. The severe deformation in this figure occurred exactly at the same position identified by the simulations performed in this work. The reason for this is the strongest temperature gradient and less constraints. Thus the intersection between the



**Figure 11.16:** Visual appearance (a) of a properly installed peripheral joint and (b) a rammed incline at the end of the preheating period (partly redrawn from [3]).

carbon block and the rammed paste is indeed the "weak part" of the bottom lining. In brief, the temperature gradient is the driving force to initiate the stresses and the resulting deformations as observed in autopsies. This could only be shown by inserting the collector bar into the 2-dimensional model.

As mentioned in Section 11.3 the restriction of this model is the physical contact between the different materials. The different material layers in the cell act like one block, which means that the sliding of interior boundaries is impossible. Thus the stress profile is only controlled by the constraints of the outer boundaries. If the interior boundaries were able to move independently of each other it is expected that the stress release preferably occur through the "weak part". This would enhance the upwards deflection as already shown in Fig. 11.9. Due to the predefined restrictions of the model (reflected by the observed stress profiles) the resulting deformations were presented in this work.



**Figure 11.17:** Examples of collector bar deformation caused by bottom heave: (a) top=angled deformation, bottom=parallel deformation [3]; (b) from an 2168 days old pot.

## 12 Conclusion Part II

The objective of the second part of the study was to evaluate the stress level acting on the collector bars and to identify possible forces leading to the cathode heave phenomenon. Especially the influence of sodium uptake was considered. It was demonstrated that the forces acting upwards are indeed caused by the thermal expansion of the cathode lining materials and in addition the expansion due to the sodium infiltration of the carbon block. From the FEM simulations it was evident that the chemical expansion has a less influence on the stress build up in graphitized carbon cathodes. The thermal gradients are the main reason for the stresses within the cell and the sodium expansion adds on to the effect of the thermal expansion. Moreover, the stresses observed were sufficient to exceed the materials strength, especially of the carbon block and the collector bar. Stress relaxation occurred by compression of the less dense and softer materials (e.g. insulation and ramming paste) and by vertical upward deformations (regions with less constrain).

The most severe deformations (maximum upwards deflection) occurred in the intersection between the carbon block and the ramming paste/refractory material, where the collector bar leaves the carbon material. This region was exactly the same region with the largest temperature gradient. Therefore, this intersection was termed the "weak part" of the cell lining. As the rigidity of the steel shell increases the maximum deflection moved to the center part of the carbon block towards the symmetry plane of the model. As demonstrated from the simulations the temperature gradient is the driving force to cause the deformations as cathode heave observed in autopsies of shut down cells.



## 13 Outlook

It is well known that sodium plays an crucial role in the entire cathode lining, especially in the carbon cathode and as a consequence in the refractory and side lining. In the present work sodium was identified as the principle attacking agent initiating the degradation at the reaction front. Previous investigations showed that bath components are also harmful in contact with refractory material and only sodium enables the bath components to penetrate through the carbon block. Based on these findings it is clear that in the absence of sodium the cathode lining would last much longer. Until today extensive industrial trials have been performed to stop the sodium at the carbon cathode surface. Dense, drained or coated cathodes are attempts, but these alternatives are not yet competitive due to cost and lack of inert materials.

The present simulations revealed that the sodium expansion of the cathode block is not the main reason for the cathode heave. Thus it might be satisfying to stop the sodium at the lower surface of the cathode block right before sodium reaches the refractory layer. Steel plates as diffusion barriers have been extensively used in some cathode designs. Unfortunately these plates are not stable in contact with molten aluminum. From autopsies it was shown that the collector bar is deformed but still intact in contact with Na. Sodium does not form intermetallic compounds or has a low solubility in the steel collector bar. Steel is therefore a material which can be used to retard the sodium transport. This might also work for the sidelining.

In the present work measurements of the electrical conductivity right above the reaction front have been performed to support the proposed diffusion mechanism of sodium below the cathode block. Due to the lack of proper samples these measurements could not be performed to gain reliable results. It is recommended to carry out these experiments in the future.

Nowadays computer simulations are an essential tool for the construction of modern cells. The simulation in the present work has shown that the thermal gradients inside the cell cause severe stress in the cathode lining and especially in the collector bar. Thermal expansions provide forces high enough to lift the cathode block, to bend the collector bar and to compress the insulation material. The "weak part" of the lining was identified. Furthermore the simulations revealed the influence of the rigidity of the steel shell on the stress build up in the cell lining. Further designs need to incorporate compressible materials not only at the lower corners of the steel shell. Compressible areas and thus the refractory material itself inside the "weak part" could be shaped depending on the demand and not necessarily rectangular as applied in the present cell design. In order to make precise suggestions the model need to incorporate the temperature dependent material data for the steel collector bar. Besides the insulation, the collector bars are turned out to be the most critical material in the cell lining, since they are made of normal structural steel, which softens at elevated temperatures.

In this context creep is a material property that becomes more important the higher the temperature. Attempts have been made to incorporate the creep behaviour of the collector bar, but due to the complexity of the model no solutions could be gained so far. Thus further simulation work should focus on the incorporation of the creep behaviour of the collector bar. It is also recommended to control the physical contact of interior boundaries. Furthermore, the two dimensional simulation in this work should be extended into the three dimensions to allow a more detailed display of the cell design.

The finite element simulation in this work reflected the difference between graphitized and non-graphitized carbon cathodes in terms of their chemical and thermal expansion coefficients [8]. To evaluate this relationship more precisely it is suggested that the data collection during autopsies regarding the cathode heave phenomenon should be extended by comparing the amount of deflection to the kind of the cathode material. So far no such reports are available.

## Bibliography

- [1] P.F.J. Thonstad and G.M. Haarberg. *Aluminium Electrolysis*. Aluminium-Verlag Marketing and Kommunikation GmbH, Düsseldorf, Germany, 3rd edition, 2001.
- [2] H.A. Øye et al. Aluminum: Approaching the New Millenium. *Journal of the Minerals, Metals and Materials Society (JOM)*, 51, No.2:29–42, 1999.
- [3] M. Sørliie and H.A. Øye. *Cathodes in Aluminium Electrolysis*. Aluminium-Verlag, Düsseldorf, Germany, 2nd edition, 1994.
- [4] K. Grjotheim and B.J. Welch. *Aluminium Smelter Technology*. Aluminium-Verlag Marketing and Kommunikation GmbH, Düsseldorf, Germany, 2nd edition, 1988.
- [5] K. Grjotheim and H. Kvande. *Introduction to Aluminium Electrolysis*. Aluminium-Verlag Marketing and Kommunikation GmbH, Düsseldorf, Germany, 2nd edition, 1993.
- [6] P.-Y. Geay, B.J. Welch and P. Homsí. Sludge in Operating Aluminium Smelting Cells. *Light Metals*, pages 541–547, 2001.
- [7] S. Rolseth, R. Hovland and O. Kobbeltvelt. Alumina Agglomeration and Dissolution in Cryolitic Melts. *Light Metals*, pages 351–357, 1994.
- [8] M. Sørliie and H.A. Øye. *Cathodes in Aluminium Electrolysis*. Aluminium-Verlag, Düsseldorf, Germany, 3rd edition, 2010.
- [9] K. Billehaug and H.A. Øye. Inert Anodes for Aluminium Electrolysis in Hall-Héroult Cells (i). *Aluminium*, 56, No.10:642–648, 1980.
- [10] C. Schøning, T. Grande and O.-J. Siljan. Cathode Refractory Materials for Aluminium Reduction Cells. *Light Metals*, pages 231–238, 1999.
- [11] O.-J. Siljan, C. Schøning and T. Grande. State-of-the-Art Alumino-Silicate Refractories for Al Electrolysis Cells. *Journal of the Minerals, Metals and Materials Society (JOM)*, 54, No.5:46–55, 2002.
- [12] C. Schøning and T. Grande. The Stability of Refractory Oxides in Sodium-Rich Environments. *Journal of the Minerals, Metals and Materials Society (JOM)*, 58, No.2:58–61, 2006.
- [13] O.-J. Siljan, C. Schøning and T. Grande. Refractories for Aluminium Electolysis Cells Part I. *Aluminium*, 77:294–299, 2001.
- [14] O.-J. Siljan, C. Schøning and T. Grande. Refractories for Aluminium Electolysis Cells Part II. *Aluminium*, 77:385–390, 2001.

- [15] O.-J. Siljan, C. Schøning and T. Grande. Refractories for Aluminium Electolysis Cells Part III. *Aluminium*, 77:610–615, 2001.
- [16] O.-J. Siljan, C. Schøning and T. Grande. Refractories for Aluminium Electolysis Cells Part IV. *Aluminium*, 77:809–814, 2001.
- [17] O.J. Siljan. *Sodium Aluminium Fluoride Attack on Alumino Silicate Refractories*. PhD Thesis at Department of Inorganic Chemistry, Norges Teknisk-Naturvitskaplege Universitet (NTNU), 1990.
- [18] J. Rutlin. *Chemical Reactions and Mineral Formation during Sodium Aluminium Fluoride Attack on Aluminosilicate and Anorthite based Refractories*. PhD Thesis at Norges Teknisk-Naturvitskaplege Universitet (NTNU), 1998.
- [19] F. Brunk. Corrosion and Behaviour of Fireclay Bricks of Varying Chemical Composition Used in Bottom Lining of Reduction Cells. *Light Metals*, pages 477–482, 1994.
- [20] A. Solheim and C. Schøning. Sodium Vapour Degradation of Refractories Used in Aluminium Cells. *Light Metals*, pages 967–972, 2008.
- [21] A. Solheim, C. Schøning and E. Skybakmoen. Reactions in the Bottom Lining of Aluminium Reduction Cells. *Light Metals*, pages 877–882, 2010.
- [22] R. Pelletier et al. The Corrosion of Potlining Refractories: A Unified Approach. *Journal of the Minerals, Metals and Materials Society (JOM)*, 53, No.8:18–22, 2001.
- [23] R. Pelletier and C. Allaire. Corrosion of Potlining Refractories: Effect of Cathode Material Interpreted Using a Unified Approach. *Journal of the Minerals, Metals and Materials Society (JOM)*, 55, No.11:58–62, 2003.
- [24] H.A. Øye et al. Reduction of Sodium Induced Stresses in Hall Héroult Cells. *Aluminium*, 72:918–924, 1996.
- [25] J. Hop et al. Chemical and Physical Changes of Cathode Carbon by Aluminium Electrolysis. *VII International Conference on Molten Slags Fluxes and Salts, The South African Institute of Mining and Metallurgy*, pages 775–781, 2004.
- [26] M. Imris, G. Soucy and M. Fafard. Carbon Cathode Resistance Against Sodium Penetration During Aluminum Electrolysis - An Overview. *Acta Metallurgica Slovaca*, 11, No.2:231–243, 2005.
- [27] Z. Wang. *Aging of Si<sub>3</sub>N<sub>4</sub>-Bonded SiC Sidewall Materials in Hall-Héroult Cells-Material Characterization and Computer Simulations*. PhD Thesis at Department of Materials Science and Engineering, Norges Teknisk-Naturvitskaplege Universitet (NTNU), 2010.
- [28] Z. Wang, E. Skybakmoen and T. Grande. Chemical Degradation of Si<sub>3</sub>N<sub>4</sub>-Bonded SiC Sidelining Materials in Aluminum Electrolysis Cells. *Journal of the American Ceramic Society*, 92, No.6:1296–1302, 2009.

- [29] Z. Wang, E. Skybakmoen and T. Grande. Spent  $\text{Si}_3\text{N}_4$ -Bonded SiC Sidelineing Materials in Aluminum Electrolysis Cells. *Light Metals*, pages 353–358, 2009.
- [30] Z. Wang, E. Skybakmoen and T. Grande. Sodium Diffusion in Cathode Lining in Aluminum Electrolysis Cells. *Light Metals*, pages 841–847, 2010.
- [31] H. Marsh. *Introduction to Carbon Science*. Butterworth & Company, 1989.
- [32] H.O. Pierson. *Handbook of Carbon, Graphite, Diamond and Fullerenes*. Noyes Publication, 1993.
- [33] H. Marsh, E.A. Heintz and F. Rodíges-Reinoso. *Introduction to Carbon Technologies*. Publicaciones de la Universidad de Alicante, 1997.
- [34] F. Hiltmann and K.H Meulemann. Ramming Paste Properties and Cell Performance. *Light Metals*, pages 405–411, 2000.
- [35] E. Skybakmoen et al. Qualitative Evaluation of Nitride Bonded Silicon Carbide Sidelineing Materials. *Light Metals*, pages 773–778, 2005.
- [36] R.P. Pawlek. SiC in Electrolysis Pots: An Update. *Light Metals*, pages 655–658, 2006.
- [37] J. Schoennahl et al. Optimization of  $\text{Si}_3\text{N}_4$  Bonded SiC Refractories for Aluminium Reduction Cells. *Light Metals*, pages 251–256, 2001.
- [38] Saint-Gobain Ceramics. <http://www.refractories.saintgobain.com/data /element/node/application>, Quotation day: 2009.
- [39] Hydro Aluminium. New Sidewall Lining in Modern High Current Hall-Héroult Electrolysis Cell. *Symposium, Düsseldorf, Germany*, 2003.
- [40] C. Liu et al. Excellent Cryolite Resistance and High Thermal Conductivity SiC Sidewall Material for High Amperage Aluminium Reduction Cells. *Light Metals*, pages 889–894, 2010.
- [41] G. Routschka. *Taschebuch Feuerfeste Werkstoffe*. Vulkan-Verlag Essen, 3rd edition, 2001.
- [42] A.M. Alper. *Phase Diagrams in Advanced Ceramics*. Academic Press, 1995.
- [43] A.T. Tabereaux. Reviewing Advances in Cathode Refractory Materials. *Journal of the Minerals, Metals and Materials Society (JOM)*, 38. No.11:20–26, 1992.
- [44] Skamol. Insulation Moler Supra/Hipor. <http://www.skamol.com/-Bricks++blocks.88.aspx>, Quotation day: January, 2009.
- [45] H. Scholze. *Glass: Nature, Structure and Properties*. Springer-Verlag, 1990.
- [46] W.D. Kingery, H.K Bowen and D.R. Uhlmann. *Introduction to Ceramics*. John Wiley & Sons, New York, 2nd edition, 1976.
- [47] W.J. Zachariasen. The Atomic Arrangement in Glass. *Journal of the American Ceramic Society*, 54, No.10:38–41, 1932.

- [48] D.R. Uhlmann and N.J. Kreidl. *Glass Science and Technology*. Academic Press, 1st edition, 1983.
- [49] W.D. Kingery. *Introduction to Ceramics*. John Wiley & Sons, New York, 1960.
- [50] B.E. Warren. *Zeitschrift für Kristallographie, Mineralogie und Petrographie*, 86:349, 1933.
- [51] G.N. Greaves. EXAFS and the Structure of Glass. *Journal of Non-Crystalline Solids*, 71:203–217, 1985.
- [52] X. Liao and H.A. Øye. Physical and Chemical Wear of Carbon Cathode Materials. *Light Metals*, pages 667–674, 1998.
- [53] E. Skybakmoen et al. Laboratory Test Methods for Determining the Cathode Wear Mechanism in Aluminium Cells. *Light Metals*, pages 815–820, 2007.
- [54] K. Vasshaug et al. Wear of Carbon Cathodes in Cryolite-Alumina Melts. *Light Metals*, pages 821–826, 2007.
- [55] M. Sørli and H.A. Øye. Laboratory Testing of Carbon Cathode Materials at Operational Temperatures. *Light Metals*, pages 625–631, 1989.
- [56] C. Allaire. Refractory Lining for Alumina Electrolytic Cells. *Journal of the American Ceramic Society*, 75, No.8:2308–2311, 1992.
- [57] J.G. Hop. *Sodium Expansion and Creep of Cathode Carbon*. PhD Thesis at Norges Teknisk-Naturvitskapelege Universitet (NTNU), 2003.
- [58] P.Y. Brisson et al. The Effect of Sodium on the Carbon Lining of the Aluminium Electrolysis Cell - A Review. *Canadian Metallurgical Quarterly*, 44, No.2:265–280, 2005.
- [59] C. Krohn, M. Sørli and H.A. Øye. Penetration of Sodium and Bath Constituents into Cathode Carbon Materials Used in Industrial Cells. *Light Metals*, pages 311–324, 1982.
- [60] P. Brilliot, L.P. Lossius and H.A. Øye. Penetration and Chemical Reactions in Carbon Cathodes during Aluminium Electrolysis: 1. Laboratory Experiments. *Metallurgical Transaction B*, 24B:75–89, 1993.
- [61] P. Brilliot, L.P. Lossius and H.A. Øye. Melt Penetration and Chemical Reactions in Carbon Cathodes during Aluminium Electrolysis: 1. Laboratory Experiments. *Light Metals*, pages 321–330, 1993.
- [62] L.P. Lossius and H.A. Øye. Melt Penetration and Chemical Reactions in 16 Industrial Aluminium Carbon Cathodes. *Metallurgical And Materials Transactions B*, 31B:1213–1224, 2000.
- [63] M.B. Rapoport and V.N. Samoilenko. Deformation of Cathode Blocks in Aluminium Baths during Process of Electrolysis. *Tsvtnye Metalli*, 30, No.2:44–51, 1957.

- [64] H.-P. Boehm, R. Setton and E. Stumpp. Nomenclature and Terminology of Graphite Intercalation Compounds. *Pure & Applied Chemistry*, 66, No.9:1893–1901, 1994.
- [65] M.B. Dell. Reactions between Carbon Lining and Hall Bath. *Extractive Metallurgy Aluminum*, Wiley Interscience publishers, New York, 2:403–416, 1963.
- [66] L.L. Schramm. *The Language of Colloid & Interface Science*. ACS Professional Reference Series, American Chemical Society, Washington, 1993.
- [67] E.W. Dewing. The Reaction of Sodium with Nano-Graphitic Carbon: Reactions Occurring in the Lining of Alumina Reduction Cells. *Transaction of the Metallurgical Society of AIME*, 227:1328–1333, 1963.
- [68] A.P. Ratvik et al. The Effect of Current Density on Cathode Expansion During Start-Up. *Light Metals*, pages 973–978, 2008.
- [69] A. Zolochovsky et al. Rapoport-Samoilenko Test for Cathode Carbon Materials, I. Experimental Results and Constitutive Modelling. *Carbon*, 41, No.3:497–505, 2003.
- [70] B.J. Welch et al. Interrelationship of Cathode Mechanical Properties and Carbon/Electrolyte Reactions During Start-Up. *Light Metals*, pages 727–733, 1991.
- [71] M. Sørli and H.A. Øye. Chemical Resistance of Cathode Carbon Materials During Electrolysis. *Light Metals*, pages 1059–1070, 1984.
- [72] C. Schøning, A. Solheim and E. Skybakmoen. Deterioration of the Bottom Lining in Aluminium Reduction Cells, Part II: Laboratory Data and Autopsies. *Paper presented at the Aluminium of Siberia 2008*, XIV International Conference:76–82, 2008.
- [73] J. Rutlin and T. Grande. Fluoride Attack on Alumino-Silicate Refractories in Aluminium Electrolysis Cells. *Light Metals*, pages 295–301, 1997.
- [74] J. Rutlin and T. Grande. Phase Equilibria in Subsystems of the Quarternary Reciprocal System  $\text{Na}_2\text{O}-\text{SiO}_2-\text{Al}_2\text{O}_3-\text{NaF}-\text{SiF}_4-\text{AlF}_3$ . *Journal of the American Ceramic Society*, 82, No.9:2538–2544, 1999.
- [75] P.A. Foster. Phase Equilibria in the Sodium Fluoride Enriched Region of the Reciprocal System  $\text{Na}_6\text{F}_6-\text{Al}_2\text{F}_6-\text{Na}_6\text{O}_3-\text{Al}_2\text{O}_3$ . *Journal of Chemical and Engineering Data*, 9:200–203, 1964.
- [76] M.W. Chase. *JANAF Thermochemical Tables*. Journal of Physical and Chemical Reference Data, 14 edition, 1985.
- [77] J.L. Holm. *Thermodynamic Properties of Molten Cryolite and Other Fluoride Mixtures*. PhD Thesis at Department of Inorganic Chemistry, Norges Teknisk-Naturvitskaplege Universitet (NTNU), 1979.

- [78] L.N. Kogarko and L.D. Krigman. Phase Equilibria in the Subsystem Nepheline-NaF. *Geochemistry International*, pages 103–107, 1970.
- [79] J. Rutlin and T. Grande. Viscosity of Oxyfluoride Melts Relevant to the Deterioration of Refractory Linings in Aluminium Electrolysis Cells. *Light Metals*, pages 431–437, 1999.
- [80] M. Rolin and H.T. Pham. Phase Diagrams of Mixtures not Reacting with Molybdenum. *Rev. Hautes Temp. Refract.*, 2:175–185, 1965.
- [81] F.C. Kracek. The System Sodium Oxide-Silica. *Journal of Physical Chemistry*, 34:1583–1598, 1930.
- [82] J. Williamson and F.P. Glasser. Phase Relations in the System  $\text{Na}_2\text{Si}_2\text{O}_5\text{-SiO}_2$ . *Science*, 148, No.6:1589–1591, 1965.
- [83] C. Tan. *Models for Degradation of Refractory Lining in Aluminium Electrolysis Cells*. Diploma Thesis (NTNU), 2008.
- [84] G. Hetherington, K.H. Jack and J.C. Kennedy. The Viscosity of Vitreous Silica. *Physics and Chemistry of Glasses*, 5, No.5:130–136, 1964.
- [85] M.J. Toplis et al. Viscosity, Fragility, and Configurational Entropy of Melts Along the Join  $\text{SiO}_2\text{-NaAlSiO}_4$ . *Journal of Non-Crystalline Solids*, 71:203–217, 1985.
- [86] O.V. Mazurin. *Handbook of Glass Data-Physical Sciences Data 15*. Elsevier, 1987.
- [87] W. Brockner, K. Tørklep and H.A. Øye. Viscosity of Sodium Fluoride-Aluminium Fluoride Melt Mixtures. *Berichte der Bunsengesellschaft Physical Chemistry*, 83:12–19, 1979.
- [88] G. Urbain, Y. Bottinga and R. Richet. Viscosity of Liquid Silica, Silicates and Alumino-Silicates. *Geochimica et Cosmochimica Acta*, 46:1061–1072, 1982.
- [89] R. Terai and R. Hayami. Ionic Diffusion in Glasses. *Journal of Non-Crystalline Solids*, pages 217–264, 1975.
- [90] J.E. Shelby. *Introduction to Glass Science and Technology*. The Royal Society of Chemistry, 2nd edition, 2005.
- [91] A. Jambon and J.P. Carron. Diffusion of Na, K, Rb and Cs in Glasses of Albite and Orthoclase Composition. *Geochimica et Cosmochimica Acta*, 40:897–903, 1976.
- [92] A. Jambon. Tracer Diffusion in Granitic Melts: Experimental Results for Sodium, Rubidium, Cesium, Calcium, Strontium, Barium, Cerium and Europium to 1300 °C and a Model of Calculation. *Journal of Geophysical Research*, 87:10797–10810, 1982.
- [93] D.B. Dingwell. Effect of Structural Relaxation on Cationic Tracer Diffusion in Silicate Melts. *Chemical Geology*, 82:209–216, 1990.



- [94] D.B. Dingwell and C.M. Scarfe. Chemical Diffusion of Fluorine in Melts in the System  $\text{Na}_2\text{O}-\text{Al}_2\text{O}_3-\text{SiO}_2$ . *Earth and Planetary Science Letters*, 73:377–384, 1985.
- [95] H. Behrens. Na and Ca Tracer Diffusion in Plagioclase Glasses and Supercooled Melts. *Chemical Geology*, 96:267–275, 1992.
- [96] M. Margaritz and A.W. Hofmann. Diffusion of Sr, Ba, and Na in Obsidian. *Geochimica et Cosmochimica Acta*, 42, No.6:595–605, 1978.
- [97] G.H. Frischat. Ionic Diffusion in Oxide Glasses. *Trans Tech publication, Aedermannsdorf, Diffusion and Defect. Monograph Series*, 1975.
- [98] E.B. Watson and D.R. Baker. Chemical Diffusion in Magmas. An Overview of Experimental Results and Geochemical Applications. *Advances in Physical Geochemistry*, 9:120–131, 1991.
- [99] P. Henderson et. al. Structural Controls and Mechanisms of Diffusion in Natural Silicate Melts. *Contributions to Mineralogy and Petrology*, 89, No.2-3:263–272, 1985.
- [100] V.A. Zhabrev and S.I. Sviridov. Ion Diffusion in Oxide Glasses and Melts: I. Bibliography. *Glass Physics and Chemistry*, 29, No.2:140–159, 2003.
- [101] H. Reuter, J. Wiegman and W. Hinz. Thermotransport in Silikatgläsern. *Glastechnische Berichte*, 56, No.1:19–25, 1983.
- [102] W. Müller and M. Hähnert. Zum Mechanismus des Alkalitransports in Gläsern. *Silikattechnik*, 32, No.2:55–56, 1981.
- [103] A. Kolitsch, E. Richter and W. Hinz. Untersuchungen zur Ionenbeweglichkeit in einem Natrium-Kalium Aluminosilikatglas: I and II. *Silikattechnik*, 31, No.2, 5:41–44, 136–139, 1980.
- [104] H.M. Garfinkel H.E. Rauscher. Diffusion of Radiotracer Sodium by the Residual Surface Counting Technique in Soda-Alumina-Silica Glasses. *Journal of Applied Physics*, 37, No.5:2169–2174, 1966.
- [105] W. Köhler and G.H. Frischat. Iron and Sodium Self-Diffusion in Silicate Glasses. *Physics and Chemistry of Glasses*, 19, No.5:103–107, 1978.
- [106] J.L. Karsten, J.R. Holloway and J.R. Delaney. Ion Microprobe Studies of Water in Silicate Melts: Temperature-Dependent Water Diffusion in Obsidian. *Earth and Planetary Science Letters*, 59:420–428, 1982.
- [107] J. Waddington. Processes Occurring in the Carbon Lining of an Aluminium Reduction Cell. *Extractive Metallurgy of Aluminum, New York: Interscience*, 2, ed. G. Gerard, 1963.
- [108] O.J. Siljan. Refractories and Bottom Heaving in Electrolysis Cells for Aluminium Production. *Internal Report, Corporate Research Centre Porsgrunn*, 2003.

- [109] M. Sørli and H.A. Øye. Evaluation of Cathode Material Properties Relevant to the Life of Hall-Héroult Cells. *Journal of Applied Electrochemistry*, 19:580–588, 1989.
- [110] H. Schreiner and H.A. Øye. Sodium Expansion of Cathode Carbon Materials under Pressure. *Light Metals*, pages 463–469, 1995.
- [111] J.M. Peyneau et al. Laboratory Testing of the Expansion under Pressure due to Sodium Intercalation in Carbon Cathode Materials for Aluminium Smelters. *Light Metals*, pages 801–808, 1992.
- [112] E.W. Dewing. Longitudinal Stresses in Carbon Lining Blocks due to Sodium Penetration. *Light Metals*, 3:879–887, 1974.
- [113] A. Zolochovsky et al. Rapoport-Samoilenko Test for Cathode Carbon Materials, II. Swelling with External Pressure and Effect of Creep. *Carbon*, 43, No.6:1222–1230, 2005.
- [114] A. Zolochovsky et al. Creep and Sodium Expansion in a Semigraphitic Cathode Carbon. *Light Metals*, pages 595–602, 2003.
- [115] X. Liao, T. Naas and H.A. Øye. Enhanced Sodium Expansion in Carbon Cathode Materials due to the Presence of Alumina Slurries. *Aluminium*, 73:528–531, 1997.
- [116] I. Nygård and S.K. Ratkje. Temperature Gradient Melt Transport and Chemical Reaction in Used Carbon Cathode. *Light Metals*, pages 457–461, 1994.
- [117] S.K. Ratkje and B. Hafskjold. Coupled Transport of Heat and Mass. Theory and Applications. *Bokk Series: Understanding Chemical Reactivity - Entropy and Entropy Generation*, 18:197–219, 1996.
- [118] A. Seltveit. Autopsi av Elektrolyseovner. Kjemiske Omsetninger. Teoretiske Betragtninger. *Lecture given at NIF-course: Ildfaste materialer i aluminiumindustrien. Porsgrunn, Norway*, 1987.
- [119] Y. Sun et al. Modelling of Thermal and Sodium Expansion in Prebaked Aluminium Reduction Cells. *Light Metals*, pages 605–610, 2003.
- [120] Y. Sun et al. 3-D Modelling Thermal and Sodium Expansion in Søderberg Aluminium Reduction Cells. *Light Metals*, pages 587–592, 2004.
- [121] Z. Wang. *Thermo-Mechanical Models for Degradation of Sidelining in Aluminium Electrolysis Cells*. Diploma Thesis (NTNU), 2007.
- [122] E. Hagen, M.-A. Einarsrud and T. Grande. Chemical Stability of Ceramic Sidelinings in Hall-Héroult Cells. *Light Metals*, pages 257–264, 2001.
- [123] J.R. Davis. *Carbon and Alloy Steels*. ASM International, Specialty Handbook, 1996.
- [124] H.M. Rietveld. A Profile Refinement Method for Nuclear and Magnetic Structures. *Journal of Applied Crystallography*, 2:65–71, 1969.

- [125] J.W. Anthony et al. Handbook of Mineralogy. *Mineral Data Publishing*, 1:192, 1990, reprinted 2003.
- [126] H. Lipson and A.R. Stokes. The Structure of Graphite. *Proceedings of the Royal Society, London*, 181, No.984:101–105, 1942.
- [127] F.C. Hawthorne and R.B. Ferguson. Refinement of the Crystal Structure of Cryolite. *The Canadian Mineralogist*, 13:377–382, 1975.
- [128] V.T. Deshpande. Thermal Expansion of Sodium Fluoride and Sodium Bromide. *Acta Crystallographica*, 14:794, 1961.
- [129] J. Felsche. The Alkali Problem in the Crystal Structure of Beta Alumina. *Zeitschrift für Kristallographie*, 127, No.1-4:94–100, 1968.
- [130] T.S. Duffy. Single-Crystal Elastic Constant of Fluorite ( $\text{CaF}_2$ ) to 9.3 GPa. *The Canadian Mineralogist*, 29:465–472, 2002.
- [131] T.M. Gesing and W. Jeitschko. The crystal Structure and Chemical Properties of  $\text{Al}_4\text{C}_3$  and Structure Refinement of  $\text{Al}_4\text{C}_3$ . *Zeitschrift für Naturforschung B*, 50b:196–200, 1995.
- [132] W.J. Parker et al. Flash Method of Determining Thermal Diffusivity, Heat Capacity, and Thermal Conductivity. *Journal of Applied Physics*, 32, Number 9:1679–1684, 1961.
- [133] A.P. Albers et al. Effect of Testing Conditions on the Laser Flash Thermal Diffusivity Measurements of Ceramics. *Thermochimica Acta*, 370:111–118, 2001.
- [134] Netzsch. LF457 Microflash Instrument. [www.netzsch-thermal-analysis.com](http://www.netzsch-thermal-analysis.com), Quotation day: 01.08.2009.
- [135] V. Danielik et al. Solubility of Aluminium in Cryolite-Based Melts. *Metallurgical And Materials Transaction B*, 41B:430–436, 2010.
- [136] R. Shamsili and H.A. Øye. Melt Penetration and Chemical Reactions in Carbon Cathodes during Aluminium Electrolysis. *Light Metals*, pages 731–738, 1994.
- [137] SINTEF Materials and Chemistry. Internal report. Internal, 2009.
- [138] G. Eriksson, P. Wu and A.D. Pelton. Critical Evaluation and Optimization of the Thermodynamic Properties and Phase Diagrams of the  $\text{MgO-Al}_2\text{O}_3$ ,  $\text{MnO-Al}_2\text{O}_3$ ,  $\text{FeO-Al}_2\text{O}_3$ ,  $\text{Na}_2\text{O-Al}_2\text{O}_3$  and  $\text{K}_2\text{O-Al}_2\text{O}_3$  Systems. *Calphad*, 17, No.2:189–205, 1993.
- [139] R.C. DeVries and W.L. Roth. Critical Evaluation of the Literature Data on Beta Alumina and Related Phases: I, Phase Equilibria and Characterization of Beta Alumina Phases. *Journal of the American Ceramic Society*, 52, No.7:364–369, 1968.
- [140] J.F. Schairer and N.L. Bowen. The System  $\text{Na}_2\text{O-Al}_2\text{O}_3\text{-SiO}_2$ . *American Journal of Science*, 254, No.3:129–195, 1956.

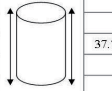
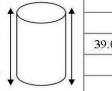
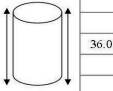









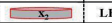











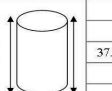





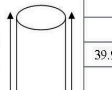
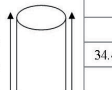
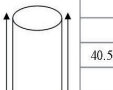













- [141] E.F. Osborn and A. Muan. Phase Equilibrium Diagrams of Oxide Systems. *American Ceramic Society, Columbus OH*, Plate 4, 1960.
- [142] G.W. Morey and N.L. Bowen. The Binary System Sodium Metasilicate-Silica. *Journal of Physical Chemistry*, 28:1167–1179, 1924.
- [143] K. Tschöpe and T. Grande. Chemical Degradation Map for Sodium Attack in Refractory Linings. *Light Metals*, pages 871–876, 2010.
- [144] M.J. Turner et al. Stiffness and Deflection Analysis of Complex Structures. (first use of fem with computer programs). *Journal of Aeronautical and Space Science*, 23:805–824, 1956.
- [145] R.W. Clough. The Finite Element Method in Plane Stress Analysis. (probably the first use of the term finite elements). *Proceedings of the Second ASCE Conference on Electronic Computation, Pittsburgh, PA*, 1960.
- [146] J.N. Reddy. *An Introduction to the Finite Element Methode*. McGraw-Hill Higher Education, 3rd edition, 2006.
- [147] N. S. Ottosen and H. Petersson. *Introduction to the Finite Element Methode*. Prentice Hall Europe, 1992.
- [148] COMSOL Mutliphysics 3.5a. *COMSOL Multiphysics-User's Guide*. COMSOL AB, 2008.
- [149] COMSOL AB. Comsol mutliphysics 3.5a. <http://www.comsol.de>, 2010.
- [150] COMSOL Mutliphysics 3.5a. *Heat Transfer Module-User's Guide*. COMSOL AB, 2008, pages 54-66.
- [151] COMSOL Mutliphysics 3.5a. *Heat Transfer Module-User's Guide*. COMSOL AB, 2008, pages 67-76.
- [152] COMSOL Mutliphysics 3.5a. *Structural Mechanics-Modelling Guide*. COMSOL AB, 2008, pages 203-215.
- [153] COMSOL Mutliphysics 3.5a. *Structural Mechanics Module-User's Guide*. COMSOL AB, 2008.
- [154] J.R. Barber. *Solid Mechanics and its Application Elasticity*. Kluwer Academic Publishers, 2nd edition, 2002.
- [155] B. Nistad, Sales manager and application Engineer at COMSOL. Personal communications. e-mail support, 2009-2010.
- [156] I. Barin. *Thermochemical Data of Pure Substances*. VHC Verlagsgesellschaft, 3rd edition, 1995.
- [157] H. Schreiner. *Sodium Expansion of Carbon Cathodes for Aluminium Electrol-ysis*. PhD Thesis at Norges Teknisk-Naturvitskaplege Universitet (NTNU), 1994.
- [158] J. Rutlin from Hydro Aluminium. Personal communications, 2009.

- [159] Sumitomo Corporation SEC CARBON, Ltd. Cathode Blocks (SK-B). <http://www.sumitomocorp.co.jp/energy/skb/novel.htm>, Quotation day: March 2009.
- [160] A. Solheim from SINTEF Materials and Chemistry. Personal communications, Mai.2010.

# Appendix

## A Part I

**Table A.1:** Second autopsy, cutting position of tablets with 25.4 mm diameter.

2A Carbon Slice 2			2A Carbon Slice 3			2A Carbon Slice 4		
37.5 mm		37.7 mm	39.0 mm		39.0 mm	36.0 mm		36.0 mm
[mm]		[mm]	[mm]		[mm]	[mm]		[mm]
8.4		7.7	2.0		1.5	3.0		4.0
2.5			3.0			3.0		
8.3			6.0			6.0		
3.0		LF/D	3.0			3.0		
13.1		13.3	4.0			6.0		
			3.0		LF/D	3.0		LF/D
			11.0		10.0	9.0		
2A Carbon Slice 5								
37.8 mm		37.7 mm						
[mm]		[mm]						
3.8		4.0						
3.3								
9.2								
3.0		LF/D						
16.1		15.8						
2A Lens Slice 1			2A Lens Slice 2			2A Lens Slice 3		
34.2 mm		39.9 mm	34.1 mm		34.4 mm	40.5 mm		40.5 mm
[mm]		[mm]	[mm]		[mm]	[mm]		[mm]
13.0		13.4	15.8			30.4		
2.2		LF/D	2.7			2.0		
2.3			2.2		LF/D	1.8		LF/D
22.26		17.7	4.1		XRD	5.1		4.8
			7.0					

**Table A.2:** Third autopsy, cutting position of tablets with 25.4 mm diameter.

3A Carbon Slice 6			3A Carbon Slice 5			3A Carbon Slice 4		
38.8 mm		39.1 mm	42.4 mm		42.4 mm	42.5 mm		42.6 mm
[mm]		[mm]	[mm]		[mm]	[mm]		[mm]
4.68		5.33	4.84		5.59	8.33		8.91
3.52		<b>LF</b>	2.77		<b>D</b>	2.75		<b>D</b>
12.98		13.01	3.33		<b>LF</b>	3.75		<b>LF</b>
3.20		<b>D</b>	9.30		10.10	2.77		3.90
12.13		13.08	2.69		2.73	3.82		2.42
			16.36		16.02	2.53		2.42
						2.71		2.71
						13.05		12.85
3A Carbon Slice 1								
42.4 mm		42.4 mm						
[mm]		[mm]						
4.61		5.11						
3.41		<b>LF</b>						
7.16		7.30						
2.95		<b>D</b>						
14.18		15.39						
3A Lens Slice 1			3A Lens Slice 5					
37.2 mm		36.8 mm	32.3 mm		39.1 mm			
[mm]		[mm]	[mm]		[mm]			
7.82			24.04					
2.00		<b>LF/D</b>	1.80		<b>LF/D</b>			
25.14			5.40		5.17			

Table A.3: Bulk density, apparent porosity and distance values for 2. Autopsy (1767 days). GC is the abbreviation for graphitized carbon.

Nr.	Sample Name	Length Drill [mm]	Position in Cross section [mm]	m1 [g]	m2 [g]	m3 [g]	Density of liquid [g/cm <sup>3</sup> ]	Bulk Density [g/cm <sup>3</sup> ]	Apparent Porosity [%]
1	Virgin GC			2.54	1.58	2.77	0.785	1.67	19.13
2	2A Carbon Slice1	45.00	19.00	2.46	1.55	2.53	0.785	1.95	7.69
3	2A Carbon Slice2	82.55	65.35	3.16	2.00	3.23	0.784	2.01	5.49
4	2A Carbon Slice3	121.55	101.85	3.23	2.04	3.26	0.784	2.06	2.75
5	2A Carbon Slice4	157.55	144.60	3.19	2.01	3.22	0.784	2.07	2.15
6	2A Carbon Slice5	195.35	175.50	3.13	1.98	3.17	0.784	2.05	3.44
7	2A Carbon Slice6	212.35					too brittle		
8	Virgin Chamotte			2.25	1.56	2.38	0.784	2.15	16.09
9	2A Lens Slice1	37.05	14.30	2.39	1.57	2.43	0.784	2.19	4.46
10	2A Lens Slice2	71.30	56.65	3.03	2.14	3.04	0.784	2.63	1.97
11	2A Lens Slice3	111.80	104.60	2.64	1.84	2.66	0.784	2.53	2.92
12	2A Lens Slice4	142.80	139.63	6.85	4.81	6.87	0.785	2.62	0.82



Table A.4: Bulk density, apparent porosity and distance values for 3. Autopsy (2168 days).

Nr.	Sample Name	Length Drill [mm]	Position in Cross section [mm]	m1 [g]	m2 [g]	m3 [g]	Density of liquid [g/cm <sup>3</sup> ]	Bulk Density [g/cm <sup>3</sup> ]	Apparent Porosity [%]
13	3A Carbon Slice7	30					too brittle		
14	3A Carbon Slice6	69.75	53.12	3.47	2.24	3.50	0.785	2.16	2.25
15	3A Carbon Slice5	109.25	75.555	3.02	1.95	3.05	0.785	2.17	2.07
16	3A Carbon Slice4	147.25	121.34	2.95	1.84	2.97	0.785	2.05	1.42
17	3A Carbon Slice3	186.75	163.75	3.41	2.18	3.45	0.785	2.10	3.53
18	3A Carbon Slice2	224.25	200.25	3.35	2.14	3.37	0.785	2.15	1.47
19	3A Carbon Slice1	256.00	247.88	3.05	1.95	3.12	0.785	2.05	5.80
20	3A Lens Slice1	32.30	8.82	3.21	2.41	3.28	0.784	2.90	7.60
21	3A Lens Slice2	69.50	36.50	3.14	2.31	3.16	0.785	2.89	2.73
22	3A Lens Slice3	104.50	98.25	5.92	4.35	5.99	0.786	2.84	3.67
23	3A Lens Slice4	125.00	121.00	2.80	1.97	2.81	0.785	2.61	1.48
24	3A Lens Slice5	162.00	153.53	2.40	1.65	2.41	0.784	2.50	1.20

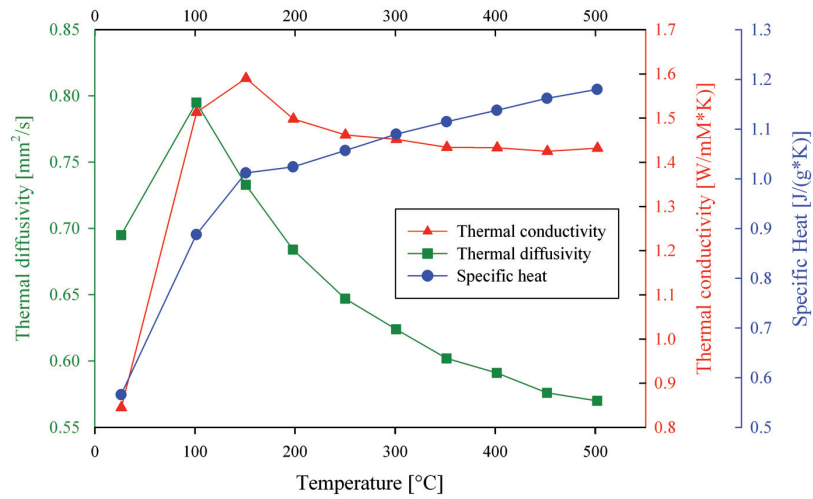


Figure A.1: Virgin refractory (chamotte) material.

Table A.5: Virgin refractory (chamotte) material.

Temperature [°C]	Thermal Diffusivity [mm <sup>2</sup> /s]	Thermal Conductivity [W/(m·K)]	Specific Heat [J/(g·K)]
26.4	0.70	0.85	0.57
101.5	0.80	1.51	0.89
150.9	0.73	1.59	1.01
198.2	0.68	1.50	1.02
250.2	0.65	1.46	1.06
301.1	0.62	1.45	1.09
351.5	0.60	1.43	1.12
401.7	0.59	1.43	1.14
451.9	0.58	1.43	1.16
502.0	0.57	1.43	1.18

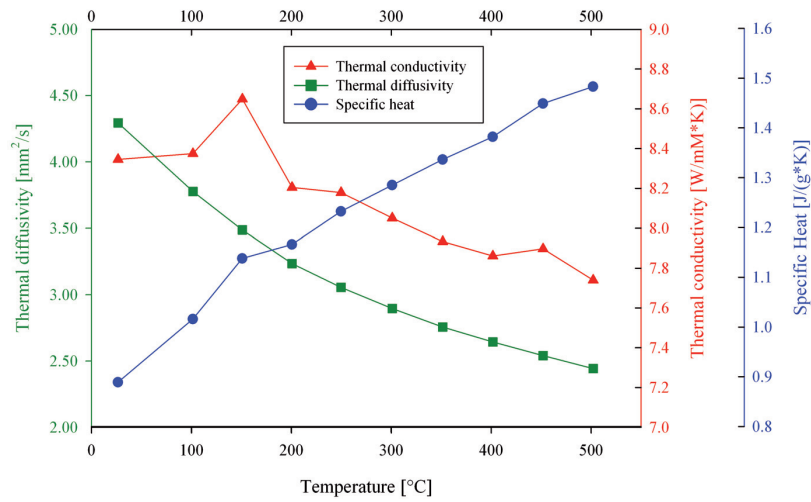


Figure A.2: 2A Lens Slice1.

Table A.6: 2A Lens Slice1.

Temperature [°C]	Thermal Diffusivity [mm <sup>2</sup> /s]	Thermal Conductivity [W/(m·K)]	Specific Heat [J/(g·K)]
26.6	4.290	8.35	0.89
101.6	3.78	8.38	1.02
151	3.49	8.65	1.14
200.7	3.24	8.21	1.17
249.8	3.06	8.18	1.23
301	2.90	8.05	1.29
351.5	2.76	7.93	0.89
401.7	2.64	7.86	1.38
451.9	2.54	7.90	1.45
502.1	2.44	7.74	1.48

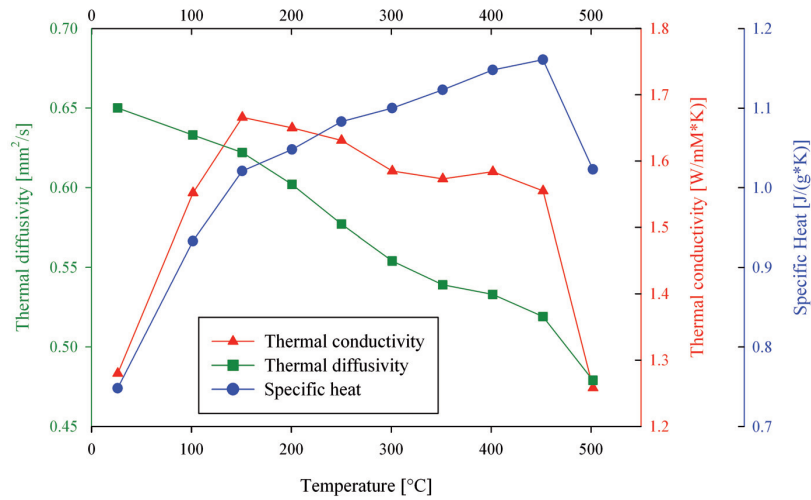


Figure A.3: 2A Lens Slice2.

Table A.7: 2A Lens Slice2.

Temperature [°C]	Thermal Diffusivity [mm <sup>2</sup> /s]	Thermal Conductivity [W/(m·K)]	Specific Heat [J/(g·K)]
26.2	0.65	1.28	0.75
101.6	0.63	1.55	0.93
150.9	0.62	1.67	1.02
200.8	0.60	1.65	1.05
250.2	0.58	1.63	1.08
301.0	0.55	1.59	1.10
351.5	0.54	1.57	1.12
401.7	0.53	1.58	1.15
451.9	0.52	1.56	1.16
502.0	0.48	1.26	1.02

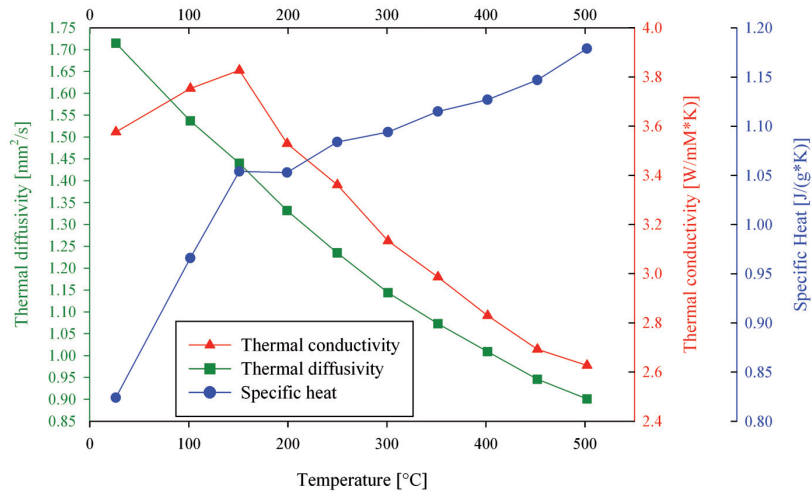


Figure A.4: 2A Lens Slice3.

Table A.8: 2A Lens Slice3.

Temperature [°C]	Thermal Diffusivity [mm <sup>2</sup> /s]	Thermal Conductivity [W/(m·K)]	Specific Heat [J/(g·K)]
26.4	1.71	3.58	0.82
101.6	1.54	3.76	0.97
151	1.44	3.83	1.06
199.3	1.34	3.53	1.06
249.9	1.24	3.37	1.09
301.2	1.15	3.14	1.10
351.5	1.08	2.99	1.12
401.7	1.01	2.83	1.13
451.9	0.95	2.70	1.15
502.1	0.90	2.63	1.18

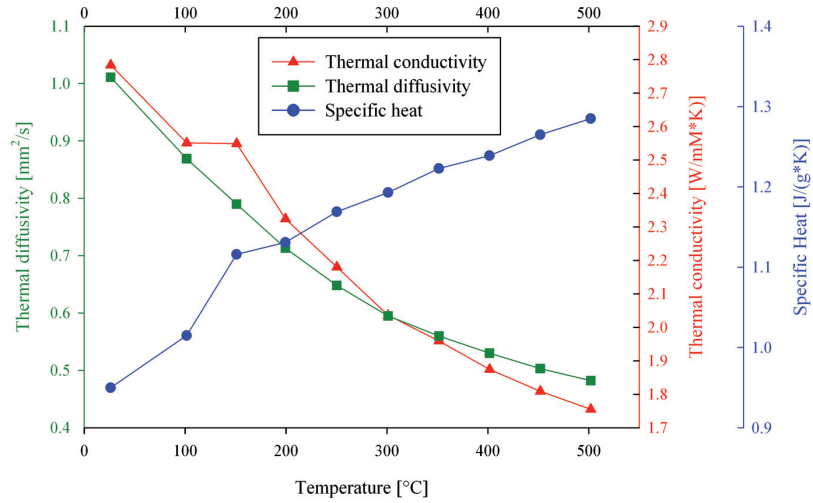


Figure A.5: 3A Lens Slice1.

Table A.9: 3A Lens Slice1.

Temperature [°C]	Thermal Diffusivity [mm <sup>2</sup> /s]	Thermal Conductivity [W/(m· K)]	Specific Heat [J/(g· K)]
26.2	1.01	2.78	0.95
101.6	0.87	2.55	1.02
151	0.79	2.55	1.12
199.4	0.71	2.32	1.13
250.3	0.65	2.18	1.17
301.1	0.60	2.04	1.19
351.6	0.56	1.96	1.22
401.7	0.53	1.87	1.24
451.9	0.50	1.81	1.27
502	0.48	1.76	1.29

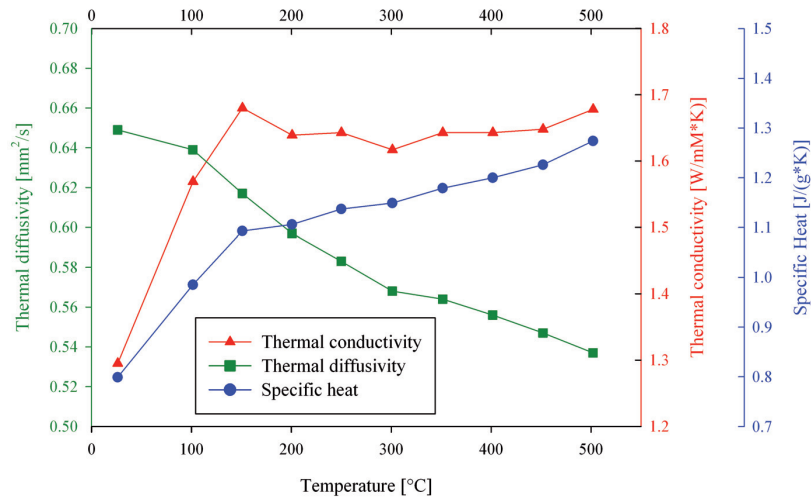


Figure A.6: 3A Lens Slice5.

Table A.10: 3A Lens Slice5.

Temperature [°C]	Thermal Diffusivity [mm <sup>2</sup> /s]	Thermal Conductivity [W/(m·K)]	Specific Heat [J/(g·K)]
26.2	0.65	1.30	0.80
101.6	0.64	1.57	0.99
151	0.62	1.68	1.09
200.8	0.60	1.64	1.11
250.1	0.58	1.64	1.14
301.1	0.57	1.62	1.15
351.5	0.56	1.64	1.18
401.7	0.56	1.64	1.20
451.9	0.55	1.65	1.23
502.1	0.54	1.68	1.27

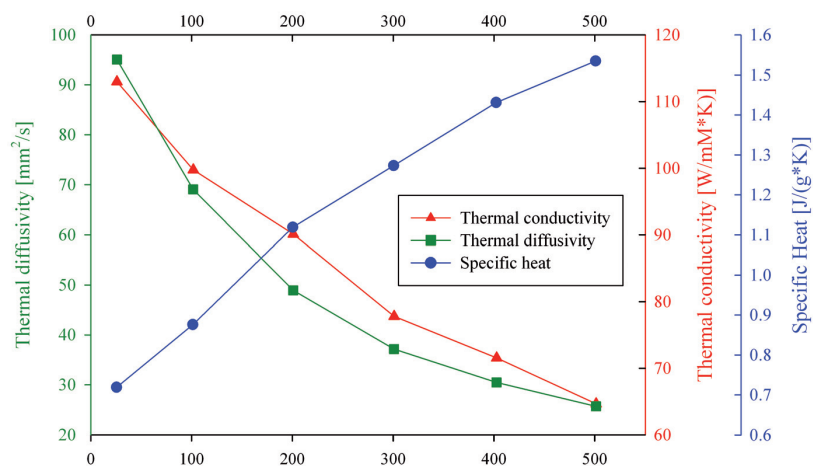


Figure A.7: Virgin Graphitized Carbon (GC).

Table A.11: Virgin Graphitized Carbon (GC).

Temperature [°C]	Thermal Diffusivity [mm²/s]	Thermal Conductivity [W/(m·K)]	Specific Heat [J/(g·K)]
25.9	95.06	113.0	0.7
101.6	69.06	99.7	0.9
200.8	48.93	90.1	1.1
300.9	37.18	77.8	1.3
402.6	30.48	71.5	1.4
501.3	25.71	64.7	1.5
602.1	22.45	59.4	1.6
702	19.84	54.8	1.7
801.4	17.96	52.0	1.8
900.6	16.42	47.8	1.8



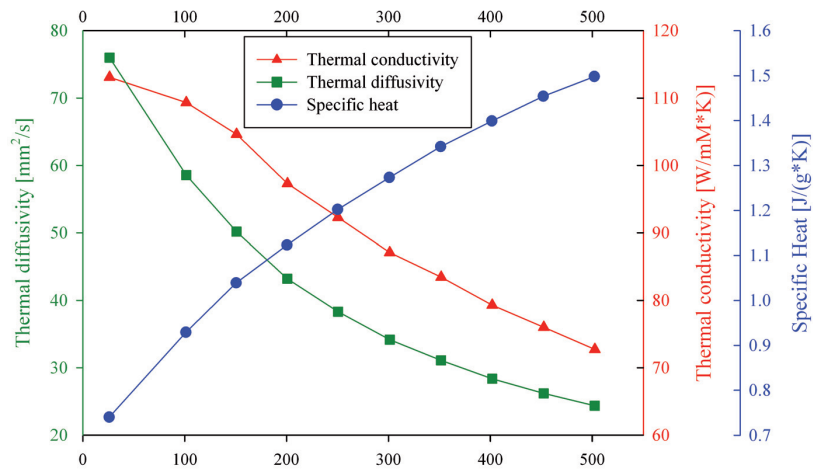


Figure A.8: 2A Carbon Slice2.

Table A.12: 2A Carbon Slice2.

Temperature [°C]	Thermal Diffusivity [mm <sup>2</sup> /s]	Thermal Conductivity [W/(m·K)]	Specific Heat [J/(g·K)]
26.2	75.99	113.08	0.74
101.5	58.555	109.32	0.93
150.9	50.169	104.61	1.04
200.8	43.205	97.31	1.12
250.5	38.33	92.29	1.20
301.2	34.167	87.09	1.27
351.6	31.095	83.45	1.34
401.8	28.361	79.28	1.40
452.4	26.189	76.01	1.45
502.5	24.35	72.72	1.50

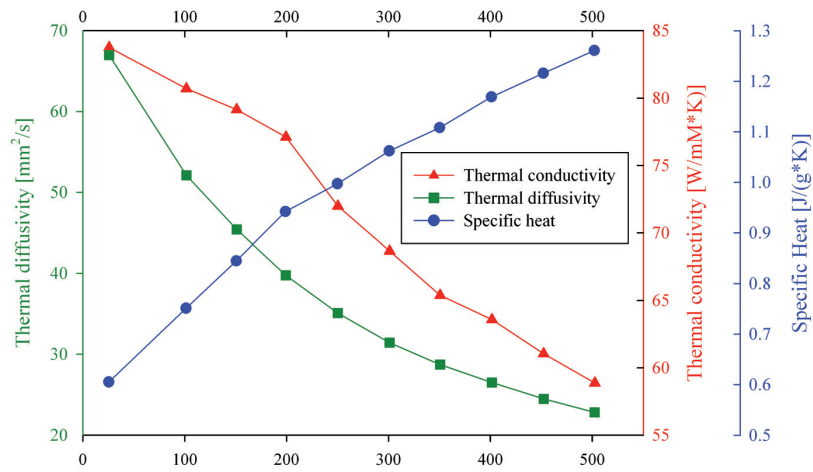


Figure A.9: 2A Carbon Slice3.

Table A.13: 2A Carbon Slice3.

Temperature [°C]	Thermal Diffusivity [mm <sup>2</sup> /s]	Thermal Conductivity [W/(m·K)]	Specific Heat [J/(g·K)]
25.9	66.98	83.75	0.61
101.7	52.11	80.70	0.75
151	45.42	79.14	0.85
199.3	39.76	77.10	0.94
250.3	35.09	71.98	1.00
301.1	31.43	68.66	1.06
350.6	28.72	65.38	1.11
401.5	26.50	63.57	1.17
452.3	24.48	61.04	1.22
502.5	22.80	58.86	1.26

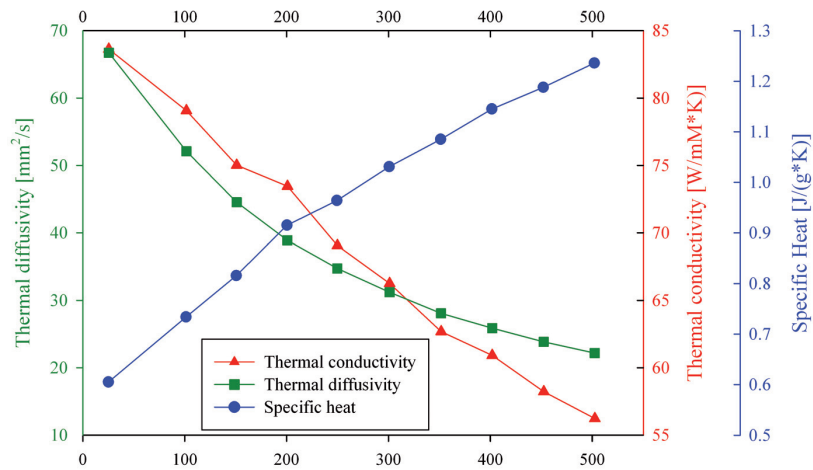


Figure A.10: 2A Carbon Slice4.

Table A.14: 2A Carbon Slice4.

Temperature [°C]	Thermal Diffusivity [mm <sup>2</sup> /s]	Thermal Conductivity [W/(m·K)]	Specific Heat [J/(g·K)]
25.9	70.43	112.12	0.77
101.6	53.16	102.93	0.94
150.9	47.01	102.24	1.06
200.8	40.75	96.59	1.15
250.5	36.00	89.70	1.21
301.3	32.25	85.39	1.29
351.6	29.22	81.26	0.90
401.8	26.64	76.56	1.40
452	24.57	73.83	1.47
502.2	22.72	69.82	1.50

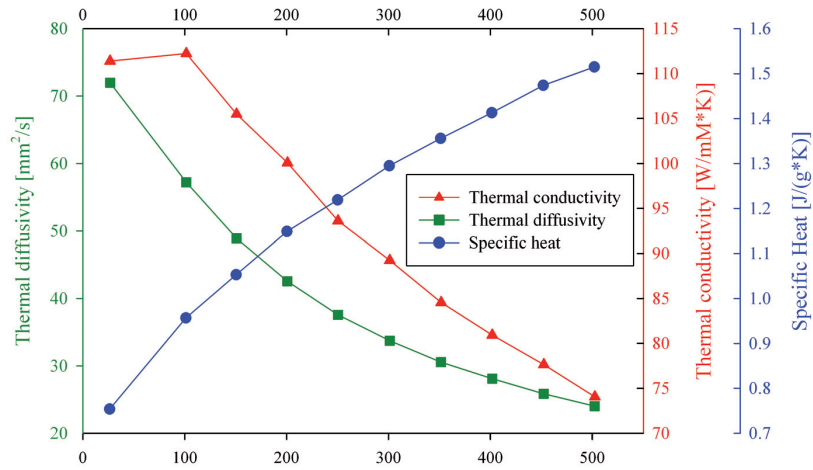


Figure A.11: 2A Carbon Slice5.

Table A.15: 2A Carbon Slice5.

Temperature [°C]	Thermal Diffusivity [mm <sup>2</sup> /s]	Thermal Conductivity [W/(m· K)]	Specific Heat [J/(g· K)]
25.9	70.43	112.12	0.77
26.8	71.98	111.40	0.75
101.5	57.21	112.24	0.96
150.9	48.90	105.49	1.05
200.8	42.56	100.06	1.15
250.5	37.56	93.62	1.22
301.2	33.72	89.23	1.30
351.6	30.54	84.55	1.36
401.8	28.08	80.92	1.41
452.4	25.85	77.64	1.47
502.5	24.02	74.05	1.52

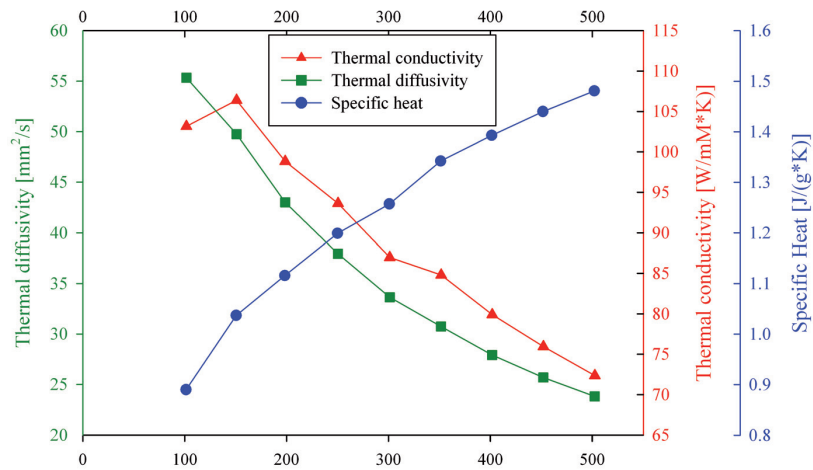


Figure A.12: 3A Carbon Slice5.

Table A.16: 3A Carbon Slice5.

Temperature [°C]	Thermal Diffusivity [mm <sup>2</sup> /s]	Thermal Conductivity [W/(m· K)]	Specific Heat [J/(g· K)]
26.8	75.53	hidden	hidden
101.7	55.34	103.17	0.89
150.9	49.77	106.39	1.04
198.6	43.00	98.83	1.12
250.4	37.95	93.64	1.20
301.2	33.65	86.97	1.26
351.6	30.74	84.81	1.34
401.7	27.92	79.90	1.39
452	25.69	75.95	1.44
502.5	23.82	72.36	1.48

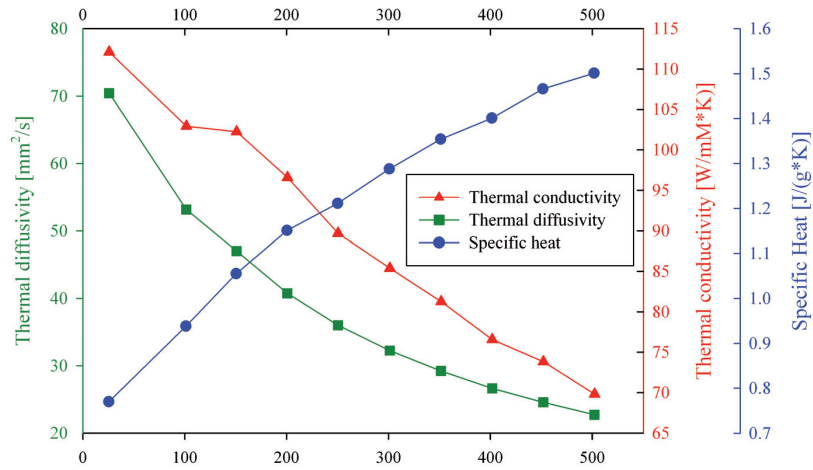


Figure A.13: 3A Carbon Slice4.

Table A.17: 3A Carbon Slice4.

Temperature [°C]	Thermal Diffusivity [mm <sup>2</sup> /s]	Thermal Conductivity [W/(m·K)]	Specific Heat [J/(g·K)]
25.9	70.43	112.12	0.77
101.6	53.16	102.93	0.94
150.9	47.01	102.24	1.06
200.8	40.75	96.59	1.15
250.5	36.00	89.70	1.21
301.3	32.25	85.39	1.29
351.6	29.22	81.26	0.90
401.8	26.64	76.56	1.40
452	24.57	73.83	1.47
502.2	22.72	69.82	1.50

## B Part II

### B.1 Thermal Model

**Table B.18:** Chemical composition of lining materials [wt%] (respective reference in squared brackets), GC is the abbreviation for graphitized carbon.

	Refract.	Insul. (4b)	Insul. (4a)	Ramming paste	Sidewall block	Collector bar / Steel shell	Side-ledge	Carbon block
Specific.	Chamotte					S235JRG2		GC
SiO <sub>2</sub>	68	77						
Al <sub>2</sub> O <sub>3</sub>	26	9					2	
CaO		0.8						
MgO		1.3						
Fe <sub>2</sub> O <sub>3</sub>		7				99.83		
Fe								
K <sub>2</sub> O		1.6						
C				100		0.17		100
SiC					75			
Si <sub>3</sub> N <sub>4</sub>					25			
Na <sub>3</sub> AlF <sub>6</sub>							90	
CaF <sub>2</sub>							3	
AlF <sub>3</sub>							5	

**Table B.19:** Density of virgin and spent lining materials (respective reference in squared brackets). The spent data was measured during this work. GC is the abbreviation for graphitized carbon.

	<b>Refract.</b>	<b>Insul. (4b)</b>	<b>Insul. (4a)</b>	<b>Ramming paste</b>	<b>Sidewall block</b>	<b>Collector bar / Steel shell</b>	<b>Side-ledge</b>	<b>Carbon block</b>	<b>Mortar</b>
<b>Specific.</b>	Chamotte					S235JRG2		GC	
Density [kg/m <sup>3</sup> ] (virgin)	2150	550	750	1500	2680	7850	1957	1650	1050
Density [kg/m <sup>3</sup> ] (spent)	2623				2600 top, 2900 bottom			2097	



**Table B.20:** Thermal conductivity of lining materials.

<b>Material</b>	<b>T [K]</b>	<b><math>\kappa</math> [W/(m·K)]</b>
Collector bar - S235JRG2	373.15	58
	573.15	49
	873.15	36
	1273.15	27
Insulation (4b)	473.15	0.091
	673.15	0.101
	873.15	0.113
Insulation (4a)	473.15	0.15
	673.15	0.17
	873.15	0.19
Refractory - Chamotte	573.15	0.23
	873.15	0.49
	1173.15	0.50
Sidelining	293.15	44
	473.15	41
	673.15	38
	873.15	28
Sideledge	573.15	1.36
	773.15	1.50
	973.15	2.03
	1173.15	2.94
Cathode Carbon - Graphitized	298.15	125
	473.15	105
	673.15	90
	873.15	80
	1073.15	70
	1273.15	65
Ramming Paste		10
Steel Shell	373.15	58
	573.15	49
	873.15	36
	1273.15	27
Mortar (sidewall)		0.4

**Table B.21:** Calculated heat capacity of lining materials. The data for the single components as function of temperature were taken from [76].

<b>Material</b>	<b>T [K]</b>	<b>C<sub>p</sub> [J/(kg·K)]</b>	<b>Reference</b>
Collector bar - S235JRG2	298.15	160.76	[156]
	300	161.19	
	400	177.82	
	500	194.09	
	600	210.25	
	700	227.08	
	800	248.71	
	900	281.31	
	1000	352.30	
Insulation (4a/b)	298.15	745.84	[156]
	300	748.95	
	400	890.87	
	500	991.07	
	600	1067.05	
	700	1135.20	
	800	1210.84	
Refractory - Chamotte	298.15	748.13	[156]
	300	751.40	
	400	899.06	
	500	1001.56	
	600	1077.95	
	700	1144.98	
	800	1217.82	
	900	1144.15	
	1000	1161.55	
	1100	1189.62	
	1200	1201.77	
	1300	1211.95	

Continued on next page

Table B.21 – continued from previous page

Material	T [K]	C <sub>p</sub> [J/(kg·K)]	Reference
Sidelineing	298.15	675.98	[156]
	300	678.76	
	400	834.76	
	500	954.74	
	600	1038.64	
	700	1098.75	
	800	1143.49	
	900	1178.04	
	1000	1205.60	
	1100	1228.17	
	1200	1247.07	
1300	1263.19		
Sideledge	400	1086.56	[156]
	500	1156.21	
	600	1220.16	
	700	1286.37	
	800	1332.50	
	900	1269.75	
	1000	1274.79	
	1100	1337.61	
	1200	1400.38	
1300	1463.11		
Cathode Carbon - Graphitized	298.15	708.70	[156]
	300	715.53	
	400	993.03	
	500	1218.33	
	600	1405.75	
	700	1547.79	
	800	1650.78	
	900	1731.12	
	1000	1795.57	
	1100	1847.69	
	1200	1890.15	
1300	1924.70		

Continued on next page

Table B.21 – continued from previous page

Material	T [K]	C <sub>p</sub> [J/(kg·K)]	Reference
Ramming Paste	298.15	708.70	[156]
	300	715.53	
	400	993.03	
	500	1218.33	
	600	1405.75	
	700	1547.79	
	800	1650.78	
	900	1731.12	
	1000	1795.57	
	1100	1847.69	
	1200	1890.15	
1300	1924.70		
Steel Shell	298.15	160.76	[156]
	300	161.19	
	400	177.82	
	500	194.09	
	600	210.25	
	700	227.08	
	800	248.71	
	900	281.31	
1000	352.30		
Mortar (sidewall)		1000	[160]

**Table B.22:** Comparison of temperatures within the cell between the models with and without collector bar.

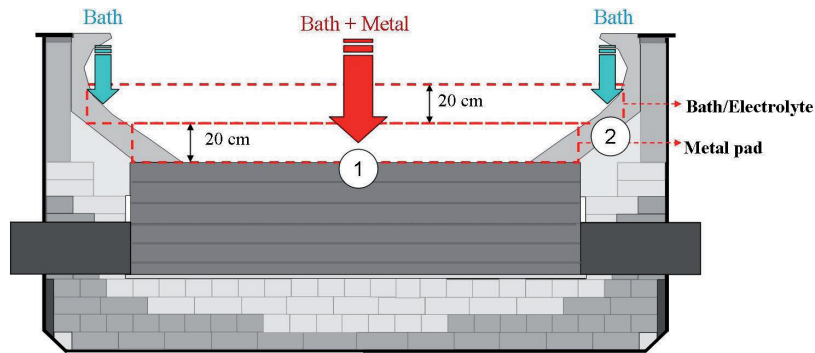
Material	Position (x,y) [m]	T [°C]	Position (x,y) [m]	T [°C]
	Model with collector bar		Model without collector bar	
Carbon block	(0.4,0.696)	965	(0.4,0.696)	965
Collector bar	(0.4,0.446)	958		
Refractory	(0.4,0.266)	947	(0.4,0.266)	954
Insulation	(0.4,0.074)	745	(0.4,0.074)	750
Steel shell	(0.4,0)	165	(0.4,0)	166
Carbon block	(1.4,0.696)	965	(1.4,0.696)	965
Collector bar	(1.4,0.446)	901		
Refractory	(1.4,0.266)	866	(1.4,0.266)	949
Insulation	(1.4,0.138)	779	(1.4,0.138)	855
Steel shell	(1.4,0)	124	(1.4,0.0)	128
Sidededge	(1.813,1.1)	962	(1.813,1.1)	962
SiC block	(1.925,1.1)	492	(1.925,1.1)	492
Mortar	(2,1.1)	472	(2,1.1)	471
Steel shell	(2.015,1.1)	357	(2.015,1.1)	356
Sidededge	(1.53,1.1)	958	(1.53,1.1)	959
Ramming paste	(1.67,1.1)	836	(1.67,1.1)	855
SiC block	(1.925,1.1)	510	(1.925,1.1)	508
Mortar	(2,1.1)	480	(2,1.1)	478
Steel shell	(2.015,1.1)	338	(2.015,1.1)	328

**B.2 Thermal-Mechanical Model****Table B.23:** Thermal expansion coefficients.

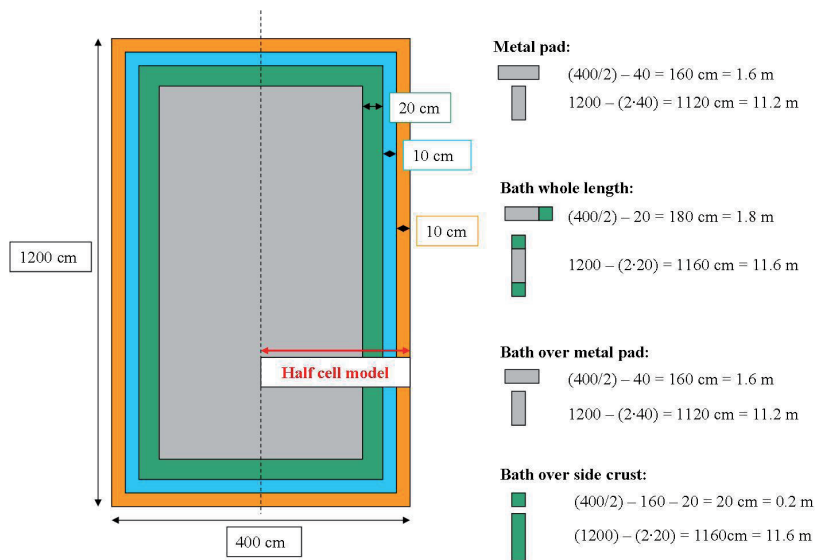
<b>Material</b>	<b>T [K]</b>	<b><math>\alpha</math> [<math>10^{-6}/\text{K}</math>]</b>
Collector bar - S235JRG2	311.15	11.7
	366.15	12.0
	422.15	12.4
	477.15	12.7
	533.15	13.1
	589.15	13.4
	644.15	13.7
	700.15	14.0
Insulation (4b)		2.0
Insulation (4a)		2.0
Refractory - Chamotte	473.15	3.65
	673.15	4.00
	873.15	4.35
	1123.15	4.74
	1273.15	5.01
Sidelining	873.15	4.00
	1073.15	4.30
	1273.15	4.50
Sidededge		1.00
Cathode Carbon - Graphitized		4.00
Ramming Paste	473.15	2.50
	673.15	4.00
	873.15	3.50
	1073.15	-1.00
	1273.15	2.50
Steel Shell	with reference to collector bar	
Mortar (sidewall)	293.15	10
	1023.15	

**Table B.24:** Poisson's ratio and Young's Modulus.

<b>Material</b>	<b>T [K]</b>	<b>E [10<sup>9</sup>Pa]</b>	<b><math>\mu</math></b>
Collector bar - S235JRG2	298.15	210	0.30
	473.15	190	
	673.15	120	
	873.15	60	
	1023.15	18	
	1073.15	10	
	1123.15	4.2	
	1223.15	3.7	
Insulation (4b)	298.15	0.35	0.12
Insulation (4a)	298.15	2.2	0.15
Refractory - Chamotte	298.15	19.1	0.22
	298.15	16.9	0.22
Sidelining	298.15	183.8	0.25
Sidededge		6	0.20
Cathode Carbon - Graphitized	298.15	4	0.11
Ramming Paste	473.15	0.001	0.10
	773.15	0.003	
	973.15	4	
	1273.15	5	
Steel Shell	298.15	206.8	0.30
	673.15	128	
	873.15	61	
Mortar (sidewall)	over 298.15	0.09	0.20



**Figure B.14:** Sketch of the short cross section of the cathode lining in aluminium electrolysis cell including the dimensions and positions used to represent the boundary conditions 1 and 2 from Fig. 11.4.



**Figure B.15:** Top view of the pot lining including the dimensions used to represent the boundary conditions 1 and 2 from Fig. 11.4.



### B.3 Chemical Expansion

Reformulation of the COMSOL code with respect to  $Ent$  the entropy per unit volume [ $J/(m^3 \cdot K)$ ]:

$$\begin{aligned}
 Ent = [\alpha_{th} + \alpha_{ch}] \cdot \left\{ \right. & \sigma_x - j \cdot \left[ \text{imag} \left( E \cdot \frac{(1-\nu)}{(1+\nu) \cdot (1-2 \cdot \nu)} \right) \cdot \epsilon_x \right. \\
 & + \text{imag} \left( E \cdot \frac{\nu}{(1+\nu) \cdot (1-2 \cdot \nu)} \right) \cdot \epsilon_y + \text{imag}(0) \cdot \epsilon_{xy} \left. \right] \\
 & + \sigma_y - j \cdot \left[ \text{imag} \left( E \cdot \frac{\nu}{(1+\nu) \cdot (1-2 \cdot \nu)} \right) \cdot \epsilon_x \right. \\
 & + \text{imag} \left( E \cdot \frac{(1-\nu)}{(1+\nu) \cdot (1-2 \cdot \nu)} \right) \cdot \epsilon_y + \text{imag}(0) \cdot \epsilon_{xy} \left. \right] \\
 & + \sigma_z - j \cdot \left[ \text{imag} \left( E \cdot \frac{\nu}{(1+\nu) \cdot (1-2 \cdot \nu)} \right) \cdot \epsilon_x \right. \\
 & \left. \left. + \text{imag} \left( E \cdot \frac{\nu}{(1+\nu) \cdot (1-2 \cdot \nu)} \right) \cdot \epsilon_y + \text{imag}(0) \cdot \epsilon_{xy} \right] \right\} \quad (1)
 \end{aligned}$$